Erosion-Corrosion of Carbon Steel in Complex Flow Geometries in Oil & Gas CO_2 Environments

Joshua James Owen

Submitted in accordance with the requirements for the degree of
Doctor of Philosophy

The University of Leeds
Institute of Functional Surface, IFS
School of Mechanical Engineering

June 2018

Publication Statement

The candidate confirms that the work submitted is his/her own, except where work which has formed part of jointly-authored publications has been included. The contribution of the candidate and the other authors to this work has been explicitly indicated below. The candidate confirms that appropriate credit has been given within the thesis where reference has been made to the work of others.

In all papers listed below, the primary author completed all experimental studies, evaluation of data and preparation of publications. All authors contributed to proof reading of the articles prior to publication.

Papers contributing to this thesis:

- Owen, J., Ramsey, C., Barker, R. and A. Neville. *Erosion-corrosion interactions of X65 carbon steel in CO_2 oil and gas environments.* Submitted to Wear, May 2018.

Acknowledgements

I would like to thank my primary supervisor Professor Anne Neville for her supervision, enthusiasm and advice throughout my PhD. I am also extremely grateful for the supervision provided by Dr. Richard Barker during my PhD and the daily support and advice he provided to help with my experimental work and the development of CFD models. Without their support this thesis would not have been possible.

I would like to thank Shell UK for their financial sponsorship and technical advice provided throughout the course of the PhD.

I would also like to express my sincere appreciation to the IFS technicians Jordan Thomas, Mick Huggan, Paul Kilburn and Andrew O'Brien for their hard work and support in the labs. I am particularly grateful for the support provided by Mick, who was always willing to help during the design of my pipe elbow component, which would not have been successful without his expert advice and patience. I would also like to thank Graham Brown for his advice on 3D printing to manufacture the elbow component.

I would like to thank Hannah for her support during my PhD and my family (Mum, Dad, Keith and Ben). I would also like to thank all of my friends and colleagues who I have worked with in IFS at the University of Leeds during my PhD and in particular Ben, Danny, Rehan, Andy, Leo, Mohammed al-Khateeb, Will, Tayo, Kevin and Abi.

Abstract

When sand is present in carbon dioxide (CO_2) corrosion environments in oil and gas pipe flow, wear rates of carbon steel pipelines can be severe. This wear mechanism is known as erosion-corrosion and consists of erosion and corrosion components, with degradation enhanced by interactions between the mechanisms. A lack of understanding of erosion-corrosion of carbon steel and the mechanisms contributing to enhanced degradation through erosion and corrosion interactions exists. Erosion-corrosion of carbon steel in CO_2 conditions was the subject of investigation in this work.

A submerged impinging jet (SIJ) was used to complete a case study of erosion-corrosion degradation of X65 carbon steel in field conditions at high flow velocities up to 20 m/s in a 60°C, pH 4.7, 2 wt.% NaCl solution containing up to 1000 mg/L of sand particles with an average diameter of 250 µm. High degradation rates, some in excess of 25 mm/yr, were measured and whilst corrosion inhibitors added to protect the X65 surface did reduce corrosion rates, they did not reduce erosion degradation, resulting in degradation rates remaining greater than 10 mm/yr in the most severe conditions evaluated.

An investigation into the mechanisms of erosion-corrosion interactions revealed that work-hardened layers were thick and more refined on samples subject to erosion conditions compared with samples used in erosion-corrosion tests. This was explained by removal of the work-hardened layers, formed after particle impacts, through electrochemical dissolution, resulting in corrosion-enhanced erosion, which accounted for up to 20% of overall erosion-corrosion degradation at a flow velocity of 20 m/s in a 60°C, CO_2-saturared solution containing 1000 mg/L of sand. Erosion-enhanced corrosion was shown not to be significant in the conditions tested.

Flow geometry was also shown to have a significant influence on the erosion-corrosion degradation rates. A 90° elbow was designed to evaluate erosion-corrosion in pipe flow, CO_2-saturated, pH 4 conditions at a flow velocity of 6 m/s that showed small erosion contributions to erosion-corrosion degradation on the outer radius of the elbow, with flow induced corrosion accounting for the majority of degradation. To fully understand erosion-corrosion conditions in both flow geometries, computational fluid dynamics (CFD) was used to predict mass transfer coefficients and sand particle trajectories in the flow. Predictions were used to define the erosion mechanisms in the different geometries and to explain why degradation rates could vary significantly between different flow geometries.

Table of Contents

Publication Statement ... **ii**

Acknowledgements ... **iii**

Abstract ... **iv**

Table of Contents ... **v**

List of Tables ... **xi**

List of Figures ... **xiv**

List of Abbreviations ... **xxx**

Chapter 1 Introduction, Research Objectives and Project Background ... **1**

1.1 Introduction ... 1

1.2 Significance of Corrosion and Erosion-Corrosion in the Oil and Gas Industry ... 2

1.3 Project Objectives ... 3

1.4 Thesis Structure ... 4

Chapter 2 Fundamentals of Erosion-Corrosion and Fluid Dynamics ... **6**

2.1 Introduction ... 6

2.2 Definition of Erosion-Corrosion ... 6

2.3 Mechanisms of Erosion ... 7

2.4 Aqueous Corrosion Mechanisms ... 8

2.4.1 Fundamentals of Aqueous Corrosion ... 8

2.4.2 Electrical Double Layer ... 10

2.5 Fundamentals of Computational Fluid Dynamics ... 11

2.5.1 Laws of Fluid Motion ... 11

2.5.2 Navier-Stokes Equations ... 13

Chapter 3 Review of Carbon Steel and Chemical Inhibitor Performance in Sand-Producing CO_2 Oil and Gas Conditions ... **14**

3.1 Introduction ... 14

3.2 Parameters Influencing Corrosion Mechanisms ... 15

3.2.1 Anodic and Cathodic Reactions in CO_2 Conditions ... 16

3.2.2 Effects of Temperature, Water Chemistry & Partial Pressure ... 19

3.2.3 Flow-Induced Corrosion ... 20

3.3 Parameters Influencing the Erosion of Ductile Materials ... 23

3.3.1 Impingement of Particles on Metal Surfaces ... 24

3.3.2 Effect of Flow on Particles 28
3.3.3 Particle Properties 33
3.3.4 Target Surface Properties 35
3.4 Modelling Erosion of Ductile Materials 37
3.4.1 Finnie Erosion Model 38
3.4.2 Erosion/Corrosion Research Centre Erosion Models 40
3.4.3 CFD Predictions of Particle Trajectories 42
3.5 Erosion-Corrosion of Carbon Steel 47
3.5.1 Contributing Parameters to Erosion-Corrosion 47
3.5.2 Erosion-Enhanced Corrosion 50
3.5.3 Corrosion-Enhanced Erosion 51
3.5.4 Erosion-Corrosion in Different Flow Geometries 53
3.6 Modelling Erosion-Corrosion 56
3.7 Mitigating Erosion-Corrosion 57
3.8 Summary of Erosion-Corrosion Literature and Further Research Required 61
Chapter 4 Experimental and CFD Modelling Methodology 64
4.1 Introduction 64
4.2 Flow-Induced Corrosion, Erosion and Erosion-Corrosion Tests using an SIJ 65
4.2.1 Description of the SIJ & Basic Test Methodology 66
4.2.2 Sample Preparation 68
4.3 Test Conditions 69
4.3.1 Field Conditions Replicated in the SIJ 70
4.3.2 Corrosion Inhibitors 72
4.4 Static Corrosion Tests 73
4.5 Measurement Techniques 74
4.5.1 Mass Loss Measurements 74
4.5.2 Three Electrode Cell 75
4.5.3 Direct Current Techniques 76
4.5.4 Alternating Current Techniques 78
4.5.5 Electrochemistry in SIJ Tests 79
4.6 Surface Analysis Techniques 80
4.6.1 White Light Interferometry 81
4.6.2 SEM Analysis 81
4.6.3 Hardness Testing 82

4.6.4 Analysis of Sand Particle Size 82
4.6.5 Subsurface Analysis Using a Focused Ion Beam (FIB) 83
4.7 Using CFD to Predict Fluid Flow, Particle Trajectories and the Transport of Diluted Species 83
4.7.1 Developing CFD Models Using COMSOL Multiphysics 84
4.7.2 Effects of Turbulence 85
4.7.3 Turbulence Models 86
4.7.4 Law of the Wall 89
4.7.5 Relevance of Turbulence to SIJ and Pipe Flow 90
Chapter 5 Case Study of Erosion-Corrosion of X65 Carbon Steel and Chemical Inhibitor Evaluation in Oil & Gas CO_2 Environments 92
5.1 Introduction 92
5.2 Static Corrosion Rates 93
5.3 Flow-Induced Corrosion of X65 and Inhibitor Evaluation 94
5.3.1 Flow-Induced Corrosion of X65 in Blank Conditions 94
5.3.2 Evaluation of Corrosion Inhibitor A 100
5.3.3 Evaluation of Corrosion Inhibitor B 104
5.3.4 Flow-Induced Corrosion Efficiency of Inhibitors 107
5.4 Erosion-Corrosion 109
5.4.1 Erosion and Erosion-Corrosion of X65 Carbon Steel..... 110
5.4.2 Evaluation of Corrosion Inhibitor A & Inhibitor B 112
5.4.3 Erosion-Corrosion Interactions 114
5.5 Summary and Conclusions 116
Chapter 6 Erosion-Corrosion Interactions of X65 Carbon Steel in CO_2 Oil & Gas Environments 118
6.1 Introduction 118
6.2 Experimental Methodology 119
6.3 Prediction of Flow in the SIJ 120
6.3.1 Theory of Turbulent Axisymmetric Jet Flow 121
6.3.2 Model Description 123
6.3.3 Mesh Sensitivity Study & Model Validation 125
6.3.4 Prediction of Flow through SIJ Nozzle 128
6.4 Prediction of Particle Trajectories in the SIJ 130
6.4.1 Mesh Sensitivity Study 134
6.4.2 Prediction of Particle Trajectories 136
6.4.3 Influence of Particle Size on Prediction 137

6.4.4 Influence of Surface Profile on Prediction 139
6.4.5 Influence of Repeated Particle Impacts on Prediction 141
6.4.6 Influence of the Squeeze Film on Prediction 143
6.4.7 Particle-Particle Interactions and Fluid Coupling 144
6.4.8 Influence of Particle Initial Velocity and Turbulent Dispersion 144
6.4.9 Comparison with Gnanavelu Model 147
6.5 Measurement of Erosion-Corrosion and Interactions in SIJ Tests 148
6.5.1 Definition of Regions on the Surface of X65 Samples Used in the SIJ 148
6.5.2 Erosion-Corrosion and Erosion-Corrosion Interactions 150
6.6 Analysis of Surfaces 154
6.6.1 Surface Profiles 154
6.6.2 Degradation of Sand Particles over Time 155
6.6.3 SEM Analysis of Surfaces 156
6.6.4 Surface Roughening and Erosion-Enhanced Corrosion 158
6.6.5 Work-Hardening, Removal of Work-Hardened Layers and Corrosion-Enhanced Erosion 161
6.6.6 Analysis of Work-Hardened Layers 163
6.7 Summary and Conclusions 167
Chapter 7 Development of an Elbow for Erosion-Corrosion Evaluation of X65 Carbon Steel 168
7.1 Introduction 168
7.2 Design Criterion 169
7.3 Elbow Design Detail 171
7.3.1 Design Overview 171
7.3.2 Manufacturing the Elbow 174
7.3.3 X65 Samples 174
7.3.4 Creating a Flow Loop Using the SIJ 176
7.4 Evaluation of X65 Degradation in Pipe Flow Conditions 177
7.4.1 Experimental Procedure and Operating Conditions 177
7.4.2 Erosion-Corrosion Tests 180
7.5 Summary and Conclusions 185
Chapter 8 Using CFD to Evaluate the Influence of Flow Parameters on Erosion-Corrosion Mechanisms 186
8.1 Introduction 186

8.2 Prediction of Particle Trajectories in the Elbow 188
8.2.1 Elbow Model Description 189
8.2.2 Validation and Prediction of Fluid Flow 190
8.2.3 Prediction of Particle Trajectories 192
8.3 Influence of Flow on Corrosion 194
8.3.1 Mass Transfer and Corrosion 194
8.3.2 Theory of Species Transport in Turbulent Flow 196
8.3.3 CFD Prediction of H^+ Mass Transport 199
8.4 Validation of Methodology for Predicting Mass Transfer Coefficients Using CFD 200
8.4.1 Straight Pipe Model Description 200
8.4.2 Model Sensitivity Study 201
8.4.3 Prediction of Mass Transfer Coefficients & Validation 204
8.5 Prediction of Mass Transfer Coefficients in the Elbow 206
8.5.1 Model Description 207
8.5.2 Prediction of Mass Transfer Coefficients 208
8.6 Prediction of Mass Transfer Coefficients in the SIJ 208
8.6.1 Model Description 209
8.6.2 Prediction of Mass Transfer Coefficients 210
8.7 Summary and Conclusions 211

Chapter 9 Discussion of Erosion-Corrosion Mechanisms and Erosion-Corrosion in Complex Flow Geometries 213

9.1 Introduction 213
9.2 Flow-Induced Corrosion and Erosion-Corrosion of X65 214
9.2.1 Corrosion Rate Measurements 215
9.2.2 Flow-Induced Corrosion Mechanisms 217
9.2.3 Effects of Sand Particle Impingement on X65 Degradation 220
9.2.4 Interactions between Erosion and Corrosion 222
9.2.5 Influence of Flow and Sand on Corrosion Inhibitors 224
9.3 Mechanisms of Erosion-Corrosion Interactions 227
9.3.1 Erosion-Enhanced Corrosion 228
9.3.2 Corrosion-Enhanced Erosion 230
9.4 Using CFD to Improve the Understanding of Material Removal Mechanisms after Particle Impingement 237
9.4.1 Significance of Assumptions in CFD Simulations 237

9.4.2 Validation of CFD Model and Recommended Methodology 239
9.4.3 Influence of Particle Impingement Parameters 240
9.5 Erosion-Corrosion of Carbon Steel in Pipe Flow 242
9.5.1 Comparison of Erosion Conditions in the Elbow and SIJ . 243
9.5.2 Erosion-Corrosion Evaluation of X65 Using an Elbow 244
9.6 An Improved Methodology for Erosion-Corrosion Testing 247
9.6.1 Suggested Approach to Erosion-Corrosion Testing 247
9.6.2 Using CFD Particle Trajectory and Mass Transfer Predictions to Define Erosion-Corrosion Conditions 249
9.6.3 Potential for Erosion-Corrosion Model Development 251
Chapter 10 Conclusions from Erosion-Corrosion Analysis of Carbon Steel, Industrial Relevance and Future Work 254
10.1 Conclusions 254
10.2 Industrial Relevance and Novelty of Work Completed 258
10.3 Future Work 260
References 262
Appendix A COMSOL Multiphysics Model Worksheets for CFD Simulations in SIJ Nozzle Flow 276
A.1 Simulation of Particle Trajectories in an SIJ Nozzle 276
A.2 Simulation of Particle Trajectories in an Elbow 284
A.3 Prediction of Mass Transfer Coefficients in the SIJ 284
A.4 Mass Transfer Coefficients in Other Geometries 289

List of Tables

Table 1.1 Causes of pipeline failure in the oil and gas industry [9] 2

Table 1.2 Corrosion failure in the oil and gas industry [9] 3

Table 3.1 Constants used in the E/CRC erosion model for carbon steel determined from dry impact testing at different impingement angles and impingement velocities [110] 41

Table 3.2 Typical forces acting on a particle in fluid flow [4, 10, 132, 133] 44

Table 3.3 Potential causes of erosion-enhanced corrosion and corrosion-enhanced erosion suggested by Wood and Hutton [15] 48

Table 3.4 Erosion-corrosion regimes defined by Stack et al. [160] as a ratio of erosion wear (K_e) to corrosion degradation (K_c) 50

Table 4.1 Summary of test conditions for flow-induced corrosion (FIC), erosion (E) and erosion-corrosion (E-C) tests using the SIJ 68

Table 4.2 Operating conditions for erosion-corrosion tests using the SIJ 70

Table 4.3 Composition of X65 carbon steel samples (wt.%) 71

Table 4.4 Chemical components of corrosion inhibitor A 73

Table 4.5 Chemical components of corrosion inhibitor B 73

Table 5.1 Parameters of the equivalent circuit for blank flow-induced corrosion SIJ tests in a 2% NaCl, 60°C, pH 4.7, CO_2-saturated solution at flow velocities of 10 m/s, 15 m/s and 20 m/s 97

Table 5.2 Mass loss of X65 carbon steel during a 240-minute test period for blank flow-induced corrosion SIJ tests in a 2% NaCl, 60°C, pH 4.7, CO_2-saturated solution at flow velocities of 10 m/s, 15 m/s and 20 m/s 100

Table 5.3 Parameters of the equivalent circuit after 250 ppm of inhibitor A was added to flow-induced corrosion SIJ tests in a 2% NaCl, 60°C, pH 4.7, CO_2-saturated solution at a flow velocity of 20 m/s 103

Table 5.4 Parameters of the equivalent circuit after 250 ppm of inhibitor B was added to flow-induced corrosion SIJ tests in a 2% NaCl, 60°C, pH 4.7, CO_2-saturated solution at a flow velocity of 20 m/s 106

Table 5.5 Mass loss of X65 carbon steel during a 240-minute test period for blank erosion-corrosion SIJ tests in a 2% NaCl, 60°C, pH 4.7, CO_2-saturated solution and erosion SIJ tests in a 60°C, N_2-saturated solution at flow velocities of 10 m/s, 15 m/s and 20 m/s containing 500 mg/L of sand 110

Table 5.6 Mass loss of X65 carbon steel during a 240-minute test period for blank erosion-corrosion SIJ tests in a 2% NaCl, 60°C, pH 4.7, CO_2-saturated solution and erosion SIJ tests in a 60°C, N_2-saturated solution at flow velocities of 10 m/s, 15 m/s and 20 m/s containing 1000 mg/L of sand 112

Table 6.1 Particle impact data from CFD predictions of particle trajectories at a flow velocity of 20 m/s in the four regions identified on the surface of the SIJ sample, assuming a flat surface 150

Table 7.1 Description of components in the elbow shown in Figure 7.2 171

Table 8.1 CFD predicted number of particle impacts, impact angles and impact velocities at each of the six samples on the outer radius of the elbow at a flow velocity of 6 m/s and solution temperature of 60°C 194

Table 9.1 Degradation maps from degradation rates in mm/yr measured in 2% NaCl, 60°C solution at flow velocities of 10 m/s, 15 m/s and 20 m/s in (a) blank erosion-corrosion pH 4.7, CO_2-saturated conditions containing 500 mg/L of sand, (b) erosion-corrosion pH 4.7, CO_2-saturated conditions containing 500 mg/L of sand and 250 ppm of inhibitor B, (c) blank erosion-corrosion pH 4.7, CO_2-saturated conditions conditions containing 1000 mg/L of sand and (d) erosion-corrosion pH 4.7, CO_2-saturated conditions conditions containing 1000 mg/L of sand and 250 ppm of inhibitor B 215

Table 9.2 Tafel constants and Stern-Geary coefficients determined over a 240-minute test period in flow-induced corrosion tests completed at a flow velocity of 20 m/s in a 2% NaCl, 60°C, pH 4.7, CO_2-saturated solution 217

Table 9.3 Ratio of corrosion degradation ($\mathbf{C} + \Delta\mathbf{CE}$) determined from the sum of EIS-measured flow-induced corrosion rates and EIS-measured erosion-enhanced corrosion to erosion degradation ($\mathbf{E} + \Delta\mathbf{EC}$) determined from the sum of erosion rates measured from mass loss erosion tests and corrosion-enhanced erosion, calculated using equation (2.1), measured in flow-induced corrosion tests in a CO_2-saturated, pH 4.7, 2% NaCl, 60°C solution; erosion tests in a N_2-saturated, 60°C solution containing 500 mg/L and 1000 mg/L of sand and erosion-corrosion SIJ tests in a CO_2-saturated, pH 4.7, 2% NaCl, 60°C solution containing 500 mg/L and 1000 mg/L of sand at flow velocities of 10 m/s, 15 m/s and 20 m/s 221

Table 9.4 Experimental conditions used for the comparison of the ratio of erosion-corrosion degradation to flow-induced corrosion degradation of carbon steel in CO_2-saturated conditions shown in Figure 9.19 245

Table A.1 Parameters for particle tracking SIJ nozzle model 277

Table A.2 Control points for SIJ nozzle polygon consisting of linear segments 278

Table A.3 Control points for SIJ sample and sample holder consisting of linear segments 278

Table A.4 Control points for fluid flow domain consisting of linear segments 278

Table A.5 Parameters added to material properties settings 279

Table A.6 Mesh size parameters for SIJ nozzle mesh 282

Table A.7 Parameters for SIJ mass transfer coefficient predictions .. 285

Table A.8 Parameters for SIJ nozzle mesh used for mass transfer coefficient predictions 287

List of Figures

Figure 1.1 Project framework showing the aims and objectives of the research to understand erosion-corrosion of carbon steel in CO_2 environments **4**

Figure 2.1 Influence of particle impact angle on erosion degradation of ductile and brittle materials adapted from [4] **8**

Figure 2.2 EDL and equivalent circuit consisting of a solution resistance (R_s), charge transfer resistance (R_{ct}) and capacitance (C_{edl}) [24, 26] **11**

Figure 2.3 A small element of fluid adapted from [13] **12**

Figure 3.1 Parameters influential on the corrosion of carbon steel in oil and gas conditions adapted from [5] **16**

Figure 3.2 Mechanisms of the 'buffering effect' in CO_2 corrosion of carbon steel, whereby CO_2 dissolves in water to produce carbonic acid which dissociates to form H^+ ions that are reduced at the steel surface [39, 41] **17**

Figure 3.3 Effect of flow velocity on (a) the corrosion rate of carbon steel in a CO_2-saturated, 1% NaCl, 20°C solution rotating cylinder electrode (RCE) and straight pipe geometries and (b) cathodic potentiodynamic sweeps in a straight pipe in the same conditions showing increasing cathodic current densities [30] **20**

Figure 3.4 Corrosion rate of carbon steel in a CO_2-saturated, 1% NaCl, 20°C solution in a rotating cylinder electrode (labelled as RC) and in a straight pipe in equivalent mass transfer conditions [30] **22**

Figure 3.5 Parameters influencing the erosion of ductile materials adapted from [4] **24**

Figure 3.6 Three wear mechanisms after a particle impact on a ductile metal surface at different impingement angles showing (a) normal impingement, (b) type I cutting and (c) type II cutting, adapted from [16] **25**

Figure 3.7 Effect of impingement angle on the degradation of aluminium in erosion tests completed using different sized silicon carbide (SiC) particles, where 120 mesh (larger particles) and 1000 mesh (particle sizes) is used to define the particle sizes by Finnie [18] **26**

Figure 3.8 Transportation of particles in a fluid stream through a nozzle showing particle deviation from a fluid streamline as a surface is approached, adapted from [4] **28**

Figure 3.9 Effect of momentum equilibration number on the trajectories of particle in impinging jet flow adapted from [4] **29**

Figure 3.10 Forces acting on the particles at a surface as a result of flow through a fluid medium and impingement on a surface [96] **30**

Figure 3.11 Effect of fluid viscosity on the erosion rates of copper specimens in slurry pot erosion tests completed at velocities of 18.7 m/s (solid lines) and 9.35 m/s (dashed lines) using different sized glass beads [75] **30**

Figure 3.12 Effect of fluid viscosity on the collision efficiency of particle impacts on copper specimens in slurry pot erosion tests completed at a velocity of 18.7 m/s using different sized glass beads [75] **31**

Figure 3.13 Effect of particle size on the erosion rates of carbon steel in slurry pot erosion tests containing 1.2 wt% of SiC particles in a diesel oil solution at a nominal velocity of 18.7 m/s [83] **34**

Figure 3.14 Effect of particle size on the impact velocity of carbon steel in slurry pot erosion tests containing 1.2 wt% of SiC particles in a diesel oil solution at a nominal velocity of 18.7 m/s [83] **34**

Figure 3.15 Effect of Vickers hardness on the erosion resistance of different metals [16] **35**

Figure 3.16 Effect of carbon steel microstructure on erosion rates in dry erosion testing completed at a flow velocity of 61 m/s using 240 µm diameter SiC particles [76] **36**

Figure 3.17 Theoretical effect of surface topography on the impact angle of a particle on a rough surface adapted from [80], where θp is the impact angle and θS is the additional angle as a result of surface texture **37**

Figure 3.18 Model of an abrasive grain impacting on a surface and removing material developed by Finnie [17] **38**

Figure 3.19 CFD prediction of (a) erosion rates in an elbow caused by the impact of 150 µm diameter sand particles in 3 m/s water flow and (b) trajectories of the sand particles [110] **45**

Figure 3.20 Effect of sand concentration and flow velocity on the total erosion-corrosion degradation of X65 carbon steel in CO_2 environments, where TWL is the erosion-corrosion mass loss [34] **48**

Figure 3.21 Effect of solution temperature on contributions of erosion, corrosion and synergistic components to total erosion-corrosion degradation of X65 carbon steel in CO_2 environments containing a sand concentration of 200 mg/L at a flow velocity of 20 m/s [34] **49**

Figure 3.22 Pure erosion (E_0) and corrosion-enhanced erosion (ΔE_C) of X70 carbon steel in erosion-corrosion conditions (E_C) [149] **51**

Figure 3.23 FIB analysis of UNS S31603 subsurface after slurry pot erosion-corrosion tests showing (a) subsurface cracks at the root of an extruded lip [139] and (b) work-hardening of the sample after particle impacts [108] **53**

Figure 3.24 SIJ used for erosion-corrosion testing of materials at the University of Leeds [34, 35, 60, 63, 120, 144] **54**

Figure 3.25 Elbow component designed for erosion-corrosion testing of carbon steel where (a) shows the full test setup, (b) the outer radius of the test elbow, (c) the inner radius and (d) the complete test elbow assembly, designed by Zeng et al. [174] **55**

Figure 3.26 CFD prediction of erosion-corrosion regimes in an elbow by Stack and Abdelrahman [151] with a particle mass flow rate of 0.957 kg/s **57**

Figure 3.27 Effect of flow on the performance of a corrosion inhibitor on two carbon steel ring samples with different shear stress conditions in SIJ tests completed by Gulbrandsen and Grana [51] **59**

Figure 3.28 Effect of sand on the performance of a corrosion inhibitor used to protect a carbon steel sample in impinging jet tests completed by Tummala et al. [194] **60**

Figure 4.1 SIJ used for flow-induced corrosion, erosion and erosion-corrosion tests showing (a) the full SIJ apparatus and (b) a cross section of the nozzle and X65 sample **67**

Figure 4.2 Carbon steel samples embedded in epoxy resin used as a working electrode a three electrode cell **69**

Figure 4.3 X65 carbon steel sample (a) observed using an SEM, showing an untested polished surface [41] and (b) observed using an optical microscope after being etched in a 2% Nital solution for 10 seconds showing the microstructure as consisting of ferrite grains (lighter coloured) and pearlite regions (darker) **71**

Figure 4.4 Size distribution of HST60 silica sand particles used in SIJ erosion and erosion-corrosion tests **72**

Figure 4.5 SEM image of HST60 sand particles used in SIJ erosion and erosion-corrosion tests [35] **72**

Figure 4.6 Static test setup for corrosion measurement of X65 and evaluation of inhibitor performance in static conditions adapted from [41] **74**

Figure 4.7 Three electrode cell consisting of a working electrode, reference electrode and counter electrode submerged in an electrolyte [24] **75**

Figure 4.8 LPR measurement showing the relationship between current and voltage in a potential range of ±15 mV about OCP, showing how Rp is determined from the gradient [41] **76**

Figure 4.9 Tafel plot showing the relationship between potential and current showing how β_a, β_a and i_{corr} are determined, adapted from [35] **78**

Figure 4.10 EIS behaviour showing (a) phase shift between current and voltage and (b) calculation of phase angle adapted from [24] **79**

Figure 4.11 Method of hardness testing showing (a) applied load, Fi, from a pyramid indenter and (b) indentation of area, A, produced on the surface adapted from [165] **82**

Figure 4.12 Stages involved in the development of CFD models adapted from [13] **84**

Figure 4.13 Different regions near to the wall showing the viscous sub-layer and the log-law layer [13] **90**

Figure 5.1 Static corrosion rates of X65 carbon steel in blank conditions polished to a surface roughness of 0.15 µm ± 0.02 µm and after 250 ppm of Inhibitor A and Inhibitor B was added to a 2% NaCl, 60°C, pH 4.7, CO_2-saturated, 1 L solution in static cell tests **93**

Figure 5.2 Corrosion rate of X65 measured using EIS during 240-minute blank flow-induced corrosion SIJ tests in a 2% NaCl, 60°C, pH 4.7, CO_2-saturated solution at flow velocities of 10 m/s, 15 m/s and 20 m/s **95**

Figure 5.3 Nyquist and Bode plots for blank flow-induced corrosion SIJ tests in a 2% NaCl, 60°C, pH 4.7, CO_2-saturated solution at flow velocities of 10 m/s, 15 m/s and 20 m/s **96**

Figure 5.4 Equivalent circuit representing blank flow-induced corrosion SIJ tests in a 2% NaCl, 60°C, pH 4.7, CO_2-saturated solution at flow velocities of 10 m/s, 15 m/s and 20 m/s where R_S is the solution resistance, R_{ct} is the charge transfer resistance and CPE_{edl} represents the EDL constant phase element **97**

Figure 5.5 Tafel plot for blank flow-induced corrosion SIJ tests in a 2% NaCl, 60°C, pH 4.7, CO_2-saturated solution at a flow velocity of 20 m/s, demonstrating linear region on plots for measurement of Tafel constants **98**

Figure 5.6 Tafel plots for blank flow-induced corrosion SIJ tests in a 2% NaCl, 60°C, pH 4.7, CO_2-saturated solution at flow velocities of 10 m/s, 15 m/s and 20 m/s **98**

Figure 5.7 Tafel plots during a 240-minute test period for blank flow-induced corrosion SIJ tests in a 2% NaCl, 60°C, pH 4.7, CO_2-saturated solution at a flow velocity of 20 m/s **99**

Figure 5.8 Comparison of corrosion rates determined by mass loss and electrochemistry in flow-induced corrosion SIJ tests in a 2% NaCl, 60°C, pH 4.7, CO_2-saturated solution at flow velocities of 10 m/s, 15 m/s and 20 m/s **100**

Figure 5.9 Measurement of X65 corrosion rate after 250 ppm of inhibitor A added in flow-induced corrosion SIJ tests in a 2% NaCl, 60°C, pH 4.7, CO_2-saturated solution at flow velocities of 10 m/s, 15 m/s and 20 m/s **101**

Figure 5.10 Nyquist and Bode plots from AC impedance measurements after 250 ppm of inhibitor A was added to flow-induced corrosion SIJ tests in a 2% NaCl, 60°C, pH 4.7, CO_2-saturated solution at a flow velocity of 20 m/s **102**

Figure 5.11 Tafel plots for X65 after 250 ppm of inhibitor A was added to flow-induced corrosion SIJ tests in a 2% NaCl, 60°C, pH 4.7, CO_2-saturated solution at flow velocities of 10 m/s, 15 m/s and 20 m/s **103**

Figure 5.12 Measurement of OCP after 250 ppm of inhibitor A was added to flow-induced corrosion SIJ tests in a 2% NaCl, 60°C, pH 4.7, CO_2-saturated solution at flow velocities of 10 m/s, 15 m/s and 20 m/s **104**

Figure 5.13 Measurement of X65 corrosion rate over time after 250 ppm of inhibitor B was added to flow-induced corrosion SIJ tests in a 2% NaCl, 60°C, pH 4.7, CO_2-saturated solution at flow velocities of 10 m/s, 15 m/s and 20 m/s **104**

Figure 5.14 Nyquist and Bode plots from AC impedance measurements after 250 ppm of inhibitor B was added to flow-induced corrosion SIJ tests in a 2% NaCl, 60°C, pH 4.7, CO_2-saturated solution at a flow velocity of 20 m/s **105**

Figure 5.15 Tafel plots for X65 after 250 ppm of inhibitor B was added to flow-induced corrosion SIJ tests in a 2% NaCl, 60°C, pH 4.7, CO_2-saturated solution at flow velocities of 10 m/s, 15 m/s and 20 m/s **106**

Figure 5.16 Measurement of OCP after 250 ppm of inhibitor B was added to flow-induced corrosion SIJ tests in a 2% NaCl, 60°C, pH 4.7, CO_2-saturated solution at flow velocities of 10 m/s, 15 m/s and 20 m/s **107**

Figure 5.17 Efficiency of inhibitor A and inhibitor B at the end of tests after 250 ppm of inhibitor was added in static cell tests in a 2% NaCl, 60°C, pH 4.7, CO_2-saturated, 1 L solution and flow-induced corrosion SIJ tests in a 2% NaCl, 60°C, pH 4.7, CO_2-saturated solution at flow velocities of 10 m/s, 15 m/s and 20 m/s **108**

Figure 5.18 Efficiency of inhibitor A and inhibitor B approximately 4 minutes after 250 ppm of inhibitor was added in static cell tests in a 2% NaCl, 60°C, pH 4.7, CO_2-saturated, 1 L solution and flow-induced corrosion SIJ tests in a 2% NaCl, 60°C, pH 4.7, CO_2-saturated solution at flow velocities of 10 m/s, 15 m/s and 20 m/s **109**

Figure 5.19 Contribution of flow-induced corrosion, pure erosion and erosion-corrosion interactions to total erosion-corrosion degradation in SIJ flow-induced corrosion tests in a 2% NaCl, 60°C, pH 4.7, CO_2-saturated solution at flow velocities of 10 m/s, 15 m/s and 20 m/s, erosion-corrosion SIJ tests in the same conditions containing 500 mg/L of sand and pure erosion SIJ tests in 60°C, pH 7, N_2-saturated conditions containing 500 mg/L of sand **111**

Figure 5.20 Contribution of flow-induced corrosion, pure erosion and erosion-corrosion interactions to total erosion-corrosion degradation in SIJ flow-induced corrosion tests in a 2% NaCl, 60°C, pH 4.7, CO_2-saturated solution at flow velocities of 10 m/s, 15 m/s and 20 m/s, erosion-corrosion SIJ tests in the same conditions containing 1000 mg/L of sand and pure erosion SIJ tests in 60°C, pH 7, N_2-saturated conditions containing 1000 mg/L of sand **112**

Figure 5.21 Contribution of flow-induced corrosion, pure erosion and erosion-corrosion interactions to total erosion-corrosion degradation in SIJ flow-induced corrosion tests in a 2% NaCl, 60°C, pH 4.7, CO_2-saturated solution at flow velocities of 10 m/s, 15 m/s and 20 m/s after the addition of 250 ppm of inhibitor B, erosion-corrosion SIJ tests in the same conditions containing 500 mg/L of sand after the addition of 250 ppm of inhibitor B and pure erosion SIJ tests in blank, 60°C, pH 7, N_2-saturated conditions containing 500 mg/L of sand **113**

Figure 5.22 Contribution of flow-induced corrosion, pure erosion and erosion-corrosion interactions to total erosion-corrosion degradation in SIJ flow-induced corrosion tests in a 2% NaCl, 60°C, pH 4.7, CO_2-saturated solution at flow velocities of 10 m/s, 15 m/s and 20 m/s after the addition of 250 ppm of inhibitor B, erosion-corrosion SIJ tests in the same conditions containing 1000 mg/L of sand after the addition of 250 ppm of inhibitor B and pure erosion SIJ tests in blank, 60°C, pH 7, N_2-saturated conditions containing 1000 mg/L of sand **114**

Figure 5.23 Comparison of erosion-enhanced corrosion measured using EIS in SIJ erosion-corrosion tests in blank conditions and after the addition of 250 ppm of inhibitor B in a 2% NaCl, 60°C, pH 4.7, CO_2-saturated solution at flow velocities of 10 m/s, 15 m/s and 20 m/s containing 500 mg/L and 1000 mg/L of sand..... **115**

Figure 5.24 Comparison of corrosion-enhanced erosion calculated using equation (2.1) in SIJ erosion-corrosion tests in blank conditions and after the addition of 250 ppm of inhibitor B in a 2% NaCl, 60°C, pH 4.7, CO_2-saturated solution at flow velocities of 10 m/s, 15 m/s and 20 m/s containing 500 mg/L and 1000 mg/L of sand **116**

Figure 6.1 Fluid flow through a turbulent axisymmetric impinging jet representative of fluid flow through the SIJ nozzle, where dN is the nozzle diameter, H is the distance from the exit of the nozzle to the sample and r is the radial distance from the centre of the sample, adapted from [28, 211]..... **121**

Figure 6.2 Regions on a sample surface in axisymmetric impinging jet flow where expressions developed by Giralt and Trass [213] and Poreh et al. [65] used to calculate wall shear stress can be applied, and the conditions under which they can be applied in **123**

Figure 6.3 Representation of 2D axisymmetric model of SIJ nozzle developed for CFD predictions of fluid flow and particle trajectories **124**

Figure 6.4 CFD prediction of wall shear stress on a sample surface in SIJ nozzle flow comparing different turbulence models with the analytical solution of Poreh et al. [65] at a flow velocity of 8 m/s, solution temperature of 60°C and HdN ratio of 2 ..... **127**

Figure 6.5 Mesh sensitivity study of CFD prediction of wall shear stress on a target in SIJ nozzle flow using the k-ω turbulence model compared with the analytical solution of Poreh et al. [65] at a flow velocity of 8 m/s, solution temperature of 60°C and HdN ratio of 2 ..... **127**

Figure 6.6 Calculation of $y+$ from CFD prediction of shear stress using the k-ω turbulence model over the target surface representing the sample surface in the SIJ nozzle at a flow velocity of 20 m/s, solution temperature of 60°C and HdN ratio of 1.25 ..... **128**

Figure 6.7 CFD prediction using the k-ω turbulence model of 60°C water flow through an SIJ nozzle with a nozzle diameter of 4 mm, distance to sample of 5 mm and an inlet flow velocity of 20 m/s showing (a) flow velocity and (b) turbulent kinetic energy, k **129**

Figure 6.8 CFD prediction using the k-ω turbulence model of flow velocity adjacent to the X65 sample surface for 60°C water flow through an SIJ nozzle with a diameter of 4 mm, distance to sample of 5 mm and at a flow velocity of 20 m/s **129**

Figure 6.9 Representation of 2D axisymmetric model of SIJ nozzle developed to predict particle trajectories **130**

Figure 6.10 Mesh sensitivity study of CFD prediction of particle impact velocities on a target surface in an SIJ nozzle, with a diameter of 4 mm and distance to sample of 5 mm, using the k-ω turbulence model to predict fluid flow through the SIJ nozzle at a flow velocity of 20 m/s and solution temperature of 60°C, containing 250 µm diameter sand particles **135**

Figure 6.11 Mesh sensitivity study of CFD prediction of particle impact angles on a target surface in an SIJ nozzle, with a diameter of 4 mm and distance to sample of 5 mm, using the k-ω turbulence model to predict fluid flow through the SIJ nozzle at a flow velocity of 20 m/s and solution temperature of 60°C, containing 250 µm diameter sand particles **135**

Figure 6.12 CFD prediction of particle trajectories in an SIJ nozzle, with a diameter of 4 mm and distance to sample of 5 mm, using the k-ω turbulence model to predict fluid flow through the SIJ nozzle at a flow velocity of 20 m/s and solution temperature of 60°C, containing 250 µm diameter sand particles **136**

Figure 6.13 CFD prediction of particle impact velocities and impact angles on a target surface in an SIJ nozzle, with a diameter of 4 mm and distance to sample of 5 mm, using the k-ω turbulence model to predict fluid flow through the SIJ nozzle at a flow velocity of 20 m/s and solution temperature of 60°C, containing 250 µm diameter sand particles **137**

Figure 6.14 CFD prediction of particle impact velocities on a target surface in an SIJ nozzle, with a diameter of 4 mm and distance to sample of 5 mm, using the k-ω turbulence model to predict fluid flow through the SIJ nozzle at a flow velocity of 20 m/s and solution temperature of 60°C, comparing 100 µm, 250 µm and 500 µm diameter sand particles **138**

Figure 6.15 CFD prediction of particle impact angles on a target surface in an SIJ nozzle, with a diameter of 4 mm and distance to sample of 5 mm, using the k-ω turbulence model to predict fluid flow through the SIJ nozzle at a flow velocity of 20 m/s and solution temperature of 60°C, comparing 100 µm, 250 µm and 500 µm diameter sand particles **139**

Figure 6.16 CFD prediction of particle impact velocities on a target surface in an SIJ nozzle, with a diameter of 4 mm and distance to sample of 5 mm, using the k-ω turbulence model to predict fluid flow through the SIJ nozzle at a flow velocity of 20 m/s and solution temperature of 60°C, containing 250 µm diameter sand particles, comparing a flat surface and a surface with a wear scar with a maximum depth of 120 µm, representing wear after a 240-minute erosion-corrosion test with 1000 mg/L of sand at a flow velocity of 20 m/s **140**

Figure 6.17 CFD prediction of particle impact angles on a target surface in an SIJ nozzle, with a diameter of 4 mm and distance to sample of 5 mm, using the k-ω turbulence model to predict fluid flow through the SIJ nozzle at a flow velocity of 20 m/s and solution temperature of 60°C, containing 250 µm diameter sand particles, comparing a flat surface and a surface with a wear scar with a maximum depth of 120 µm, representing wear after a 240-minute erosion-corrosion test with 1000 mg/L of sand at a flow velocity of 20 m/s **140**

Figure 6.18 CFD prediction of particle trajectories in an SIJ nozzle, with a diameter of 4 mm and distance to sample of 5 mm, using the k-ω turbulence model to predict fluid flow through the SIJ nozzle at a flow velocity of 20 m/s and solution temperature of 60°C, containing 250 µm diameter sand particles, comparing particle rebounds using coefficient of restitution of (a) 0.2, (b) 0.4, (c) 0.6, (d) 0.8, (e) 1.0 and (f) coefficients calculated using the Grant & Tabakoff [136] equations **142**

Figure 6.19 CFD prediction of particle impact velocities on a surface in an SIJ nozzle, with a diameter of 4 mm and distance to sample of 5 mm, using the k-ω turbulence model to predict fluid flow through the SIJ nozzle at a flow velocity of 20 m/s and solution temperature of 60°C, containing 250 µm diameter sand particles, comparing stationary particles at inlet and a particles with initial velocities equal to the fluid inlet velocity of 20 m/s **145**

Figure 6.20 CFD prediction of particle impact angles on a surface in an SIJ nozzle, with a diameter of 4 mm and distance to sample of 5 mm, using the k-ω turbulence model to predict fluid flow through the SIJ nozzle at a flow velocity of 20 m/s and solution temperature of 60°C, containing 250 µm diameter sand particles, comparing stationary particles at inlet and a particles with initial velocities equal to the fluid inlet velocity of 20 m/s **146**

Figure 6.21 CFD prediction of particle impact velocities on a target surface in an SIJ nozzle, with a diameter of 4 mm and distance to sample of 5 mm, using the k-ω turbulence model to predict fluid flow through the SIJ nozzle at a flow velocity of 20 m/s and solution temperature of 60°C, containing 250 µm diameter sand particles, comparing the use of a discrete random walk (DRW) model to predict turbulent dispersion **146**

Figure 6.22 CFD prediction of particle impact angles on a target surface in an SIJ nozzle, with a diameter of 4 mm and distance to sample of 5 mm, using the k-ω turbulence model to predict fluid flow through the SIJ nozzle at a flow velocity of 20 m/s and solution temperature of 60°C, containing 250 µm diameter sand particles, comparing the use of a discrete random walk (DRW) model to predict turbulent dispersion **147**

Figure 6.23 CFD prediction of particle impact velocities on a target surface in an SIJ nozzle, with a diameter of 7 mm and distance to sample of 5 mm, using the k-ω turbulence model to predict fluid flow through the SIJ nozzle at a flow velocity of 5 m/s and solution temperature of 25°C, compared with the model developed by Gnanavelu [105] **148**

Figure 6.24 Identification of four regions on the profile of an X65 sample after a 240-minute erosion-corrosion test at 20 m/s, 60°C with 1000 mg/L of sand showing different erosion conditions in each of the regions as defined by CFD predictions of impact angle and impact velocity on a flat surface **150**

Figure 6.25 Contributions of erosion-corrosion components to total degradation over time in SIJ mass loss tests, where 'E-C' is erosion-corrosion degradation at a flow velocity of 20 m/s in a CO_2-saturated, 60°C, pH 4.7, 2% NaCl solution containing 1000 mg/L of sand particles with an average diameter of 250 µm; 'E' is pure erosion degradation at a flow velocity of 20 m/s in a N_2-saturated, 60°C, pH 7 solution containing 1000 mg/L of sand; 'C' is flow-induced corrosion degradation at a flow velocity of 20 m/s in a CO_2-saturated, 60°C, pH 4.7, 2% NaCl solution and 'ΔE_C' is corrosion-enhanced erosion calculated using equation (2.1) **151**

Figure 6.26 Comparison of in-situ corrosion rates measured using EIS in flow-induced corrosion tests at a flow velocity of 20 m/s in a CO_2-saturated, 60°C, pH 4.7, 2% NaCl solution and erosion-corrosion tests in the same conditions containing 1000 mg/L of sand **152**

Figure 6.27 Tafel plots of X65 carbon steel samples measured using in flow-induced corrosion tests at a flow velocity of 20 m/s in a CO_2-saturated, 60°C, pH 4.7, 2% NaCl solution and erosion-corrosion tests in the same conditions containing 1000 mg/L of sand **153**

Figure 6.28 Contribution to total erosion-corrosion degradation of erosion (E), corrosion (C) and corrosion-enhanced erosion (ΔE_C) to total erosion-corrosion degradation in (a) 30-minute, (b) 60-minute, (c) 120-minute and (d) 240-minute SIJ tests **154**

Figure 6.29 Surface profiles of surfaces after 240-minute SIJ erosion tests at a flow velocity of 20 m/s in a N_2-saturated solution at 60°C containing 1000 mg/L of sand and SIJ erosion-corrosion tests in CO_2-saturated conditions **155**

Figure 6.30 Change in size distribution of sand particles after a 240-minute erosion test in a N_2-saturated, 60°C solution containing 1000 mg/L of sand at a flow velocity of 20 m/s compared with sand size before the test **156**

Figure 6.31 SEM images of erosion (a-d) and erosion-corrosion (e-h) samples after 240 minute tests in the SIJ at a flow velocity of 20 m/s in a solution at a temperature of 60°C containing 1000 mg/L of sand in region 1 (a, e), region 2 (b, f), region 3 (c, g) and region 4 (d, h) **157**

Figure 6.32 Measurement of X65 sample surface roughness (Sa) after pure erosion SIJ tests in a N_2-saturated 60°C solution containing 1000 mg/L of sand at a flow velocity 20 m/s **159**

Figure 6.33 Measurement of X65 sample surface roughness (Sa) after erosion-corrosion SIJ tests in a CO_2-saturated 60°C, pH 4.7, 2% NaCl solution containing 1000 mg/L of sand at a flow velocity 20 m/s **159**

Figure 6.34 Comparison of in-situ corrosion rates of X65 carbon steel samples with a smooth surface of Sa = 0.15 µm ± 0.02 µm and a rough surface of Sa = 0.73 µm ± 0.06 µm in SIJ flow-induced corrosion tests in a CO_2-saturated, 2% NaCl, 60°C, pH 4.7 solution at a flow velocity of 20 m/s in blank conditions and after adding 250 ppm of inhibitor B **160**

Figure 6.35 Comparison of Tafel plots measured using X65 carbon steel samples with a smooth surface of Sa = 0.15 ± 0.02 µm and a rough surface of Sa = 0.73 ± 0.06 µm in SIJ flow-induced corrosion tests in a CO_2-saturated, 2% NaCl, 60°C, pH 4.7 solution at a flow velocity of 20 m/s in blank conditions and after adding 250 ppm of inhibitor B **160**

Figure 6.36 Measurements of Vickers hardness (H_V) after pure erosion SIJ tests in a N_2-saturated, 60°C solution containing 1000 mg/L of sand at a flow velocity 20 m/s **162**

Figure 6.37 Measurements of Vickers hardness (H_V) after erosion-corrosion SIJ tests in a CO_2-saturated, 60°C, 2% NaCl, pH 4.7 solution containing 1000 mg/L of sand at a flow velocity 20 m/s **162**

Figure 6.38 Measurements of the increase in Vickers hardness (H_V) after erosion tests in a N_2-saturated, 60°C solution containing 1000 mg/L of sand at a flow velocity 20 m/s and removal of work-hardened layers in pure corrosion tests at a flow velocity of 20 m/s in a 60°C, pH 4.7, 2% NaCl, CO_2-saturated solution using samples that had been work-hardened in pure erosion conditions for 120 minutes prior to the test **163**

Figure 6.39 Cross sections of an X65 sample, prior to SIJ testing after being wet-ground to a surface finish of 0.15 ± 0.02 µm milled using FIB and imaged using (a) SEM at 30,000x magnification and (b) FIB etching **164**

Figure 6.40 FIB-SEM images of cross sections in the centre of region 1 on the samples measured after (a) 30-minute erosion tests in a N_2-saturated, 60°C solution containing 1000 mg/L of sand at a flow velocity of 20 m/s, (b) 30-minute erosion-corrosion tests in a CO_2-saturated, 60°C, pH 4.7, 2% NaCl solution containing 1000 mg/L of sand at a flow velocity of 20 m/s, (c) 240-minute erosion tests and (d) 240-minute erosion-corrosion tests **165**

Figure 6.41 FIB images of cross sections in the centre of region 1 on the samples measured after (a) 30-minute erosion tests in a N_2-saturated, 60°C solution containing 1000 mg/L of sand at a flow velocity of 20 m/s, (b) 30-minute erosion-corrosion tests in a CO_2-saturated, 60°C, pH 4.7, 2% NaCl solution containing 1000 mg/L of sand at a flow velocity of 20 m/s, (c) 240-minute erosion tests and (d) 240-minute erosion-corrosion tests **166**

Figure 7.1 Overview of requirements that were considered for the development of the elbow to complete flow-induced corrosion, erosion and erosion-corrosion evaluation of X65 carbon steel **170**

Figure 7.2 Fully assembled elbow design consisting of twelve X65 samples located on the inner and outer radius of the elbow **172**

Figure 7.3 X65 carbon steel samples used in the elbow with a curved radius and a pin used as a connection for electrochemistry measurements **174**

Figure 7.4 Procedure for inserting and securing samples in the elbow body. Removal of samples was completed in reverse order **175**

Figure 7.5 Diagram of the elbow used for flow-induced corrosion, erosion and erosion-corrosion tests fitted into the SIJ to create a flow loop **176**

Figure 7.6 Calibration of pump frequency vs flow velocity measured using an ultrasonic flow meter at the inlet of the elbow **178**

Figure 7.7 Degradation of X65 carbon steel samples on the inner radius and outer radius of an elbow in 8-hour flow-induced corrosion tests at a flow velocity of 6 m/s in a 2% NaCl, pH 4, CO_2-saturated solution at 60°C **180**

Figure 7.8 Nyquist plot from EIS measurements on the inner radius of the elbow on the sample positioned at 0° in 2% NaCl, pH 4, CO_2-saturated conditions at a temperature of 60°C **181**

Figure 7.9 Comparison of polarisation resistance from LPR measurements on the inner radius of an elbow in flow-induced corrosion tests at a flow velocity of 6 m/s in a 2% NaCl, pH 4, CO_2-saturated solution at 60°C **182**

Figure 7.10 Comparison of polarisation resistance from LPR measurements on the outer radius of an elbow in flow-induced corrosion tests at a flow velocity of 6 m/s in a 2% NaCl, pH 4, CO_2-saturated solution at 60°C **182**

Figure 7.11 Mass loss degradation of X65 carbon steel samples on the inner radius of an elbow in 8-hour flow-induced corrosion tests at a flow velocity of 6 m/s in a 2% NaCl, pH 4, CO_2-saturated solution at 60°C and erosion-corrosion tests containing 1000 mg/L of sand **183**

Figure 7.12 Mass loss of X65 samples on the outer radius of an elbow in 8-hour flow-induced corrosion tests at a flow velocity of 6 m/s in a 2% NaCl, pH 4, CO_2-saturated solution at 60°C; erosion tests containing 1000 mg/L of sand in N_2-saturated conditions and erosion-corrosion tests containing 1000 mg/L of sand in CO_2-saturated conditions **183**

Figure 7.13 Contribution of corrosion (CFIC) in flow-induced corrosion elbow tests at a flow velocity of 6 m/s in a CO_2-saturated, 2% NaCl, pH 4, 60°C solution; pure erosion ($\mathrm{E0}$) elbow tests at a flow velocity of 6 m/s in a N_2-saturated, 60°C solution containing 1000 mg/L of sand and interactions ($\Delta\mathrm{CE} + \Delta\mathrm{EC}$) to total erosion-corrosion degradation (ECTML) on the outer radius of the elbow at a flow velocity of 6 m/s in a CO_2-saturated, 2% NaCl, pH 4, 60°C solution containing 1000 mg/L of sand in 8-hour tests **184**

Figure 8.1 Flow parameters influencing flow-induced corrosion, erosion and erosion-corrosion degradation of carbon steel..... **187**

Figure 8.2 Geometry of the 3D 25.4 mm diameter pipe elbow CFD model **189**

Figure 8.3 Dimensionless fluid velocity measured across the diameter of the pipe in a RcDp = 2.8 elbow at 30° after the inlet for a fluid with Re = 43,000 by Enayet et al. [225] compared with CFD predictions using the k-ω turbulence model **191**

Figure 8.4 Prediction of flow velocity using the k-ω turbulence model through the central plane of a RcDp = 5 elbow at an inlet flow velocity of 6 m/s and solution temperature of 60°C **192**

Figure 8.5 CFD prediction of 250 µm diameter sand particle trajectories through a RcDp = 5 elbow at a flow velocity of 6 m/s and solution temperature of 60°C..... **193**

Figure 8.6 Geometry of the straight pipe 2D axisymmetric CFD model with a 15.9 mm diameter and H^+ bulk concentration of 0.1 mol/m^3, equivalent to pH 4 ..... **201**

Figure 8.7 Sensitivity of CFD-predicted mass transfer coefficients using the SST turbulence model to changes in changes in the number of elements in the mesh for a straight pipe with diameter of 15.9 mm at an inlet flow velocity of 5 m/s, solution temperature of 25°C and Sct = 0.71..... **202**

Figure 8.8 Sensitivity of CFD-predicted mass transfer coefficients using the SST turbulence model to changes in Sct for a straight pipe with diameter of 15.9 mm at an inlet flow velocity of 5 m/s and solution temperature of 25°C..... **203**

Figure 8.9 Sensitivity of CFD-predicted mass transfer coefficients using the SST turbulence model to changes in $y+$ of the first element centre thickness for a straight pipe with diameter of 15.9 mm at an inlet flow velocity of 5 m/s and solution temperature of 25°C **203**

Figure 8.10 CFD prediction of H^+ concentration in a 15.9 mm diameter straight pipe using the SST turbulence model at a flow velocity of 5 m/s and solution temperature of 25°C **205**

Figure 8.11 CFD prediction of H^+ concentration gradient and flow velocity profile in a 15.9 mm diameter straight pipe using the SST turbulence model at a flow velocity of 5 m/s and solution temperature of 25°C..... **205**

Figure 8.12 CFD prediction of mass transfer coefficients in a 15.9 mm diameter straight pipe using the SST turbulence model at flow velocities of 1 m/s - 11 m/s and a solution temperature of 25°C, compared with the Berger and Hau [55] correlation for mass transfer coefficients in a straight pipe and experimental mass transfer coefficients obtained by Nesic et al. [30] **206**

Figure 8.13 Geometry of the 2D elbow CFD model with a 25.4 mm diameter, R_cD_p ratio of 5 and H^+ bulk concentration of 0.1 mol/m^3, equivalent to pH 4 ..... **207**

Figure 8.14 CFD prediction of mass transfer coefficients in a 90° elbow using the SST turbulence model for an elbow with an R_cD_p ratio of 5, with an inlet flow velocity of 6 m/s at a temperature of 60°C, predicting the transport of H^+ ions **208**

Figure 8.15 Geometry of the SIJ CFD model with an 8 mm diameter nozzle, distance from nozzle to sample of 5 mm and bulk H^+ concentration of 0.1 mol/m^3 equivalent to pH 4 ..... **209**

Figure 8.16 CFD prediction of mass transfer coefficients on an SIJ sample using the SST turbulence model for an SIJ nozzle diameter of 8 mm and distance to sample of 5 mm at a flow velocity of 6 m/s and solution temperature of 60°C, predicting the transport of H^+ ions **211**

Figure 9.1 Effect of flow velocity on corrosion rates measured using electrochemical techniques in SIJ flow-induced corrosion tests compared with static 1 L tests in a 2% NaCl, 60°C, pH 4.7, CO_2-saturated solution **218**

Figure 9.2 Relationship between shear stress and CO_2 corrosion rates predicted using the NORSOK model in a pH 4.7 solution at a temperature of 60°C [177] **219**

Figure 9.3 Effect of flow velocity on erosion and erosion-corrosion rates of X65 carbon steel measured from SIJ erosion tests in an N_2-saturated, 60°C solution containing 500 mg/L and 1000 mg/L of sand and SIJ erosion-corrosion tests in an CO_2-saturated, 60°C, pH 4.7, 2% NaCl solution containing 500 mg/L and 1000 mg/L of sand **220**

Figure 9.4 Corrosion-enhanced erosion and erosion-enhanced corrosion of X65 carbon steel measured from SIJ tests in 500 mg/L sand concentration erosion-corrosion tests in a 2% NaCl, 60°C, pH 4.7 solution at flow velocities of 10 m/s, 15 m/s and 20 m/s **222**

Figure 9.5 Corrosion-enhanced erosion and erosion-enhanced corrosion of X65 carbon steel measured from SIJ tests in 1000 mg/L sand concentration erosion-corrosion tests in a 2% NaCl, 60°C, pH 4.7 solution at flow velocities of 10 m/s, 15 m/s and 20 m/s **223**

Figure 9.6 Effect of sand concentration on the efficiency of 250 ppm of inhibitor B in erosion-corrosion SIJ tests at flow velocities of 10 m/s, 15 m/s and 20 m/s in a 2% NaCl, 60°C, pH 4.7, CO_2-saturated solution containing 500 mg/L and 1000 mg/L of sand **227**

Figure 9.7 Comparison of surface roughness (Sa) measured in different regions of X65 samples after 240-minute erosion SIJ tests at a flow velocity of 20 m/s in a N_2-saturated, 60°C solution containing 1000 mg/L of sand and 240-minute erosion-corrosion SIJ tests at a flow velocity of 20 m/s in a CO_2-saturated, 60°C, pH 4.7, 2% NaCl solution containing 1000 mg/L of sand **229**

Figure 9.8 Variation of surface roughness with CFD predicted particle impact angles of X65 samples measured after 240-minute erosion SIJ tests at a flow velocity of 20 m/s in a N_2-saturated, 60°C solution containing 1000 mg/L of sand and erosion-corrosion 240-minute SIJ tests at a flow velocity of 20 m/s in a CO_2-saturated, 60°C, pH 4.7, 2% NaCl solution containing 1000 mg/L of sand **230**

Figure 9.9 Comparison of Vickers hardness measured in the wear scar of erosion and erosion-corrosion samples by averaging hardness in regions 1 - 3 after 30, 60, 120 and 240-minute erosion SIJ tests at a flow velocity of 20 m/s in a N_2-saturated, 60°C solution containing 1000 mg/L of sand and 240-minute erosion-corrosion SIJ tests at a flow velocity of 20 m/s in a CO_2-saturated, 60°C, pH 4.7, 2% NaCl solution containing 1000 mg/L of sand **231**

Figure 9.10 FIB analysis of X65 carbon steel samples after (a) 30-minute and (b) 240-minute erosion SIJ tests at a flow velocity of 20 m/s in a N_2-saturated, 60°C solution containing 1000 mg/L of sand showing the different grain sizes as a result of work-hardening **232**

Figure 9.11 Mechanisms of work-hardening of carbon steel after particle impingement in different stages as determined from FIB analysis of erosion samples after SIJ erosion tests at a flow velocity of 20 m/s in a N_2-saturated, 60°C solution containing 1000 mg/L of sand **233**

Figure 9.12 FIB analysis of X65 samples after 240-minute (a) erosion SIJ tests at a flow velocity of 20 m/s in a N_2-saturated, 60°C solution containing 1000 mg/L of sand and (b) erosion-corrosion SIJ tests at a flow velocity of 20 m/s in a CO_2-saturated, 60°C, pH 4.7, 2% NaCl solution containing 1000 mg/L of sand, showing the (1) nano-grain layer, (2) micro-grain layer, (3) deformed bulk grains and (4) bulk grains **234**

Figure 9.13 FIB-SEM images of X65 carbon steel samples after 240-minute erosion-corrosion SIJ tests at a flow velocity of 20 m/s in a CO_2-saturated, 60°C, pH 4.7, 2% NaCl solution containing 1000 mg/L of sand compared with the FIB analysis of UNS S31603 completed by Rajahram et al. [139] **235**

Figure 9.14 Propagation of cracks in the nano-grain work-hardened layer of carbon steel samples in erosion-corrosion SIJ tests at a flow velocity of 20 m/s in a CO_2-saturated, 60°C, pH 4.7, 2% NaCl solution containing 1000 mg/L of sand **236**

Figure 9.15 Variation of impact velocity and erosion rate for varying particle sizes as shown by Lynn et al. [83] compared with the range of sizes of particles used in erosion and erosion-corrosion SIJ tests in this thesis **238**

Figure 9.16 Comparison of CFD predicted impact angles over the different regions of an X65 sample compared with SEM images of the three regions experiencing particle impact after completing 240-minute erosion SIJ tests at a flow velocity of 20 m/s in a N_2-saturated, 60°C solution containing 1000 mg/L of sand **240**

Figure 9.17 Strain rate predictions using CFD across the surface of the sample in the SIJ after particle impingement at a flow velocity of 20 m/s in a 60°C solution **241**

Figure 9.18 Range of impact angles predicted using CFD in the SIJ at a flow velocity of 20 m/s and in the elbow at a flow velocity of 6 m/s when compared with erosion degradation typical of ductile materials adapted from [17] **243**

Figure 9.19 Comparison of the ratio of erosion-corrosion degradation to pure flow-induced corrosion degradation for the conditions shown in Table 9.4 ..... **246**

Figure 9.20 Framework for improved approach to erosion-corrosion evaluation of field problems and applications **249**

Figure 9.21 Comparison of CFD predicted mass transfer coefficients in different flow geometries at flow velocities of 10 m/s, 15 m/s and 20 m/s at a solution temperature of 60°C **251**

Figure 9.22 Key flow parameters that can be predicted using CFD on the surface of an SIJ sample to determine thickness loss, h, as a function of impact angle, impact velocity and mass transfer coefficient **253**

Figure 10.1 Future work suggestions in the field of erosion-corrosion of carbon steel in oil and gas conditions **260**

Figure A.1 SIJ nozzle model geometry used for fluid flow and particle tracking predictions **277**

Figure A.2 Domain 1 showing the geometry of the SIJ nozzle and the regions where fluid flow was modelled, highlighted in blue **279**

Figure A.3 Inlet boundary (highlighted in blue) at the top of the SIJ nozzle used as fluid inlet **280**

Figure A.4 Outlet boundaries (highlighted in blue) at the top and bottom of the SIJ fluid reservoir used as fluid outlets **280**

Figure A.5 Distribution mesh on boundary '9' (highlighted in blue), with a higher concentration of elements in this region **282**

Figure A.6 Boundary layer mesh on 'boundary 6' and 'boundary 12' (highlighted in blue), for a highly refined mesh at the sample surface to complete mass transfer coefficient predictions. **288**

List of Abbreviations

A	Area (m^2)
A_1	Material specific constant (E/CRC erosion model)
ABS	Acrylonitrile Butadiene Styrene
AC	Alternating Current
Ag/AgCl	Silver/silver chloride
B	Stern-Geary coefficient
BH	Brinell hardness
C	Carbon
C	Operational constant in API-RP-14E equation
C_0	Static corrosion rate (mm/yr)
c_a	Concentration of species a (mol/m^3)
C_D	Drag coefficient
C_{edl}	Electrical double layer capacitance (F/m^2)
C_{EC}	Corrosion rate in erosion-corrosion conditions (mm/yr)
CFD	Computational Fluid Dynamics
C_{FIC}	Flow induced corrosion rate (mm/yr)
CO_2	Carbon dioxide
c_p	Fraction of particles cutting in idealised manner
CPE	Constant Phase Element
$c_{products}$	Concentration of product species (mol/m^3)
CR	Corrosion Rate (mm/yr)
$c_{reactants}$	Concentration of reactant species (mol/m^3)
D	Diffusion coefficient (m^2/s)
D_0	Diffusion coefficient at ambient conditions (m^2/s)
DC	Direct Current
d_N	Diameter of SIJ nozzle (m)
d_p	Diameter of particle (m)
D_p	Internal diameter of pipe (m)

DRW	Discrete Random Walk
E	Applied potential (V)
E^0	Standard cell potential (V)
E_0	Pure erosion rate (mm/yr)
e^-	Negative electron
E-C	Erosion-Corrosion
E_{corr}	Free corrosion potential (V)
EC_{TML}	Erosion-corrosion degradation rate (mm/yr)
EDL	Electrical Double Layer
EIS	Electrochemical Impedance Spectroscopy
e_N	Coefficient of restitution (normal component)
ER	Erosion ratio (mm/yr)
e_T	Coefficient of restitution (tangential component)
EW	Equivalent weight (g)
F	Faraday's constant (96,485 C/m)
f	Frequency (Hz)
f_{CO_2}	Fugacity of CO_2 (Pa)
F_d	Drag force (N)
Fe	Iron
Fe^{2+}	Iron ion
Fe_3C	Iron carbide
$FeCO_3$	Iron carbonate
F_i	Indentation load (N)
FIB	Focused Ion Beam
F_M	Material hardness constant in E/CRC equation
F_P	Particle penetration factor in E/CRC equation
$F_{particle}$	Forces acting on a particle (N)
f_{pH}	pH function used in NORSOK model

F_s	Particle shape coefficient
F_{R_c/D_p}	Penetration factor for elbow radius in E/CRC equation
h	Erosion thickness loss (mm)
H	Distance from nozzle to specimen (m)
H^+	Hydrogen ion
H_2CO_3	Carbonic acid
HCl	Hydrochloric acid
HCO_3^-	Bicarbonate ion
H_V	Vickers hardness
i	Current density (A/m^2)
i_a	Anodic current density (A/m^2)
i_c	Cathodic current density (A/m^2)
i_{corr}	Corrosion current density (A/m^2)
i_d^{lim}	Diffusion limiting current density (A/m^2)
I_p	Particle moment of inertia (kg·m^2)
J	Diffusive flux (mol/m^2)
j	Imaginary number, $\sqrt{-1}$
k	Turbulent kinetic energy (m^2/s^2)
K	Ratio of vertical to horizontal particle impact forces
K_1	Material specific constant (general erosion model)
K_c	Corrosion components of erosion-corrosion (mm/yr)
K_e	Erosion components of erosion-corrosion (mm/yr)
K_T	Temperature parameter in NORSOK model
k_m	Mass transfer coefficient (m/s)
L	Characteristic fluid length (m)
l	Depth of contact from particle impact (m)
$\dot{m}$	Mass flow rate (kg/s)
M	Total mass of particles in concentration (kg)
Mn	Manganese

Mo	Molybdenum
m_p	Mass of individual particle (kg)
n	Charge number
n_{CPE}	Exponent relating CPE behaviour to ideal capacitor
n_p	Particle velocity exponent
N	Flux of chemical species (mol/m^2)
N_2	Nitrogen
NaCl	Sodium chloride
Nb	Niobium
Ni	Nickel
N_i	Number of particle impacts
N_v	Number of particles in swept volume
O_2	Oxygen
OCP	Open Circuit Potential
p	Pressure (Pa)
P	Phosphorous
p_{CO_2}	Carbon dioxide partial pressure (bar)
Pt	Platinum
PVC-C	Chlorinated Polyvinyl Chloride
Q	Volume removal after particle impact (m^3)
Q_o	Constant phase element constant (s^n/(Ω·cm^2))
r	Radial distance (m)
R	Universal gas constant (8.314 J/(mol·K))
r_a	Mass of species a produced by chemical reaction (kg)
R_a	Concentration of species a produced by chemical reaction (mol/m^3)
R_c	Elbow radius (m)
RCE	Rotating Cylinder Electrode
R_{ct}	Charge transfer resistance (Ω·cm^2)

RDS	Rate Determining Step
Re	Reynolds number
Re_J	Jet Reynolds number
Re_p	Particle Reynolds number
r_N	SIJ nozzle radius (m)
r_p	Particle radius (m)
R_p	Polarisation resistance ($\Omega \cdot cm^2$)
R_s	Solution resistance ($\Omega \cdot cm^2$)
S	Sulphur
S	Particle boundary layer stopping distance (m)
S_a	Ariel surface texture (m)
Sc	Schmidt number
SEM	Scanning Electron Microscope
Sh	Sherwood number
Si	Silicon
SiC	Silicon carbide
SIJ	Submerged Impinging Jet
S_M	Momentum source
SST	Shear Stress Transport
T	Temperature (K)
t	Time (s)
TML	Total Material Loss
U	Flow velocity (m/s)
u, v, w	Flow velocity in x, y and z directions (m/s)
u_τ	Friction velocity (m/s)
u^+	Dimensionless velocity
u^T	Tangential velocity (m/s)
V	Vanadium
v_e	Limiting erosion velocity in API-RP-14E equation (m/s)

V_f	Fluid volume (m^3)
v_p	Particle impact velocity (m/s)
v_L	Characteristic particle impact velocity (m/s)
W	Sand production rate (kg/day)
x, y, z	Cartesian coordinates (m)
$\dot{x}$	Horizontal particle velocity (m/s)
x_{cut}	Particle cutting distance (m)
y^+	Dimensionless wall distance
y_{cut}	Particle cutting depth (m)
Z	Impedance ($\Omega \cdot cm^2$)
Z'	Real component of impedance ($\Omega \cdot cm^2$)
Z''	Imaginary component of impedance ($\Omega \cdot cm^2$)
Z_{CPE}	Constant phase element impedance ($\Omega \cdot cm^2$)
α	Angle in elbow sweep (°)
β_a	Anodic Tafel constant (mV/decade)
β_c	Cathodic Tafel constant (mV/decade)
γ	Particle equilibration number
ΔC_E	Erosion-enhanced corrosion (mm/yr)
ΔE_C	Corrosion-enhanced erosion (mm/yr)
ΔG	Gibbs free energy change (J)
$\Delta_r \bar{G}$	Electrochemical Gibbs energy change (J)
$\Delta_r \overline{G^0}$	Standard electrochemical Gibbs energy change (J)
Δm	Mass loss (g)
δ	Boundary layer thickness (m)
$\dot{\epsilon}$	Strain rate (1/s)
$\eta_{collision}$	Particle collision efficiency
θ_p	Particle impact angle (°)
θ_S	Particle impact angle caused by surface profile (°)

κ	Smooth wall empirical constant
λ	Particle equilibration number
μ	Dynamic viscosity (Pa·s)
ξ	Normally distributed random number
ρ_m	Material density (kg/m^3)
ρ_f	Fluid density (kg/m^3)
ρ_p	Particle density (kg/m^3)
τ	Shear stress (Pa)
τ_w	Wall shear stress (Pa)
ψ	Cutting depth ratio
ω	Specific turbulent dissipation rate (1/s)

Chapter 1
Introduction, Research Objectives and Project Background

1.1 Introduction

Internal corrosion of carbon steel oil and gas pipelines, caused by the presence of carbon dioxide (CO_2) dissolved in the produced fluids, is a significant issue. Failure of pipeline components as a result of corrosion mechanisms can result in serious environmental and financial consequences. The presence of sand particles in the produced fluid results in further mechanisms of degradation, as mechanical removal of material after particle impacts on the pipe wall occurs in addition to corrosion degradation. Sand particles are usually produced in ageing assets when reservoir pressure drops, and become entrained in the fluid and transported through the pipelines [1]. The wear mechanism when surfaces are exposed to impact by a sand-laden corrosive fluid is known as erosion-corrosion. Erosion-corrosion consists of an erosion component, a corrosion component and interactions between erosion and corrosion, resulting in enhanced rates of degradation.

Erosion-corrosion rates of carbon steel pipelines can be very high and disturbances in the flow caused by changes in the pipe geometry, such as elbows and tees, can suffer from high quantities of particle impingement [2]. High flow velocities in pipelines can also increase the rates of erosion-corrosion through enhanced transportation of corrosive species to and from the corroding metal surface and high particle impact velocities [3, 4]. Despite being highly susceptible to erosion-corrosion degradation, carbon steel is widely used as a pipeline material due to its low cost and ease of manufacturing [5]. Therefore methods used to mitigate the loss of pipeline material are essential to prevent excessive degradation. Corrosion inhibitors are chemicals that are used to prevent corrosion of carbon steel, and function by adsorbing to the surfaces of pipelines [3]. However, the presence of sand particles and high flow velocities can reduce the effectiveness of these chemicals [6, 7]. Erosion-corrosion research remains an important challenge to the oil and gas industry, as there exists a lack of understanding about the mechanisms of erosion-corrosion and in particular the interactions between erosion and corrosion of carbon steel in CO_2 environments [8].

1.2 Significance of Corrosion and Erosion-Corrosion in the Oil and Gas Industry

Corrosion is a common cause of pipeline failure, as shown in Table 1.1, in a study completed by Kermani and Harr [9] on the causes of failures in oil and gas pipelines. Corrosion represented the most significant proportion of failures, and it has been reported that corrosion has an equivalent cost of approximately 3% of turnover for oil and gas pipeline operators [5]. The significance of corrosion degradation is clear and reducing its effects could result in reduced maintenance costs and fewer corrosion related failures.

Table 1.1 Causes of pipeline failure in the oil and gas industry [9]

Causes of Failure	Proportion of Failures (%)
Corrosion	33
Fatigue	18
Mechanical damage/overload	14
Brittle fracture	9
Fabrication defects (excluding weld defects)	9
Welding defects	7
Others	10

The corrosion related failures are shown in more detail in Table 1.2, where the specific causes of corrosion failure are shown [9]. Several mechanisms of corrosion failure exist, with CO_2 corrosion accounting for the most significant proportion of failure. Erosion-corrosion failures accounted for 9% of the failures shown in Table 1.2, highlighting the significance of sand production in CO_2 environments. Sand production is considered inevitable in fields that have a relatively low formation strength, and is more likely later in the life cycle of the reservoir, resulting in erosion degradation of pipelines if particles impinge on the pipe walls [1]. If sand is expected early in the life cycle of the reservoir, sand exclusion systems are installed, but they can result in a loss of production, so sand is often managed when production starts [10, 11]. A recent review of erosion-corrosion explained that erosion-corrosion has become a much more relevant area of research in recent years and is significant in many industries, but that a general understanding of erosion-corrosion mechanisms was still lacking [8].

Table 1.2 Corrosion failure in the oil and gas industry [9]

Causes of Failure	Proportion of Failures (%)
CO_2 related	28
Hydrogen sulphide related	18
Preferential weld	18
Pitting	12
Erosion-corrosion	9
Galvanic	6
Crevice	3
Impingement	3
Stress corrosion	3

1.3 Project Objectives

It has been highlighted that erosion-corrosion of carbon steel in CO_2 environments is a significant challenge in the oil and gas industry. In collaboration with Shell UK, the aim of this research was to understand the mechanisms of erosion-corrosion of carbon steel in CO_2 environments and the interactions between erosion and corrosion in different flow geometries. The understanding of erosion-corrosion interactions and methodology used to define erosion-corrosion conditions in different flow geometries was expected to be improved by the work completed in this thesis. The objectives of this project, summarised in Figure 1.1, were to:

- Complete a parametric study of erosion-corrosion of carbon steel in conditions representative of a Shell UK field where erosion-corrosion is a significant issue, to determine the contribution of corrosion, erosion and erosion-corrosion interactions to total erosion-corrosion degradation;
- Complete an evaluation of two corrosion inhibitors used in the field to investigate how hydrodynamic conditions and the presence of sand particles influence the performance of inhibitors;
- Investigate the mechanisms of corrosion-enhanced erosion and erosion-enhanced corrosion of carbon steel using different test methods and various surface analysis techniques;

- Determine the hydrodynamic conditions and the trajectories of particles through different flow geometries used in erosion-corrosion testing of carbon steel;
- Develop a pipeline component geometry for erosion-corrosion testing of carbon steel that more accurately represents the typical erosion-corrosion conditions in pipe flow in the field;
- Develop a methodology for predicting the erosion-corrosion conditions in different flow geometries to understand the influence of flow and particle trajectories in erosion-corrosion.

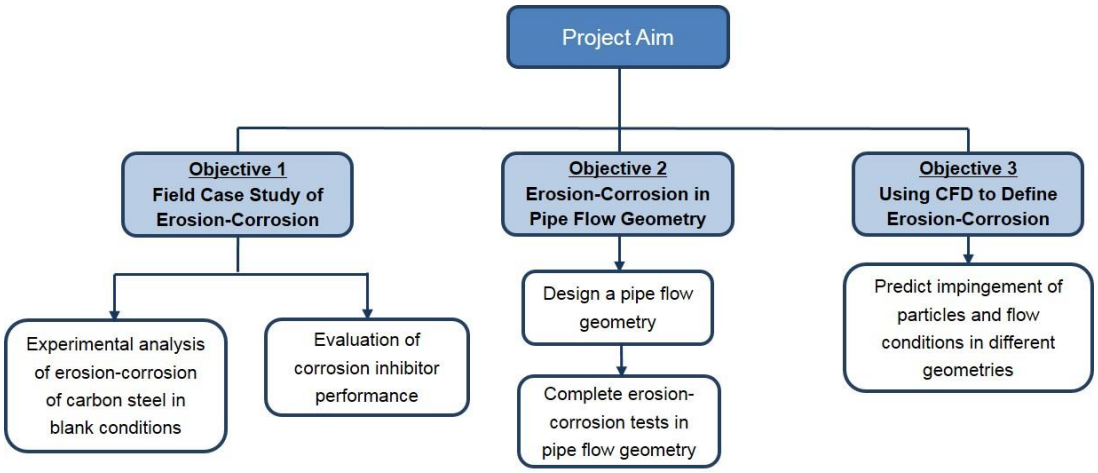

Figure 1.1 Project framework showing the aims and objectives of the research to understand erosion-corrosion of carbon steel in CO_2 environments

1.4 Thesis Structure

This thesis is written in ten chapters. The first chapters of the thesis explain the background and relevant theory in the field of erosion-corrosion and present a review of literature relevant to erosion-corrosion. The second section of chapters explain the experimental methodology, the results from erosion-corrosion experimental analysis and prediction of fluid and particle flow in different geometries. The final chapters consist of a discussion of the experimental and computational results, key findings from the work and conclusions from the research.

The current chapter has summarised the background and aims and objectives of the project. Chapter 2 explains the fundamental theory of erosion-corrosion, CO_2 corrosion mechanisms and fluid flow. Chapter 3 provides a review of the literature that investigates the mechanisms of erosion-corrosion, the influence

of different parameters on erosion-corrosion and methods used to predict erosion-corrosion and the flow of sand particles in different geometries.

Chapter 4 describes the main experimental methods used to complete erosion-corrosion testing of carbon steel and the main techniques used to analyse the surfaces of carbon steel samples used in erosion-corrosion testing. A case study of erosion-corrosion in conditions representative of the conditions in the Shell UK fields investigated was completed in Chapter 5 using a submerged impinging jet (SIJ), with the evaluation of two corrosion inhibitors completed in erosion-corrosion conditions. In Chapter 6, the mechanisms of erosion-enhanced corrosion and corrosion-enhanced erosion were investigated in more detail, with multiple surface analysis techniques utilised alongside predictions of particle flow in the SIJ using computational fluid dynamics (CFD) to aid the understanding of erosion-corrosion interactions. Chapter 7 explains the design of a 90° elbow, used for erosion-corrosion testing of carbon steel in conditions more representative of pipe flow field conditions. A methodology for predicting and comparing the erosion-corrosion conditions between different flow geometries is presented in Chapter 8.

In the final section, the results in Chapters 5 to 8 are discussed in Chapter 9, with the theories for the main mechanisms of the interactions between erosion and corrosion discussed. The comparison between different flow geometries and the success of the methodology for comparing erosion-corrosion conditions between different geometries are also discussed. The conclusions from the work and suggestions for future work are given in Chapter 10.

Chapter 2
Fundamentals of Erosion-Corrosion and Fluid Dynamics

2.1 Introduction

Erosion-corrosion consists of mechanical damage from particle impacts, electrochemical material dissolution through corrosion mechanisms and interactions between the two mechanisms. A brief overview of the fundamental mechanisms of erosion-corrosion of carbon steel in CO_2 environments is given in this chapter. The fundamentals of aqueous corrosion in a CO_2 environment are well documented in the literature and are relatively well understood [3, 5, 12]. More debate exists with regards to erosion mechanisms and, in particular, erosion-corrosion mechanisms, as less understanding of the field exists. Therefore a brief overview of erosion-corrosion is given in this chapter, with the main theories discussed in more detail in Chapter 3.

The fundamental theory of fluid flow used in CFD simulations is also explained. CFD is commonly used to predict fluid flows and particle trajectories in different flow geometries [13]. CFD was used in this thesis to predict the flow of fluid, transport of species and trajectories of particles through the different flow geometries used in experimental erosion-corrosion analysis of carbon steel. CFD is a valuable tool for understanding fluid flow without requiring experimental techniques to provide information about the flow through a particular geometry, often beyond the capability of experimental techniques or measuring equipment [13]. The main equations used in CFD analysis and the fundamentals of fluid flow are given in this chapter.

2.2 Definition of Erosion-Corrosion

Erosion-corrosion degradation consists of mechanical damage from an impacting particle on a surface, corrosion and interactions between erosion and corrosion, as defined by Equation (2.1) [14-16]:

$$EC_{TML} = C_0 + E_0 + \Delta C_E + \Delta E_C \qquad (2.1)$$

where EC_{TML} is the total erosion-corrosion material loss, C_0 is the static corrosion component, E_0 is the pure erosion component, ΔC_E is the erosion-enhanced corrosion component and ΔE_C is the corrosion-enhanced erosion

component. The mechanisms and significance of the individual contributions of each of these parameters to total erosion-corrosion are discussed in the literature review in Chapter 3, with no complete understanding of the mechanisms of erosion-corrosion of active materials existing [8]. Interactions between erosion and corrosion are known to be significant in certain conditions, but the reasons for these mechanisms are not fully understood and are investigated in this thesis. Equation (2.1) was used throughout this thesis to quantify the corrosion, erosion and interaction components in a range of erosion-corrosion, flow-induced corrosion and pure erosion experiments.

2.3 Mechanisms of Erosion

Erosion degradation of a material is a tribological process, whereby particles suspended in a fluid impact on the surface of a material causing mechanical degradation [16]. Sand particles suspended in the produced fluid of oil and gas pipelines can cause two problems in the industry. Sand settling occurs at low velocities, where sand settles in horizontal sections of pipes and is not transported through the pipe [1]. The other issue that sand can cause is erosion, where the fluid velocity is sufficient to transport the particles and cause impingement of particles onto the carbon steel pipeline surface [1]. The focus of this work was on the mechanisms of erosion and erosion-corrosion, where sand particles are transported through the pipeline at high velocities and impinge onto the surfaces of pipelines.

The theory of material removal after the impingement of a particle has been debated on several occasions, and the main mechanisms are discussed in Chapter 3. However, it is well known that erosion degradation is highly dependent on the impingement angle of the particle on the surface of the material and the properties of the target material, i.e. the material subject to particle impingement [10]. Erosion mechanisms vary significantly between brittle and ductile materials. The typical variation of erosion degradation at different particle impingement angles for ductile and brittle materials is shown in Figure 2.1 [4, 17-21]. Erosion degradation behaviour is significantly different for ductile and brittle materials, with highest rates of degradation at impact angles in the range of 15° to 25° observed on ductile materials, before decreasing at higher impact angles. The highest rates of degradation for brittle materials are observed impact angles closer to 90°. The focus of this work was on the erosion and erosion-corrosion of carbon steel, a ductile material.

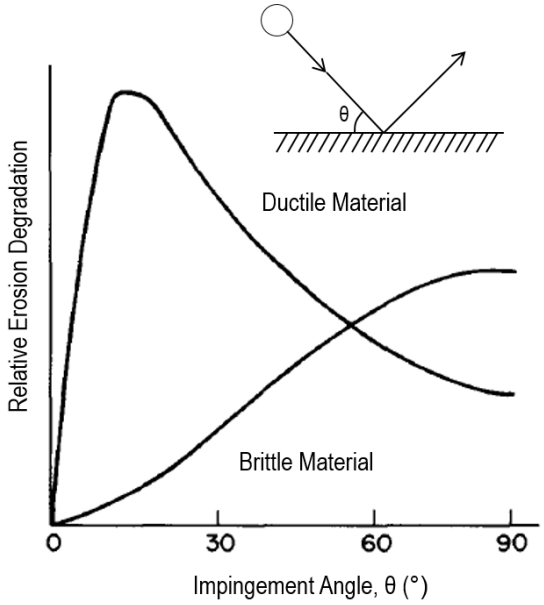

Figure 2.1 Influence of particle impact angle on erosion degradation of ductile and brittle materials adapted from [4]

2.4 Aqueous Corrosion Mechanisms

In oil gas pipelines when CO_2 is present in produced fluids, carbon steel corrodes [5]. CO_2 corrosion, also referred to as sweet corrosion, is one of the most significant mechanisms of failure of oil and gas pipelines, as shown previously [5]. Other mechanisms of corrosion exist, such as hydrogen sulphide corrosion, preferential weld corrosion and galvanic corrosion that were beyond the scope of this thesis that contribute to corrosion failures of oil and gas pipelines [5]. The fundamental mechanisms of aqueous corrosion of a metal are explained in this section.

2.4.1 Fundamentals of Aqueous Corrosion

Corrosion is the destructive attack of a metal by electrochemical reaction with its environment [22]. Corrosion degradation can be broadly classified into two categories, uniform (or general) corrosion and localised corrosion. Uniform corrosion occurs when the corrosion mechanisms are consistent across an entire surface area, whereas localised corrosion occurs over much smaller regions on a surface [5, 23, 24]. An electrochemical corrosion reaction requires an anode, a cathode, a metallic conductor and an electrolytic conductor, with corrosion reactions separated into anodic and cathodic

reactions [23]. A typical anodic reaction of a corroding metal is defined by Equation (2.2):

$$M \rightarrow M^{n+} + ne^{-} \tag{2.2}$$

where n is the number of electrons (e^{-}) released by the metal, M. The metal ions are transported from the anode to the cathode through the electrolyte, typically a liquid containing a concentration of electrochemically active species [23]. Anodic and cathodic sites can exist on the same metal sample, which also acts as the metallic conductor, providing three of the four components required for electrochemical corrosion [23]. The final component, the electrolyte, consists of anions, negatively charged ions that move towards the anode, and cations, positively charged ions that move towards the cathode, where they are reduced [23]. The electrons produced in the anodic reaction remain on the corroding metal and migrate to the cathode [25]. The cathodic reaction consumes the electrons, achieved through reducible species in the electrolyte adsorbing onto the metal surface, removing the electrons [25].

Metals corrode as they have a tendency to return to a low energy state after being extracted from their ore [23]. The tendency of a metal to corrode is defined by the Gibbs free energy change (ΔG) [22]. If the free energy change as a result of a reaction is negative, then the reaction is in a lower energy state and is more stable, so the reaction occurs spontaneously. If the free energy change is positive, then the reaction does not occur spontaneously [23]. The more negative the Gibbs free energy, the greater the tendency of the reaction to occur [22]. The Gibbs free energy change is defined by Equation (2.3):

$$\Delta_r \bar{G} = -nFE \tag{2.3}$$

where $\Delta_r \bar{G}$ is the electrochemical Gibbs energy change, E is the potential, n is the number of electrons and F is the Faraday constant. The Gibbs free energy at standard conditions of ambient temperature and atmospheric pressure is defined by Equation (2.4):

$$\Delta_r \overline{G^0} = -nFE^0 \tag{2.4}$$

where $\Delta_r \overline{G^0}$ is the standard electrochemical Gibbs energy change, E^0 is the standard redox potential, defined as the potential of a metal in contact with its own ions at a concentration equal to unit activity at 25°C [23]. The Nernst equation is used to determine the potential of a metal in a solution in which the ions are not at unit activity or in a solution of ions other than its own, Equation (2.5) [22]:

$$\mathrm{E} = E^0 - \frac{RT}{nF}\ln\frac{[c_{products}]}{[c_{reactants}]} \tag{2.5}$$

where R is the universal gas constant, $c_{products}$ is the concentration of the product species and $c_{reactants}$ is the concentration of the reactant species. The Nernst equation does not contain a current term, which is typically of interest from a corrosion perspective as it can be used to calculate the corrosion rate of a metal [24]. The Buttler-Volmer equation is used to relate electrical current to changes in metal potential from an external source, Equation (2.6) [24]:

$$i = i_{corr}\left[e^{\left(\frac{(1-\alpha)nF(E-E_{corr})}{RT}\right)} - e^{\left(\frac{-\alpha nF(E-E_{corr})}{RT}\right)}\right] \tag{2.6}$$

where i is the external current density flowing to or from an electrode as a result of an applied potential, i_{corr} is the corrosion current density, α is a coefficient ranging from 0 to 1 and E_{corr} is the free corrosion potential.

2.4.2 Electrical Double Layer

When a metal corrodes, metal atoms are removed from their lattice sites to ionise as cations, leaving a negatively charged metal surface due to excess electrons [26]. Water molecules surround the metal ions as they leave the lattice, hydrating them. Some of the positively charged metal ions remain at the surface due to the negative charge [24]. The water layer around the ions prevents them from making contact with excess electrons and reducing to form metal atoms. Positively charged ions present in the bulk solution, are also attracted to the negatively charged metal surface [26]. The electrolyte layer adjacent to an electrode surface contains water molecules and ions from the metal and the bulk electrolyte. The metal surface and the adjacent electrolyte is referred to as the electrical double layer (EDL), shown in Figure 2.2, with the typical components of a representative electrical circuit of the EDL also shown [24].

The EDL is typically represented as a capacitor due to the physical separation of two oppositely charged planes. The EDL also acts as a resistor, as the metal resists transferring excess electrons to the electrochemically active species. Electrochemically active species diffuse from the bulk solution to the metal surface and discharge the EDL [24].

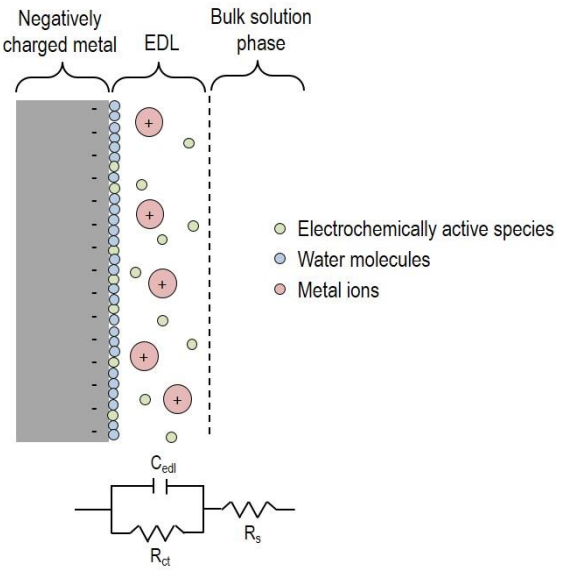

Figure 2.2 EDL and equivalent circuit consisting of a solution resistance (R_s), charge transfer resistance (R_{ct}) and capacitance (C_{edl}) [24, 26]

2.5 Fundamentals of Computational Fluid Dynamics

CFD is the analysis of systems, such as fluid flow, by means of computer based simulation [13]. CFD is regularly used in predictions of fluid flow through different geometries and has a wide range of uses and applications, with it becoming a more essential component in the design of components and understanding of systems [13]. A brief overview of the theory used in CFD simulations of fluid flow are explained in this section.

2.5.1 Laws of Fluid Motion

The governing equations of fluid flow are based on the following conversation laws of physics, that state that [13]:

- The mass of a fluid is conserved in a fluid element;
- The rate of change of momentum equals the sum of the forces on a fluid particle;
- The rate of change of energy is equal to the sum of the rate of heat addition to and the rate of work done on a fluid particle.

In CFD, the fluid is represented by small elements, an example of a fluid element is shown in Figure 2.3. The fluid in the element is regarded as a continuum, therefore macroscopic properties of the fluid, such as velocity, pressure and density are assumed to be averaged over the entire element [13]. All fluid properties are functions of space and time, and are therefore

vectors. For example, the fluid pressure vector would be written as $\mathbf{p}(x, y, z, t)$ and the velocity vector $\mathbf{u}(x, y, z, t)$, where x, y and z are Cartesian coordinates and t is time. As the fluid element is small in size, the properties of the fluid at the faces of the element can be defined by the first two terms in a Taylor series expansion. The pressure at the two faces in the x axis is defined by Equation (2.7), where p is the pressure in the centre of the fluid element [13]:

$$p \pm \frac{\partial p}{\partial x}\frac{1}{2}\delta x \tag{2.7}$$

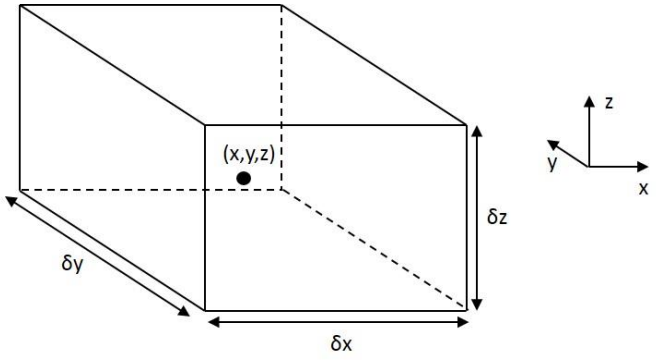

Figure 2.3 A small element of fluid adapted from [13]

For mass conservation in each of the three dimensions, the rate of increase of mass in the fluid element is equal to the net rate of flow of mass into the fluid element [13]. The rate of increase of mass in the fluid element is defined by Equation (2.8):

$$\frac{\partial}{\partial t}(\rho\delta x\delta y\delta z) = \frac{\partial \rho}{\partial t}\delta x\delta y\delta z \tag{2.8}$$

where ρ is the density of the fluid. The mass flow rate across the face of the element is defined by Equation (2.9):

$$\begin{gathered}\dot{m}_{in} - \dot{m}_{out} = \\ \left(\rho u - \frac{\partial(\rho u)}{\partial x}\frac{1}{2}\delta x\right)\delta y\delta z - \left(\rho u + \frac{\partial(\rho u)}{\partial x}\frac{1}{2}\delta x\right)\delta y\delta z + \\ \left(\rho v - \frac{\partial(\rho v)}{\partial y}\frac{1}{2}\delta y\right)\delta x\delta z - \left(\rho v + \frac{\partial(\rho v)}{\partial y}\frac{1}{2}\delta y\right)\delta x\delta z + \\ \left(\rho w - \frac{\partial(\rho w)}{\partial z}\frac{1}{2}\delta z\right)\delta x\delta y - \left(\rho w - \frac{\partial(\rho w)}{\partial z}\frac{1}{2}\delta z\right)\delta x\delta y\end{gathered} \tag{2.9}$$

where $\dot{m}_{in}$ is the mass flow rate into the element and $\dot{m}_{out}$ is the mass flow rate out of the element.

Flow entering the element produces an increase in mass and flow leaving the element reduces the mass, and therefore is negative in Equation (2.9). For the law of mass conservation to apply, Equation (2.8) must be equal to

Equation (2.9). The sum of Equation (2.8) and Equation (2.9) after dividing by the element volume, is given by Equation (2.10) [13]:

$$\frac{\partial \rho}{\partial t} + \frac{\partial (\rho u)}{\partial x} + \frac{\partial (\rho v)}{\partial y} + \frac{\partial (\rho w)}{\partial z} = 0 \tag{2.10}$$

In vector notation, Equation (2.10) is written as Equation (2.11), known as the continuity equation:

$$\frac{\partial \rho}{\partial t} + \nabla \cdot (\rho \mathbf{U}) = 0 \tag{2.11}$$

where $\mathbf{U}$ is the velocity vector and ∇ is the divergence. For an incompressible fluid, density is constant, therefore it does not vary with time and Equation (2.11) becomes Equation (2.12) [13]:

$$\nabla \cdot \mathbf{U} = 0 \tag{2.12}$$

2.5.2 Navier-Stokes Equations

The Navier-Stokes equations define fluid motion and are solved with the continuity equation in fluid flow problems [13]. The Navier-Stokes equation is derived from Newton's second law, and is defined as [13, 27]:

$$\rho \frac{Du}{Dt} = -\frac{\partial p}{\partial x} + \nabla \cdot (\mu \cdot \nabla u) + S_{Mx} \tag{2.13}$$

$$\rho \frac{Dv}{Dt} = -\frac{\partial p}{\partial y} + \nabla \cdot (\mu \cdot \nabla v) + S_{My} \tag{2.14}$$

$$\rho \frac{Dw}{Dt} = -\frac{\partial p}{\partial z} + \nabla \cdot (\mu \cdot \nabla w) + S_{Mz} \tag{2.15}$$

where μ is the fluid dynamic viscosity and S_M represents a momentum source. A general form of Equations (2.13), (2.14) and (2.15) can be written, as the equations share similar parameters. To account for all scalar quantities, a term denoted by φ is used [13]:

$$\frac{\partial (\rho \varphi)}{\partial t} + \nabla \cdot (\rho \varphi \mathbf{U}) = \nabla \cdot (\Gamma \cdot \nabla \varphi) + S_{\varphi} \tag{2.16}$$

where Γ is a diffusion coefficient. In words this equation can be written as:

Rate of increase of φ of fluid element	+	Net rate of flow of φ out of fluid element	=	Rate of increase of φ due to diffusion	+	Rate of increase of φ due to sources

The application of these equations in CFD analysis to predict fluid flow in the conditions relevant to this thesis is discussed in more detail in the Methodology in Chapter 4.

Chapter 3
Review of Carbon Steel and Chemical Inhibitor Performance in Sand-Producing CO_2 Oil and Gas Conditions

A brief overview of the main theories of erosion-corrosion was given in Chapter 2. This theory is applied to the relevant oil and gas erosion-corrosion conditions in this chapter, along with a review of the research that has been completed in the field of erosion-corrosion with relevance to CO_2 flow-induced corrosion, erosion and erosion-corrosion of carbon steel in the oil and gas industry. The main parameters that influence flow-induced corrosion, erosion and erosion-corrosion are discussed and the main theories that have been suggested to explain the mechanisms of wear and interactions between erosion and corrosion. Gaps in the literature and areas of further required research within the field are identified.

3.1 Introduction

In recent years, more research has been completed in the field of erosion-corrosion but a lack of general understanding of erosion-corrosion exists with some uncertainty about the mechanisms of erosion-corrosion and the interaction between erosion and corrosion that are applicable across a range of materials and applications [8]. Equation (2.1) defined erosion-corrosion total material loss as the sum of a corrosion component, an erosion component and components related to the interaction between the erosion and corrosion mechanisms. Therefore, several areas of research were required to fully understand how each of these mechanisms influenced erosion-corrosion degradation of carbon steel, with a knowledge of both corrosion and erosion mechanisms required.

Fluid flow is highly influential on CO_2 corrosion. Flow has a significant effect on the corrosion of carbon steel in CO_2-saturated conditions and corrosion rates have been shown to increase as a result of increasing flow velocity [5, 28-31]. Erosion in oil and gas pipelines is usually significant above a threshold flow velocity and high flow velocities are typical in erosion-corrosion conditions, with threshold velocities defining the transition between sand settling in horizontal pipelines and erosion are influenced by conditions in the pipeline, such as fluid density, pipe diameter and particle diameter [11]. Several models exist that can be used to predict threshold velocities above which erosion degradation becomes significant [32, 33]. Hu et al. [34] showed

negligible erosion at flow velocities of 7 m/s in SIJ tests but showed erosion rates were significant at 14 m/s. Flow velocities in oil and gas pipelines can vary based on pipe geometry, and have been reported to be less than 3 m/s [35]. However, field data also shows that smaller diameter sections of pipelines, such as topside components, can experience flow velocities in excess of 20 m/s. The interactions between erosion and corrosion also further complicate the understanding of erosion-corrosion mechanisms [8]. The review of literature for erosion-corrosion of carbon steel is categorised into the following key sections:

- Flow-induced corrosion and the influence of parameters on corrosion mechanisms of carbon steel in CO_2 environments;
- Mechanisms of material removal as a result of the impingement of sand particles on metal surfaces and the parameters that influence erosion of ductile materials;
- Erosion-corrosion and the causes of the interactions between erosion and corrosion resulting in corrosion-enhanced erosion and erosion-enhanced corrosion;
- CFD prediction of particle trajectories and erosion rates in different flow geometries;
- Overview of the main mathematical models used for the prediction of erosion and erosion-corrosion rates;
- Influence of flow geometry on erosion-corrosion of carbon steel;
- Mitigation of erosion-corrosion through the use of corrosion inhibitors used to reduce corrosion rates and their effectiveness in high flow velocity and sand-containing conditions.

3.2 Parameters Influencing Corrosion Mechanisms

A review of CO_2 corrosion mechanisms, without sand, is completed first. A significant amount of research had been completed to evaluate the influence of different parameters on corrosion, with the main parameters summarised in in Figure 3.1 [3, 5, 12, 28-31, 36-38]. Flow is a very influential parameter and flow-induced corrosion is the main focus of this literature review due to the high flow velocities typical of erosion-corrosion conditions. However, a wide range of parameters are known to influence the corrosion of carbon steel in CO_2 conditions and some of the main parameters are briefly discussed.

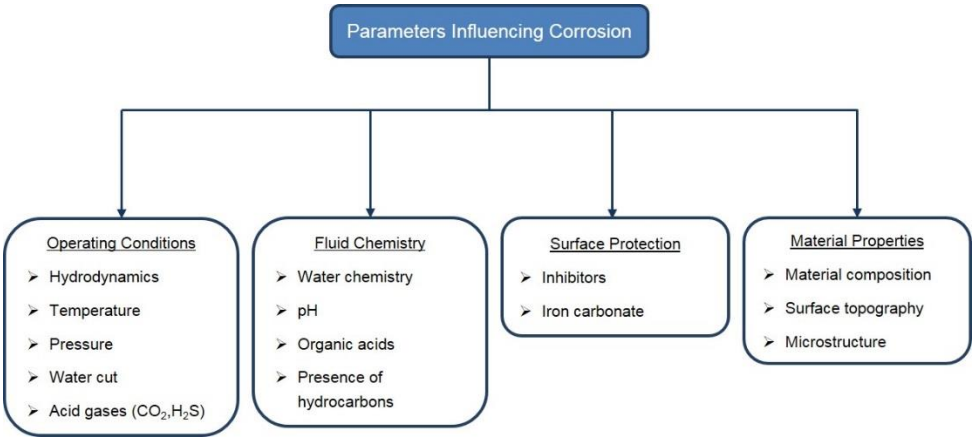

Figure 3.1 Parameters influential on the corrosion of carbon steel in oil and gas conditions adapted from [5]

3.2.1 Anodic and Cathodic Reactions in CO_2 Conditions

An overview of the theory of aqueous corrosion mechanisms was given in Chapter 2, where it was highlighted that corrosion reactions were split into anodic and cathodic reactions. The theory is extended in this chapter and applied to CO_2 corrosion of carbon steel. Dry CO_2 gas is not corrosive in the temperatures typical of oil and gas production, but is corrosive when dissolved in an aqueous phase, thus promoting an electrochemical reaction when in contact with steel [5]. CO_2 dissolves in water, Equation (3.1), of which a small fraction hydrates to form carbonic acid (H_2CO_3), Equation (3.2) [39]:

$$CO_{2(g)} \Leftrightarrow CO_{2(aq)} \tag{3.1}$$

$$CO_{2(aq)} + H_2O \Leftrightarrow H_2CO_{3(aq)} \tag{3.2}$$

where (g) represents a gas, and (aq) represents an aqueous species. Carbonic acid is a weak acid compared to mineral acids as it does not fully dissociate [5]. The dissociation of carbonic acid provides a source of H^+ ions and bicarbonate (HCO_3^-) ions, Equation (3.3). Further dissociation of bicarbonate ions forms additional hydrogen and carbonate ions, Equation (3.4) [39]:

$$H_2CO_{3(aq)} \Leftrightarrow H^+_{(aq)} + HCO^-_{3(aq)} \tag{3.3}$$

$$HCO^-_{3(aq)} \Leftrightarrow H^+_{(aq)} + CO^{2-}_{3(aq)} \tag{3.4}$$

The dissociation of carbonic acid provides a source of H^+ ions which are reduced at the steel surface to produce hydrogen gas [39]. There exists some debate about the mechanisms of the cathodic reaction as carbonic acid reduction at the surface has also been reported in addition to reduction of H^+ ions produced from carbonic acid dissociation [3, 5, 39]. de Waard and

Milliams [40] proposed that direct reduction of carbonic acid occurred at the surface, and it is typically assumed that both reactions can occur [3, 39]. The cathodic half reactions are therefore defined as:

$$2H^{+}_{(aq)} + 2e^{-} \leftrightarrow H_{2(g)} \tag{3.5}$$

$$2H_2CO_{3(aq)} + 2e^{-} \rightarrow H_{2(g)} + 2HCO^{-}_{3(aq)} \tag{3.6}$$

where Equation (3.5) represents H^+ reduction at the surface, known as the 'buffering effect' and Equation (3.6) represents 'direct reduction' of carbonic acid at the surface [39]. pH also has an influence on the cathodic reactions, with Equation (3.5) more dominant when pH < 4, and the reduction of carbonic acid more significant at pH > 4 [3, 30]. In oil and gas pipelines, pH can vary significantly depending on conditions in the field, and can range from less than 4 to up to 7 [3].

Iron atoms at the surface give up electrons and dissolve into the aqueous solution, producing ferrous ions [39]. The anodic reaction is defined as:

$$Fe_{(s)} \rightarrow Fe^{2+}_{(aq)} + 2e^{-} \tag{3.7}$$

Under certain conditions, iron carbonate ($FeCO_3$) is formed on the surface of carbon steel samples, defined in Equation (3.8). When the solubility of iron ions in the solution is exceeded, iron carbonate precipitates, potentially leading to the formation of a protective layer on the carbon steel surface which can reduce corrosion rates [3].

$$Fe^{2+} + CO^{2-}_{3} \rightarrow FeCO_3 \tag{3.8}$$

A schematic of the reactions occurring in CO_2 corrosion of carbon steel is shown in Figure 3.2, summarising the equations shown above and showing the process of CO_2 dissolving in an aqueous phase, forming carbonic acid, which then dissociates to produce a hydrogen ion and a bicarbonate ion, with the hydrogen ion being reduced at the surface to form hydrogen gas.

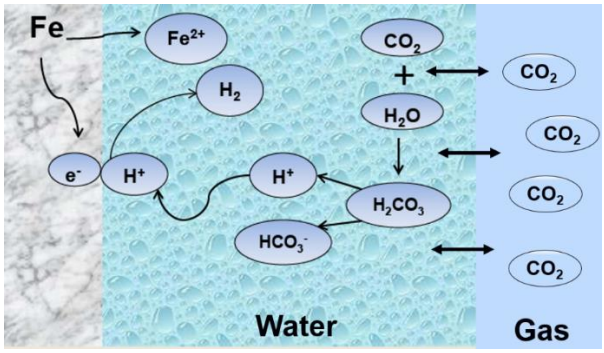

Figure 3.2 Mechanisms of the 'buffering effect' in CO_2 corrosion of carbon steel, whereby CO_2 dissolves in water to produce carbonic acid which dissociates to form H^+ ions that are reduced at the steel surface [39, 41]

The cathodic reactions and anodic reactions have been the subject of a significant amount of debate in CO_2 corrosion research [3, 5, 39]. de Waard and Milliams [40] measured higher corrosion rates in CO_2-saturated conditions than tests completed in dilute hydrochloric acid (HCl) solution. In a dilute HCl solution, the only cathodic reaction present is the reduction of H^+ ions at the surface, Equation (3.5). Higher cathodic currents were observed in CO_2-saturated conditions than in the dilute HCl conditions, with the additional cathodic reaction of carbonic acid reduction at the steel surface explaining the increase. However, it has recently been suggested that H_2CO_3 dissociates at the metal-electrolyte interface, producing H^+ ions, which are then reduced at the surface [39].

CO_2-saturated conditions are achieved after bubbling CO_2 into a solution. Saturated conditions in CO_2 corrosion environments are often defined as a partial pressure of CO_2, with a minimum time period for bubbling specified prior to starting CO_2 corrosion tests [3, 34, 42]. The concentration of CO_2 can be determined from the CO_2 partial pressure and the solubility limit, which is influenced by the ionic species in the solution [3].

The anodic reaction has been researched significantly, with the reaction originally suggested by Bockris et al. [43] for anodic dissolution of iron in strong acids, widely assumed for the anodic dissolution of iron in CO_2 environments. Bockris et al. [43] suggested that anodic dissolution of iron occurs in three stages:

$$Fe + H_2O \leftrightarrow FeOH_{(ad)} + H^+ + e^- \tag{3.9}$$

$$FeOH \xrightarrow{RDS} FeOH^+ + e^- \tag{3.10}$$

$$FeOH^+ + H^+ \rightarrow Fe^{2+}_{(aq)} + H_2O \tag{3.11}$$

In the first two stages, Equation (3.9) and (3.10), the iron is oxidised, before an Fe^{2+} ion is produced in the final stage, Equation (3.11), with Equation (3.10) being the rate determining step (RDS) [43]. FeOH is an adsorbed species. However, this mechanism does not fully define conditions in CO_2-saturated environments at pH > 4, due to the presence of carbonic species in the electrolyte [3]. An alternative mechanism for the anodic reaction was suggested by Nesic et al. [44] for pH > 5 in CO_2-saturated conditions. However, this was not relevant to the pH (pH < 5) conditions of interest in this thesis.

3.2.2 Effects of Temperature, Water Chemistry & Partial Pressure

Several parameters influence corrosion, as was shown in Figure 3.1. A brief overview of the main parameters relevant to the erosion-corrosion tests completed in this thesis is given. However, a wide range of parameters can influence the corrosion of metals in CO_2 environments, summarised in reviews of CO_2 corrosion completed by Nesic [3], Dugstad [12] and Kermani and Morshed [5]. It has been widely reported that temperature, partial pressure and the water chemistry have a significant influence on the corrosion of carbon steel, and these parameters have most relevance to this thesis [3, 5, 12].

Temperature is an important parameter as it accelerates the processes involved in corrosion, including the electrochemical, chemical and transport processes [3]. When protective corrosion products do not precipitate in low pH conditions, higher temperatures typically increase the corrosion rate of carbon steel [3]. High temperatures, typically greater than 60°C, and higher pH conditions (pH > 6) can result in the precipitation of $FeCO_3$, a corrosion product that can protect carbon steel surfaces and reduce corrosion rates in some conditions, but this was beyond the scope of this thesis [3, 5].

The water chemistry is a very influential parameter in CO_2 corrosion. Oil and gas pipe flow chemistry can be complex containing numerous species [3]. The presence of CO_2 dissolved in the aqueous phase of the produced fluid results in corrosion of the carbon steel pipeline. pH is also significant in CO_2 corrosion. pH in CO_2 saturated conditions in oil and gas pipe flow can range from less than 4 to pH 5-7 in buffered brines [3]. At pH 4 or below, direct reduction of H^+ ions is the dominant process, particularly at low partial pressures of CO_2, due to the high concentration of H^+ ions [3]. pH also has a significant influence on $FeCO_3$ precipitation. $FeCO_3$ precipitation usually becomes more likely when solution pH increases towards 7. For example, in a CO_2-saturated solution at pH 6.6 and temperature of 80°C, $FeCO_3$ precipitation is highly likely and is reported to precipitate within an hour of exposing carbon steel to these experimental conditions [3].

The formation and growth of $FeCO_3$ in conditions representative of CO_2 oil and gas conditions is an important area of research [42, 45, 46]. In this thesis, however, the focus was pH (pH < 5) conditions where protective iron carbonate films are not formed. However, sand can also be transported through pipelines in higher pH conditions where protective $FeCO_3$ films form. Some research has been completed on the protectiveness of $FeCO_3$ films in sand-containing flows, but has not been investigated in significant detail [47, 48].

The partial pressure of CO_2 also influences CO_2 corrosion of carbon steel. An increase in the partial pressure of CO_2 usually results in an increase in the corrosion rate of carbon steel in conditions when protective films have not formed. The increase in corrosion rate is explained by an increase in the concentration of carbonic acid in the solution and an accelerated cathodic reaction [3].

3.2.3 Flow-Induced Corrosion

One of the most important parameters in erosion-corrosion is hydrodynamics, which has a significant effect on corrosion. Flow can enhance the corrosion rate of carbon steel when surface films are not present, by increasing the transportation of corrosive species to and from the surface [3]. The effect of flow velocity on the corrosion rate, determined from the corrosion current, of carbon steel in pH 4, CO_2-saturated conditions, where surface films were not present, is shown in Figure 3.3 [30].

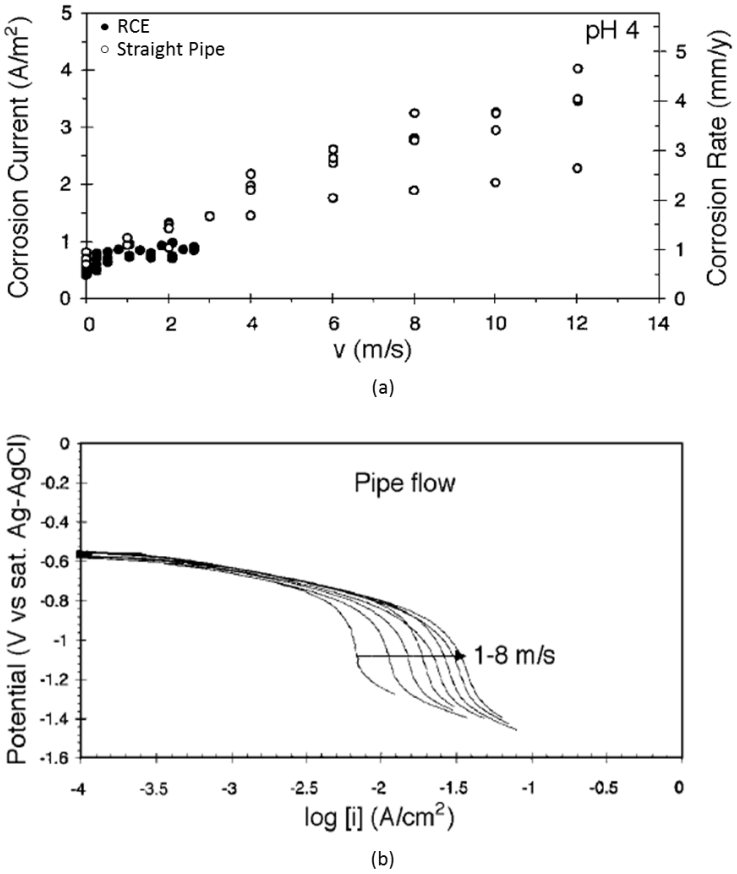

Figure 3.3 Effect of flow velocity on (a) the corrosion rate of carbon steel in a CO_2-saturated, 1% NaCl, 20°C solution rotating cylinder electrode (RCE) and straight pipe geometries and (b) cathodic potentiodynamic sweeps in a straight pipe in the same conditions showing increasing cathodic current densities [30]

It was observed that corrosion rates were significantly greater at high flow velocities compared with static conditions. Transport of electrochemically active species from the bulk solution to the carbon steel surface resulted in an increased corrosion current due to an increased hydrogen evolution cathodic reaction, limited in these conditions by the transport of H^+ ions to the surface, shown in Figure 3.3 [30]. Disturbances in the flow caused by changes in pipe flow geometry can also increase the rates of corrosion by increasing the transport of species, as local turbulence changes through the geometry [3]. Malka et al. [49] showed that corrosion rates of carbon steel were approximately five times larger in some regions of pipe flow immediately after rapid expansions and contractions in the geometry.

Several parameters can be used to define hydrodynamic conditions in a flow geometry, including flow velocity, shear stress and mass transfer coefficient and are often used to relate flow to corrosion rates [50]. Flow velocity is dependent on geometry, therefore the same flow velocity in two different geometries does not always result in the same flow-induced corrosion conditions [50]. Shear stress has been used to define the hydrodynamic conditions but this parameter does not directly relate flow to a corrosion mechanism [28, 51]. In certain conditions, mass transfer coefficients are more relevant to flow-induced corrosion, according to some authors, as this defines both the hydrodynamic conditions and the transport of corrosive species to the surface of a material and therefore has relevance to both flow and corrosion [30, 31].

In low pH conditions (pH < 4) when no surface films are present, the most convenient parameter used to relate the flow to corrosion rates is the mass transfer coefficient, defining the rate at which corrosive species are transported to the surface of a specimen [30, 31]. In strong acids and low pH conditions, the cathodic reaction is defined by hydrogen evolution at the surface, Equation (3.5) shown previously. In mass transfer control, the rate at which hydrogen evolution occurs cannot exceed the rate at which H^+ ions are transported to the surface from the bulk solution [12]. Mass transfer coefficient is also an effective parameter when comparing conditions between different flow geometries [30, 31, 52-54]. Nesic et al. [30, 31] showed that mass transfer coefficient translated reliably between a straight pipe and a rotating cylinder electrode (RCE) on carbon steel corrosion tests in CO_2 conditions, as shown in Figure 3.4.

Silverman [52] defined equations that can be used to replicate other geometries through mass transfer coefficient. Straight pipes and RCEs have

been widely researched and the mass transfer coefficients in those geometries have been well defined [52, 55, 56]. More complex geometries, however, are less well understood. A commonly used geometry for erosion-corrosion and flow-induced corrosion testing is the SIJ, used extensively in erosion-corrosion research [6, 34, 35, 57-63]. However, mass transfer coefficients in SIJ geometries are not as thoroughly defined. Furthermore, complex pipe flow geometries, such as elbows, also do not have well defined mass transfer coefficient equations.

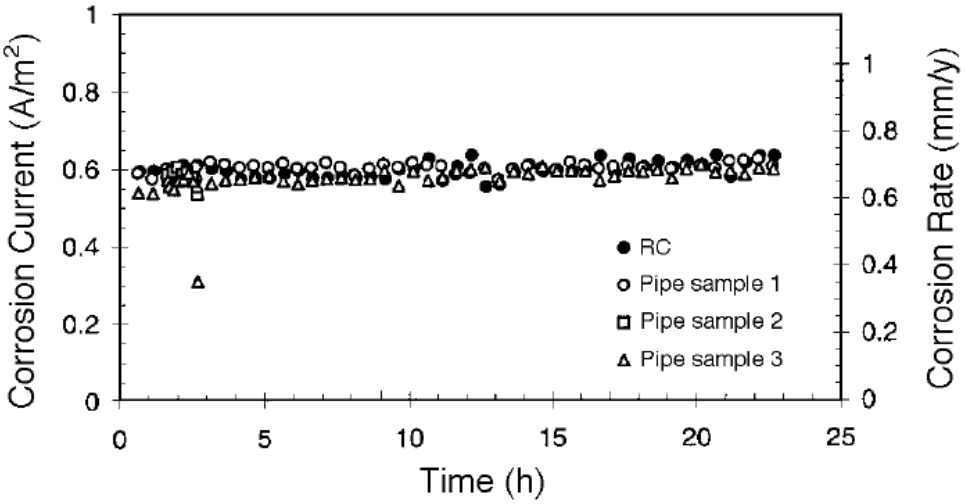

Figure 3.4 Corrosion rate of carbon steel in a CO_2-saturated, 1% NaCl, 20°C solution in a rotating cylinder electrode (labelled as RC) and in a straight pipe in equivalent mass transfer conditions [30]

Shear stress is more regularly used to define conditions in SIJ testing [51]. Efird [28, 29, 36] completed flow-induced corrosion tests using carbon steel in different flow geometries, a straight pipe, an SIJ and an RCE at pH 6 in CO_2 saturated conditions. The corrosion rates of carbon steel samples in each of these three geometries were compared using wall shear stress on the surface of the specimen. However, calculation of shear stress in SIJ geometries is not always possible in some conditions and varies across the test specimen surface [36, 51, 64, 65]. An increase in shear stress resulted in an increase in corrosion rate in all geometries, but it was shown that shear stress was not a reliable parameter for translating between different flow geometries as corrosion rates were not the same for similar shear stress values [36]. In high pH conditions (pH > 4) the effect of flow on corrosion is less well defined due to the different mechanisms associated with the presence of carbonic species in higher pH conditions.

Mass transfer coefficients in complex pipe flow geometries have been predicted using CFD [66-70]. Keating and Nesic [66] predicted the mass

transfer coefficients on the surfaces of a 180° pipe bend, and Wang et al. [67] predicted the mass transfer coefficients in a 90° elbow. However, there currently does not exist any reliable correlations for simple prediction of mass transfer coefficients in elbows and some other complex flow geometries that can be used in a wide range of conditions.

To determine mass transfer coefficients experimentally, limiting currents are obtained using a three electrode cell setup by completing a cathodic potentiodynamic sweep [30, 71]. The limiting current technique is used to determine when changing the applied potential no longer causes the cathodic current density to change beyond a potential of approximately 50 mV below open circuit potential (OCP), representing a diffusion-controlled reaction [24]. At pH < 4, this is significant as the cathodic reaction is dominated by the reduction of H^+ ions at the surface, rather than direct reduction of carbonic acid [3]. Limiting currents have been obtained by Nesic et al. [30, 31] to determine mass transfer coefficients in different hydrodynamic conditions in N_2-saturated solutions buffered to pH 3 using HCl. The mass transfer coefficient can be determined from the limiting current using Equation (3.12) [30]:

$$k_m = \frac{i^d_{\mathrm{lim}}}{F \cdot 10^{-pH}} \tag{3.12}$$

where k_m is the mass transfer coefficient, F is the Faraday constant and i^d_{lim} is the diffusion limiting current density.

A water phase, an oil phase and a gas phase can be present in oil and gas pipe flow, resulting in significantly different flow conditions when more than one phase is present in the flow [3]. Annular flow, slug flow and stratified flow are examples of multiphase flows, where the type of flow is defined by the proportion of different phases in the flow [3]. Multiphase flow can have a significant influence on the corrosion rate of carbon steel through fluctuating mass transfer rates [3]. Multiphase flows, however, were beyond the scope of this thesis.

3.3 Parameters Influencing the Erosion of Ductile Materials

The influence of parameters on pure erosion in particle-laden conditions with no corrosive species present, are discussed in this section. Finnie [17], Bitter [19, 20] and Hutchings et al. [72-74] made significant contributions to the understanding of particle impingement on ductile materials in erosion

environments in the 1960s-1980s. Since the development of their theories for the mechanisms of material removal after particle impingement, a significant amount of research has been completed to understand the influence of a wide range of parameters on the erosion of ductile materials [18, 74-85]. Several models have also been developed to predict erosion material loss after the impingement of particles [17, 18, 20, 86, 87]. A summary of the parameters that influence erosion of ductile materials is shown in Figure 3.5. A review of the main theories and the most significant parameters influencing erosion are discussed in this chapter. Whilst these parameters have been separated into different groups, these parameters are often not independent of other parameters in their influence on erosion. Therefore studies and understanding of erosion can be complex [4].

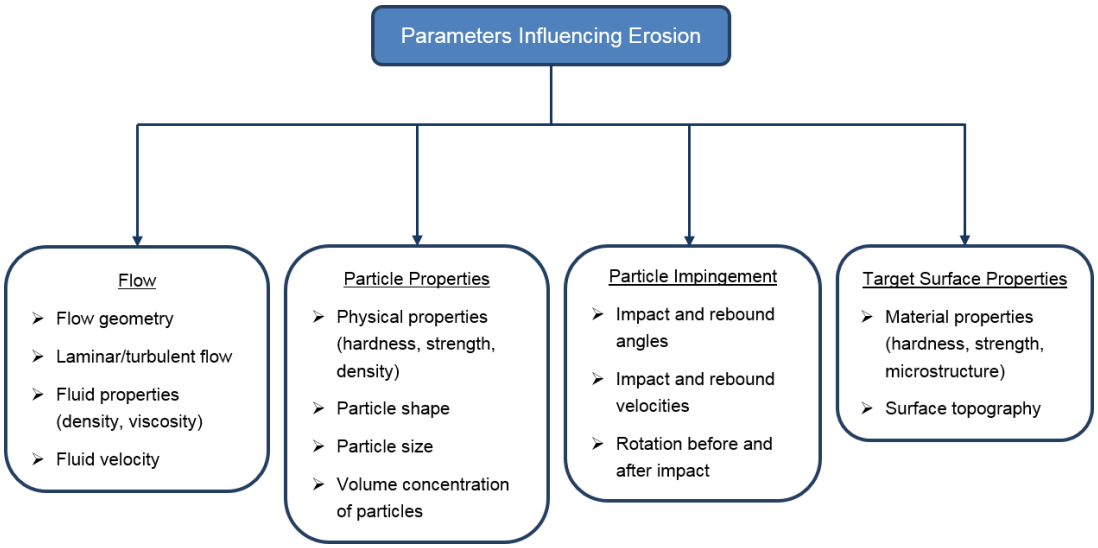

Figure 3.5 Parameters influencing the erosion of ductile materials adapted from [4]

3.3.1 Impingement of Particles on Metal Surfaces

For ductile materials, the mechanisms of material removal are highly dependent upon the impact angle of the particle as it is transported through the fluid medium and onto a material surface [17]. The three different types of material removal mechanisms are shown in Figure 3.6 [16]. At high impingement angles, indentation occurs as a result of plastic deformation [20]. The particle leaves a crater in the surface with small lips on both sides of the crater. Further particle impacts in this region can remove the material from the lips [74]. At shallower impingement angles, when the particle impacts on the surface and rolls forward, the particle cuts the surface, leaving a large lip of material that can also be removed from further particle impacts, known as ‘type I’ cutting [16]. When a particle impacts at shallow angles and rotates

backwards, known as ‘type II’ cutting, material is removed during the cutting process but no significant lip is produced [16].

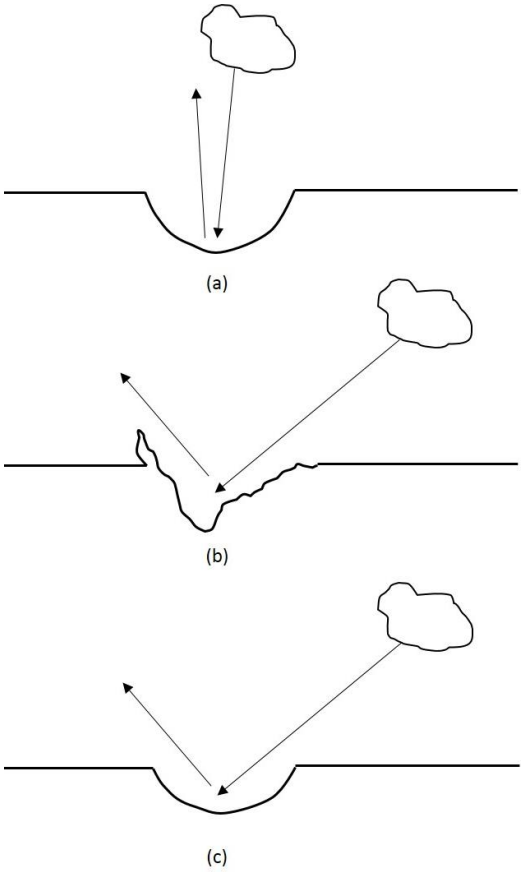

Figure 3.6 Three wear mechanisms after a particle impact on a ductile metal surface at different impingement angles showing (a) normal impingement, (b) type I cutting and (c) type II cutting, adapted from [16]

Bitter [20] appeared to be one of the first researchers that classified the material removal mechanisms in terms of cutting erosion at shallow impact angles and deformation erosion at high impact angles. In 1960, Finnie [17] originally classified material removal as a cutting mechanism, whereby a particle impacts and cuts into a surface, removing material, but this did not represent wear at high impact angles accurately and did not account for the effects of multiple particle impacts. It is now known that several different mechanisms occur after a single particle impact and that multiple particle impacts are also significant in erosion, which basic theories of material removal did not account for [74]. In 1972, Finnie [18] suggested several possible explanations that accounted for material removal at high impact angles, that the original theory did not account for. It was suggested that surface roughening caused particles to strike to surfaces at impact angles closer to 20-30° rather than the nominal impact angle of 90°. It was also suggested that particles rotated, which contributed to higher rates of wear and

that particles fractured upon impact, resulting in further particle impacts [18]. Material properties were also suggested to be influential, with multiple impacts causing material fracture as a result of low cycle fatigue and work-hardening of the surface eventually resulting in failure of the material in a manner similar to brittle materials [18]. However, limited experimental evidence was given to prove these theories.

Since existing theories were developed by Finnie [17] and Bitter [20], it was clear that erosion was highly dependent on the impingement angle of particles on the surface of a material. A significant amount of research has been completed to analyse the effects of particle impact angle on erosion and it has been shown that different rates of degradation were observed as the impact angle was varied [17, 20, 76, 78, 84, 88, 89]. The erosion degradation of ductile materials determined from air impact testing by Finnie [18] at different impact angles showed that maximum rates of erosion were observed at impact angles of approximately 15°-30°, as shown in Figure 3.7. The effect of impingement angle has been studied on several occasions and it is accepted that for ductile materials, the highest rates of degradation are measured at these impingement angles [16, 76, 84, 88].

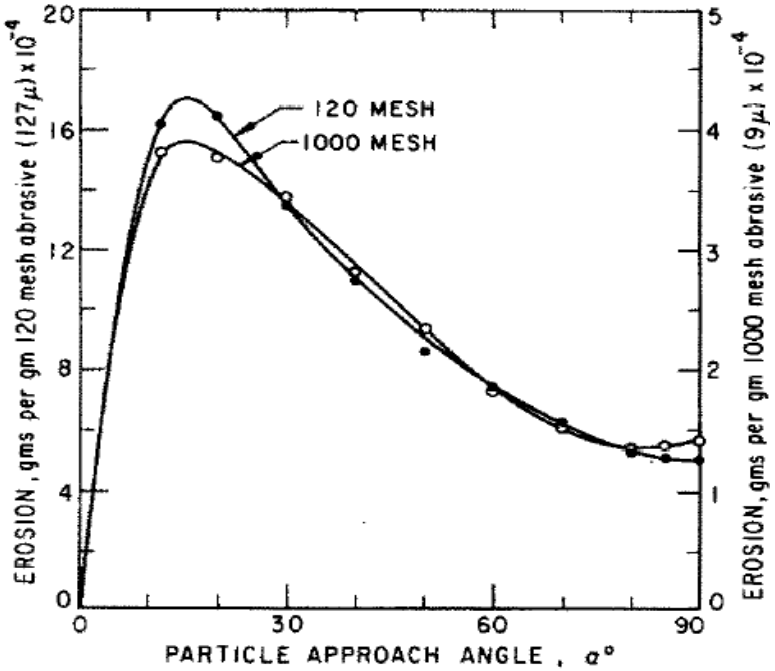

Figure 3.7 Effect of impingement angle on the degradation of aluminium in erosion tests completed using different sized silicon carbide (SiC) particles, where 120 mesh (larger particles) and 1000 mesh (particle sizes) is used to define the particle sizes by Finnie [18]

Hutchings et al. [72-74] developed the understanding of erosion further in the 1970's and 1980's by accounting for multiple particle impacts, with previous

erosion theories limited to single particle impacts. They completed erosion tests on ductile materials using steel balls at impact angles of 18.5° [74]. Lips were formed from displaced material on the edge of impact craters, as a result of shearing of surface layers in the direction of particle travel during impact. Multiple impacts were required to remove this lip, something originally neglected by Finnie [17]. Multiple further impacts were also shown to be required before material was removed in similar erosion tests [90]. Hutchings and Winter [91] also showed that impact craters increased in size when the impact angle was varied from 10° to 40°. In 1981, Hutchings and Winter [73] developed the understanding of both deformation by normal impact at high impact angles and cutting from low angles. At high impact angles, it was suggested that material was removed when the maximum plastic strain within a fragment of material exceeded a critical value after particle impacts. Therefore an incubation period is typically seen, where no erosion occurs after initial impacts before the plastic strain accumulates in excess of the critical value. Several cycles of impacts in neighbouring regions are required before material can be removed [16].

It has also been suggested that high rates of strain occurring during impact produce heat in the surface local to the impact region, causing softening near the surface [72, 91]. However, this was observed in tests completed at very high impact velocities in excess of 300 m/s with 9.5 mm diameter hardened steel balls. This effect was shown to be negligible for low velocity impacts with smaller sand particles [81]. Therefore it would be expected that in typical sand particle flows in oil and gas pipe flow, the focus of this thesis, that this would not be a significant effect.

The effect of impingement angle was shown to have a significant influence on erosion. One of the other parameters characterising the impingement of a particle on a surface is the impact velocity [17, 20, 92]. Impact velocity has regularly been studied in addition to impact angle and a basic relationship was determined that related both of these parameters to erosion, Equation (3.13) [4, 93].

$$E_0 = K_1 v_p^{n_p} f(\theta_p) \tag{3.13}$$

where E_0 represents the erosion degradation, K_1 is a constant specific to the material, v_p is the impact velocity, n_p is a material specific velocity exponent that was shown to be approximately in the range from 2.3 to 2.7 and $f(\theta_p)$ is a function of the impingement angle [4, 16-18]. Originally the degradation of material was thought to be proportional to velocity squared, relating erosion to the kinetic energy of the particle impact [18, 89]. However, it was shown

that a power of approximately 2.4 was more appropriate by Finnie [18]. The reason for the slightly higher value was explained by the rotation of the particle at shallower impact angles that caused additional volume removal [79].

3.3.2 Effect of Flow on Particles

Erosion research was originally focused on the mechanisms at, or close, to the surface after particle impingement, and how parameters, such as impact angle and impact velocity influenced material removal from surfaces. However, in most applications, the transport of the particles in a fluid is critical due to the influence of impact angle and impact velocity on erosion rates [4]. Finnie [17] acknowledged that fluid dynamics had a significant effect on erosion, but the effects were not investigated in detail. Flow has a significant effect on the transport of particles entrained in a fluid medium and hence the impact angles and impact velocities of the particles on surfaces [4]. When a particle is entrained in a fluid flow approaching a surface, the fluid surrounding the particle deviates from the particle trajectory in order to flow along the surface. The drag produced on the surface as a result of the flow deviation causes the particle trajectory to be altered, as represented by Figure 3.8 [4]. The components of particle motion normal and parallel to the surface are affected by this drag component, which causes the particle to follow a certain trajectory that does not necessarily follow the streamlines of the fluid [4].

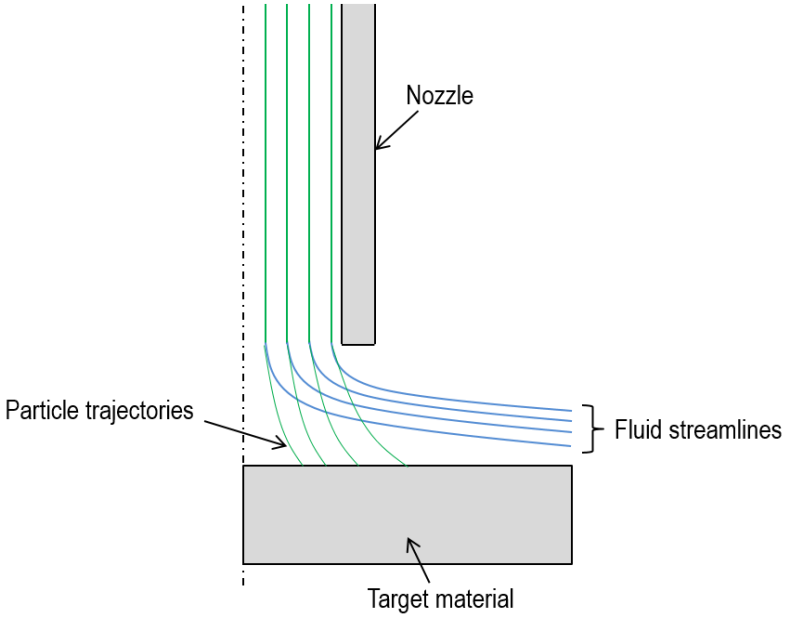

Figure 3.8 Transportation of particles in a fluid stream through a nozzle showing particle deviation from a fluid streamline as a surface is approached, adapted from [4]

Disturbances in the flow, such as changes in geometry, can cause high rates of erosion degradation of ductile materials, as particle trajectories deviate from the fluid streamlines, increasing the probability of impacts on a surface. The significance of geometry changes in erosion environments was first noted by Bitter [20]. In oil and gas pipelines, changes in geometries, such as elbows and plugged tees can cause high rates of erosion as sand particles entrained in the flow deviate from fluid streamlines and impact on the surfaces [87].

The fluid properties have a significant effect on the particle flow. The fluid viscosity is a very influential property of the fluid from a particle transport perspective. The likeliness of a particle to deviate from its fluid streamline, as demonstrated in Figure 3.8, is defined by the particle momentum equilibration number, λ, Equation (3.14) [94].

$$\lambda = \frac{\rho_p d_p^2 \overline{v_f}}{18\mu\bar{L}} \tag{3.14}$$

where $\overline{v_f}$ is the characteristic mean fluid velocity and $\bar{L}$ is the characteristic length scale that would be equivalent to the flow velocity and nozzle diameter, respectively, in SIJ flow [94]. Equation (3.14) is the ratio of particle response time due to viscous drag to a characteristic turbulent eddy time in the fluid medium [95]. The effect of this parameter on the trajectories of particle flow is shown in Figure 3.9, where smaller particles conform to fluid streamlines more closely, with less particle-wall interactions expected [4].

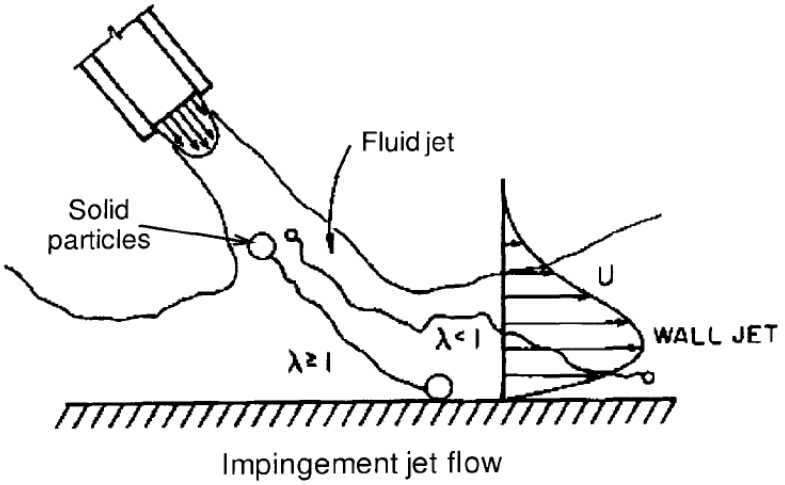

Figure 3.9 Effect of momentum equilibration number on the trajectories of particle in impinging jet flow adapted from [4]

The typical forces exerted on the body of a particle are shown in Figure 3.10 [96]. One of the most significant fluid forces acting on the particle is the drag force [10]. Fluid drag on a particle is a function of several parameters,

including the density of the fluid, the viscosity of the fluid, and the particle Reynolds number, a function of the fluid and particle velocity [4].

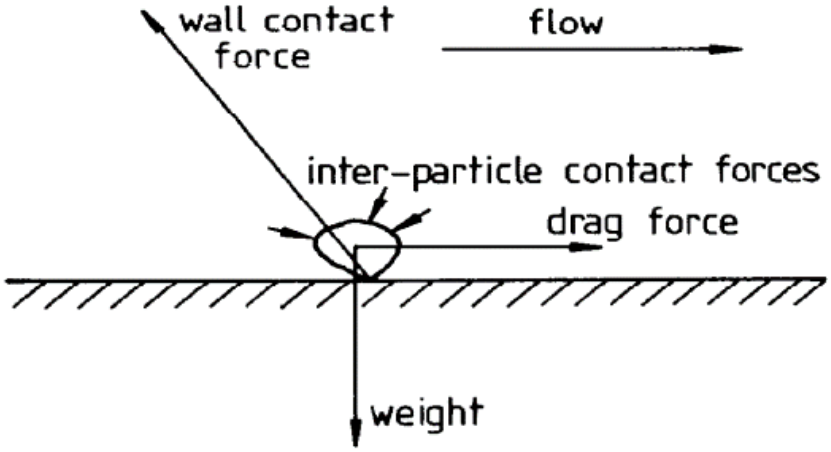

Figure 3.10 Forces acting on the particles at a surface as a result of flow through a fluid medium and impingement on a surface [96]

Several parameters can influence the drag force acting on a particle. One of the most important of these parameters is the viscosity of the fluid, which is directly related to the temperature of the fluid. Clark [75] completed erosion tests in a slurry pot tester using water/glycerine solutions with different viscosities, and showed that erosion rates were significantly reduced in higher viscosity fluids, shown in Figure 3.11.

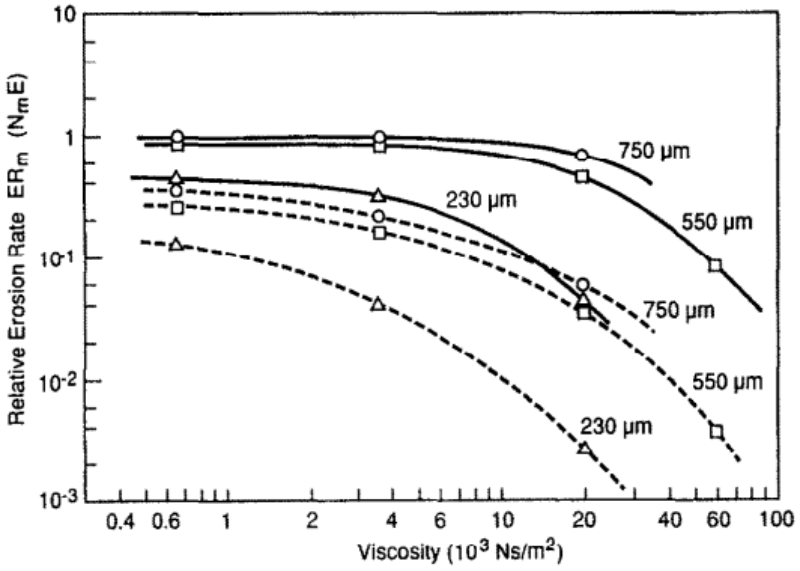

Figure 3.11 Effect of fluid viscosity on the erosion rates of copper specimens in slurry pot erosion tests completed at velocities of 18.7 m/s (solid lines) and 9.35 m/s (dashed lines) using different sized glass beads [75]

The effect of increasing viscosity was shown to be more significant on smaller particles. Particle size effects on erosion are discussed later. The reduction of

erosion rates at higher viscosities has been shown on several occasions [75, 77, 88]. Okita et al. [88] also showed that reduced erosion rates were measured as the viscosity of the fluid increased, and that viscosity had a more significant effect on smaller particles. Clark [75] used a parameter known as collision efficiency, $\eta_{collision}$, to define the number of impacts on the surface as a proportion of the number of expected impacts on the surface, Equation (3.15):

$$\eta_{collision} = \frac{N_i}{N_v} \tag{3.15}$$

where N_i is the impact frequency on the normal surface of the test specimen and N_v is the number of particles calculated to be in the volume swept by the test specimen surface [75]. A collision efficiency equal to one showed that all particles in the swept volume of slurry pot tests impacted on the sample surface. There are difficulties in precisely determining the collision efficiency, as N_i was determined by quantifying the number of impact craters on surfaces after tests and N_v was determined mathematically. However, the same methodology was used for all of the tests completed by Clark [75] and it was shown that collision efficiency decreased as viscosity increased, Figure 3.12.

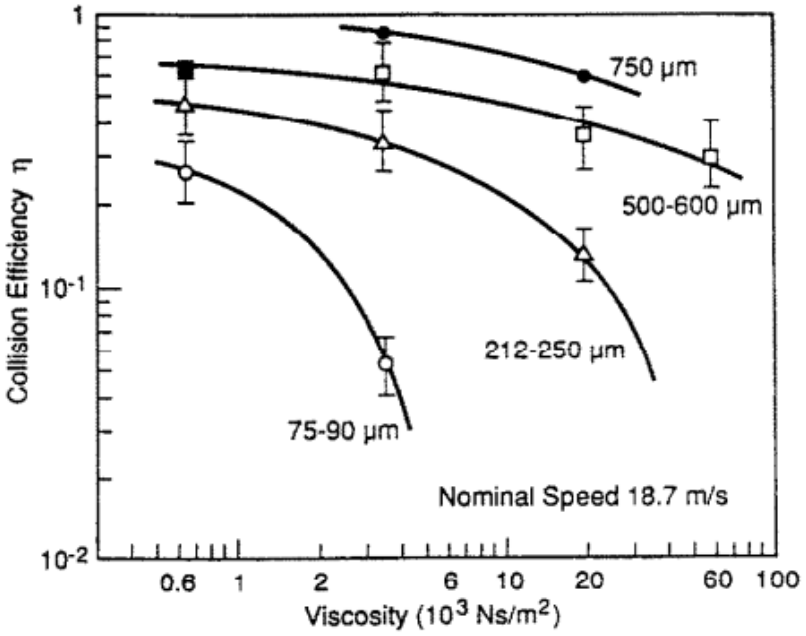

Figure 3.12 Effect of fluid viscosity on the collision efficiency of particle impacts on copper specimens in slurry pot erosion tests completed at a velocity of 18.7 m/s using different sized glass beads [75]

Similarly to erosion rate, the collision efficiency of larger particles was higher and less influenced by the increasing viscosity than smaller particles used in the tests. Therefore, increased fluid viscosity reduced erosion rates by reducing the velocity of impact and also reducing the number of impacts on

the surface. Clark and Burmeister [77] later suggested that the reduction in impact velocity and collision efficiency was due to the presence of a squeeze film between the particle and the surface, reducing the impact velocity and in some cases preventing impacts from occurring at the surface in slurry erosion flows. A squeeze film is produced when a solid body moves towards another solid body with appreciable relative perpendicular motion, and is typically present in the lubricant films of journal bearings [16]. Clark and Burmeister [77] suggested that the squeeze film reduced particle impacts on the surface as energy was required to displace the film by the particle as it approached the surface, thus reducing the impact energy.

However, several assumptions were made to reach this conclusion. A simple mathematical model of the trajectories of the particles in the slurry was developed by Wong and Clark [97] and used to predict the expected impact velocities on the surface of test specimens. The use of mathematical models to predict particle trajectories in fluid flow has limitations, which are discussed later in this chapter, as validation of models can prove to be difficult [4]. The predictions from the model developed by Wong and Clark [97] were then used to make a direct comparison between the experimentally measured impact velocities in the original erosion tests completed by Clark and Burmeister [77] and assumed to be accurate.

Further to this assumption, the method for determining the experimental impact velocities, whereby the size of impact craters were compared with a reference crater produced from indentation tests using one size of particle from the range reported, could also be inaccurate [77]. A range of particle sizes were used in the experiments, with it reasonable to assume that indentation size would change depending on the size of the particle, as was shown by Oka et al. [98]. The measured indent size after erosion testing was then related to the reference indentation to determine the particle velocity. Whilst the presence of a squeeze film at the surface may influence the impacts of sand particles, particularly at the high fluid viscosities in the water/glycerine and water/oil solutions used during tests completed by Clark and Burmeister [77], quantifying its effect is limited by the assumptions made and lack of thorough experimental data to validate results. Clark [99] later acknowledged that these assumptions could significantly limit the theory that the squeeze film influenced erosion and explained how there was a lack of understanding of the fluid flow in slurry pot tests.

Clearly the fluid directly affects the velocity of impact and the number of impacts on the surface of a target material. Higher velocity flows transport the

particles at higher velocities, therefore particles impact on the surface at higher velocities. At Reynolds numbers above 4000 in straight pipes, fluid flow is considered to be turbulent [100]. Turbulence can have a significant influence on the particle trajectories. Finnie [17] originally suggested that erosion could be increased by fluid flow over a rough surface due to increased local turbulence. However, experimental analysis of this was not provided. Dosanjh and Humphrey [94] completed numerical analysis of the influence of turbulence intensity on particle motion in an impinging jet geometry and suggested that turbulence had a significant influence on erosion rates when small particles, with a diameter of 5 μm, were transported in the flow.

Multiple phases in the fluid flow also influence particle trajectories. The majority of erosion research shown up this point were completed in particle-laden single phase fluid flows, usually either water or air. Erosion analysis has been completed in multiphase flows previously on several occasions, but in general has received less attention than single phase fluid flow [82, 101, 102].

3.3.3 Particle Properties

Several particle-related properties, including the particle size and the material properties of the particle, can influence the erosion of ductile materials [16]. The effect of particle size on erosion has been investigated on several occasions [18, 83, 103]. Typically the rate of wear is proportional to the mass of particles impacting on the surface [16]. The particle size can have two effects on erosion, as both the transport of the particle through the fluid medium and the subsequent impact of the particle on the surface are effected by particle size. Smaller particles are more difficult to separate from flow fields and are more likely to follow the fluid streamlines when they approach a surface [18, 83]. Lynn et al. [83] completed erosion tests in slurry pot testers with varying particle sizes in diesel oil solutions at a nominal flow velocity of 18.7 m/s. The measurement of erosion rates from increasing particle size are shown in Figure 3.13. An increase in erosion rate was observed as a result of the increasing particle size, explained by the relationship between the kinetic energy of the particle impact and the resulting rate of degradation. Lynn et al. [83] also showed that the particle velocity at impact increased as the size of the particle increased, Figure 3.14. The impact velocity of small particles was very strongly influenced by the flow. It was suggested that the deceleration of small particles as they approach the surface was due to the effects of the squeeze film. The increasing particle size became less significant on erosion and impact velocity for large particles.

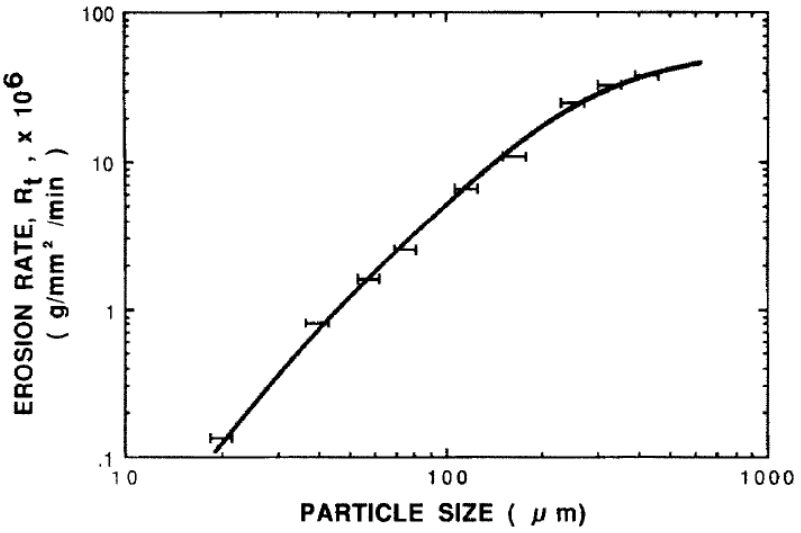

Figure 3.13 Effect of particle size on the erosion rates of carbon steel in slurry pot erosion tests containing 1.2 wt% of SiC particles in a diesel oil solution at a nominal velocity of 18.7 m/s [83]

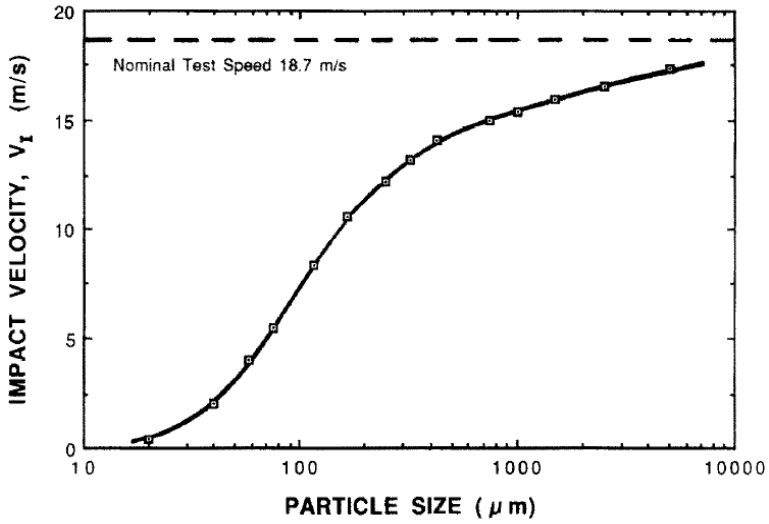

Figure 3.14 Effect of particle size on the impact velocity of carbon steel in slurry pot erosion tests containing 1.2 wt% of SiC particles in a diesel oil solution at a nominal velocity of 18.7 m/s [83]

It has been suggested on several occasions that the fracturing of particles after impact resulted in secondary impacts on a surface [4, 18]. Hu [104] showed that particle sizes did not change significantly after erosion impacts in SIJ erosion tests in water-sand flows after 240 minutes of testing [105]. Therefore, in some conditions particle fracture may be an issue, but did not appear to be a frequent occurrence in SIJ erosion test conditions. Hutchings [73] reported that in high velocity air erosion tests, less than 1% of the glass beads used as impacting particles fractured, and that the steel balls used did not fracture in the same conditions. The hardness of the particle has been reported to be important as fewer fractures were reported for harder particles [106].

Particle shape is also important in the erosion of materials [16]. Erosion theory typically assumed that the mechanisms of removal occur as a result of the impact from perfectly spherical particles. However, particle shape can have a significant influence. More rounded particles lead to less localised deformation and more impacts are required to remove material [16]. Generally, particles of a more angular shape cause greater rates of erosion wear than spherical particles, as angular particles produce more lips of material that can be removed in subsequent particle impacts [17, 96, 106, 107]. It has also been suggested that different shaped particles could be transported through the fluid medium in a different manner to spherical particles [96].

3.3.4 Target Surface Properties

It has been well established that ductile materials behave in a significantly different way to brittle materials in erosion conditions [17, 18, 20, 76]. However, other properties including the hardness, ductility, roughness and microstructure of the material being subject to erosion have been acknowledged to be of significant importance [18, 76, 84]. It has often been claimed that one of the most important surface properties from an erosion perspective is the hardness of the target material, with an increase in hardness of a surface offering greater erosion resistance [16, 18]. Finnie [18] and Oka et al. [85] showed that increased hardness of materials in some cases reduced the erosion rate of materials. The effect of increasing hardness is shown in Figure 3.15 for different ductile materials [16]. Generally an increase in hardness showed greater erosion resistance for some metals, however, this was not always the case.

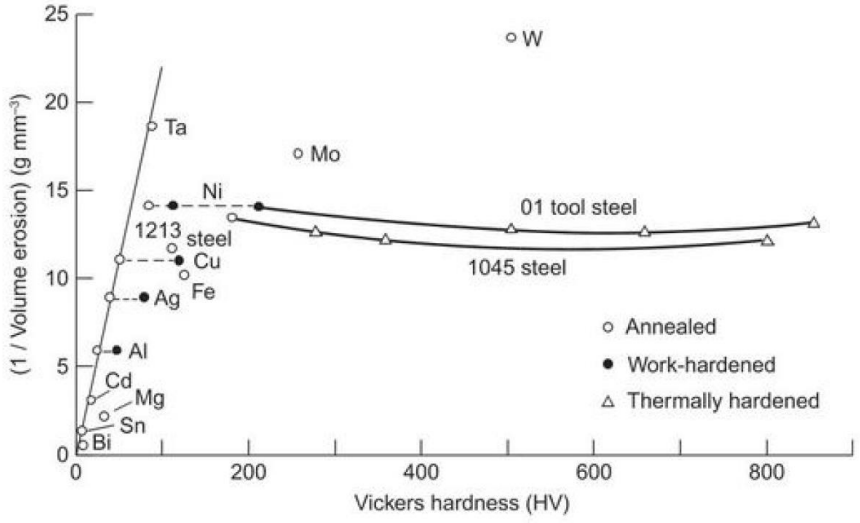

Figure 3.15 Effect of Vickers hardness on the erosion resistance of different metals [16]

Levy [76] completed high velocity air erosion testing of ductile carbon steels with different microstructural properties at three different impact angles, to evaluate how significant the microstructure was on erosion performance. Test specimens consisting of fine pearlite, coarse pearlite and spheroidised microstructures with Vickers hardness values of 250 H_V, 191 H_V and 162 H_V respectively were used. Whilst it is typically claimed that increasing material hardness increases erosion resistance of a ductile material, Levy [76] showed that hardness did not necessarily result in higher erosion resistance, Figure 3.16.

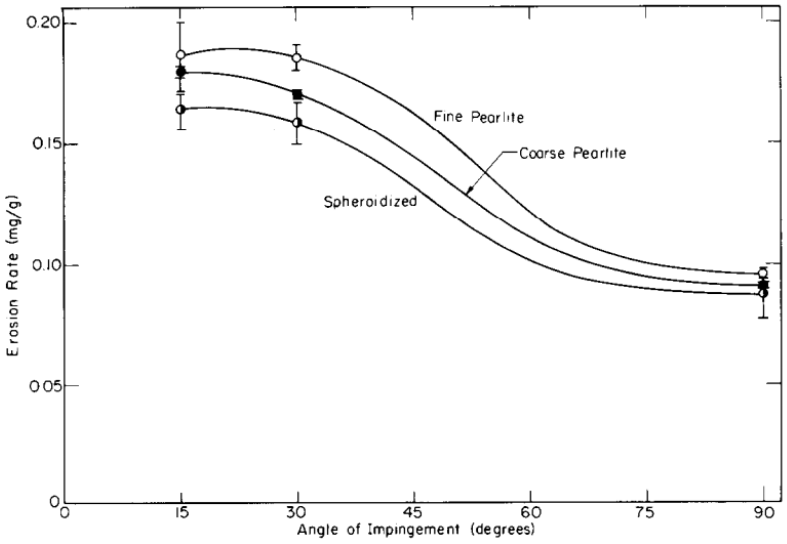

Figure 3.16 Effect of carbon steel microstructure on erosion rates in dry erosion testing completed at a flow velocity of 61 m/s using 240 µm diameter SiC particles [76]

The reasons for the higher rates of wear observed on the pearlitic steel was explained by fracturing of the iron carbide (Fe_3C) plates after particle impacts, whereas the steels containing higher proportions of the ductile ferrite phase degraded at a lower rate. McCabe et al. [84] also showed that the presence of Fe_3C resulted in increased rates of erosion in similar erosion tests. It was acknowledged that the materials would work-harden in the tests completed by McCabe et al. [84] and Levy [76] but the effects on the microstructure were not considered. Rajahram et al. [108] showed in stainless steel erosion tests that grain size was significantly reduced near to the surface as a result of repeated particle impacts.

Less research has been completed to investigate the effects of surface roughness on particle impacts. Roughness can influence erosion in two ways, by changing local flow conditions near the surface and by changing the angle of impact of the particle on the surface [80]. Finnie [80] investigated the effects of surface roughness mathematically by determining the typical profile of an

eroded ductile material surface measured using profilometry techniques, and stated that the change in surface roughness resulted in a different angle of impact angle than the nominal angle of impact reported. An example of a surface profile is shown in Figure 3.17, with the true impact angle equal to the sum of the nominal impact angle, θ_p, and the change in angle caused by the surface profile, θ_S. Particle impacts can also cause surface roughening and Bitter [20] stated that particle impact angles between 40° and 60° produced the most surface roughening after impact.

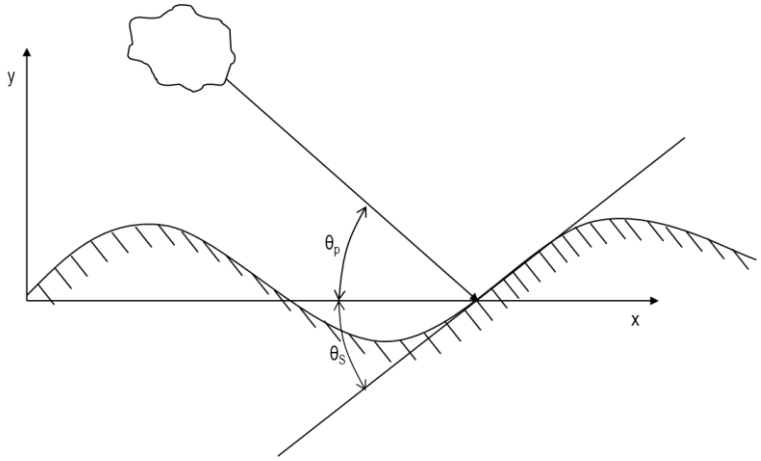

Figure 3.17 Theoretical effect of surface topography on the impact angle of a particle on a rough surface adapted from [80], where $\boldsymbol{\theta_p}$ is the impact angle and $\boldsymbol{\theta_S}$ is the additional angle as a result of surface texture

3.4 Modelling Erosion of Ductile Materials

Prediction of erosion rates has been of interest in the field of erosion since first theories were suggested by Finnie and Bitter in the 1960's [17, 20]. Finnie [17] developed equations that could be used to predict the volume of material removed by the impact of a solid particle on a target surface. Finnie's model and theory was shown to be inaccurate as it did not account for the fact that multiple impacts are required to remove material and the mechanisms of wear at high impact angles were not considered, as has already been explained [10, 16]. Bitter [20] developed a model that accounted for the different mechanisms of wear as a function of impact angle but material parameters were not accounted for. Since the development of these two models, several different models have been developed to predict erosion [10, 18, 86, 109].

To accurately predict erosion, models usually rely on knowledge of the impact angle and impact velocity and these two parameters are regularly included in erosion models [4, 10]. One of the first erosion models that was used to

provide guidance to industry was the API-RP-14E, which specified a limiting velocity above which erosion damage would occur in pipe flow, defined by Equation (3.16) [32].

$$v_e = \frac{C}{\sqrt{\rho_f}} \tag{3.16}$$

where v_e is the erosional velocity, C is an operational constant defined as 100 for continuous service and 125 for intermittent service and ρ_f is the fluid density [109]. However, this model was very basic and did not account for a wide range of parameters known to influence the erosion of materials, including the particle impact angle. Researchers at the Erosion/Corrosion Research Centre (E/CRC) at the University of Tulsa have developed models since the API-RP-14E model that can be used with more accuracy and relevance from an oil and gas industry perspective [87, 109].

In recent years, CFD has become a more powerful tool in the prediction of erosion, as it provides an effective method of determining the impact angles and impact velocities at surfaces in different flow geometries, two essential parameters for the calculation of erosion rates [2, 10, 110]. An overview of some of the main erosion models and the methodology for using CFD to predict erosion is provided in this section.

3.4.1 Finnie Erosion Model

One of the first models developed to predict erosion rates of ductile materials was the Finnie [17] model. A very basic definition of material removal from a surface after particle impact was used for the development of the model, where a particle impacts on a surface at a low impact angle, cuts into the surface and removes material, as demonstrated in Figure 3.18. The particle impacts on the surface and cuts through a distance of x_{cut}, and removes a maximum thickness of material, y_{cut}.

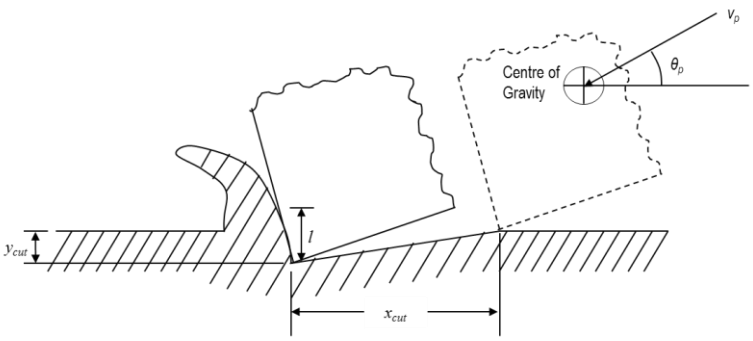

Figure 3.18 Model of an abrasive grain impacting on a surface and removing material developed by Finnie [17]

The volume of material removed, Q, by a single abrasive grain of mass, m_p, and velocity, v_p, was defined by Equations (3.17) and (3.18) for different impact angles, θ_p.

$$Q = \frac{m_p v_p^2}{p\psi K}\left(\sin 2\theta_p - \frac{6}{K}\sin^2\theta_p\right) \text{ if } \tan\theta_p \leq \frac{K}{6} \quad (3.17)$$

$$Q = \frac{m_p v_p^2}{p\psi K}\left(\frac{K\cos^2\theta_p}{6}\right) \text{ if } \tan\theta_p \geq \frac{K}{6} \quad (3.18)$$

where p is the plastic flow stress reached immediately upon impact, K is the ratio of vertical to horizontal force components acting on the particle, usually assumed to be equal to 2, and ψ is the ratio of l, the depth of contact, to y_{cut} in Figure 3.18. This model was used to predict the volume removal of ductile materials as a function of different impact angles, and showed relatively good agreement with experimental data from erosion tests using copper, steel and aluminium, at low angles of impact. At higher angles of impact closer to 90°, the model significantly under predicted the volume removal [17].

To account for multiple particle impacts, Finnie [17] suggested the use of empirical corrections from erosion tests that determined volume removal as the mass of particles was changed. However, this assumed that all mechanisms of material removal remained the same after multiple impacts. Equations (3.17) and (3.18) were extended to include the total mass of particles. K and ψ were both assumed to equal 2, based on limited experimental observations. Further to this, a correction factor was also applied to account for the fact that not all particles cut the material in an idealised manner. This correction factor was assumed to be 0.5, effectively assuming 50% of the particles removed material [17]. The modified equations are shown in Equations (3.19) and (3.20).

$$Q = \frac{Mv^2}{8p}\left(\sin 2\theta - 3\sin^2\theta_p\right) \text{ if } \theta_p \leq 18.5° \quad (3.19)$$

$$Q = \frac{Mv^2}{24p}\cos^2\theta_p \text{ if } \theta_p \geq 18.5° \quad (3.20)$$

The measurement of several of these parameters was challenging, and there appeared to be very limited experimental evidence provided to justify the choice of the values assumed for K, ψ and the correction factor applied for ideal cutting. Finnie [17] further stated that plastic flow stress would also increase during the erosion process. The main limitation of the model was the assumption that all particle impacts resulted in the same mechanism of material removal, which has been shown not to be the case as material removal mechanisms are dependent on impact angle, with high impact angles causing indentations in the sample [16]. Material properties were also

relatively ignored in the model, as the effect of material hardness, work-hardening of the material and surface topography were not considered and have been shown to effect the erosion performance of materials [4, 79]. Finnie [18] updated the model in 1972, to Equation (3.21):

$$Q = \frac{c_p M v_p^2}{4p\left(1 + \frac{m_p {r_p}^2}{I_p}\right)}\left[\cos^2\theta_p - \left(\frac{\dot{x}}{v_p}\right)^2\right] \tag{3.21}$$

where c_p is the fraction of particles cutting in idealised manner, r_p is the radius of the particle, I_p is the moment of inertia of the particle, typically assumed to equal $\frac{m_p {r_p}^2}{3}$, and $\dot{x}$ is the horizontal particle velocity of the tip of the particle when cutting ceases. Another limitation of the original model was the idealised cutting factor of 0.5 that was applied. A more realistic value of 0.1 was suggested by Finnie [18] based on the development of a model for abrasion of material [111]. These modifications improved the prediction at angles closer to 90°. Despite the limitations of the Finnie model, it has been regularly used in recent studies of erosion [66, 112].

3.4.2 Erosion/Corrosion Research Centre Erosion Models

A significant amount of research into the prediction of erosion in oil and gas pipeline geometries has been completed at the E/CRC and several different erosion models have been developed to predict erosion rates [87, 109, 113-115]. From analysis of the typical parameters that influence erosion, it was suggested that the erosion rate was a function of the target material properties, the impact velocity and the impact angle of the sand particles on a surface [93]. This basic relationship, Equation (3.22), was used to develop a model at the E/CRC to predict erosion of materials and has regularly been used in CFD predictions of erosion [2, 110, 116, 117].

$$ER = A_1 F_s {v_p}^{n_p} f(\theta_p) \tag{3.22}$$

where ER is the erosion ratio, A_1 is a dimensionless material specific empirical constant dependent on the Brinell hardness (BH) of the material, F_s is a dimensionless particle shape coefficient, v_p is the particle impact velocity, n_p is the velocity exponent and $f(\theta_p)$is a function of the impact angle defined by:

$$f(\theta) = a_1\theta_p^2 + a_2\theta_p \quad \text{if } \theta_p \le \theta_0 \tag{3.23}$$

$$f(\theta) = a_3\cos^2\theta_p \sin(a_4\theta_p) + a_5\sin^2\theta_p + a_6 \quad \text{if } \theta_p > \theta_0 \tag{3.24}$$

where a_1 to a_6 are all empirically determined dimensionless constants. Ahlert [114] completed erosion dry impingement tests at various impingement angles and impingement velocities using a range of materials to determine the value of empirical constants used in Equations (3.22), (3.23) and (3.24). The full list of constants used for the prediction of carbon steel are shown in Table 3.1 [110]. Oka et al. [86, 118] developed a similar model to the E/CRC model which included particle property terms and target surface properties with plastic deformation and cutting terms to account for different wear mechanisms at different impact angles that showed good agreement in erosion tests on carbon steel.

Table 3.1 Constants used in the E/CRC erosion model for carbon steel determined from dry impact testing at different impingement angles and impingement velocities [110]

Constant	Value
A_1	$1559(BH)^{-0.59} \times 10^{-9}$
F_s	1 (sharp particles), 0.53 (semi-rounded), 0.2 (spherical)
n_p	1.73
a_1	38.4
a_2	22.7
θ_0	15°
a_3	1
a_4	3.147
a_5	0.3609
a_6	2.532

Shirazi et al. [87] developed a basic model at the E/CRC to predict erosion in pipe tee and elbow geometries using an input of particle impact velocity as a function of the fluid flow, Equation (3.25). This model appears to be one of the first models that considered fluid flow effects on the actual impact velocities at a surface without the need for complex particle tracking models before an erosion rate could be determined. The model showed good agreement with experimental data but it could only be used for high impact angle, direct impingement erosion.

$$ER = 1.73 \times 10^{-6} v_L^{1.623} F_s W \tag{3.25}$$

where v_L is the characteristic impact velocity determined by geometry specific equations and W is the sand concentration. A further improvement to this model was developed at the E/CRC by McLaury et al. [109, 115] to predict the maximum erosion rates in an elbow flow relevant to oil and gas pipelines, Equation (3.26). This model was adapted to also include the effects of multiphase flow but could be used for single phase flows.

$$h = F_M F_S F_P F_{R_c/D_p} \frac{W v_L^2}{\left(D_p/D_{p0}\right)^2} \tag{3.26}$$

where h is the erosion penetration rate, F_M is an empirical constant that accounts for material hardness, F_S is an empirical sand sharpness factor, F_P is a penetration factor for steel based on a 1 inch pipe diameter, F_{R_c/D_p} is a penetration factor for the elbow radius, W is the sand production rate, v_L is the characteristic impact velocity determined using the same method as the Shirazi et al. [87] model shown above, D_p is the pipe diameter and D_{p0} is a reference 1 inch pipe diameter. Other models have also been developed at the E/CRC to predict erosion in multiphase flows [33, 119].

3.4.3 CFD Predictions of Particle Trajectories

It has been shown that erosion of materials is highly dependent on the impact velocity and impact angle of the particles impacting on the surface, with all of the erosion models reviewed requiring an input of these parameters to determine erosion rates. However, accurate measurements of impact velocity and impact angle are difficult, limiting the effectiveness of the use of erosion models [4]. Numerical predictions of particle trajectories and impacts can be highly uncertain due to the number of assumptions required to complete predictions, but CFD has been frequently used as a method to predict the trajectories of particles in fluid flow [2, 4, 88, 110, 116, 120-124]. CFD has shown to be effective for predictions of particle trajectories, but validation of models is challenging [4]. The majority of CFD models of particle trajectories have been used to predict erosion rates in different geometries and compared with experimentally measured erosion rates to validate results, rather than experimentally determining impact angles and impact velocities [2, 88, 120-123]. Due to the difficulty in measuring these parameters, erosion rates are the most convenient method of validation [4]. However, Vieira et al. [123] showed that different erosion models predict significantly different erosion rates, with some being more accurate than others.

There are three stages in the development of particle trajectory models using CFD [2, 110, 122]. The first stage is to develop a flow model that predicts the fluid flow through a geometry. Fluid flow models are developed using the theory explained in Chapter 2 and are reliable and well validated for a range of common flow geometries [13]. Once this stage has been completed, particle trajectories are predicted through the geometry. Prediction of particle motion is more complex and requires significant computational demand and resources [109]. The final stage is to predict erosion rates on a surface of interest after the impact angles and impact velocities have been predicted.

Two methods are used to numerically define the motion of particles, Lagrangian and Eulerian. Lagrangian motion implies a discrete particle phase, whereas Eulerian motion treats the particle as a continuum, where properties are averaged over the volume of the particle [4]. Lagrangian motion was favoured in the models developed by Chen et al. [2], Gnanavelu et al. [120] and Mansouri et al. [122], and is typically preferred for erosion modelling, as individual particle velocities and angles can be determined at the target surface, enabling erosion rates to be determined [4]. The Lagrangian approach predicts particle trajectories from a force balance equation [125]. In high particle concentrations, the Lagrangian approach is less effective due to a lack of understanding of the interactions between particles in the flow, with the Eulerian approach being favoured for high particle concentrations [4]. Gnanavelu [105] showed that the mass loading of sand particles relative to the mass of water used in SIJ erosion tests was much lower than the threshold concentration suggested by Humphrey [4] where particle-particle interactions needed to be considered.

The Lagrangian equation of motion for particle flow through a fluid, based on Newton's second law, is shown in Equation (3.27) [125].

$$m_p \frac{dv_p}{dt} = \sum F_{particle} \tag{3.27}$$

where m_p is the mass of the particle, v_p is the particle velocity and t is the time. A range of forces, $F_{particle}$, can act on the particle depending on the conditions present, summarised in Table 3.2.

One of the most influential forces on the particle is the drag force, which is a function of the drag coefficient [10]. In relatively viscous fluids such as water, drag forces are highly significant on particle motion, whilst being less significant in gas flows [110]. The drag force, buoyancy, pressure gradient and added mass are regularly included in the equations of motion for a sand particle in fluid flow [2, 110, 116, 120]. The Saffman force is significant for very

fine particles in flow, much smaller than typical sand particles sizes in oil and gas erosion conditions, therefore it is usually neglected [126, 127]. The Magnus force is usually neglected as it often assumed that particles are not rotating [128, 129]. It has been reported that Magnus force is more influential on the trajectories of very small particles after rebounding on a surface [4]. The Basset history term is usually neglected at high Reynolds numbers and has been shown to be insignificant in comparison to the drag force [125, 130]. Basset force was neglected by Berlemont et al. [131] in predictions of particle trajectories in turbulent jet flow that showed good agreement with experimental results.

Table 3.2 Typical forces acting on a particle in fluid flow [4, 10, 132, 133]

Force	Description
Drag	Fluid force acting on a particle due to viscous effects. Calculated from drag coefficient
Buoyancy	Force acting on particle opposing the weight of the particle if particle density is less than fluid density
Pressure gradient	Force caused by local pressure gradients in the fluid
Added mass	Force required to displace a volume of fluid around an accelerating or decelerating particle
Saffman force	Force resulting from fluid shear, significant closer to a solid surface than in the bulk fluid
Basset force	Viscous drag due to unsteady relative acceleration. Usually neglected in high Reynolds number flow
Magnus force	Force caused by particle rotation

A range of different flow geometries and conditions have been the subject of CFD particle trajectory predictions reported in the literature. The majority of research has been completed in oil and gas relevant conditions at the E/CRC [2, 88, 110, 121-123]. Chen et al. [2, 110] predicted the flow of sand particles in gas flow through an elbow and plugged tee. Vieira et al. [123] also completed erosion predictions using CFD in elbow gas flow. Mansouri et al. [122] and Gnanavelu et al. [105, 120] predicted the trajectories of sand particles in fluid flow through SIJ nozzles and predicted surface profiles after erosion tests and compared results with experimentally measured surface profiles. An example of using CFD to predict particle flow through an elbow completed by Chen et al. [110] is shown in Figure 3.19. The results showed

how the majority of erosion was predicted on the outer radius of an elbow towards the exit of the elbow. It also showed that not all particles impacted on the elbow wall.

Mansouri et al. [121] investigated the significance of turbulence models on the prediction of erosion, as they reported that some CFD models had over predicted erosion rate. They showed that using turbulence models with wall functions, which are less accurate at predicting flow close to the wall, gave sufficient accuracy for larger sand particles of 256 μm diameter. Smaller particles, approximately a tenth of this diameter, required fully resolved turbulence models in order to predict erosion rates, as wall function models over predicted the erosion rates, due to the lack of accuracy of the fluid flow model near to the wall.

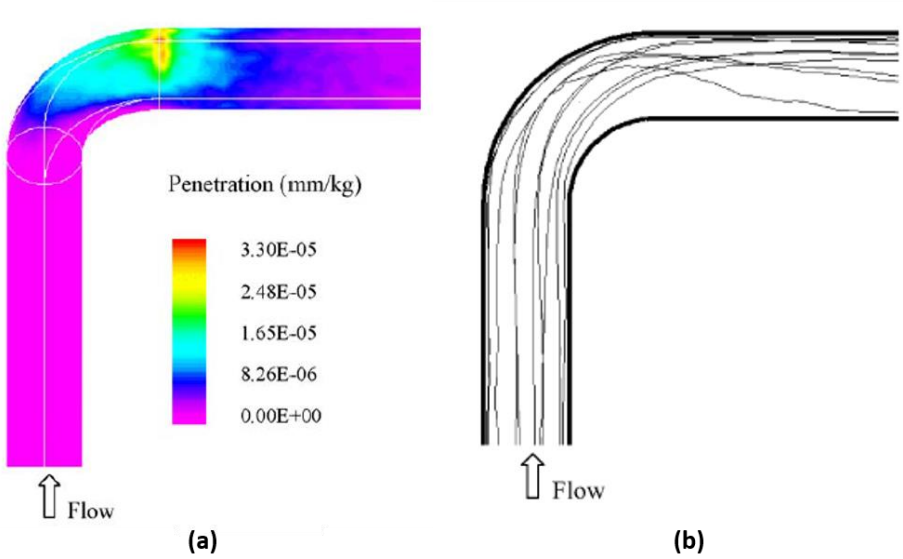

Figure 3.19 CFD prediction of (a) erosion rates in an elbow caused by the impact of 150 μm diameter sand particles in 3 m/s water flow and (b) trajectories of the sand particles [110]

All of the above models were validated using predictions of erosion rate compared with experimentally determined erosion rates. One of the limitations of this, however, is that a range of particle sizes would typically be present in the particles used experimentally, whereas CFD models normally use only one input of the mean particle diameter. Gnanavelu et al. [105, 120] reported a range of particle sizes in their erosion tests, whilst nominal sand sizes have been reported in E/CRC without the full size distribution given [2, 110, 121-123]. Therefore there are some limitations in using this method to validate CFD predictions. As was reported earlier in this chapter, Lynn et al. [83] showed that erosion rates were dependent on particle size. However, CFD

predictions of erosion rate were similar to measured erosion rates in the models reported.

Another source of uncertainty in models is accounting for the effects of turbulence and modelling the rebounds of particles at the walls. Turbulence can significantly influence particle flow [4]. Turbulent dispersion is usually applied in CFD models through the use of a particle-eddy interaction model to calculate the fluctuation in particle velocity as it travels through turbulent eddies in the flow [2, 10, 88, 110, 124, 134]. Validation of the effects of this is difficult, for the same reasons as validation of all particle CFD models. It has regularly been reported that turbulence has less influence on larger particles and is only significant for very small particles [10, 105, 135].

Particle impact and rebound is another area of importance in the development of CFD models. It has been suggested that particle impacts should be modelled at the radius of the particle, rather than as a point with no size assumed in particle trajectory predictions [120, 135]. However, this was shown not be significant for large particles [135]. Modelling the rebound of particles after they impact on a surface is also complicated. Particles lose energy as they impact on a target surface so coefficients of restitution are used to account for the loss of energy at impact and to determine the velocity at which the particle rebounds [10]. Coefficients of restitution were applied in the CFD models developed by Chen et al. [2, 110] and Edwards et al. [116] who compared the coefficients of restitution equations derived by Grant and Tabakoff [136] and Forder et al. [137]. Grant and Tabakoff [136] used high speed imaging techniques in erosion tests using 200 μm diameter particles impacting on aluminium surfaces in dry conditions at velocities ranging from 76 m/s to 120 m/s and impact angles ranging from 20° to 90°, relevant to turbomachinery applications, to measure the velocity of particles before and after impact. Statistical equations for the calculation of coefficient of restitution were then derived using these results. Forder et al. [137] also developed statistical equations of coefficients of restitution for impacts on carbon steel, but the method used to determine the equations was not reported. However, both of these sets of equations were determined in conditions that were not directly relevant to the flow of sand particles in water flow in oil and gas conditions, and coefficients of restitution can be difficult to determine due to the techniques required to accurately measure particle velocities [4]. Okita et al. [88] reported that coefficients of restitution in liquid flows were not as influential on erosion rates as in gas flows.

3.5 Erosion-Corrosion of Carbon Steel

The influence of different parameters on the mechanisms of erosion and corrosion have been reviewed separately. In a corrosive environment containing erosive particles, erosion-corrosion occurs. Erosion-corrosion conditions can cause enhanced rates of degradation, whereby erosion enhances the corrosion rate and corrosion enhances the erosion rate [15]. This can lead to very high rates of degradation in oil and gas pipelines in CO_2-saturated environments when sand is produced [34]. The parameters influencing erosion-corrosion and the interactions between erosion and corrosion are discussed in this section.

3.5.1 Contributing Parameters to Erosion-Corrosion

As has already been defined in Equation (2.1), total erosion-corrosion degradation consists of an erosion component, a corrosion component and interactions between erosion and corrosion. A significant number of parameters can influence erosion-corrosion making it a complex degradation process and there currently exists a lack of thorough understanding regarding the mechanisms of erosion-corrosion [8]. Burson-Thomas and Wood [8] highlighted how a lack of understanding exists of erosion-corrosion that can generally be applied to the mechanisms of erosion-corrosion across different materials, with the majority of erosion-corrosion conclusions being specific to the application of interest.

Erosion-corrosion affects many industries and has been investigated in a range of conditions using various materials [8]. Rajahram et al. [108, 138-140] and Wood et al. [89, 141, 142] have investigated the erosion-corrosion performance of corrosion resistant alloys. Erosion-corrosion research has been completed to assess the performance of both carbon steel and corrosion resistant alloys in CO_2 oil and gas, sand-containing flow conditions [6, 34, 35, 58, 60, 61, 143-146]. The E/CRC have investigated erosion-corrosion resistance of $FeCO_3$ but the majority of their research has been focused on modelling erosion in pipe flow using CFD [87, 121, 122, 147, 148].

Interactions between erosion and corrosion have been observed on several occasions. It was suggested in a review of erosion-corrosion completed by Wood and Hutton [15] that there were several causes of corrosion-enhanced erosion and erosion-enhanced corrosion. A summary of the main relevant suggested interactions between erosion and corrosion is shown in Table 3.3.

The mechanisms of the interactions are discussed further in the next two sections.

Table 3.3 Potential causes of erosion-enhanced corrosion and corrosion-enhanced erosion suggested by Wood and Hutton [15]

Erosion-enhanced corrosion	Corrosion-enhanced erosion
Local acidification in erosion pits, accelerating rates of corrosion	Dissolution of work-hardened layers, exposing softer material
Increased transportation of corrosive species as a result of surface roughening from particle impacts	Preferential corrosive attack at grain boundaries, resulting in grain loosening
Removal of protective films from surfaces after particle impingement	

Hu and Neville [34] investigated how different parameters influenced the total erosion-corrosion degradation of X65 carbon steel in sand-laden flow in the CO_2 conditions. Increasing sand concentration and flow velocity increased total rate of erosion-corrosion degradation, as shown in Figure 3.20. When no sand was present in the flow, the degradation increased in a linear manner with flow velocity. As sand was added to the solution, degradation increased proportionally to approximately the square of flow velocity.

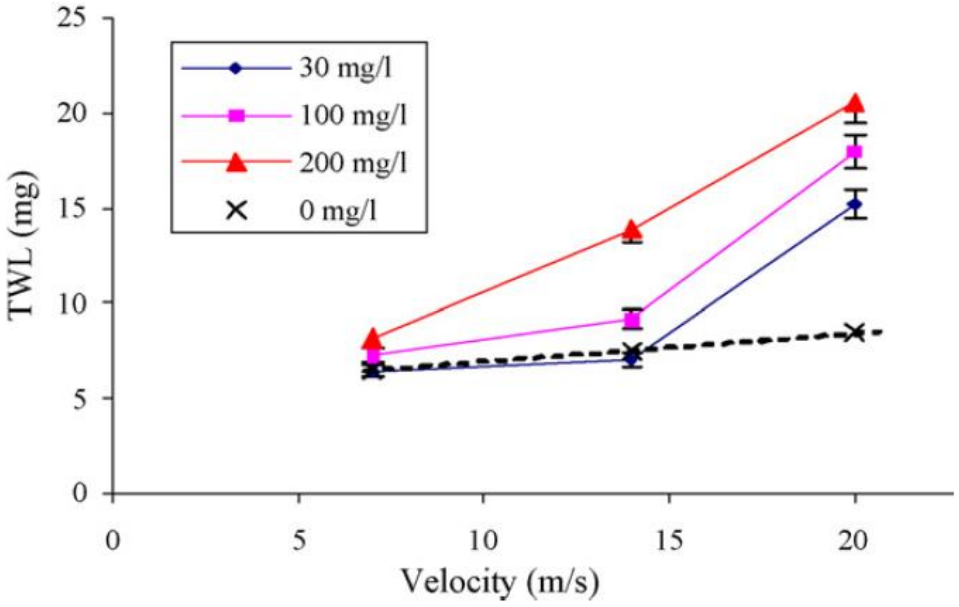

Figure 3.20 Effect of sand concentration and flow velocity on the total erosion-corrosion degradation of X65 carbon steel in CO_2 environments, where TWL is the erosion-corrosion mass loss [34]

The contribution of the individual components to total erosion-corrosion degradation are shown in Figure 3.21 from the tests completed by Hu and

Neville [34]. It was shown that synergistic effects, where corrosion enhanced the rate of erosion, accounted for a very significant proportion of the total erosion-corrosion degradation. The rates of degradation also increased as the temperature of the solution increased. Enhanced rates of degradation of carbon steel were measured in erosion-corrosion tests in other conditions [49, 140, 149, 150].

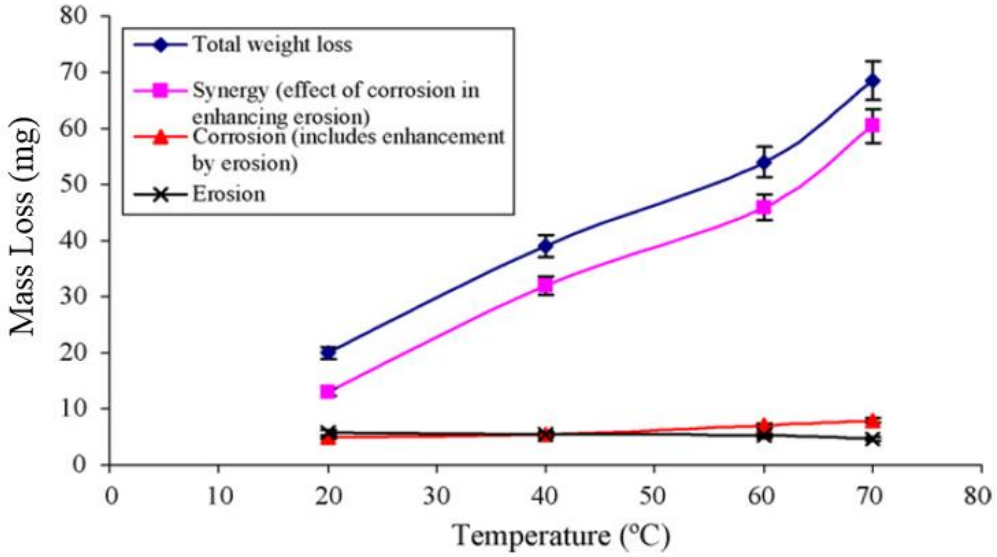

Figure 3.21 Effect of solution temperature on contributions of erosion, corrosion and synergistic components to total erosion-corrosion degradation of X65 carbon steel in CO_2 environments containing a sand concentration of 200 mg/L at a flow velocity of 20 m/s [34]

Stack et al. [112, 151-161] investigated erosion-corrosion on numerous occasions and developed a methodology for determining erosion-corrosion wear maps in a range of conditions for different materials as a function of erosion and corrosion related parameters, such as particle impact velocity, potential and temperature. Four regimes of erosion-corrosion have been regularly used by Stack et al. [160], defining the ratio of erosion to corrosion, shown in Table 3.4.

In aqueous conditions, an erosion-dominated regime is defined when erosion is the dominant mechanism of wear. In an erosion-corrosion regime, both erosion and corrosion degradation account for material loss and corrosion enhances the erosion rate. Two regimes of corrosion were defined. In the first corrosion regime, some effects of erosion are present which enhance corrosion, but corrosion accounts for the majority of the degradation. In the second corrosion-dominated regime, corrosion is the dominant mechanism of degradation and the effects of erosion are negligible.

Table 3.4 Erosion-corrosion regimes defined by Stack et al. [160] as a ratio of erosion wear (K_e) to corrosion degradation (K_c)

Ratio	Regime
$K_c/K_e < 0.1$	Erosion-dominated
$0.1 \leq K_c/K_e < 1$	Erosion-corrosion dominated
$1 \leq K_c/K_e < 10$	Corrosion 1 dominated
$K_c/K_e \geq 10$	Corrosion 2 dominated

3.5.2 Erosion-Enhanced Corrosion

Aminul Islam and Farhat [149] completed erosion-corrosion studies using different carbon steels. They showed that erosion significantly enhanced the corrosion rate of each of the carbon steels tested, and it was suggested that the reason for this was an enhanced rate of degradation caused by the work-hardening of the carbon steel from particle impacts being more anodic, making the surface more susceptible to corrosion. However, no evidence was given for this. Malka et al. [49] completed erosion-corrosion tests using carbon steel specimens in a rapid contraction/expansion section of pipe and showed that the disturbances in the flow as a result of the change in geometry affected the rates of corrosion and erosion. They also observed an enhancement in the corrosion rate as a result of erosion, but did not investigate the causes of the increased degradation. Hu and Neville [34] showed that erosion-enhanced corrosion was not significant in erosion-corrosion tests using the SIJ in the CO_2-saturated conditions tested.

Particle impacts have been shown to increase the roughness of target surfaces after impact, with the most significant increase reported to be observed at particle impact angles between 40° and 60°, leading to increased transport of corrosive species to the material surface [3, 20]. Surface roughening could also change local flow conditions near to the surface of the target material which could influence particle trajectories as well as corrosion rates [17]. Li et al. [162] showed how the corrosion rate of copper increased when the surface roughness increased, however, few studies of this effect have been completed in erosion-corrosion conditions using carbon steel.

3.5.3 Corrosion-Enhanced Erosion

For carbon steel in erosion-corrosion CO_2 conditions it has been reported that the contribution of corrosion-enhanced erosion is much more significant than erosion-enhanced corrosion. Hu and Neville [34] observed that corrosion enhanced erosion was significant but there was no explanation of the mechanisms or causes of the interaction between corrosion and erosion. Malka et al. [49] found that corrosion-enhanced erosion accounted for a much more significant proportion of enhanced degradation in tests completed in a rapid expansion contraction section of pipe. They found that corrosion-enhanced erosion accounted for 70% of the total enhancements, with erosion-enhanced corrosion accounting for the remaining 30%. Aminul Islam and Farhat [149] also observed corrosion-enhanced erosion of carbon steel, and showed that the corrosion-enhanced erosion increased with an increase in flow velocity, as shown in Figure 3.22.

Aminul Islam and Farhat [149] suggested that the cause of corrosion-enhanced erosion was the removal of work-hardened layer exposing softer material. It was also suggested that sharp edges of impacting particles created micro-cracks on the surface upon impact, with corrosion mechanisms propagating the crack and increasing the probability of material removal from subsequent impacts. This had been suggested on other occasions by Aminul Islam et al. [149, 163] but no proof was offered to support this theory.

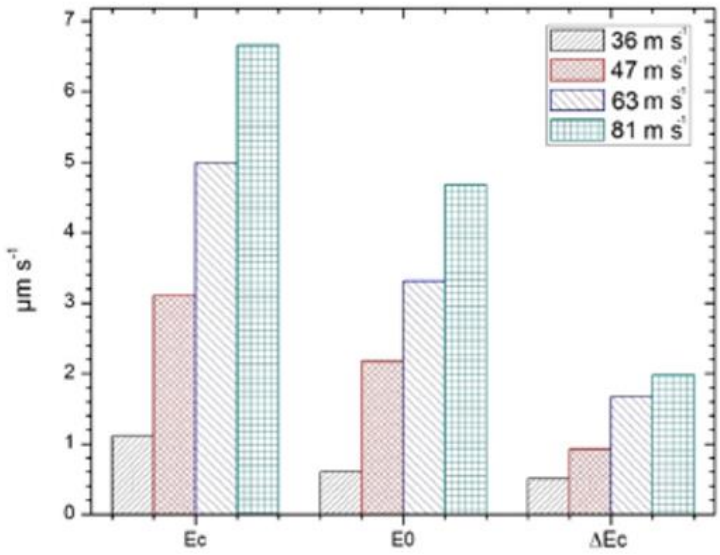

Figure 3.22 Pure erosion (E_0) and corrosion-enhanced erosion (ΔE_C) of X70 carbon steel in erosion-corrosion conditions (E_C) [149]

Corrosion of work-hardened layers exposing softer material is thought to be one of the main causes of corrosion-enhanced erosion [15, 164]. Plastic

deformation, caused by particle impacts on a metal surface, results in strain hardening of the material, due to the movements of dislocations within the crystal structure of the metal [165]. Aribo et al. [58] showed how different passive materials work-hardened in SIJ erosion tests at a flow velocity of 15 m/s with a sand concentration through the nozzle of 500 mg/L and Naim and Badahur [166] showed that brass specimens work-hardened after the impacts of particles. Nickel-aluminium-bronze alloys were shown to work-harden in SIJ tests, with hardness increasing over the width of the surface exposed to particle impacts in the SIJ flow [59].

X65 pipeline carbon steel and other ferrite-pearlite carbon steels have been shown to work-harden as a result of applying strain to the material in tensile testing [76, 167, 168]. Barker [35] showed that X65 carbon steel work-hardened in erosion-corrosion SIJ tests when inhibitor films were present on the surface, but conditions without inhibitor were not investigated. Hutchings and Winter [72] completed single impact erosion tests on carbon steel using steel balls at high velocity and showed that ferrite grains were deformed from approximately 25 µm to approximately 1 µm in size in the region closest to the surface after impact, increasing the hardness. Guo et al. [164] showed how work-hardened layers of carbon steel could be removed through corrosion mechanisms, however, the removal of work-hardened layers on carbon steel has not been shown in erosion-corrosion conditions.

Jiang et al. [169, 170] proposed that erosion rates were enhanced by micro-crack initiation and propagation. It was suggested that micro-cracks formed through a low cycle fatigue process, whereby multiple impacts on the surface cause fracture. The presence of corrosive species then accelerate the growth of the crack. As cracks propagate, it is expected that lips and platelets formed from particle impacts become weakened, thus making removal of these regions easier in subsequent particle impacts [170]. Rajahram et al. [108, 139] used a focused ion beam (FIB) to analyse the subsurface effects of particle impacts on UNS S31603 after slurry pot erosion and erosion-corrosion tests. Fine layers of grain refinement, less than 1 µm thick, were observed nearest to the surface, as shown in Figure 3.23, after 1 minute of erosion testing. The growth and propagation of micro-cracks was also observed in the subsurface of the sample after erosion-corrosion tests, also shown in Figure 3.23, with the theory developed by Jiang et al. [169, 170] of cracks caused by low cycle fatigue used to explain the enhanced rates of erosion.

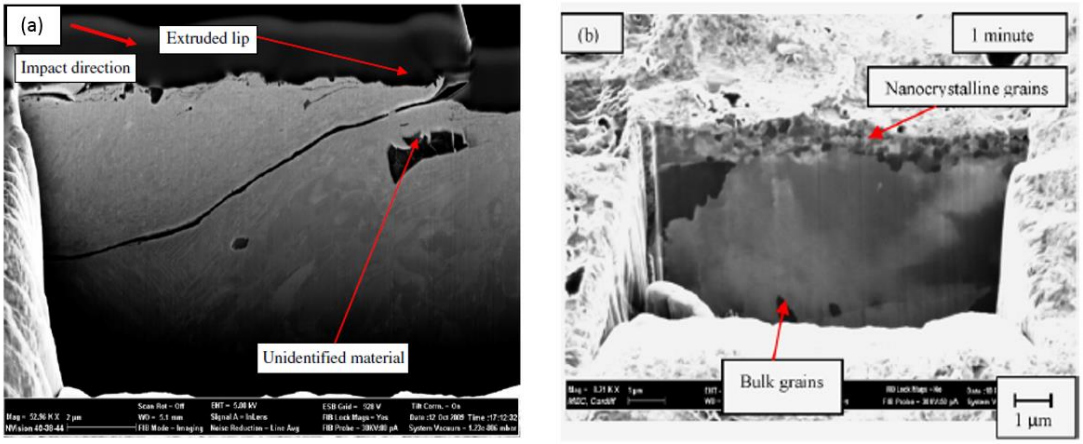

Figure 3.23 FIB analysis of UNS S31603 subsurface after slurry pot erosion-corrosion tests showing (a) subsurface cracks at the root of an extruded lip [139] and (b) work-hardening of the sample after particle impacts [108]

3.5.4 Erosion-Corrosion in Different Flow Geometries

Several test methods have been used for erosion-corrosion testing of materials [171]. The use of an RCE for flow-induced corrosion testing is commonly used, as it has well defined hydrodynamic conditions that can replicate straight pipe flow geometry conditions [31, 52]. The impact of sand particles, however, could not be tested effectively using this method to get repeatable sand particles on the surface to complete erosion-corrosion testing of carbon steel, as the geometry was not representative of erosion in pipe flow [49]. Erosion tests have been completed using dry jet testing, where sand particles are fired at the surface of target materials at different impact angles and impact velocities [17, 18, 20, 149]. However, these two methods were not appropriate for erosion-corrosion testing.

Slurry pot tests have been completed for erosion and erosion-corrosion tests, where a sand-laden solution is rotated at high velocities to cause impacts on a steel surface [78, 108, 170, 172]. One of the more commonly used methods for erosion-corrosion testing is the SIJ. An example of an SIJ is shown in Figure 3.24, used in erosion-corrosion testing at the University of Leeds [34, 35, 60, 63, 120, 144]. The SIJ has been used for erosion-corrosion testing to assess a variety of different parametric effects on erosion-corrosion, including assessing different materials [58], inhibitor performance [35, 62], flow velocity, temperature and sand concentration [34]. Particles are added to the SIJ and recirculated through a nozzle at high flow velocities, impinging onto the surface of a target specimen.

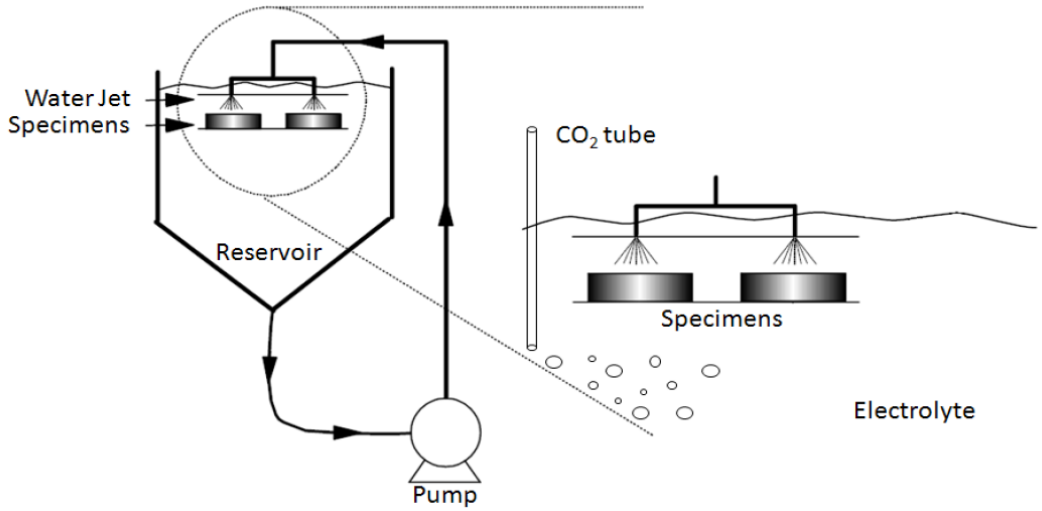

Figure 3.24 SIJ used for erosion-corrosion testing of materials at the University of Leeds [34, 35, 60, 63, 120, 144]

Jet impingement studies in water-sand mixtures have been completed on several occasions to test erosion and erosion-corrosion performance of a wide range of materials [89, 92, 122]. SIJs are ideal for completing analysis of high velocity flow in a range of temperatures in different brine chemistries and in sand-containing flows. However, the main limitation of using a SIJ for erosion-corrosion testing, is that a wide range of conditions can be present on the surface, and the sand impact conditions are not always fully defined on the surface of the sample used [120]. As the erosion rates of materials have been shown to be highly dependent on the impact angles and impact velocities of the particles on the surface, knowledge of this is essential to understand the erosion-corrosion of carbon steel and is often neglected in the analysis of performance in erosion-corrosion conditions.

The most representative method of testing erosion-corrosion in oil and gas pipe flow conditions is to complete testing in pipe flow geometries, as this directly represents flow and particle impingement conditions. Pipe flow geometries have been used occasionally for erosion testing of materials, but the understanding of erosion-corrosion in pipeline geometries is lacking. Erosion-corrosion testing has been completed in elbows at the E/CRC [147, 148, 173]. Shadley et al. [147, 148] completed erosion-corrosion testing using an elbow to assess the effect of sand particles in scale forming conditions. Zeng et al. [174, 175] completed testing using an elbow in erosion-corrosion conditions, however, it did appear that the method used to fit test samples into the elbow could have potentially created flow disturbances. The elbow designed by Zeng et al. [174] is shown in Figure 3.25.

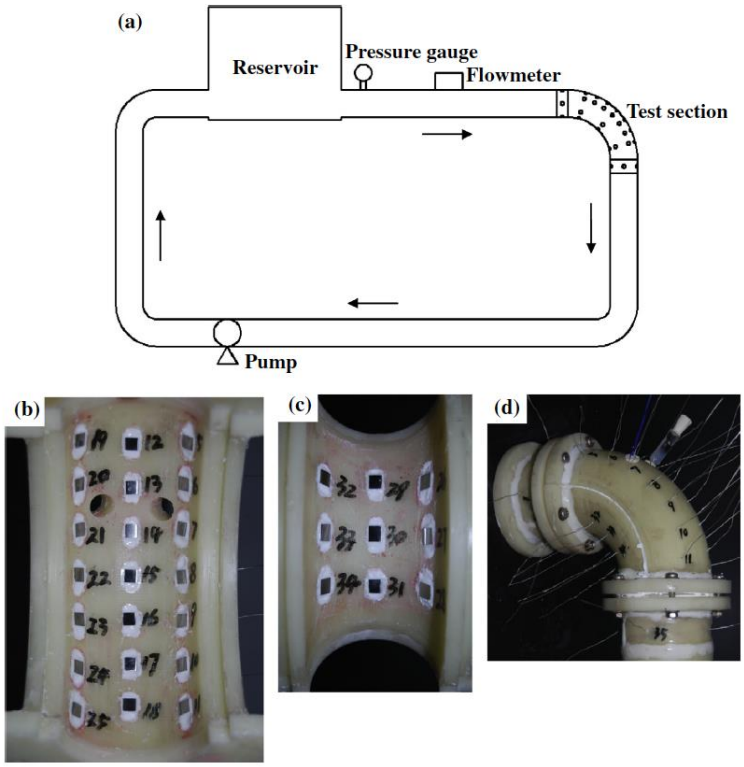

Figure 3.25 Elbow component designed for erosion-corrosion testing of carbon steel where (a) shows the full test setup, (b) the outer radius of the test elbow, (c) the inner radius and (d) the complete test elbow assembly, designed by Zeng et al. [174]

The samples appeared to have been secured in the elbow using resin or silicone. The method was not fully explained by Zeng et al. [174], but it appeared that effort hadn't been made to completely reduce disturbance to the flow caused by the samples. There were also two holes in the middle of the elbow where electrodes were located, which would have significantly disturbed the flow through the elbow, if electrodes protruded into the flow. This could significantly affect local turbulence around the sample locations. The distance of the inlet of the elbow from the other changes in geometry in the flow loop was also not specified. It is possible that a sufficient distance had not been designed to allow the flow to fully develop, potentially changing the hydrodynamic conditions in the elbow. Zeng et al. [174] also used CFD to predict particle flow in the elbow but did not fully define the impingement velocities and angles in the elbow, making it difficult to make comparisons between this geometry and other geometries.

Malka et al. [49] completed erosion-corrosion tests in a rapid expansion/contraction pipe to measure how the contribution of each parameter to erosion-corrosion varied throughout the different sections of the pipe. They stated how SIJ and RCE geometries were not accurately representative of field erosion-corrosion conditions, therefore a more

representative geometry was designed. The disruption in the flow caused a significant increase in erosion rates. The suggestion by Malka et al. [49] that existing test geometries, such as the SIJ, are not representative of field conditions is important. However, design of a new geometry does not necessarily solve the issue of understanding erosion-corrosion as it has been shown that erosion is highly dependent on particle impact angles and velocities [10]. Therefore, defining the conditions in a geometry, in terms of particle impacts and flow conditions, is just as important as developing more representative conditions for testing. This was one of the limitations of the work completed by Malka et al. [49], as the erosion-corrosion conditions were not defined in terms of impact angles and impact velocities. Their work showed that erosion-corrosion in a geometry with the exact same specification as their design would produce the same contributions of corrosion, erosion and interactions to erosion-corrosion degradation. Therefore, it is important to fully understand the conditions present in erosion-corrosion tests.

3.6 Modelling Erosion-Corrosion

Models have been developed to predict erosion and corrosion separately. However, very few reliable and widely used models exist that can predict erosion-corrosion [8]. Several models exist that can be used to predict the corrosion rate of carbon steel, including the de Waard and Milliams models [40, 176], Nesic et al. [37] and NORSOK model [177]. The discussion of these models is beyond the scope of this work, but they could be used to calculate the corrosion component of erosion-corrosion degradation. Erosion models discussed earlier in this chapter can be used to predict the erosion component of erosion-corrosion. Stack et al. [112, 151-153, 157, 159] used separate erosion and corrosion models to predict erosion-corrosion wear maps. However, due to the interactions between erosion and corrosion, a simple combination of an erosion and corrosion model would not fully predict erosion-corrosion. Some erosion-corrosion models have been developed, but they have not been widely used and do not account for all the parameters that could be present in erosion-corrosion conditions [8]. One of the main attempts to predict erosion-corrosion was completed by Harvey et al. [172, 178]. They developed a semi-empirical model to predict erosion-corrosion degradation of stainless steels. The interactions between erosion and corrosion, however, were not fully understood, limiting the general use of the model. It was,

however, shown to be effective at predicting erosion-corrosion in the conditions reported.

One of the challenges of erosion-corrosion modelling is that knowledge of the erosion and corrosion conditions in disturbed flow geometries is typically required, as these components are susceptible to erosion-corrosion degradation [128]. Nesic and Postlethwaite [179] developed a methodology to define flow induced corrosion conditions using CFD, whereby mass transfer coefficients were calculated to define the flow-induced corrosion conditions in a flow geometry. Some attempts at using CFD for understanding erosion-corrosion have been reports [112, 134, 151]. Wear maps developed by Stack et al. [160, 161] were utilised in a CFD prediction of erosion-corrosion through a pipe elbow, by Stack and Abdelrahman [151]. An example of the prediction of wear regimes through the elbow is shown in Figure 3.26. Particles are flowing into the elbow from the left hand side of the figure, and wear regimes on the outer radius of the elbow are shown. Inevitably some of the limitations already discussed in using CFD for erosion predictions would have influenced the prediction completed by Stack and Abdelrahman [151]. However, it did demonstrate the potential of using CFD for erosion-corrosion and the necessity for determining impact angle and impact velocity in the prediction of erosion-corrosion.

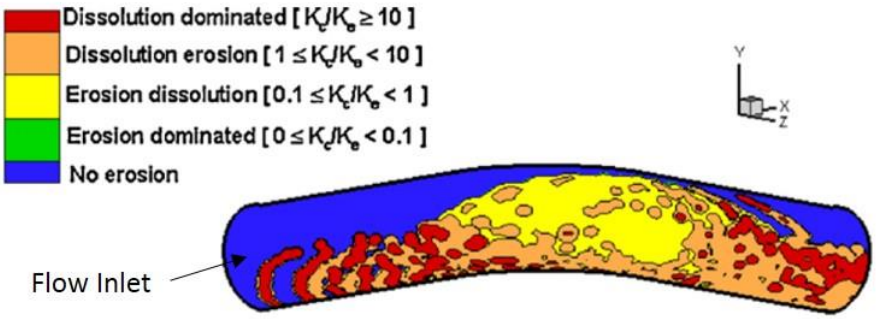

Figure 3.26 CFD prediction of erosion-corrosion regimes in an elbow by Stack and Abdelrahman [151] with a particle mass flow rate of 0.957 kg/s

3.7 Mitigating Erosion-Corrosion

Corrosion inhibitors are chemical substances that minimise corrosion [23]. They are regularly used to protect carbon steel surfaces in oil and gas pipelines to reduce the degradation of the material by adsorbing to the pipeline surface, creating a thin protective film which either limits the electrochemical reactions or limits the transport of corrosive species to the surface [6, 180].

The effectiveness of corrosion inhibitors can vary based on the conditions present, the properties of the surface and the composition of the inhibitor [6, 35, 62, 180-182]. Inhibitors are classified in terms of their inhibiting mechanism, with some inhibitors restricting the anodic reaction and some restricting the cathodic reaction. Most inhibitors used in oil and gas industry are mixed-type adsorption inhibitors, which influence both the anodic and cathodic reaction. Different types of adsorption mechanism also occur with physical adsorption, chemisorption and film forming adsorption that define how the inhibitor adsorbs onto the metal surface [23].

Inhibitors are usually evaluated in static or low flow velocity conditions of less than 1 m/s, so the effects of flow and sand on inhibitor performance have not been well understood [62]. In recent years more studies have been completed to investigate the influence of flow and sand on inhibitor performance [6, 35, 62, 143, 183]. One of the issues, however, that has limited the understanding of inhibitor performance is that chemical composition of the inhibitors used in testing is not always published, making it difficult to compare between different studies and conclude if there are particular chemicals which influence inhibitor performance [6, 35, 62, 184].

The mechanisms of inhibition from a chemical perspective were not the focus of this work, but the influence of flow and erosion on the performance of the inhibitors were of interest. Flow has regularly been of interest in the study of inhibitor performance, with shear stress often quoted as the flow parameter having the most influence on inhibitor performance [51, 185]. It has been reported on several occasions that fluid shear stress reduces the effectiveness of inhibitor films [182, 185, 186]. A critical shear stress of 500 Pa was suggested originally as a threshold shear stress above which the flow reduced the inhibitor effectiveness [7, 62].

It was suggested that the inhibitor film was removed by the shear force across the surface, however, Gulbrandsen and Grana [51] stated how shear stresses typically seen in pipelines are extremely low, even at high flow velocities, and are not sufficient enough to remove surface films. Schmitt [186, 187] also showed how shear stresses of the order of 10^6 Pa would be needed to remove surface films, such as $FeCO_3$. However, some removal of those films was observed at low fluid shear stress, explained by the effects of near wall turbulence removing the films through fatigue rather than mechanical removal from shear stress [186]. The typical shear stress range measured in pipelines is lower than the shear stress required to remove inhibitor films, therefore removal in pipelines through shear is unlikely in the field [188]. Inhibitors are

also known to have drag reducing properties, which can increase the critical shear stresses required to remove inhibitor films [186, 189, 190].

Despite research into the effects of flow on inhibitors, it remains relatively unclear how flow affects inhibitor performance. Gulbrandsen and Grana [51] completed tests using an SIJ with the addition of 20 ppm of inhibitor. Two carbon steel ring samples were used with different flow conditions predicted on each ring, due to positioning of the samples in the SIJ flow. They showed that the very low concentration of inhibitor was relatively insensitive to the flow and was not removed at the highest flow velocity of 20 m/s, equivalent to shear stresses up 1,400 Pa predicted across the surface of the samples, shown in Figure 3.27. Higher corrosion rates were also measured on the outer ring, which was in a lower shear stress region than the inner ring, showing that shear stress did not reduce the effectiveness of this inhibitor. Slight increases in corrosion rate were explained by the presence of dissolved oxygen (O_2) in the CO_2-saturated tests. Dissolved O_2 concentrations were measured from 1 ppb to 100 ppb, with slight increases in corrosion rate measured with increasing O_2 content.

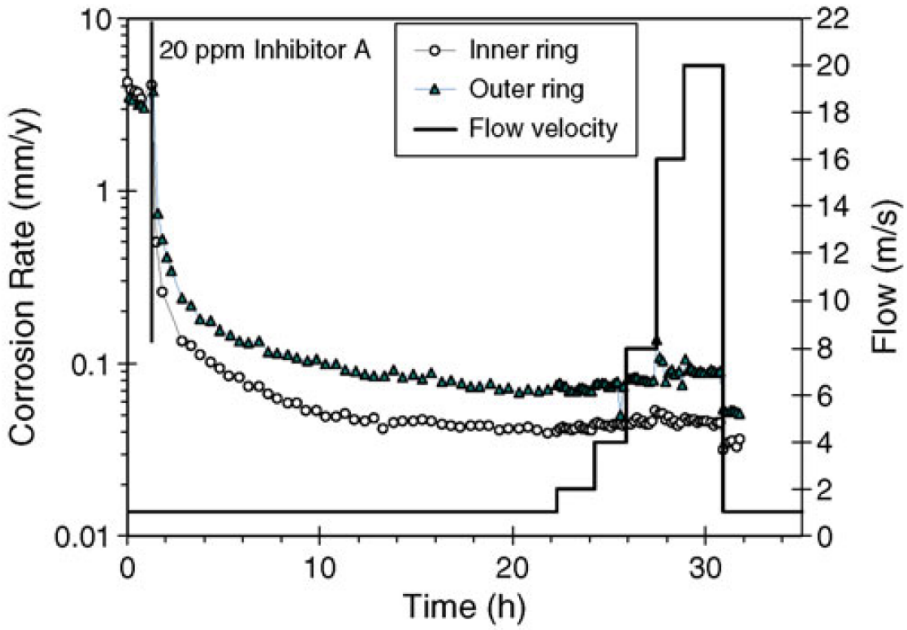

Figure 3.27 Effect of flow on the performance of a corrosion inhibitor on two carbon steel ring samples with different shear stress conditions in SIJ tests completed by Gulbrandsen and Grana [51]

Sand particles can also influence the effectiveness of corrosion inhibitors. Neville and Wang [62] and Barker [35] showed how inhibitors can reduce erosion components of total erosion-corrosion degradation in addition to reducing the corrosion mechanisms. Several theories have been proposed as to the reason for reduced erosion degradation. It has been shown that

inhibitors can adsorb to sand particles, potentially reducing material removal caused by the impacting particle as the film on the particle absorbs some of the energy upon impact [35, 191, 192]. It has also been suggested that the adsorption of inhibitor to the sand particles could also influence the trajectories of the particles, which would result in different erosion rates when compared to blank conditions [35]. Ramachandran [184] proposed that a new factor should be added to the erosion model developed at the E/CRC, Equation (3.26), to account for the reduction in erosion from the presence of an inhibitor film.

It has also been shown that the inhibitor can have no influence on the erosion component of erosion-corrosion degradation and sand can in some cases decrease inhibitor efficiency [181, 193, 194]. Impingement from sand particles can remove the inhibitor film from a surface [191]. Tummala et al. [194] showed that corrosion rates of carbon steel increased when sand particles were added to impinging jet flow, 24 hours after the addition of a corrosion inhibitor, Figure 3.28.

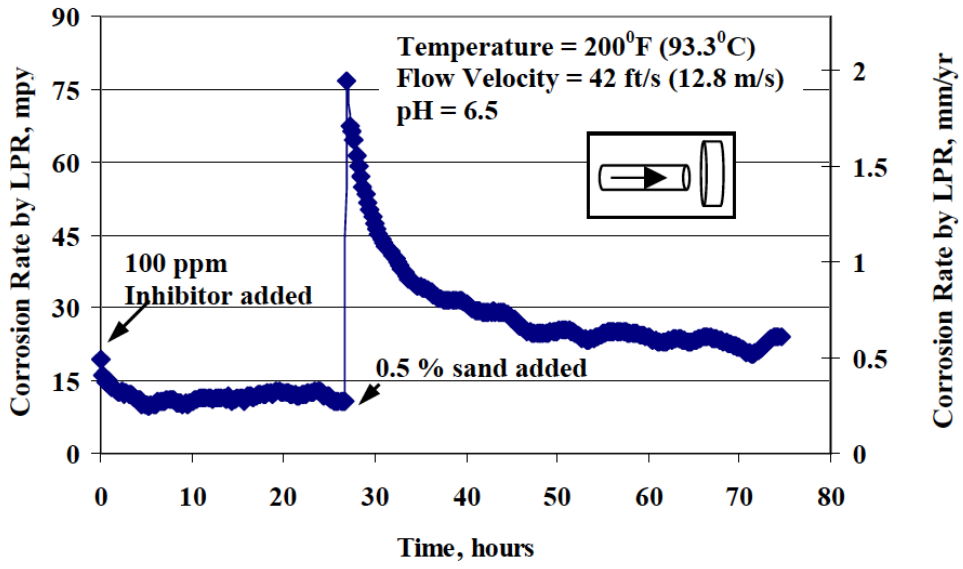

Figure 3.28 Effect of sand on the performance of a corrosion inhibitor used to protect a carbon steel sample in impinging jet tests completed by Tummala et al. [194]

Corrosion rates dropped after the initial peak, caused by the addition of sand, but did not return to the same level prior to the addition of sand, with the removal of inhibitor film by particle impingement suggested as the cause. Adsorption of inhibitor to sand particles can also be detrimental to inhibitor performance by depleting the available inhibitor in the solution, potentially reducing the surface coverage and protectiveness of the inhibitor [192, 195].

It has been reported that an oil phase can significantly reduce the erosion component of damage in erosion-corrosion conditions when an inhibitor is used, due to reduced impact energy of the particles on the sample [143]. In oil and gas pipelines crude oil can also have inhibiting properties, first through a water wetting effect, where contact of the corrosive aqueous phase with the steel surface is prevented by the crude oil and also certain chemical components of the crude oil are suggested to have an inhibiting effect on carbon steel [3, 196]. It has been shown by Shadley et al. [197] that critical velocities for the onset of significant erosion-corrosion damage are increased in the presence of crude oil, therefore suggesting it has an influence on particle impingement. Oil-water conditions, however, were beyond the scope of this thesis.

Few inhibitor evaluation studies have been completed in pipeline geometries. Shadley et al. [148] and Tandon et al. [198] completed erosion-corrosion inhibitor tests using an elbow at the E/CRC. Zeng et al. [175] completed erosion-corrosion tests using a corrosion inhibitor in the elbow developed, discussed previously, and showed that inhibitor efficiency varied at different locations in the elbow. However, there is a lack of understanding of inhibitor performance in complex flow geometries and it is unknown how representative basic lab tests are of field pipe flow.

3.8 Summary of Erosion-Corrosion Literature and Further Research Required

A review of the literature of erosion-corrosion research of carbon steel in CO_2 oil and gas pipeline conditions has shown that a lack of understanding exists with regards to the causes of interactions between erosion and corrosion. Corrosion-enhanced erosion and erosion-enhanced corrosion of carbon steel have regularly been quantified, but the mechanisms involved have rarely been investigated, in particular in conditions relevant to oil and gas pipe flow. Furthermore, understanding how these factors may influence erosion-corrosion in pipe flow geometries is lacking, as erosion-corrosion tests are not always directly applicable to industry conditions in terms of hydrodynamic conditions and particle impact angles and velocities. Basic testing has been completed in more representative flow geometries, but these conditions have not always been fully defined. It is unknown how significant these parameters are on the interactions between erosion and corrosion of carbon steel, as their effects have not been investigated thoroughly.

Impact angles in erosion-corrosion test equipment are often not known making it difficult to define how particle impacts influence corrosion-enhanced erosion and erosion-enhanced corrosion. A nominal impact angle and flow velocity is often given for SIJ erosion-corrosion tests. However, this angle does not account for the full range of impact angles and impact velocities that can be seen across the surface of the sample exposed to the flow in the SIJ [85, 120]. One method of determining the impact angles and impact velocities of sand-liquid flows is by using CFD. CFD has been used to predict the trajectories of particles in a range of different flow geometries. However, use of particle impact data has often not been applied to develop the understanding of erosion-enhanced corrosion and corrosion-enhanced erosion.

Another limitation of the erosion-corrosion research reviewed is that there is regularly no evidence for the causes of erosion-enhanced corrosion and corrosion-enhanced erosion. Typically reasons were given, such as corrosion of work-hardened layers resulting in enhanced erosion, but no evidence has been given to prove this. Reasons often given to explain the interactions are based on logical assessments of the results and comparing with theories provided in literature that also offered limited proof of the mechanisms. Therefore, there is clearly a lack of understanding of the mechanisms of erosion-enhanced corrosion and corrosion-enhanced erosion, highlighting the need for research in this area.

Predicting erosion-corrosion is significantly limited at this stage, due to the significant number of parameters that can influence erosion-corrosion. Currently, no mechanistic model for erosion-corrosion exists, and semi-empirical models have been developed for specific materials in specific conditions, with it being unknown how widely applicable these models are. The most significant limiting factor is that the causes of interactions between erosion and corrosion is lacking, in particular for carbon steel. Understanding of this could be significantly beneficial to the development of models of erosion-corrosion. Limitations of erosion modelling also apply in erosion-corrosion, where CFD is relied upon to determine impact angles and impact velocities, a necessity for using the majority of erosion models. The effects of flow-induced corrosion have also not been clearly defined in erosion-corrosion conditions. Prediction of erosion-corrosion will likely continue to prove to be challenging if the erosion-corrosion conditions are not fully understood.

Therefore the following questions were highlighted from significant gaps in the literature requiring further research which this thesis aimed to answer:

- How significant is erosion-corrosion in oil and gas flow for carbon steel and are the results comparable with other erosion-corrosion research completed, therefore showing a relationship between parametric influences on erosion-corrosion?
- What are the causes of the interactions between erosion and corrosion and do existing theories provided in the literature fully explain the mechanisms of enhanced degradation of carbon steel in erosion-corrosion environments?
- How significant is erosion-corrosion in pipe flow geometries and is it similar to erosion-corrosion results in simple erosion-corrosion test geometries, such as the SIJ?
- Can CFD be used to accurately determine erosion-corrosion conditions in different flow geometries, and can this method be used to translate conditions between different flow geometries?

Chapter 4
Experimental and CFD Modelling Methodology

This chapter gives a detailed methodology of the main experimental techniques used for flow-induced corrosion, pure erosion and erosion-corrosion testing of X65 carbon steel. Several methods were used to measure erosion-corrosion degradation rates of carbon steel samples and various techniques were used to analyse surfaces after tests. These techniques are explained in detail in this chapter. CFD was used to predict flow and particle trajectories through different geometries and the methodology for this is explained.

4.1 Introduction

The aim of this chapter is to explain the main experimental and surface analysis techniques used throughout this thesis. An overview of the main conditions, the main experimental techniques and the techniques used for analysis of surfaces after tests, including surface profiling, scanning electron microscopy (SEM) and subsurface analysis using a focused ion beam (FIB), is given. An overview of the methodology used for developing CFD models is also given, with more specific detail about the particular applications CFD was used for given in later chapters.

Several different experimental techniques have been used for the purpose of erosion-corrosion research of carbon steel, as highlighted in Chapter 3. In this thesis, the majority of erosion-corrosion tests were completed using an SIJ. The SIJ used in this work is explained in more detail in this chapter. A wide range of experimental conditions were required to be tested in to accurately represent field conditions. Therefore, the SIJ provided the most capable method for testing in flow-induced corrosion and erosion-corrosion conditions. Equation (2.1) defined erosion-corrosion degradation as consisting of a corrosion component, an erosion component, an erosion-enhanced corrosion component and a corrosion-enhanced erosion component, with the SIJ ideal for determining each of these parameters. SIJs can also be used to evaluate inhibitor performance in flow-induced corrosion and erosion-corrosion conditions [35, 62].

A small number of static tests were completed to make a comparison between static and hydrodynamic conditions to understand how flow influences the corrosion rate of carbon steel and the performance of corrosion inhibitors. To

investigate erosion-corrosion in more complex flow geometries representative of pipe flow, an elbow was designed. The full description of the design and the specific test methodology developed for using the elbow for erosion-corrosion testing is provided in Chapter 7. However, many of the main methods used in SIJ testing were used for elbow erosion-corrosion tests.

Two main methods of measuring the degradation rate of carbon steel samples used in the different tests were utilised. Mass loss tests were completed, whereby the mass of the test specimens was measured before and after a test to determine the material loss. Electrochemistry was also used to measure corrosion rates in-situ to gain more understanding of the material loss and corrosion mechanisms during a test.

An overview of the main methodology used in CFD predictions of fluid flow and particle flow in relevant geometries is provided. CFD is a powerful tool for predicting the flow of fluids when experimental data cannot be easily obtained [13]. The theory of CFD has already been explained in Chapter 2, with this chapter explaining how this theory is applied in CFD software packages to solve fluid flow problems. CFD was used in this thesis to determine the conditions in the different geometries used in flow-induced corrosion and erosion-corrosion tests. It was also used for predicting the trajectories of sand particles and determining mass transfer coefficients in the same flow geometries. The specific methods and equations used for the simulations completed are shown later in relevant chapters.

4.2 Flow-Induced Corrosion, Erosion and Erosion-Corrosion Tests using an SIJ

Three types of tests were completed to fully quantify the contribution of corrosion, erosion and interactions to erosion-corrosion of carbon steel. Flow-induced corrosion tests were completed to measure the corrosion contribution when no sand was added to the flow. Erosion tests were completed by adding sand particles to the flow in a non-corrosive environment to determine the contribution of pure erosion wear. Erosion-corrosion tests were completed in CO_2-saturated conditions containing sand particles to determine the total material degradation in these conditions. To determine the contribution of the interactions, electrochemistry was used to compare the corrosion rate in flow-induced corrosion and erosion-corrosion conditions to determine erosion-enhanced corrosion. Corrosion-enhanced erosion was then determined

mathematically by rearranging Equation (2.1). To complete each of these three tests, an SIJ was used.

SIJs have been used at the University of Leeds previously for a variety of flow-induced corrosion and erosion-corrosion tests [6, 34, 35, 120]. Barker [35] used an SIJ to analyse erosion-corrosion of carbon steel and the performance of chemical inhibitors in sand-containing flows. Aribo et al. [58] used an SIJ to complete erosion-corrosion analysis of different passive pipeline materials. SIJs have also been used for other erosion-corrosion research and provide a very good method of completing erosion-corrosion analysis of pipeline materials and chemical inhibitors [92, 122].

4.2.1 Description of the SIJ & Basic Test Methodology

The SIJ used is shown in Figure 4.1 and consisted of a 50 L reservoir which was filled with either tap water or deionised water, dependent on the type of test completed. For all tests in Chapters 5 and 6 tap water was used. In elbow tests in Chapter 7, deionised water was used. 2 wt.% sodium chloride (NaCl), 250 ppm of corrosion inhibitor and 500 mg/L or 1000 mg/L of sand particles were added when required to the reservoir to give the required conditions for testing. Full experimental conditions are given later in this chapter. The solution was then recirculated in the direction shown by the arrows, using a variable frequency centrifugal pump, through a dual nozzle arrangement, impinging onto the surface of two flat steel specimens positioned 5 mm below the exit of the nozzle, at a nominal impact angle of 90°.

A range of flow velocities, measured at the exit of the nozzle could be tested in excess of 20 m/s, depending on the diameter of the nozzle used. A 4 mm diameter nozzle was used in this thesis, with the flow rate at the exit of the nozzle measured to determine nozzle flow velocity as a function of pump frequency. The temperature of the water solution was increased and maintained using a temperature probe and stainless steel heating element. A range of temperatures up to 80°C could be tested using the SIJ. CO_2 or nitrogen (N_2) was bubbled into the SIJ reservoir to saturate the solution for the purpose of running either corrosion tests or erosion tests respectively. This was done to reduce the O_2 concentration in the solution to less than 50 ppb, which was measured previously using a colorimetric technique [34, 60, 62]. CO_2 or N_2 was bubbled into the solution for a minimum period of 12 hours prior to starting a test, with this method being used reliably for SIJ testing for

a number of years to achieve fully saturated conditions in the reservoir [6, 34, 35, 58, 60, 62, 143].

Both mass loss and electrochemistry measurements were completed to determine degradation rates, typically with one of the two nozzles used for a mass loss sample and the other for an electrochemistry sample. A standard three electrode cell was used for electrochemistry, with the carbon steel sample used as the working electrode and a silver/silver chloride (Ag/AgCl) redox reference electrode that incorporated a platinum (Pt) counter electrode used to complete the cell. Further detail on the electrochemistry setup is given later in this chapter.

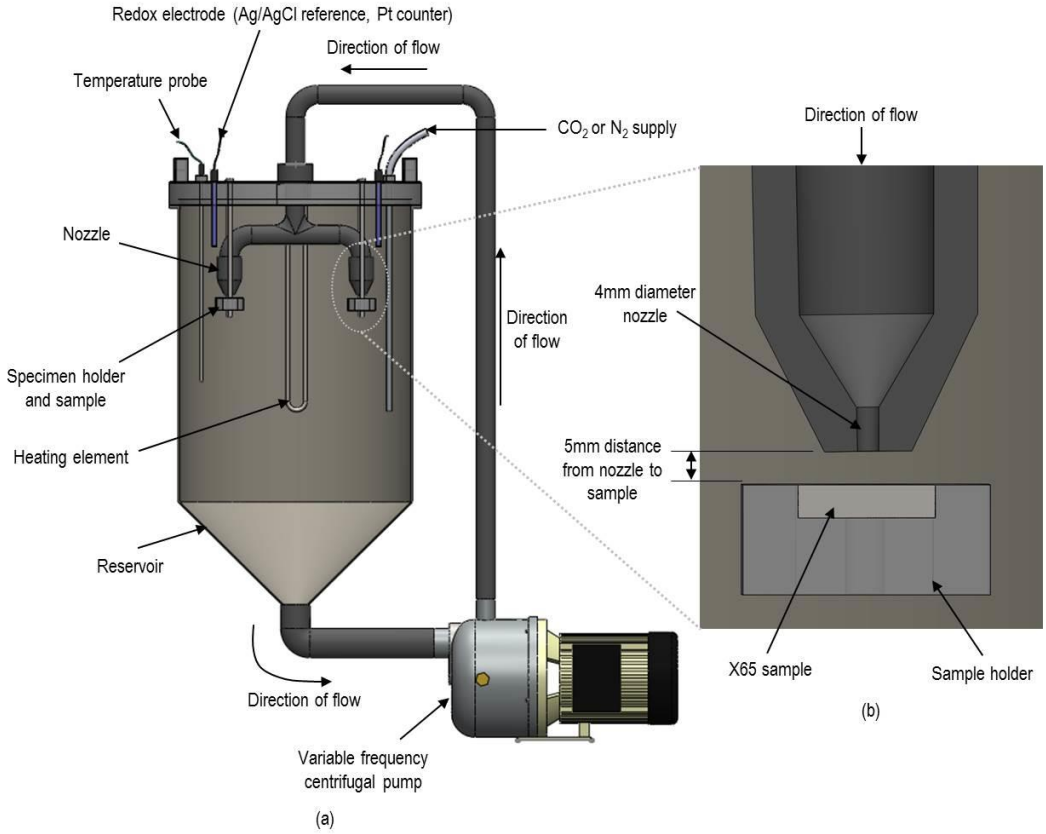

Figure 4.1 SIJ used for flow-induced corrosion, erosion and erosion-corrosion tests showing (a) the full SIJ apparatus and (b) a cross section of the nozzle and X65 sample

Sand particles were added to the reservoir to create erosion conditions. The sand concentration exiting the nozzle was required to be calibrated prior to testing as it was possible for sand particles to settle in the bottom of the reservoir, therefore reducing the actual concentration of sand flowing out of the nozzles. The sand concentration was calibrated by filtering and measuring the concentration of sand exiting the nozzle after a known mass of sand was added to the reservoir. At higher flow velocities the quantity of sand exiting the nozzle was approximately the same as the concentration added to the

reservoir. At lower velocities, higher quantities of sand were required to be added to produce the desired output from the nozzle. To remove sand particles from the SIJ, sand was filtered from the solution before being drained. This process was repeated to ensure that sand had been completely removed before further tests were completed. Sand particles were replaced for every erosion and erosion-corrosion test and only used for one 240-minute test.

The three different tests, flow-induced corrosion, erosion and erosion-corrosion, were completed using similar methodologies with the main difference being the test conditions. Flow-induced corrosion tests were run in CO_2-saturated conditions with no sand present in the flow. Erosion tests were completed in N_2-saturated conditions with no NaCl added to the tap water solution, so that no corrosive species were present in the solution and only degradation from the impacts of sand particles was measured. Erosion-corrosion tests were completed using the same method as flow-induced corrosion tests but with sand particles added to the flow. A brief summary of the three different types of test is shown in Table 4.1.

Table 4.1 Summary of test conditions for flow-induced corrosion (FIC), erosion (E) and erosion-corrosion (E-C) tests using the SIJ

	FIC	E	E-C
Addition of sand	-	✓	✓
Saturation conditions	CO_2	N_2	CO_2
NaCl added	✓	-	✓
pH after saturation	~4.7	~7	~4.7
Mass loss measurements	✓	✓	✓
Electrochemistry	✓	-	✓

4.2.2 Sample Preparation

To ensure that the surface texture of samples was consistent for each test completed, samples were wet ground using 120, 600, 800 and 1200 grit SiC polishing paper, to achieve a consistent surface texture (S_a) of 0.15 µm ± 0.02 µm, measured using a Bruker NPFLEX white light interferometer, explained in more detail later in this chapter. The samples were degreased with acetone, rinsed with deionised water and dried prior to starting the tests. For mass loss tests, the mass of the samples before and after the test was measured using

a Mettler Toledo XP205 mass balance, with a resolution of ±10 µg. To prevent the reverse side of the sample (the side of the sample not facing the SIJ nozzle) from being in contact with the corrosive water solution when fitted in the sample holder, an epoxy resin layer was applied and an o-ring was fitted around the sample in the sample holder to prevent fluid from contacting the sides and reverse side of the sample. The resin layer prevented corrosion on the reverse side of the sample and was easy to remove after the test so had no effect on the mass loss measurements. This reduced the corrosion on the reverse side of the sample which would have significantly increased the mass loss measurements. To complete electrochemistry measurements, a copper wire was soldered to the reverse side of the X65 sample that it could be used as the working electrode and connected to a computer controlled potentiostat. A Solartron SI 1280 potentiostat was used and controlled using CorrWare software for DC measurements and Zplot for AC measurements. After the wire was soldered to the reverse of the sample, the sample was embedded in non-conductive epoxy resin, as shown in Figure 4.2. The carbon steel samples used had a 25 mm diameter, resulting in a surface area of 4.9 cm^2 exposed to the flow.

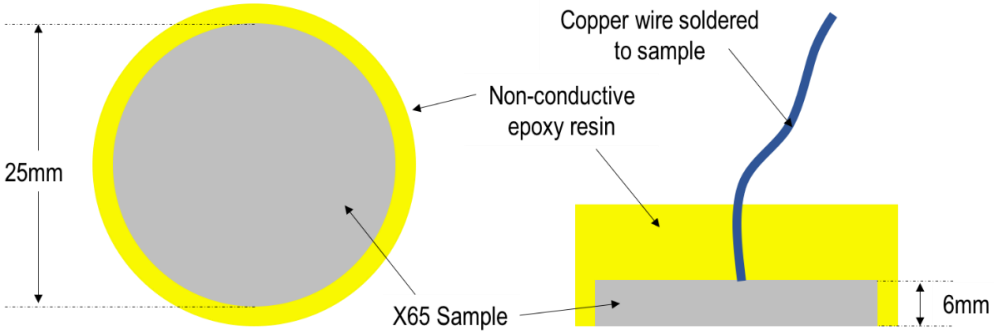

Figure 4.2 Carbon steel samples embedded in epoxy resin used as a working electrode a three electrode cell

4.3 Test Conditions

The test conditions for the majority of the work completed were based on conditions in the field to ensure the work was relevant to the oil and gas industry. Two Shell UK North Sea fields were the focus of this work and the main conditions that could be replicated (e.g. flow velocity, temperature, NaCl concentration) were used for the lab-based tests. Chemical inhibitors used in these fields were also used in the same concentrations as used in the fields.

4.3.1 Field Conditions Replicated in the SIJ

The test conditions, summarised in Table 4.2, were determined using field data so that SIJ tests replicated field conditions as closely as possible. For flow-induced corrosion and erosion-corrosion conditions, in fully saturated CO_2 conditions, 2% by weight of NaCl was added to the pH 4.7 tap water solution which was heated to 60°C prior to starting a test and maintained at this temperature throughout the test. Three different flow velocities of 10 m/s, 15 m/s and 20 m/s were compared and for erosion and erosion-corrosion tests 500 mg/L and 1000 mg/L of sand was added to the solution. For corrosion inhibitor evaluation tests, 250 ppm of inhibitor was added to the solution. Tests were completed for a period of 240 minutes. Corrosion rates were expected to stay constant throughout the test, as tests completed in similar non-scale forming conditions showed no significant change in corrosion rate over time [35]. For erosion tests and erosion-corrosion tests, wear scars were expected on the surface as shown by Barker [35] and Gnanavelu [105]. Therefore, longer tests would significantly change the flatness of the sample and consistent test conditions could not be assumed. Degradation of sand particles was also expected during the test, therefore tests were limited to 240 minutes so these effects did not become significant [104, 105].

Table 4.2 Operating conditions for erosion-corrosion tests using the SIJ

Parameter	Values
pH	4.7
NaCl	2 wt.%
Pressure	1 atm
Flow Velocity	10 m/s, 15 m/s, 20 m/s
Partial pressure	0.54 bar
Temperature	60°C
Sand Particle Average Diameter	250 µm
Sand Concentration	500 mg/L and 1000 mg/L
Test Duration	240 minutes
Inhibitor Concentration	250 ppm

X65 carbon steel, with the composition shown in Table 4.3, was used as the test material. Samples were cut to the sizes specified previously so they could be fixed into sample holders to run each of the different types of test. An SEM

image of the X65 carbon steel surface after being polished and before being used in corrosion testing is shown in Figure 4.3 [41]. The microstructure of the X65 samples is also shown in Figure 4.3, consisting of ferrite grains and pearlite regions, observed using an optical microscope after polishing the sample using 3 µm diamond suspension paste and etching for 10 seconds in a 2% Nital solution. The average grain size observed on the sample was in the range of 10 µm to 25 µm.

Table 4.3 Composition of X65 carbon steel samples (wt.%)

C	Mn	Ni	Nb	Mo	Si	V	P	S	Fe
0.15	1.42	0.09	0.054	0.17	0.22	0.06	0.025	0.002	97.8

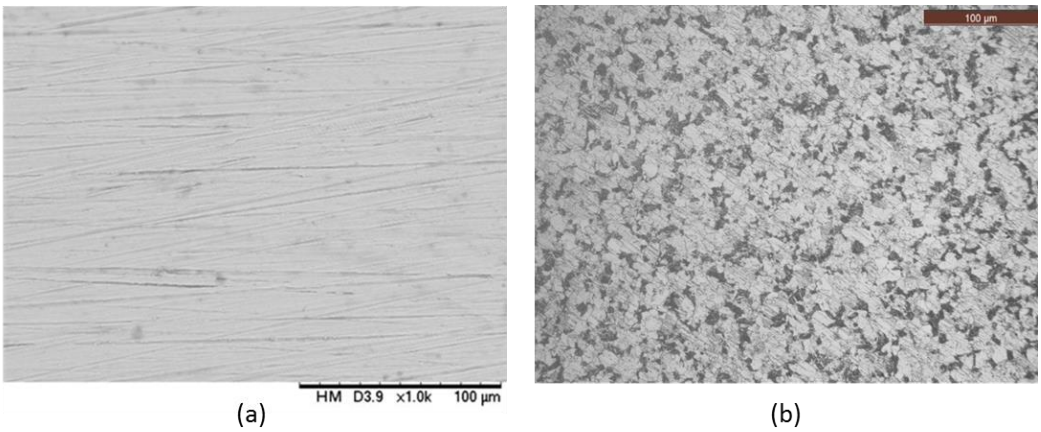

Figure 4.3 X65 carbon steel sample (a) observed using an SEM, showing an untested polished surface [41] and (b) observed using an optical microscope after being etched in a 2% Nital solution for 10 seconds showing the microstructure as consisting of ferrite grains (lighter coloured) and pearlite regions (darker)

The sand particles used in the erosion and erosion-corrosion tests were HST60 silica sand particles. The sand particles had a range of sizes, with the diameter of particles ranging from approximately 100 µm to 500 µm, and an average diameter of 250 µm. The full distribution of sand particles was measured using a Malvern Mastersizer 2000 particle sizer, explained later. The particle size distribution is shown in Figure 4.4 and an SEM image of a sample of the particles are shown in Figure 4.5, showing the angularity of the particles. HST60 sand particles have been used in previous erosion-corrosion testing as the sand particles represent the typical sand particles observed in the field [35].

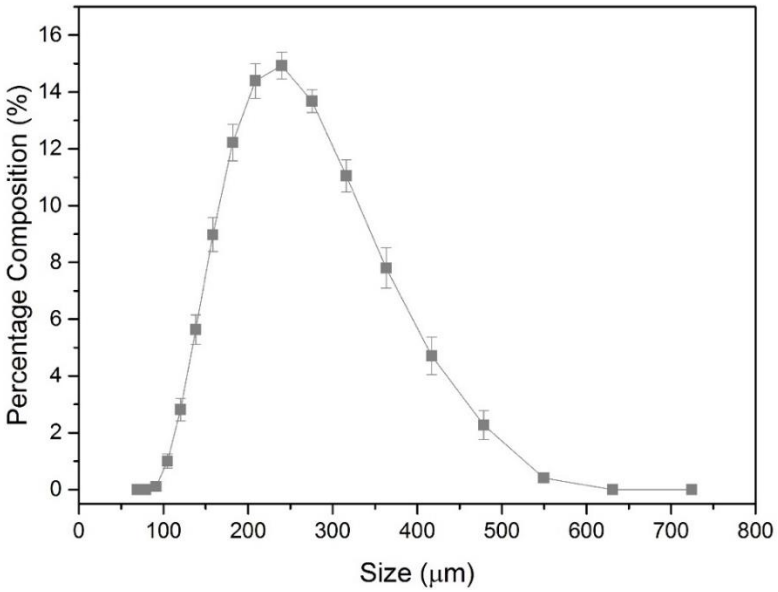

Figure 4.4 Size distribution of HST60 silica sand particles used in SIJ erosion and erosion-corrosion tests

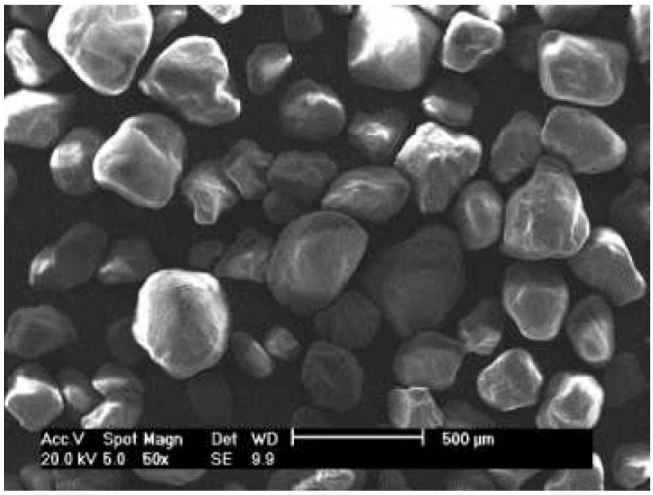

Figure 4.5 SEM image of HST60 sand particles used in SIJ erosion and erosion-corrosion tests [35]

4.3.2 Corrosion Inhibitors

Two commercially available mixed-type corrosion inhibitors were compared in flow-induced corrosion and erosion-corrosion conditions, labelled as inhibitor A and inhibitor B. The main chemical components are shown in Table 4.4 and Table 4.5. Inhibitors were added to the SIJ reservoir at the start of tests before switching on the pump for mass loss tests, and after one measurement in blank conditions for electrochemistry tests. After an inhibitor test, the SIJ was cleaned thoroughly using detergent and water to ensure that the chemical inhibitor was removed prior to the start of another test, so it did not influence further test results.

Table 4.4 Chemical components of corrosion inhibitor A

Chemical Component	Content
Hydrocarbons	30-60%
Ethylene Glycol	10-30%
Tall Oil Fatty Acids	5-<10%
Dodecyl-Dimethyl-Ammonium Chloride	5-<10%
2-Mercaptoethyl Alcohol	5-<10%
Naphthalene	1-5%
Di(2-Ethylhexyl) Sodium Sulfosuccinate	1-5%
Isopropanol	1-5%

Table 4.5 Chemical components of corrosion inhibitor B

Chemical Component	Content
Heavy Aromatic Naphtha	30-60%
Tall Oil, DETA Imidazoline Acetates	10-30%
Thioglycolic Acid	5-10%
Naphthalene	5-10%
1,2,4-Trimethylbenzene	1-5%
Benzyl-(C12-C16 Linear Alkyl)-Dimethyl-Ammonium Chloride	1-5%

4.4 Static Corrosion Tests

The SIJ was used for the majority of the tests completed. However, some static corrosion tests were completed for comparison of flow conditions with static conditions to quantify how flow influenced corrosion and corrosion inhibitor performance. Static tests are commonly used for corrosion testing and chemical inhibitor testing [35, 41, 191]. A diagram of a typical static test setup is shown in Figure 4.6. A glass beaker was filled with 1 L of tap water, to replicate the same corrosive conditions in the SIJ tests, and placed on a hot plate. 2% NaCl was added to the tap water, which was mixed throughout the test using a magnetic stirrer and heated to 60°C, measured using a temperature probe. The solution was saturated with CO_2 and a lid was placed

on top of the beaker and clamped to seal the glass cell and to prevent O_2 ingress. The same X65 sample specification and method used for SIJ electrochemistry tests was used for glass cell tests.

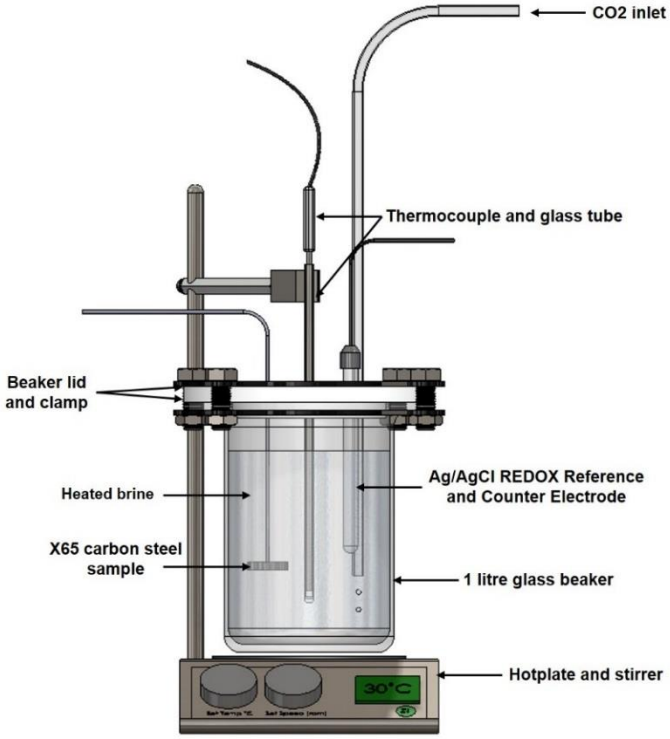

Figure 4.6 Static test setup for corrosion measurement of X65 and evaluation of inhibitor performance in static conditions adapted from [41]

4.5 Measurement Techniques

A range of electrochemical experiments can be completed to determine the rates at which metals are corroding [24]. Mass loss tests provide a rate of degradation and are essential for determining mechanical damage due to erosion mechanisms. However, to determine corrosion rates in-situ and to separate electrochemical mechanisms from mechanical damage in erosion-corrosion conditions, electrochemistry was used. The main techniques used are explained in this section and the setup used in this thesis are given.

4.5.1 Mass Loss Measurements

Mass loss of samples was measured to determine degradation rates in flow-induced corrosion, pure erosion and erosion-corrosion conditions. To determine the degradation rate of the samples using mass loss, the following equation was used:

$$CR = \frac{87{,}600\Delta m}{\rho_m A t} \tag{4.1}$$

where CR is the corrosion or degradation rate in mm/year, Δm is the mass loss of the sample in g, ρ_m is the density of the steel in g/cm^3, A is the surface area of the sample in cm^2, t is the test duration in hours and 87,600 is a conversion factor to convert the degradation rate from cm/hr into mm/yr.

4.5.2 Three Electrode Cell

A three electrode cell was used to determine the corrosion rates of X65 samples, shown in Figure 4.7, consisting of a reference electrode, a counter electrode and a working electrode submerged in an electrolyte [24].

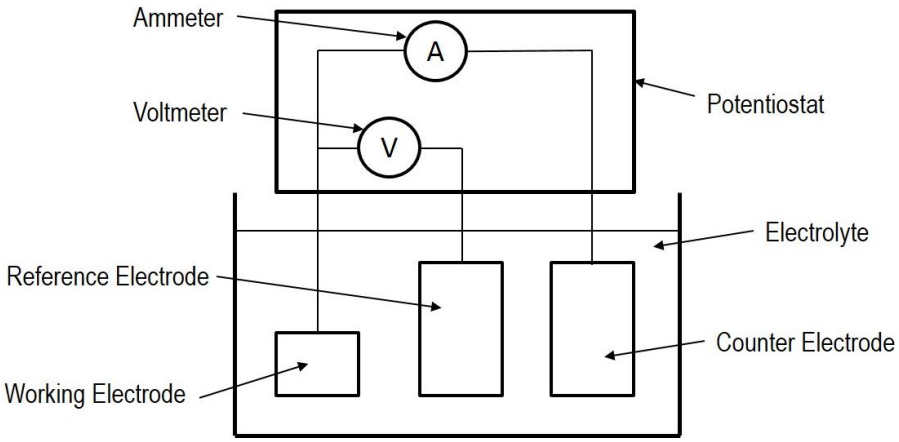

Figure 4.7 Three electrode cell consisting of a working electrode, reference electrode and counter electrode submerged in an electrolyte [24]

The working electrode is the primary electrode of which the corrosion rate is measured, the X65 carbon steel samples in this thesis [23]. The measurement of corrosion potential is completed by measuring the potential of the working electrode with respect to the reference electrode [23]. An Ag/AgCl reference electrode was used in the three electrode cell in SIJ and static tests. Electrical current supplied from a potentiostat changes the working electrode potential from its OCP, referred to as polarisation [24]. To maintain electrical neutrality, current must be withdrawn from the working electrode and supplied to the counter electrode. Electrical current does not flow between the reference electrode and the potentiostat to provide a fixed reference [24]. A Pt counter electrode was used.

4.5.3 Direct Current Techniques

Linear polarisation resistance (LPR) is one of the most common methods of measuring the corrosion rate of a working electrode [199]. Stern and Geary [200] observed that the slope of a current vs potential plot close to the OCP is approximately linear, demonstrated in Figure 4.8. LPR measurements are completed over a small applied potential range typically of the order of 15 mV below OCP to 15 mV above OCP, making the test a relatively non-destructive test [24]. The potential is applied using a direct current (DC) technique, therefore goes from peak cathodic to peak anodic in a linear manner [24].

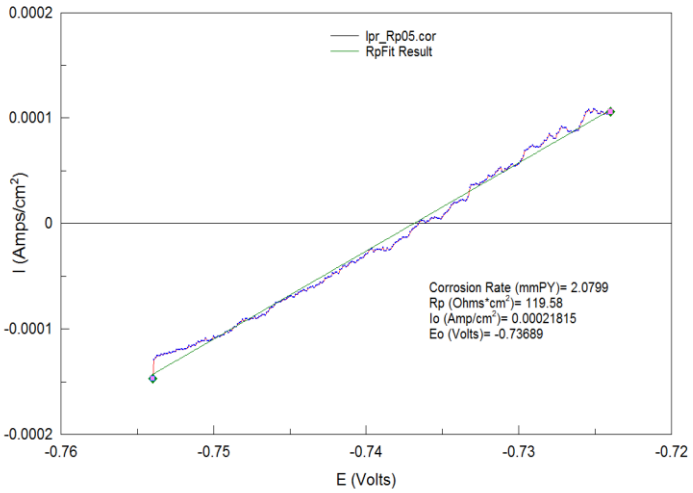

Figure 4.8 LPR measurement showing the relationship between current and voltage in a potential range of ±15 mV about OCP, showing how $\boldsymbol{R_p}$ is determined from the gradient [41]

The corrosion current is calculated from Equation (4.2):

$$i_{corr} = \frac{B}{R_{ct}} \tag{4.2}$$

where B is the Stern-Geary coefficient and R_{ct} is the charge transfer resistance. LPR measurements show polarisation resistance, R_p, but this does not account for the significance of solution resistance, R_s. R_{ct} is determined by deducting R_s from R_p using Equation (4.3). Solution resistance is affected by the geometry of the particular cell and the distance of the counter electrode from the working electrode [24].

$$R_{ct} = R_p - R_s \tag{4.3}$$

The Stern-Geary coefficient is defined by Equation (4.4):

$$B = \frac{1}{2.303}\left(\frac{\beta_a \beta_c}{\beta_a + \beta_c}\right) \tag{4.4}$$

where β_a is the anodic Tafel constant and β_c is the cathodic Tafel constant. The corrosion rate is calculated using the corrosion current density:

$$CR = 3.27 \frac{EW \cdot i_{corr}}{\rho_m} \quad (4.5)$$

where EW is the equivalent weight of steel which is equal to the molecular weight of iron (55.847 g/mol) divided by the number of electrons in the anodic reaction (2), ρ_m is the density of the steel (7.87 g/cm^3) and 3.27 is a conversion factor to determine the corrosion rate (CR) in mm/yr.

One of the limitations of LPR is that R_s must be determined separately using alternating current (AC) techniques and Tafel constants are required to calculate the corrosion rate [24]. Tafel plot corrosion measurements are completed over a much wider potential range and provide more information about the corrosion mechanisms than LPR measurements [24]. Typically electrodes are polarised in a range greater than ±200 mV relative to OCP, and the result is a non-linear plot, which is not seen in LPR analysis [24]. The determination of Tafel constants is completed at ±50 mV, where Tafel behaviour becomes linear [24]. An example of a Tafel plot is shown in Figure 4.9 highlighting how Tafel constants and corrosion current density, i_{corr}, is determined from the intersection of the linear anodic and cathodic Tafel branches. Several assumptions regarding the experimental conditions must apply, however, when using Tafel extrapolation, including [201]:

- Preferable that both branches of the polarisation curve are under charge-transfer control, obeying Tafel behaviour;
- Regions over one decade of current are required for well-defined anodic and cathodic Tafel regions;
- The anodic and cathodic reactions which occur are the only reactions that during determination of polarisation curves;
- Corrosion is uniform and localised corrosion does not occur;
- Polarisation curves are steady state.

To check conditions in this thesis met these assumptions, Tafel measurements were completed at various times during SIJ flow-induced corrosion tests to investigate if Tafel constants and Tafel behaviour changed significantly during a test.

Tafel behaviour is classified as either activation controlled or diffusion controlled depending on the corrosion mechanisms. For an activation controlled reaction, the corrosion rate is controlled by the rate at which a metal electrode can transfer its electrons to the electrolyte. For a diffusion controlled reaction the corrosion is controlled by the rate at which the electrochemically

active species diffuse to an electrode surface [24]. An example of an activation controlled reaction is shown in Figure 4.9 where current density increases linearly with potential increases on both the anodic and cathodic branch [24]. A diffusion controlled reaction is observed when the cathodic current density does not change as potential is increased beyond 50 mV below OCP [24].

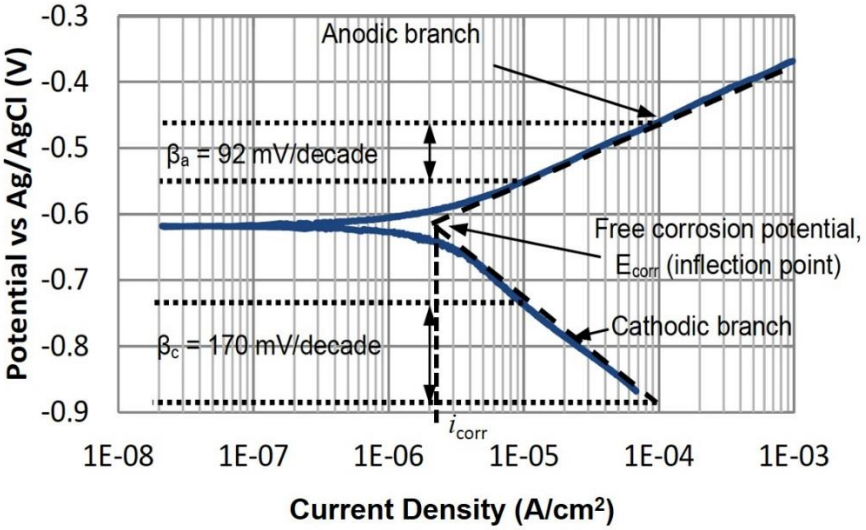

Figure 4.9 Tafel plot showing the relationship between potential and current showing how β_a, β_a and i_{corr} are determined, adapted from [35]

4.5.4 Alternating Current Techniques

Electrochemical impedance spectroscopy (EIS) uses a small range of polarisation voltages, similar to LPR, but uses AC voltage frequencies, as opposed to the DC voltage used in LPR measurements [24]. An AC voltage cycles from peak anodic to peak cathodic voltage, with ions moving back-and-forth between the counter and working electrodes [24]. EIS can provide further understanding of the mechanisms of corrosion as resistance and capacitance values can be measured at each frequency, so it has regularly been used for electrochemical analysis of corrosion inhibitors and coatings on metal surfaces [24, 182]. EDLs normally show the behaviour of a circuit with a resistance and capacitance, as was explained previously, therefore EIS can provide information about the EDL [24]. AC polarisation causes the EDL to change its chemical composition with the constantly cycling polarity causing electron transfer to change from the working electrode to the active species in the solution. As a capacitor takes time to reach full charge, a phase shift is observed between the current and voltage curves, shown in Figure 4.10 [24]. Current and voltage are vectors, therefore an AC impedance vector can be resolved into an X and Y component, with the phase angle determined from

the total impedance vector and the X-component of the vector, also shown in Figure 4.10. The magnitude of the total impedance is determined using Equation (4.6):

$$Z(\omega) = Z' + jZ'' = R_s + \frac{R_{ct}}{1 + (2\pi f R_{ct} C_{edl})^2} + \frac{j(-2\pi f R_{ct}^2 C_{edl})}{1 + (2\pi f R_{ct} C_{edl})^2} \qquad (4.6)$$

where Z' is the real magnitude of impedance, Z'' is the imaginary magnitude of impedance, f is the frequency and C_{edl} is the capacitance of the EDL.

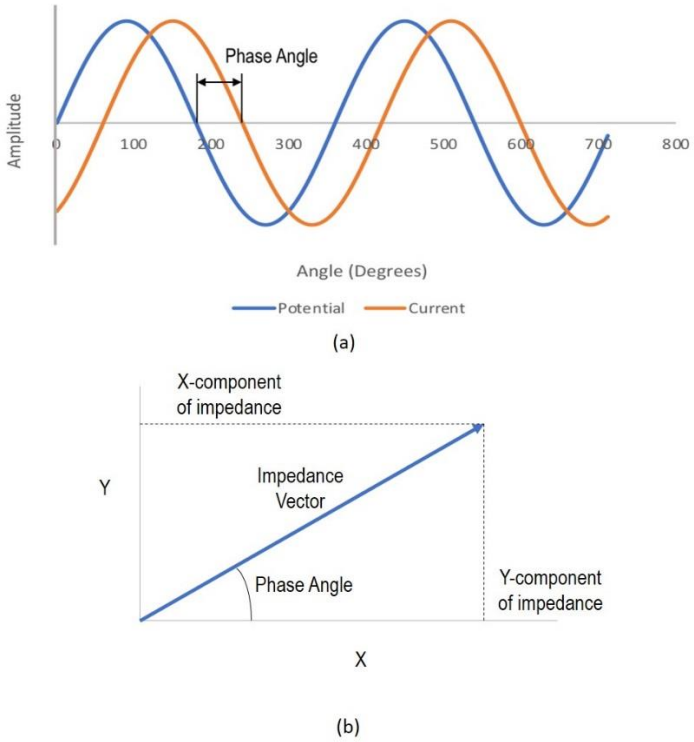

Figure 4.10 EIS behaviour showing (a) phase shift between current and voltage and (b) calculation of phase angle adapted from [24]

4.5.5 Electrochemistry in SIJ Tests

The corrosion rate of carbon steel in SIJ flow-induced corrosion and erosion-corrosion tests was measured in-situ using a standard three electrode cell connected to a computer controlled potentiostat. The X65 test specimen was used as the working electrode with a Pt counter electrode and Ag/AgCl reference electrode. For all erosion-corrosion tests using in Chapter 5 and Chapter 6, EIS was used to determine corrosion rate. EIS has been used to determine the charge transfer resistance of a corroding metal to determine corrosion rates [202-204]. Barker [35] used AC impedance to measure corrosion rates as an alternative to using LPR. Barker [35] showed that using AC impedance for capacitance loops was a reliable method of determining the

corrosion rate of carbon steel in similar flow-induced corrosion SIJ tests, with negligible difference between charge transfer resistance determined from EIS and R_s-compensated R_p from LPR measurements. Equivalent circuits can be determined from EIS results which identify the corrosion mechanisms [182, 205]. EIS was essential for determining solution resistance, which was expected to be significant in the SIJ geometry [35]. Therefore, EIS was the preferred method for corrosion rate measurements to account for solution resistance and determine charge transfer resistance without combining multiple measuring techniques, and was used in Chapter 5 and Chapter 6. For static corrosion and corrosion inhibitor tests, where solution resistance was negligible, and flow-induced corrosion elbow tests completed in Chapter 5 and Chapter 7, LPR was used to determine corrosion rates. EIS was not possible using the elbow as multiple samples were used as working electrodes, requiring the use of a multi-channel ACM Gill 12 potentiostat, which could not be used for EIS measurements. A potential range from -15 mV to +15 mV about OCP was applied at a scan rate of 0.25 mV/s for LPR measurements.

A period of four minutes was used after starting a test before electrochemistry measurements were started, allowing both OCP to stabilise and conditions in the SIJ to settle. AC impedance measurements were then completed in a frequency range from 10 kHz to 0.05 Hz at a potential of ±10 mV to obtain R_s and R_{ct} so that the corrosion rate of the X65 sample could be calculated. OCP was again allowed to stabilise after completing the EIS measurements for a period of four minutes before the next EIS measurement was completed. This cycle was repeated throughout the test. EIS measurements were completed for a period of approximately 210 minutes after starting the test before cathodic and anodic polarisation sweeps were completed to produce a Tafel plot. Tafel plots were used to obtain the Tafel constants for the calculation of corrosion rate. The cathodic branch of the Tafel plot was measured first from a potential of +15 mV to -250 mV relative to OCP at a scan rate of 0.5 mV/s. The anodic branch of the Tafel plot was then measured, after a period of 4 minutes where the OCP was allowed to stabilise, from a potential of -15 mV to +250 mV relative to OCP at a scan rate of 0.5 mV/s.

4.6 Surface Analysis Techniques

Several surface and subsurface analysis techniques were utilised to investigate the mechanisms of erosion, corrosion and erosion-corrosion and the significance of the degradation on the carbon steel surfaces used in

erosion-corrosion tests. The methodology for each of the main types of analysis used in this thesis are shown in this section.

4.6.1 White Light Interferometry

Profiling surfaces of samples was an essential technique used to measure wear of surfaces caused by particle impingements in SIJ tests. 3D profiles of the surface were measured using a Bruker NPFLEX white light interferometer. The Bruker NPFLEX uses white light interferometry to scan the surface and produce a detailed profile. This non-contacting technique was the preferred method of surface profiling as it provided a very fast and accurate method of measuring a 3D profile of the entire sample surface.

Profiles of the samples used in SIJ tests were measured using the NPFLEX by positioning the sample on the microscope and adjusting the vertical height of the microscope to locate the interference fringes on the sample. A 2.5x magnification objective was used to scan the surfaces. After the fringe was located, the measurements over the surface were started. A 3D profile was obtained by starting the measurements in the centre of the wear scar on the sample and moving the stage in two directions in a spiral motion from the centre of the sample toward the edge of the sample. A minimum diameter of 12 mm across the sample was scanned and a 25% overlap was specified between the measurements so that a continuous profile could be produced across the surface. The measurements were then stitched together to give a full 3D profile of the surface. The surface was filtered to remove the form and tilt of the sample so that the 3D profiles could be extracted from a flat surface to distinguish between the form of the sample and the mechanical damage as a result of particle impacts on the surface of the sample.

4.6.2 SEM Analysis

SEM provides high resolution, high magnification images of surfaces and can be used to analyse a variety of effects on carbon steel surfaces after erosion and erosion-corrosion tests. Barker [35] and Gnanavelu [105] used an SEM to analyse carbon steel surfaces for evidence of erosion damage on surfaces after SIJ erosion and erosion-corrosion tests. A Hitachi TM3030 Benchtop SEM was used to analyse carbon steel surfaces in this thesis in the secondary electron mode with an operating voltage of 15 kV. The Hitachi benchtop SEM was used as it provided a convenient method of analysis surfaces at high magnification with sufficient resolution and quality.

4.6.3 Hardness Testing

Micro-indentation of the X65 samples was completed using a Mitotoyo HM-122 micro-indenter to measure the Vickers hardness of samples. Micro-indentation can be used to determine the Vickers hardness (H_V) of a metal specimen by loading a pointed diamond of a known geometry into the test specimen, Figure 4.11. The deeper the indenter penetrates into the surface, the softer the material is and the larger the area of the indentation would be. To determine the hardness of the specimen, the indentation load applied is divided by the area of the indentation, Equation (4.7) [165].

$$H_V = \frac{F_i}{A} \tag{4.7}$$

where F_i is the indentation load and A is the area of the indentation. An indentation load of 4.9 N was used to indent the carbon steel samples in this work to determine the hardness of samples after erosion and erosion-corrosion testing using the SIJ.

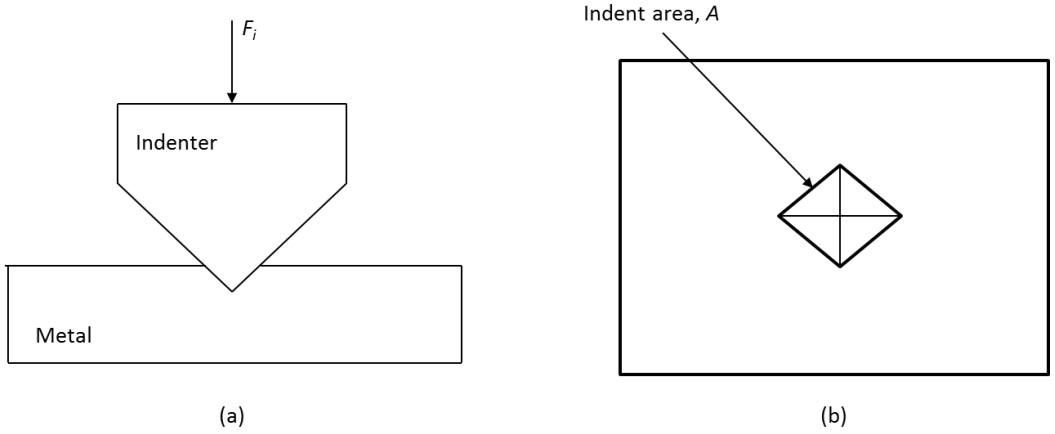

Figure 4.11 Method of hardness testing showing (a) applied load, $\boldsymbol{F_i}$, from a pyramid indenter and (b) indentation of area, $\boldsymbol{A}$, produced on the surface adapted from [165]

4.6.4 Analysis of Sand Particle Size

Sand particles were analysed to measure their size using a Malvern Mastersizer 2000 particle sizer. A sample of sand particles was added to deionised water prior to measurements and recirculated through the Mastersizer to disperse the sand particles. After dispersion, the sand-water solution was recirculated through a glass chamber and measurements of size were made using a laser diffraction technique. The sizes of the particles were measured by determining the angular variation in intensity of scattered light as the laser beam passed through the dispersed sample [206]. The scattering

pattern could then be used to determine the particle size. The refractive index of the sand particles was required to be input in order to calculate particle size. A refractive index of 1.544 and an imaginary component of refractive index, commonly referred to as absorption of the material, of 0.1 was used. Five repeated measurements of particle size were completed for each sample of sand particles measured in this thesis and three separate samples of the same particle batch was analysed to determine an average particle size distribution.

4.6.5 Subsurface Analysis Using a Focused Ion Beam (FIB)

Subsurface analysis was completed using a FEI Helios G4 CX DualBeam high resolution Field Emission Gun Scanning Electron Microscopy (FEGSEM) with a precise 30 kV liquid gallium ion beam. The FIB was used to mill sections from metal samples to analyse the subsurface of samples after erosion and erosion-corrosion tests. A Pt layer was deposited onto the sample first to prevent damage at the top surface in the region analysed. Bulk milling of the sample using the ion beam was completed at an operating current 21 nA to a depth of approximately 15 µm and width of approximately 10 µm. The milled surface was cleaned and polished using the ion beam at an operating current of 0.79 nA. The FIB could also be used to etch the surface so that the microstructure could be analysed. The surface was etched at an operating current of 7.7 pA. SEM analysis of the surface was completed to image the surface using secondary emission at an operating voltage of 5 kV and 10 kV. Final imaging using the ion beam was completed at operating currents of 7.7 pA and 24 pA.

4.7 Using CFD to Predict Fluid Flow, Particle Trajectories and the Transport of Diluted Species

CFD is a valuable technique that has been used previously to aid the understanding of flow-induced corrosion, erosion and erosion-corrosion [35, 110, 120, 151, 179]. Regularly, the hydrodynamic conditions of a system are not entirely known, with even less being known about the particle impacts in these systems. Being able to predict the hydrodynamic conditions and particle impacts in different flow geometries is essential to fully understand mechanisms of corrosion, erosion and erosion-corrosion. Along with the surface analysis techniques completed, the use of CFD enabled a much more

significant understanding of erosion-corrosion, in the geometries analysed, to be gained.

4.7.1 Developing CFD Models Using COMSOL Multiphysics

COMSOL Multiphysics 5.2a was used throughout this thesis for CFD simulations of fluid flow, particle trajectories and the transport of diluted species. COMSOL Multiphysics uses the finite element method to solve fluid flow problems and multi-physics simulations. There are three main stages involved in the development of a fluid model: a pre-processor, a solver and a post-processor, as shown by the flow diagram in Figure 4.12 [13].

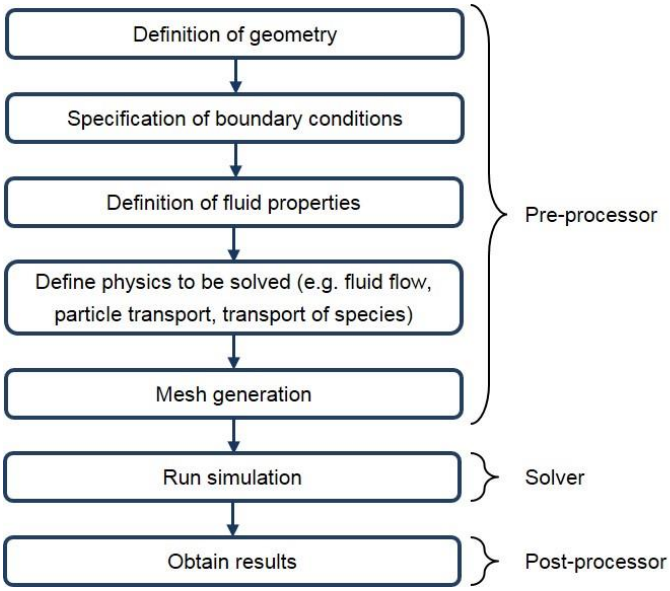

Figure 4.12 Stages involved in the development of CFD models adapted from [13]

The first stage of developing a model in CFD is to define the geometry for which the flow is required to be solved for. This geometry is either modelled in 2D or 3D dependent on the level of accuracy required from the model and the type of geometry to be modelled [13]. Boundary conditions must then be specified to define which regions of the geometry are regions of fluid flow, which parts of the geometry are walls/solid boundaries and where the inlet and outlet boundaries of the fluid flow are. Fluid properties, such as the density and temperature, inlet fluid velocity and any other relevant parameters are specified to give the required conditions for the simulation. The nature of the flow must also be specified to define whether the flow is laminar or turbulent. The effects of turbulence and types of turbulence model are discussed later in this chapter. In all of the flow geometries modelled in this work, the flow was turbulent, requiring a turbulence model to be specified to solve the fluid flow

problem. Several different turbulence models exist, and the most applicable model for the geometry and flow conditions specified was determined.

Once the fluid flow conditions and geometry were defined, the model was meshed. Meshes consist of a collection of elements of various shapes in order to solve the finite element equations involved in the process of CFD modelling [13]. The shape and number of elements in the mesh are dependent on the geometry, the flow conditions and the desired output from the model simulation. Meshes are typically required to be finer in regions requiring high levels of accuracy, such as near to walls and in abrupt changes of flow direction [13]. To ensure meshes are sufficiently fine to provide the required level of accuracy without excessive simulation time, mesh sensitivity studies are completed. In a mesh sensitivity study, the number of elements in a mesh is changed and a particular output, such as the wall shear stress, is calculated to determine how significant the effect of changing the number of elements is on this result, so that the optimum mesh can be used for further simulations. Finer meshes increase the accuracy of a solution but also increase computational time, so a compromise between accuracy and computational time is usually required [13]. After a mesh has been defined, the simulation is run and results can be processed to give the desired output after completion. Further simulations, such as the addition of particles into the flow and the transport of diluted species, discussed in more detail later, can be simulated once the fluid flow has been predicted.

For the models developed in this thesis, work sheets have been produced which detail the methodology to reproduce the models. These are included as an Appendix and can be referred to for developing similar models using COMSOL Multiphysics.

4.7.2 Effects of Turbulence

An important parameter in fluid mechanics is the Reynolds number (Re), the ratio of inertial forces to viscous forces within a fluid, which for pipe flow is defined by Equation (4.8) [100].

$$Re = \frac{\rho_f U D_p}{\mu} \tag{4.8}$$

where ρ_f is the fluid density, U is the fluid velocity, D_p is the diameter of the pipe and μ is the dynamic viscosity of the fluid. For a Reynolds number of less than 2000, the fluid flow is considered to be laminar, where Navier-Stokes equations can be applied to solve the fluid motion [13]. At Re > 4000, the flow

is typically considered to be turbulent [100]. Turbulent flow is much more complex than laminar flow due to the random nature of turbulence. Fluid properties in turbulent flow are typically characterised using mean values and statistical properties of their fluctuations as a result of turbulence [13]. For example, the flow velocity is defined as:

$$u(t) = U + u'(t) \tag{4.9}$$

where U is the steady mean velocity and $u'(t)$ is the fluctuating component of the velocity as a result of the turbulent nature of the flow. This equation also applies similarly to other flow properties, such as pressure.

Due to the complexity of turbulent flow, and presence of turbulent eddies that form in the flow, excessive computing demands are required to solve the Navier-Stokes equations to the required level of accuracy [13, 207]. Instead, Reynolds-Averaged Navier-Stokes (RANS) formulations of the Navier-Stokes equations are solved that average the velocity and pressure fields in time [207]. The RANS equivalent of the Navier-Stokes equations derived in Chapter 2 are:

$$\frac{\partial(\rho U)}{\partial t} + \nabla \cdot (\rho U \mathbf{U}) = -\frac{\partial P}{\partial x} + \nabla \cdot (\mu \nabla U) + \left[-\frac{\partial(\rho \overline{u'^2})}{\partial x} - \frac{\partial(\rho \overline{u'v'})}{\partial y} - \frac{\partial(\rho \overline{u'w'})}{\partial z} \right] + S_{Mx} \tag{4.10}$$

$$\frac{\partial(\rho V)}{\partial t} + \nabla \cdot (\rho V \mathbf{U}) = -\frac{\partial P}{\partial y} + \nabla \cdot (\mu \nabla V) + \left[-\frac{\partial(\rho \overline{u'v'})}{\partial x} - \frac{\partial(\rho \overline{v'^2})}{\partial y} - \frac{\partial(\rho \overline{v'w'})}{\partial z} \right] + S_{My} \tag{4.11}$$

$$\frac{\partial(\rho W)}{\partial t} + \nabla \cdot (\rho W \mathbf{U}) = -\frac{\partial P}{\partial z} + \nabla \cdot (\mu \nabla W) + \left[-\frac{\partial(\rho \overline{u'w'})}{\partial x} - \frac{\partial(\rho \overline{v'w'})}{\partial y} - \frac{\partial(\rho \overline{w'^2})}{\partial z} \right] + S_{Mz} \tag{4.12}$$

where U, V and W refer to the mean velocities in the x, y and z directions and $\overline{u'}$, $\overline{v'}$ and $\overline{w'}$ refer to time averaged fluctuation of those velocities known as Reynolds stresses.

4.7.3 Turbulence Models

A brief overview of the main turbulence models used in this thesis is provided. The RANS equations introduce additional unknowns to account for the turbulent fluctuation parameters of velocity, which turbulence models are used to solve [13]. There are several different turbulence models that exist that are used dependent on the particular geometry for which the flow is being solved for and the required accuracy in results [13]. Turbulence models are based on

the assumption that Reynolds stresses are linked to mean rates of deformation:

$$\tau_{ij} = -\rho\overline{u_i' u_j'} = \mu_t\left(\frac{\partial U_i}{\partial x_j} + \frac{\partial U_j}{\partial x_i}\right) \tag{4.13}$$

where i, j are equal to 1, 2 or 3, referring to the x, y and z direction respectively, and μ_t is the turbulent viscosity. For the turbulence models typically used, it is assumed that turbulent viscosity is isotropic, therefore the ratio of Reynolds stresses to mean rate of deformation are equal in all directions [13].

One of the most commonly used turbulence models is the k-ϵ model, which is widely used and validated in a range of conditions [13]. The k-ϵ model has two additional transport equations that define the turbulent kinetic energy, k, and the rate of dissipation of turbulent kinetic energy, ϵ. For the flow geometries modelled in this thesis, the k-ϵ model has been shown to be less accurate, therefore the k-ω model was used [13]. This model also utilises a turbulent kinetic energy term, but calculates the specific rate of turbulent dissipation, ω, as opposed to ϵ. The transport equation for k is defined as [208]:

$$\frac{\partial(\rho k)}{\partial t} + \mathbf{U}\cdot\nabla(\rho k) = P_k - \rho\beta^* k\omega + \nabla\cdot[(\mu + \sigma^*\mu_t)\nabla k] \tag{4.14}$$

The transport equation for specific turbulent dissipation is defined as [208]:

$$\frac{\partial(\rho\omega)}{\partial t} + \mathbf{U}\cdot\nabla(\rho\omega) = \alpha\frac{\omega}{k}P_k - \rho\beta\omega^2 + \nabla\cdot[(\mu + \sigma\mu_t)\nabla\omega] \tag{4.15}$$

where P_k is the production term, defining the rate of production of k or ω:

$$P_k = \mu_t\frac{\partial u_i}{\partial x_j}\left(\frac{\partial u}{\partial x_j} + \frac{\partial u_j}{\partial x_i}\right) \tag{4.16}$$

The turbulent viscosity is defined as Equation (4.17):

$$\mu_t = \rho\frac{k}{\omega} \tag{4.17}$$

The other terms in the equations that have not been defined are model constants and have the following values of:

$$\alpha = \frac{13}{25},\ \beta = \beta_0 f_\beta,\ \beta^* = \beta_0^* f_{\beta^*},\ \sigma = \sigma^* = \frac{1}{2},$$
$$\beta_0 = \frac{13}{125},\ f_\beta = \frac{1+70\chi_\omega}{1+80\chi_\omega},\ \chi_\omega = \left|\frac{\Omega_{ij}\Omega_{jk}S_{ki}}{(\beta_0^*\omega)^3}\right|,$$
$$\beta_0^* = \frac{9}{100},\ f_\beta = \begin{cases} 1, & \chi_k \le 0 \\ \dfrac{1+680\chi_k^2}{1+400\chi_k^2}, & \chi_k > 0 \end{cases},\ \chi_k = \frac{1}{\omega^3}(\nabla k\cdot\nabla\omega) \tag{4.18}$$

where the mean rotation rate tensor is defined as:

$$\Omega_{ij} = \frac{1}{2}\left(\frac{\partial u_i}{\partial x_j} - \frac{\partial u_j}{\partial x_i}\right) \tag{4.19}$$

The mean strain rate tensor is defined as:

$$S_{ij} = \frac{1}{2}\left(\frac{\partial u_i}{\partial x_j} + \frac{\partial u_j}{\partial x_i}\right) \tag{4.20}$$

Turbulence models treat the flow at walls in different ways and are generally grouped into two categories, turbulence models that use wall functions to resolve the flow near to wall boundaries and turbulence models that fully resolve the fluid flow down to the wall [13]. Turbulence models such as the k-ω and k-ϵ model are examples of turbulence models that use wall functions. Wall functions use empirical relationships to resolve the fluid flow near to the wall in the viscous sub-layer region, thus reducing the accuracy of the model near to the wall. However, resolving the fluid flow at the wall to such a high accuracy is not always necessary, so the k-ϵ and k-ω models are widely used and provide the benefits of reduced computational time due to less complexity [13]. However, for simulations which require accurate solutions of flow in the viscous sub-layer region, fully resolved turbulence models are required [13]. The Shear Stress Transport (SST) model interpolates between the k-ω and k-ϵ models and was used for simulations requiring higher levels of accuracy in this thesis. Two transport equations are also solved in the SST model but the simulation time is increased significantly compared to the basic k-ω model. The transport equations for the SST model in terms of k and ω are [208]:

$$\frac{\partial(\rho k)}{\partial t} + \mathbf{U}\cdot\nabla(\rho k) = \tilde{P}_k - \rho\beta_0^* k\omega + \nabla\cdot[(\mu + \sigma_k\mu_t)\nabla k] \tag{4.21}$$

$$\frac{\partial(\rho\omega)}{\partial t} + \mathbf{U}\cdot\nabla(\rho\omega) = \alpha\rho S^2 - \rho\beta\omega^2 + \nabla\cdot[(\mu + \sigma_\omega\mu_t)\nabla\omega] + 2(1-F_1)\frac{\rho\sigma_{\omega_2}}{\omega}\nabla\omega\cdot\nabla k \tag{4.22}$$

where S is the characteristic magnitude of the mean velocity gradients:

$$S = \sqrt{2S_{ij}S_{ij}} \tag{4.23}$$

The blending function F_1 is defined as:

$$F_1 = \tanh\left(\left\{\min\left[\max\left(\frac{\sqrt{k}}{\beta_0^*\omega l_w}, \frac{500\mu}{l_w^2\omega}\right), \frac{4\rho\sigma_{\omega_2}k}{CD_{k\omega}l_w^2}\right]\right\}^4\right) \tag{4.24}$$

where l_w is the distance to the closest wall and $CD_{k\omega}$ is defined as:

$$CD_{k\omega} = \max\left(\frac{2\rho\sigma_{\omega_2}}{\omega}\nabla\omega\cdot\nabla k, 10^{-10}\right) \tag{4.25}$$

Turbulent viscosity is defined by Equation (4.26):

$$\mu_t = \rho \frac{\rho \alpha_1 k}{\max(\alpha_1 \omega, SF_2)} \tag{4.26}$$

A second blending function, F_2, is defined as:

$$F_2 = \tanh\left(\left[\max\left\{\frac{2\sqrt{k}}{\beta_0^* \omega l_w}, \frac{500\mu}{\rho l_w^2 \omega}\right\}\right]^2\right) \tag{4.27}$$

A production limiter is used in the SST model, using the production term, P_k, defined by Equation (4.16):

$$\tilde{P}_k = \min(P_k, 10\rho\beta_0^* k\omega) \tag{4.28}$$

The remaining terms in the equations are model constants, defined as:

$$\alpha_1 = \frac{5}{9},\ \alpha_2 = 0.44,\ \beta_1 = \frac{3}{40},\ \beta_2 = 0.0828,$$
$$\beta_0^* = \frac{9}{100},\ \sigma_{k1} = 0.85,\ \sigma_{k2} = 1,\ \sigma_{\omega 1} = 0.5,\ \sigma_{\omega 2} = 0.856 \tag{4.29}$$

4.7.4 Law of the Wall

In pipe flow, or flows where a boundary is considered as a solid wall, at higher Reynolds numbers, inertial forces dominate over viscous forces. However, the fluid in contact with the solid wall is stationary and close to the wall behaviour of the flow changes from turbulent to laminar. In the region adjacent to the wall, Reynolds number tends to zero and is of the order of 1, meaning that viscous forces will either be equal to or greater than inertial forces [13]. Therefore, in flows along solid boundaries, inertial forces dominate in the bulk of the flow at a distance far from the wall, whilst a thin layer exists where viscous effects are significant [13]. The mean fluid velocity is a function of the distance from the wall, the fluid density, fluid viscosity and wall shear stress [13]. The law of the wall is defined as [13]:

$$u^+ = \frac{U}{u_\tau} = f\left(\frac{\rho u_\tau y}{\mu}\right) = f(y^+) \tag{4.30}$$

where u^+ is the dimensionless velocity, u_τ is the friction velocity, defined by Equation (4.31), y is the distance from the wall and y^+ is the dimensionless wall distance, defined by Equation (4.32).

$$u_\tau = \sqrt{\frac{\tau_w}{\rho}} \tag{4.31}$$

$$y^+ = \frac{\rho u_\tau y}{\mu} = \frac{y}{\mu}\sqrt{\rho \tau_w} \tag{4.32}$$

The viscous sub-layer region has a thickness, defined using the dimensionless parameter, y^+, of $y^+ < 5$. In this region, turbulent eddy motions stop and viscous forces dominate, so it assumed that the shear stress in the layer is constant and equal to the wall shear stress throughout the layer. In this region, the relationship between velocity and distance from the wall is linear, so the dimensionless velocity is equal to the dimensionless wall distance [13]:

$$u^+ = y^+ \tag{4.33}$$

Further from the wall, in the region from $30 < y^+ < 500$, both viscous and turbulent effects are significant. This region, known as the log-law layer, has the following relationship between velocity and distance from the wall:

$$u^+ = \frac{1}{\kappa}\ln(Ey^+) \tag{4.34}$$

where κ and E are empirical constants of 0.4 and 9.8 for smooth walls. Outside of these two regions, further from the wall, inertial effects dominate [13]. The relationship between u^+ and y^+ is demonstrated in Figure 4.13 [13].

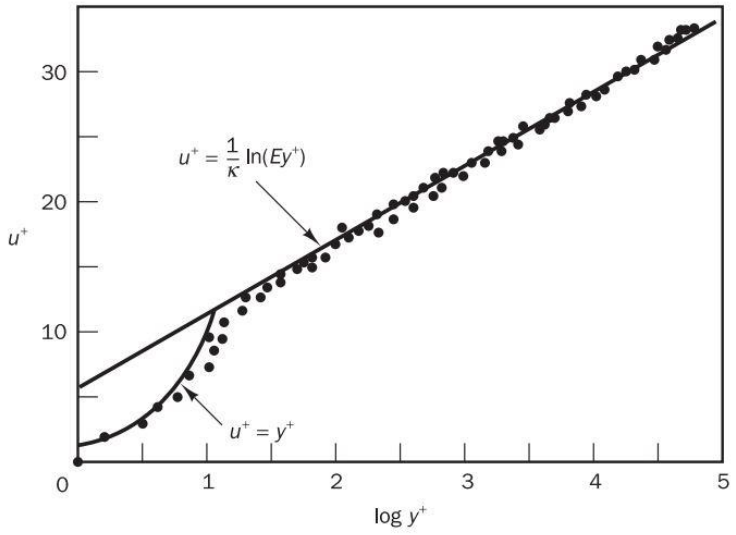

Figure 4.13 Different regions near to the wall showing the viscous sub-layer and the log-law layer [13]

4.7.5 Relevance of Turbulence to SIJ and Pipe Flow

Fluid flows above a critical Reynolds number are turbulent, explained previously [100]. The SIJ and elbow geometries used in this thesis were in the turbulent flow regime. Reynolds numbers in both geometries were of the order of 10^5 to 10^6. Therefore, the use of turbulence models was essential for the prediction of fluid flow in the relevant geometries used in this thesis. Several

different turbulence models exist that can be used to predict fluid flow, with some models showing better accuracy in some conditions than other models [13]. The most appropriate turbulence model for the prediction is discussed in the relevant chapters for the particular geometry being modelled. For fluid flows requiring high levels of accuracy, such as the for the prediction of mass transfer coefficients, turbulence models that use wall functions are not appropriate [209]. Therefore, an SST model was used for the prediction of fluid flow when mass transfer coefficients were required to be determined.

Chapter 5
Case Study of Erosion-Corrosion of X65 Carbon Steel and Chemical Inhibitor Evaluation in Oil & Gas CO_2 Environments

The presence of sand particles in corrosive environments has been shown to result in high rates of degradation of carbon steel [34, 35, 149, 159]. This chapter presents an analysis of erosion-corrosion of carbon steel in conditions representative of pipeline conditions, with the focus on two Shell fields in the North Sea, where sand production has been observed and highlighted as a significant issue. A range of erosion-corrosion tests were completed at different flow velocities and sand concentrations, representative of the two fields to understand the significance of sand on the performance of carbon steel in blank conditions (without inhibitor) and inhibited conditions.

5.1 Introduction

Erosion-corrosion of carbon steel is a significant issue. Whilst several issues and areas requiring further research have been highlighted in the review of erosion-corrosion literature, erosion-corrosion analysis in field relevant conditions was completed to highlight the issues which were most relevant to the industrial problem and to determine which issues required further research. An SIJ was used for a range of flow-induced corrosion, erosion and erosion-corrosion tests to determine the individual contribution of corrosion and erosion components to total erosion-corrosion material loss of X65 carbon steel.

Whilst the main focus of this thesis was erosion-corrosion, an understanding of flow-induced corrosion and pure erosion was required to determine the contribution of each to total erosion-corrosion degradation. Flow has been shown to accelerate CO_2 corrosion of carbon steel, and reduce the effectiveness of chemical inhibitor films [28-30, 183]. The efficiency of corrosion inhibitors can also be effected by the presence of sand particles in the flow, due to various interactions of the sand particles with inhibitors and inhibitor films [6, 35, 62]. An analysis of two field corrosion inhibitors in erosion-corrosion and flow-induced corrosion conditions was completed to assess how flow and sand particles influenced inhibitor performance. The objectives of this Chapter were to:

- Evaluate how flow and sand influence the corrosion rate of X65 carbon steel in field conditions;

- Compare the performance of two chemical inhibitors in flow-induced corrosion and erosion-corrosion conditions to understand how flow and sand affect the inhibitor efficiency;
- Identify areas of erosion-corrosion research requiring further investigation from the conclusions of the erosion-corrosion case study.

5.2 Static Corrosion Rates

To fully understand how significant the effects of flow were on the blank corrosion rate and the efficiency of corrosion inhibitors, static tests were completed initially as a comparison, using X65 carbon steel samples. Static tests were completed in a CO_2-saturated, 2% NaCl, 60°C, pH 4.7, 1 L volume tap water solution to replicate the same solution chemistry that was used in SIJ tests, shown later in this chapter. Blank tests and tests with the addition of 250 ppm of inhibitor A and inhibitor B were completed, shown in Figure 5.1. The blank static corrosion rate remained relatively constant throughout the test, similar to the blank flow-induced corrosion tests completed, giving an average corrosion rate of approximately 4.32 ± 0.25 mm/yr.

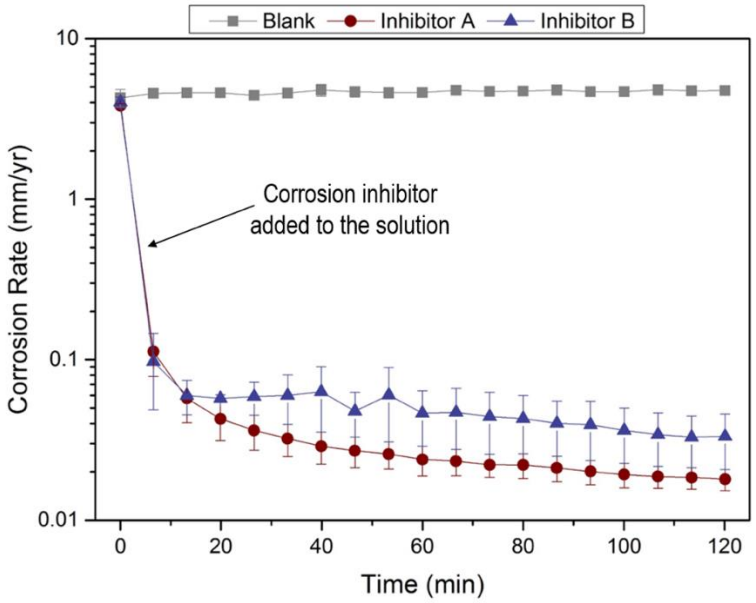

Figure 5.1 Static corrosion rates of X65 carbon steel in blank conditions polished to a surface roughness of 0.15 µm ± 0.02 µm and after 250 ppm of Inhibitor A and Inhibitor B was added to a 2% NaCl, 60°C, pH 4.7, CO_2-saturated, 1 L solution in static cell tests

Both of the chemical inhibitors significantly reduced the corrosion rate of X65 in static conditions. Initial corrosion rates in inhibited conditions was representative of conditions in blank tests, which were shown to be constant

throughout the duration of the test. The corrosion rates were reduced to less than 0.1 mm/yr in the presence of both inhibitors, approximately 15 minutes after starting the test. The test duration was shorter than the flow-induced corrosion SIJ tests because a low corrosion rate was achieved so quickly and a constant corrosion rate was achieved in blank conditions, with both inhibitors showing very good performance in static conditions. Inhibitor A was slightly more effective than inhibitor B. However, both inhibitors reduced the corrosion rates to less than 0.1 mm/yr very quickly.

5.3 Flow-Induced Corrosion of X65 and Inhibitor Evaluation

Flow-induced corrosion tests were completed in the SIJ, in conditions explained in detail in Chapter 4. Flow-induced corrosion tests were completed at three different flow velocities of 10, 15 and 20 m/s in a 2% NaCl, 60°C solution saturated with CO_2. Tests were completed in blank conditions and with the addition of 250 ppm of inhibitor A and inhibitor B.

5.3.1 Flow-Induced Corrosion of X65 in Blank Conditions

The effects of flow velocity were investigated on the corrosion rate of X65 carbon steel using the SIJ. Corrosion rates were determined from electrochemistry measurements using the three electrode cell setup and methodology explained in Chapter 4. Electrochemistry measured corrosion rates were compared with mass loss measurements in the same conditions. This section explains how the electrochemistry measured corrosion rates were obtained and used to evaluate the effects of flow on corrosion rates of carbon steel. EIS was used to measure polarisation resistance, solution resistance and charge transfer resistance and Tafel plots were used to correct the Stern-Geary coefficient used in the calculation of X65 corrosion rates. This chapter explains how the electrochemistry data was used to calculate corrosion rates. The X65 in-situ corrosion rates, measured from EIS measurements and adjusted using Tafel constants, in flow-induced corrosion conditions at different flow velocities over the 240-minute test period are shown in Figure 5.2. A constant corrosion rate was achieved approximately 20 - 30 minutes after starting the test. For the first two measurements, a settling period was typically experienced in the SIJ, where temperature and pH reached a consistency throughout the solution. This was achieved

relatively quickly after starting the test, and a constant corrosion rate was achieved from this point onwards.

Flow-induced corrosion rates were higher than the corrosion rates in static conditions, with the flow accelerating corrosion rates by increasing the transport of electrochemically active species to and from the X65 carbon steel surfaces, explaining why corrosion rates increased as flow velocity increased in Figure 5.2 [3]. H^+ ions present in the solution are transported to the surface at a much higher rate in flow-induced corrosion conditions compared to static conditions, influencing the cathodic reaction.

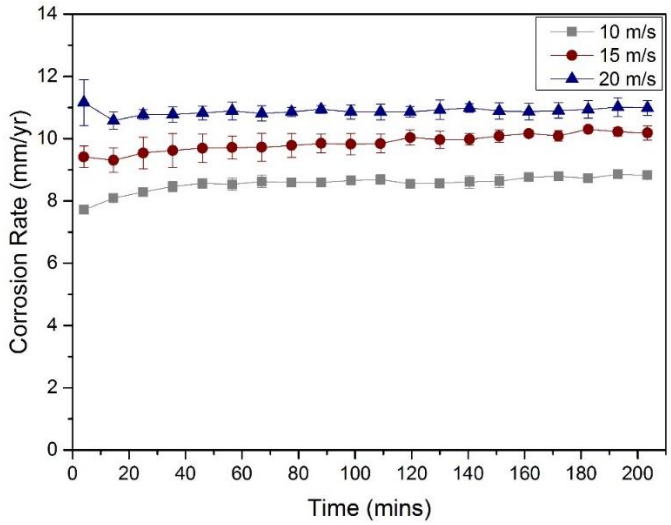

Figure 5.2 Corrosion rate of X65 measured using EIS during 240-minute blank flow-induced corrosion SIJ tests in a 2% NaCl, 60°C, pH 4.7, CO_2-saturated solution at flow velocities of 10 m/s, 15 m/s and 20 m/s

AC impedance measurements were used to determine the corrosion rates in Figure 5.2 and for the remainder of corrosion rates measured in this chapter. The Nyquist and Bode plots for each of the three flow velocities are shown in Figure 5.3, for the purpose of demonstrating how the values of solution resistance, polarisation resistance and charge transfer resistance were found in order to calculate the corrosion rate. The same method was used for all tests, including inhibitor tests. The solution resistance was approximately the same for each of the three flow velocities as redox electrodes and working electrodes were located in the same positions and the conductivity of the solution was the same for each of the three tests. The radius of the semi-circle decreased as the flow velocity increased, showing a decrease in R_{ct} and therefore an increase in corrosion rate of the X65 sample. Conditions were expected to remain constant during EIS measurements, as corrosion rates did not change during tests, conditions in the SIJ were fixed and maintained and sample surface area did not change in uniform corrosion conditions.

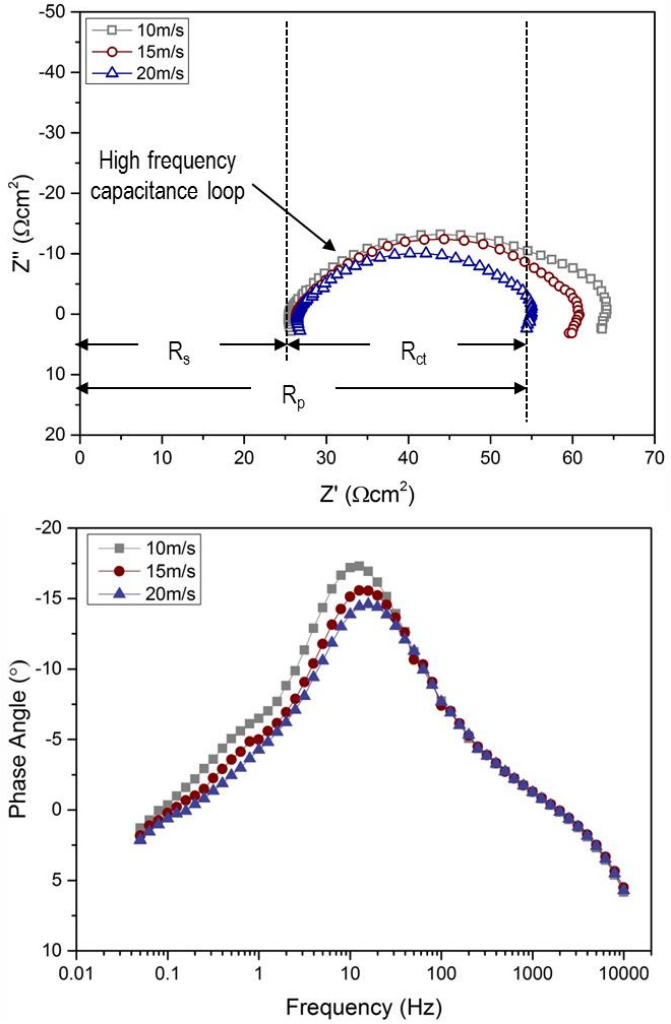

Figure 5.3 Nyquist and Bode plots for blank flow-induced corrosion SIJ tests in a 2% NaCl, 60°C, pH 4.7, CO_2-saturated solution at flow velocities of 10 m/s, 15 m/s and 20 m/s

A high frequency capacitive loop was observed in Figure 5.3, with no inductive loop, represented by the equivalent circuit shown in Figure 5.4. R_s is represented by a resistor in series to the circuit, with a constant phase element (CPE), representing the EDL and a resistor, representing R_{ct}, in parallel. A constant phase element was used rather than an ideal capacitor, due to the imperfect nature of the results as the Nyquist plots showed depressed semi-circles and a centre under the real axis, typically as a result of surface inhomogeneity and roughness [210]. Each of the three flow-induced corrosion tests at different flow velocities were represented by the same components in the equivalent circuit, with different values of parameters in the circuit, shown in Table 5.1. Equivalent circuits were fitted from the Nyquist plot data using Zview software. Percentage errors between the equivalent circuit and the plotted EIS data were within 5%. Constant phase element impedance, Z_{CPE}, was calculated using Equation (5.1) [210]:

$$Z_{CPE} = \frac{1}{Q_o(j \cdot 2\pi f)^{n_{CPE}}} \quad (5.1)$$

where Q_o is a constant phase element proportional factor with the units $s^n/(\Omega \cdot cm^2)$, j is $\sqrt{-1}$, f is the frequency and n_{CPE} is an empirical factor which varies between 0 and 1 which measures the deviation of the constant phase element from the behaviour of an ideal capacitor [210].

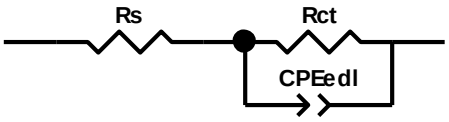

Figure 5.4 Equivalent circuit representing blank flow-induced corrosion SIJ tests in a 2% NaCl, 60°C, pH 4.7, CO_2-saturated solution at flow velocities of 10 m/s, 15 m/s and 20 m/s where $\boldsymbol{R_s}$ is the solution resistance, $\boldsymbol{R_{ct}}$ is the charge transfer resistance and CPE_{edl} represents the EDL constant phase element

Table 5.1 Parameters of the equivalent circuit for blank flow-induced corrosion SIJ tests in a 2% NaCl, 60°C, pH 4.7, CO_2-saturated solution at flow velocities of 10 m/s, 15 m/s and 20 m/s

U (m/s)	R_s ($\Omega \cdot cm^2$)	R_{ct} ($\Omega \cdot cm^2$)	Q_o ($s^n/\Omega \cdot cm^2$)	n_{CPE}
10	25.9 ± 0.12	36.7 ± 0.39	1585 ± 78	0.76 ± 0.01
15	26.3 ± 0.12	31.1 ± 0.32	1350 ± 73	0.79 ± 0.01
20	26.7 ± 0.13	28.0 ± 0.31	1240 ± 76	0.80 ± 0.01

EIS-measured corrosion rates were then calculated by determining the Tafel constants at each of the three flow velocities. The method used for determining the Tafel constants at a flow velocity of 20 m/s is demonstrated in Figure 5.5, measured by polarising the sample ±250 mV relative to OCP. Anodic and cathodic Tafel constants were determined by measuring the gradient of the slopes at ±50 mV relative to OCP, shown where a linear relationship was observed on the Tafel plots. This method was used to determine Tafel constants throughout this chapter.

The requirement that one or both of the Tafel branches should be in activation control, the ideal conditions for using Tafel plots for determining Tafel constants, are not observed in Figure 5.5 [201]. However, linear charge transfer controlled behaviour is observed at ±50 mV relative to OCP, the regions used for determining Tafel constants [24]. The use of these Tafel constants enabled corrosion rates to be calculated which showed good agreement with mass loss, shown later in this chapter.

The measured anodic, β_a, and cathodic, β_c, Tafel constants for each of the flow velocities are shown in Figure 5.6 and were relatively similar for each flow velocity. In the Tafel plots shown in Figure 5.5 and Figure 5.6, the anodic branch shows the anodic reaction of iron dissolution, Equation (3.7). The cathodic reactions, at pH 4.7 in the potential range scanned, consisted of both hydrogen evolution, Equation (3.5), and direct reduction of carbonic acid, Equation (3.6).

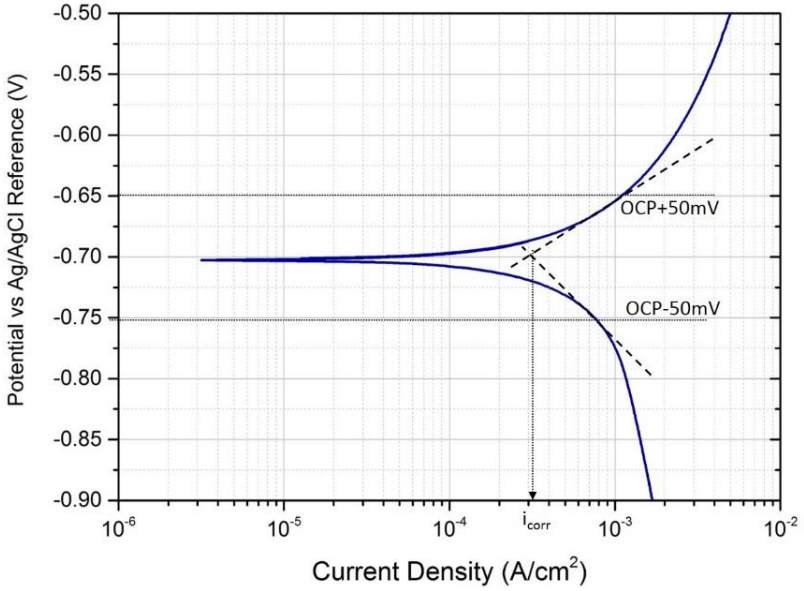

Figure 5.5 Tafel plot for blank flow-induced corrosion SIJ tests in a 2% NaCl, 60°C, pH 4.7, CO_2-saturated solution at a flow velocity of 20 m/s, demonstrating linear region on plots for measurement of Tafel constants

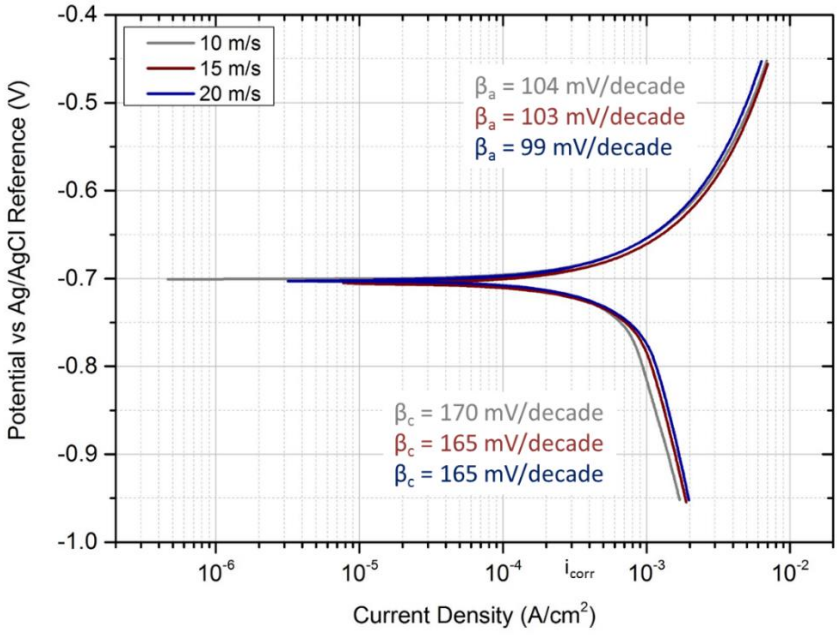

Figure 5.6 Tafel plots for blank flow-induced corrosion SIJ tests in a 2% NaCl, 60°C, pH 4.7, CO_2-saturated solution at flow velocities of 10 m/s, 15 m/s and 20 m/s

Tafel measurements were completed in separate tests at different time periods to investigate if Tafel constants changed during the test. The corrosion rates determined in Figure 5.2 were calculated assuming constant values for Tafel constants, but all Tafel plots were produced from data measured at the end of the 240-minute test period. Cathodic polarisation was completed approximately 210 minutes after the start of the test, with the anodic polarisation completed approximately 15 minutes after the cathodic sweep started. To investigate if the Tafel constants changed during the test, Tafel plots were produced after 30-minute, 90-minute and 150-minute tests and compared with the original Tafel plots measured after 210 minutes in a flow-induced corrosion test at a flow velocity of 20 m/s. The time period refers to the time at which the cathodic sweep measurements were started. The total time required to complete the full range of cathodic and anodic polarisation was approximately 30 minutes. The Tafel plots are shown in Figure 5.7. The anodic and cathodic Tafel constants are shown on the plot and did not change significantly during the test. Therefore, it was reasonable to assume that corrosion rates stayed relatively constant during the test and could be averaged during the 240-minute test period.

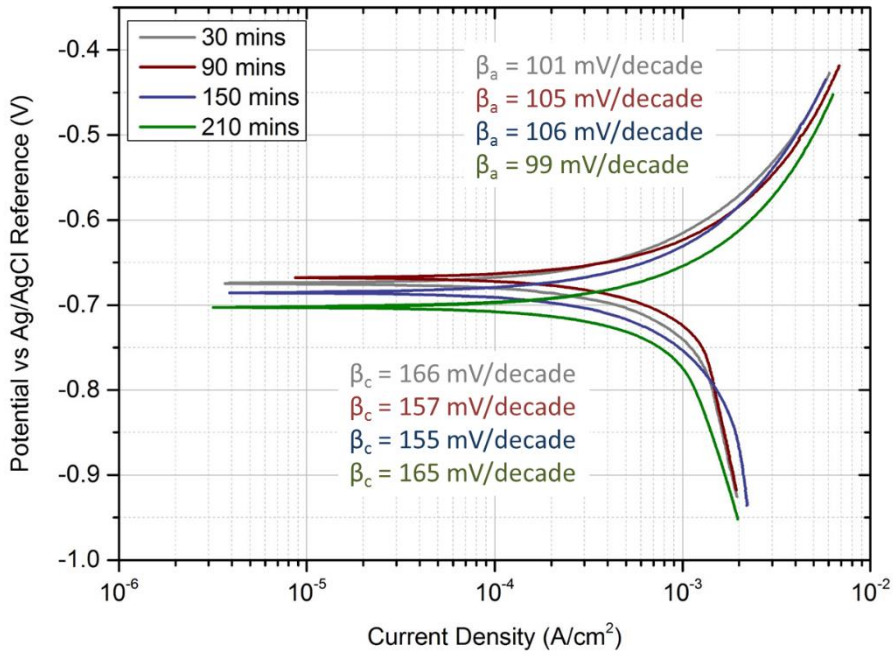

Figure 5.7 Tafel plots during a 240-minute test period for blank flow-induced corrosion SIJ tests in a 2% NaCl, 60°C, pH 4.7, CO_2-saturated solution at a flow velocity of 20 m/s

Mass loss tests were completed to validate the EIS determined corrosion rates, with the results shown in Table 5.2. The comparison of corrosion rates obtained through both methods is shown in Figure 5.8. Electrochemistry corrosion rates were determined by averaging the corrosion rates measured

over the 240-minute test period in Figure 5.2. The mass loss results showed similar corrosion rates to the corrosion rates measured using electrochemistry.

Table 5.2 Mass loss of X65 carbon steel during a 240-minute test period for blank flow-induced corrosion SIJ tests in a 2% NaCl, 60°C, pH 4.7, CO_2-saturated solution at flow velocities of 10 m/s, 15 m/s and 20 m/s

U (m/s)	Δm (mg)
10	14.6 ± 2.35
15	16.8 ± 0.50
20	20.7 ± 1.53

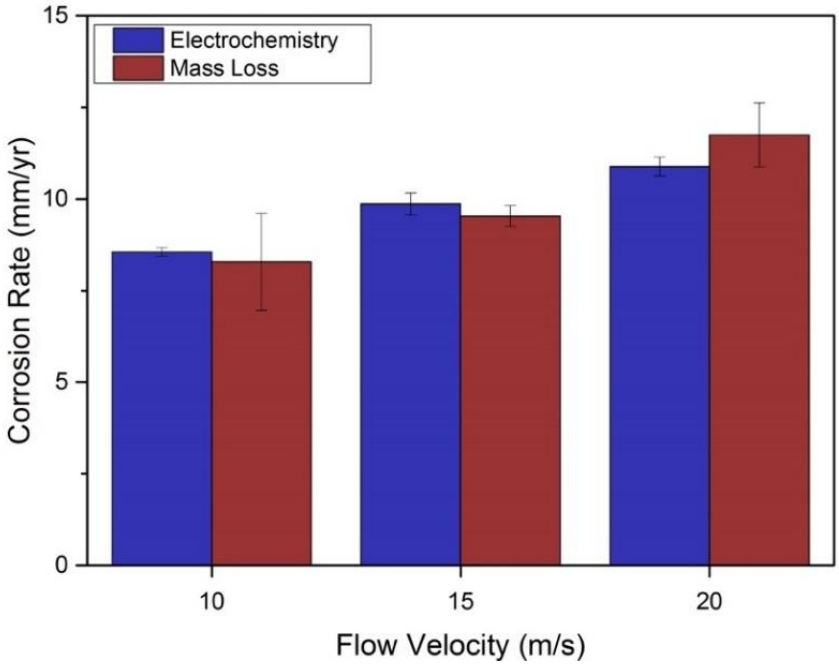

Figure 5.8 Comparison of corrosion rates determined by mass loss and electrochemistry in flow-induced corrosion SIJ tests in a 2% NaCl, 60°C, pH 4.7, CO_2-saturated solution at flow velocities of 10 m/s, 15 m/s and 20 m/s

5.3.2 Evaluation of Corrosion Inhibitor A

Typically, a corrosion rate of 0.1 mm/yr is targeted in the oil and gas industry as an acceptable rate of corrosion in the field after a corrosion inhibitor has been used to protect the carbon steel surface. It was clear from the blank flow-induced corrosion tests that the corrosion rate of carbon steel in these conditions was significantly higher than the industry desired value, so the use of a corrosion inhibitor was essential to protect the X65 surface. Both inhibitors

A and B reduced the corrosion rate of X65 to less than 0.1 mm/yr in static conditions almost immediately after being added to the solution.

In flow-induced corrosion inhibitor tests, inhibitor A was added to the SIJ reservoir in the same test conditions as blank flow-induced corrosion tests. The change in corrosion rate at a flow velocity of 10 m/s, 15 m/s and 20 m/s over a 240-minute test after 250 ppm of inhibitor A was added to the SIJ reservoir is shown in Figure 5.9. An initial measurement was completed in blank conditions, before 250 ppm of inhibitor A was added, approximately 15 minutes after the start of the test. The initial corrosion rate showed similar results at all flow velocities to the corrosion rates measured in blank conditions, shown in Figure 5.2. A rapid decrease in the corrosion rate was observed after the inhibitor was added. After this initial rapid decrease a gradual decrease in corrosion rate was observed until the end of the test. The test was only completed for 240 minutes to give a representative comparison with blank tests and erosion-corrosion tests later in the chapter. Corrosion rates were slightly lower for 10 m/s than 20 m/s as was the case in blank conditions. Corrosion rates remained above the desired 0.1 mm/yr targeted rate but tests were stopped after 240 minutes and it did appear that corrosion rates were continuing to decrease.

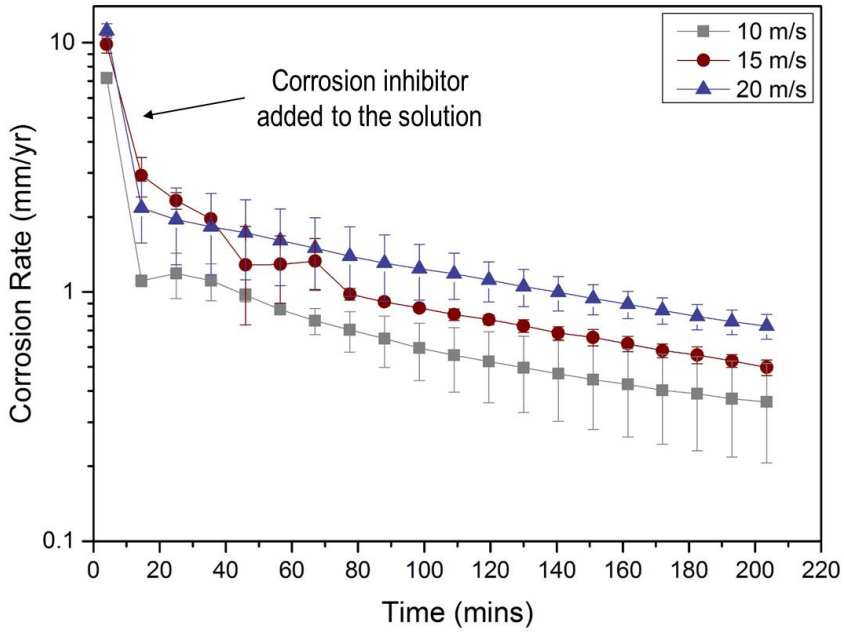

Figure 5.9 Measurement of X65 corrosion rate after 250 ppm of inhibitor A added in flow-induced corrosion SIJ tests in a 2% NaCl, 60°C, pH 4.7, CO_2-saturated solution at flow velocities of 10 m/s, 15 m/s and 20 m/s

The change in R_{ct} after inhibitor A was added to the solution until the end of the test at a flow velocity of 20 m/s is shown in the Nyquist and Bode plots in Figure 5.10. R_{ct} increased throughout the test as the inhibitor adsorbed to the

X65 sample and reduced the corrosion rate. Equivalent circuits were again fitted from the Nyquist plots in Figure 5.10, using the same equivalent circuit components as Figure 5.4. A high frequency capacitive loop was observed, with no low frequency inductive loop. Two capacitive loops are often observed when inhibitors or coatings are present on surfaces, with the protective layer acting as a second capacitor [24]. Only one capacitive loop was observed for inhibitor A. The value of the components in the equivalent circuit during the 20 m/s test after 250 ppm of inhibitor A was added are shown in Table 5.3. Similar behaviour was also seen at flow velocities of 10 m/s and 15 m/s.

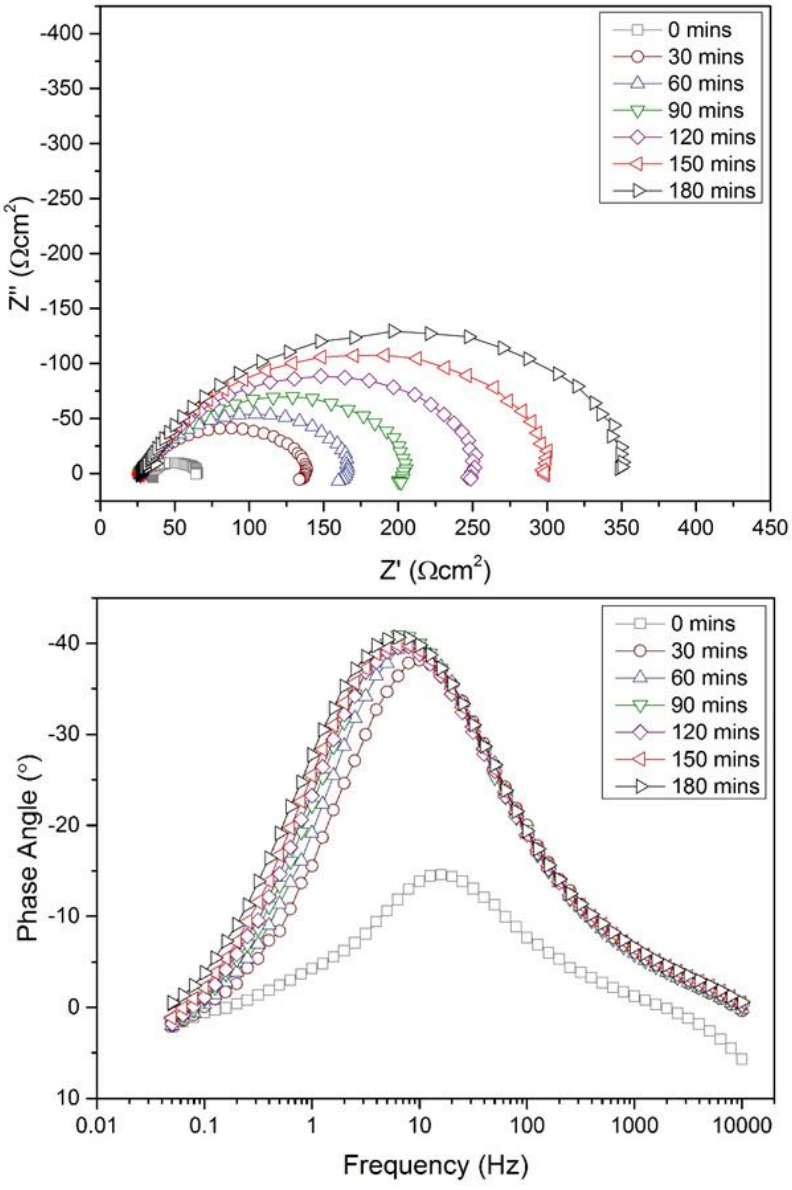

Figure 5.10 Nyquist and Bode plots from AC impedance measurements after 250 ppm of inhibitor A was added to flow-induced corrosion SIJ tests in a 2% NaCl, 60°C, pH 4.7, CO_2-saturated solution at a flow velocity of 20 m/s

Table 5.3 Parameters of the equivalent circuit after 250 ppm of inhibitor A was added to flow-induced corrosion SIJ tests in a 2% NaCl, 60°C, pH 4.7, CO_2-saturated solution at a flow velocity of 20 m/s

t (mins)	R_s (Ω·cm^2)	R_{ct} (Ω·cm^2)	Q_o (s^n/Ω·cm^2)	n_{CPE}
30	33.1 ± 0.24	244.3 ± 2.35	400.0 ± 12.2	0.78 ± 0.01
60	33.3 ± 0.26	283.7 ± 3.03	422.2 ± 12.8	0.78 ± 0.01
90	33.4 ± 0.27	315.2 ± 3.66	451.0 ± 13.6	0.77 ± 0.01
120	33.8 ± 0.28	334.5 ± 3.96	490.8 ± 14.4	0.75 ± 0.01
150	34.1 ± 0.27	380.0 ± 4.41	505.4 ± 13.4	0.74 ± 0.01
180	34.2 ± 0.24	434.8 ± 4.65	522.4 ± 11.7	0.73 ± 0.01

Corrosion rates were again determined using the measured values of R_{ct} and using the Tafel constants determined from the plots in Figure 5.11. Cathodic Tafel branches showed a diffusion-controlled reaction, resulting in much higher cathodic Tafel constants. Inhibitor A showed mixed control by influencing both the anodic and cathodic reactions.

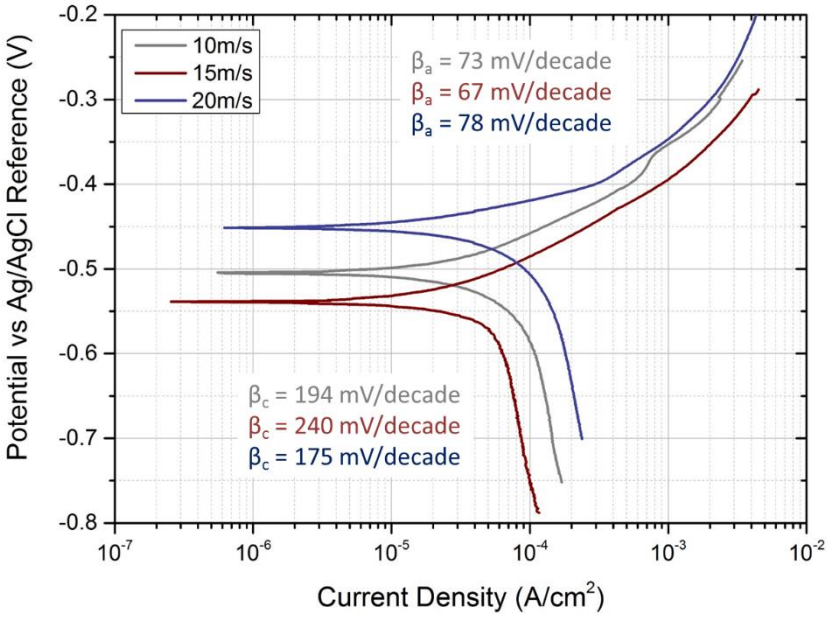

Figure 5.11 Tafel plots for X65 after 250 ppm of inhibitor A was added to flow-induced corrosion SIJ tests in a 2% NaCl, 60°C, pH 4.7, CO_2-saturated solution at flow velocities of 10 m/s, 15 m/s and 20 m/s

Variation of the OCP throughout the test was compared for each flow velocity after 250 ppm of inhibitor A was added in Figure 5.12. A rapid increase in OCP was seen after the inhibitor was added to the solution before reaching a relatively constant value that stayed constant through the 240-minute test duration.

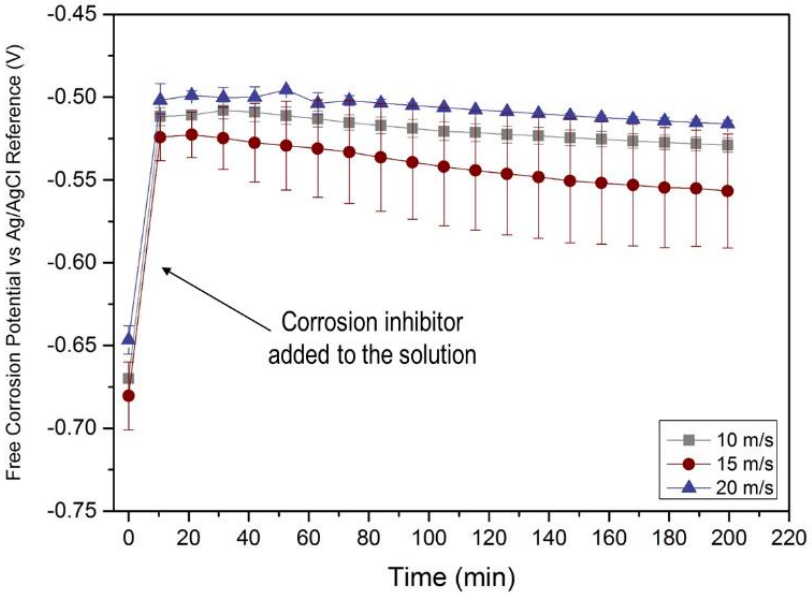

Figure 5.12 Measurement of OCP after 250 ppm of inhibitor A was added to flow-induced corrosion SIJ tests in a 2% NaCl, 60°C, pH 4.7, CO_2-saturated solution at flow velocities of 10 m/s, 15 m/s and 20 m/s

5.3.3 Evaluation of Corrosion Inhibitor B

Inhibitor B was added to the reservoir in the same test conditions as the blank tests and inhibitor A tests to give a direct comparison between the inhibitors. Similarly to inhibitor A, the corrosion rate decreased significantly when 250 ppm of inhibitor B was added, shown in Figure 5.13.

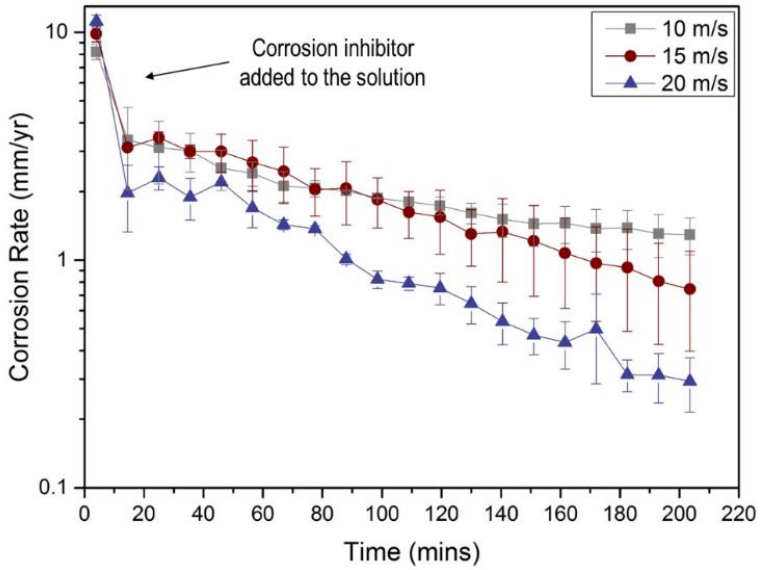

Figure 5.13 Measurement of X65 corrosion rate over time after 250 ppm of inhibitor B was added to flow-induced corrosion SIJ tests in a 2% NaCl, 60°C, pH 4.7, CO_2-saturated solution at flow velocities of 10 m/s, 15 m/s and 20 m/s

After this initial decrease a gradual decrease in corrosion rate was observed until the end of the test. Contrary to tests completed using inhibitor A, the lowest corrosion rate was observed at a flow velocity of 20 m/s after inhibitor B was added, whilst the highest corrosion rate was measured at 10 m/s, suggesting that flow potentially had more significance on the performance of inhibitor B by influencing the transport of the chemical inhibitor to the surface.

The Nyquist and Bode plots for flow-induced corrosion tests at a flow velocity of 20 m/s after 250 ppm of inhibitor B was added are shown in Figure 5.14. The Nyquist plots showed similarities to inhibitor A but the general shape of the plots varied slightly due to the much larger diameter of the semi-circles, showing higher values of R_{ct}. Equivalent circuits were again fitted to the inhibitor B data, showing the same behaviour as blank conditions and inhibitor A tests. Therefore the equivalent circuit that was used was the same circuit as in Figure 5.4, with the parameters in the circuit compared during the 20 m/s test in Table 5.4.

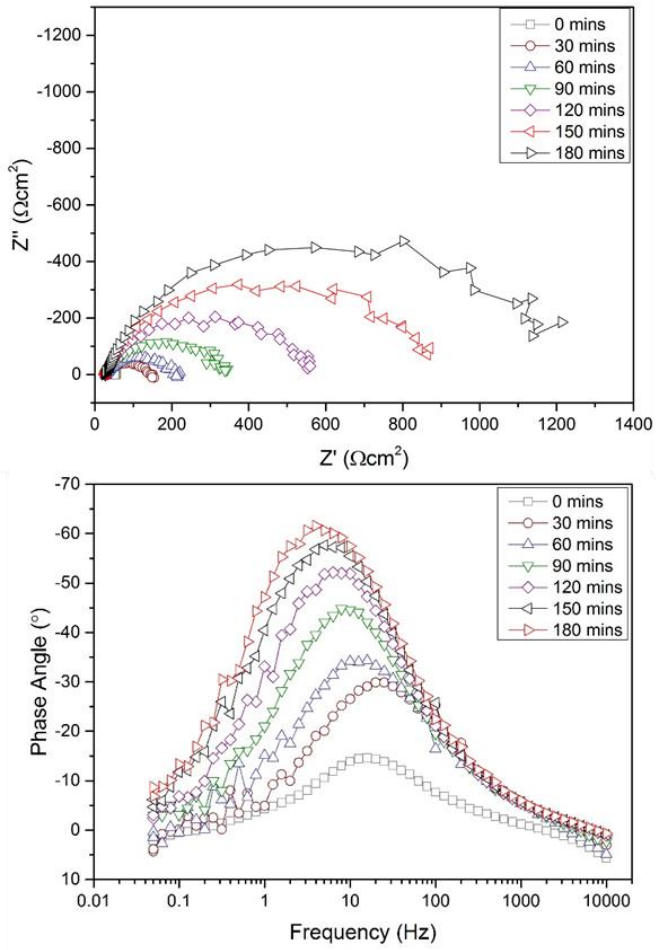

Figure 5.14 Nyquist and Bode plots from AC impedance measurements after 250 ppm of inhibitor B was added to flow-induced corrosion SIJ tests in a 2% NaCl, 60°C, pH 4.7, CO_2-saturated solution at a flow velocity of 20 m/s

Table 5.4 Parameters of the equivalent circuit after 250 ppm of inhibitor B was added to flow-induced corrosion SIJ tests in a 2% NaCl, 60°C, pH 4.7, CO_2-saturated solution at a flow velocity of 20 m/s

t (mins)	R_s (Ω·cm^2)	R_{ct} (Ω·cm^2)	Q_o (s^n/Ω·cm^2)	n_{CPE}
30	27.8 ± 0.21	117.6 ± 1.11	447.4 ± 18.8	0.76 ± 0.01
60	28.5 ± 0.25	183.5 ± 2.10	528.0 ± 20.2	0.74 ± 0.01
90	27.8 ± 0.16	316.3 ± 2.52	435.5 ± 9.00	0.79 ± 0.01
120	27.2 ± 0.16	536.2 ± 4.41	380.8 ± 6.38	0.82 ± 0.01
150	26.8 ± 0.15	857.1 ± 7.36	349.5 ± 4.85	0.82 ± 0.01
180	26.8 ± 0.19	1203 ± 13.0	311.4 ± 4.74	0.84 ± 0.01

The Tafel constants were determined from the anodic and cathodic branches of the Tafel plots measured for the inhibitor B tests, shown in Figure 5.15. Cathodic Tafel constants were lower for inhibitor B tests than inhibitor A, and were similar to blank Tafel constants. Desorption of inhibitor film from the surface was observed at high anodic potentials approximately +100 mV relative to OCP, which was not observed on the Tafel plot for inhibitor A. Inhibitor B showed mixed control by influencing both the anodic and cathodic reactions.

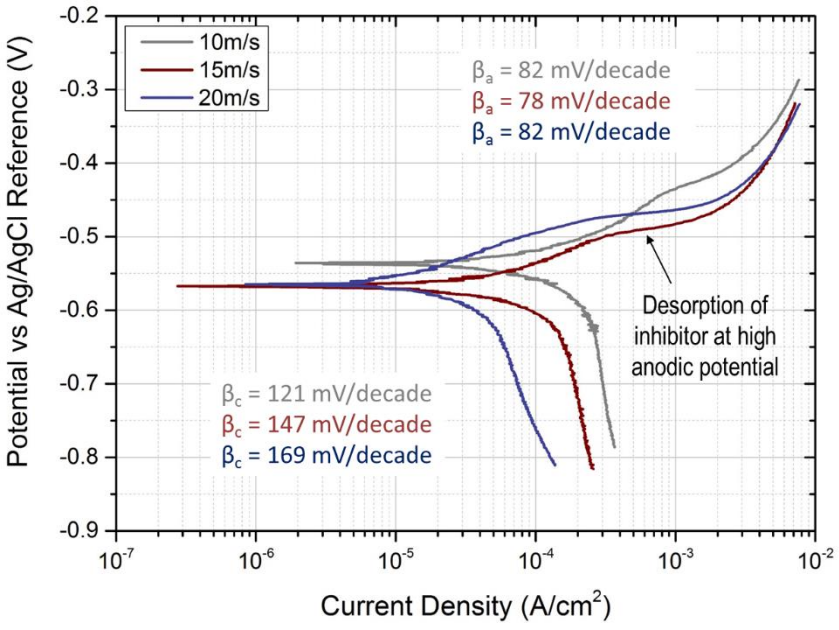

Figure 5.15 Tafel plots for X65 after 250 ppm of inhibitor B was added to flow-induced corrosion SIJ tests in a 2% NaCl, 60°C, pH 4.7, CO_2-saturated solution at flow velocities of 10 m/s, 15 m/s and 20 m/s

Similarly to inhibitor A, the OCP increased significantly when 250ppm of inhibitor B was added to the solution, as shown in Figure 5.16. OCP remained

relatively stable after the initial peak but did become more negative during the test after reaching the maximum value.

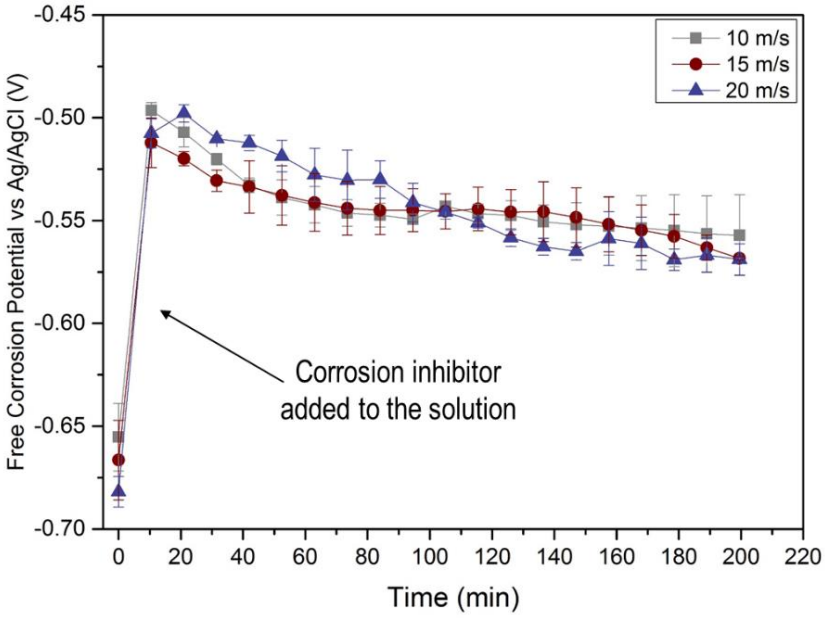

Figure 5.16 Measurement of OCP after 250 ppm of inhibitor B was added to flow-induced corrosion SIJ tests in a 2% NaCl, 60°C, pH 4.7, CO_2-saturated solution at flow velocities of 10 m/s, 15 m/s and 20 m/s

5.3.4 Flow-Induced Corrosion Efficiency of Inhibitors

Inhibitor efficiency, calculated using Equation (5.2), was used to compare inhibitor performance over a range of conditions.

$$Inhibitor\ Efficiency = \frac{CR_{blank} - CR_{inhib}}{CR_{blank}} \tag{5.2}$$

where CR_{blank} is the corrosion rate of X65 in blank conditions, CR_{inhib} is the corrosion rate of X65 after inhibitor was added. The efficiencies of the inhibitors in static and flow-induced corrosion conditions are compared in Figure 5.17. The final corrosion rate at the end of the 240-minute test was used as the inhibited corrosion rate in the efficiency calculation. In static conditions both inhibitors were very efficient. However, the efficiency of both inhibitors was reduced in flow-induced corrosion conditions. Inhibitor A was not significantly affected by the increase in flow velocity from 10 m/s to 15 m/s and 20 m/s.

The effect of flow was more significant on inhibitor B, with the inhibitor being 12% more efficient at 20 m/s than at 10 m/s. A significant amount of variation was observed for inhibitor B tests at 10 m/s and 15 m/s, with error accounting for a much more significant effect on results than at 20 m/s. Hydrodynamic

conditions across the surface of the sample in the SIJ can vary significantly, with a stagnation region in the centre of the sample and highly turbulent regions as the flow spreads from the centre of the nozzle [211]. This could have effected inhibitor efficiency by influencing how inhibitor is transported to the surface and influencing removal of inhibitor film from the surface. Gulbrandsen and Grana [51] showed that shear stress was higher in the turbulent jet region of an SIJ, but that this did not cause any mechanical removal of the inhibitor film in this region compared to the stagnation region.

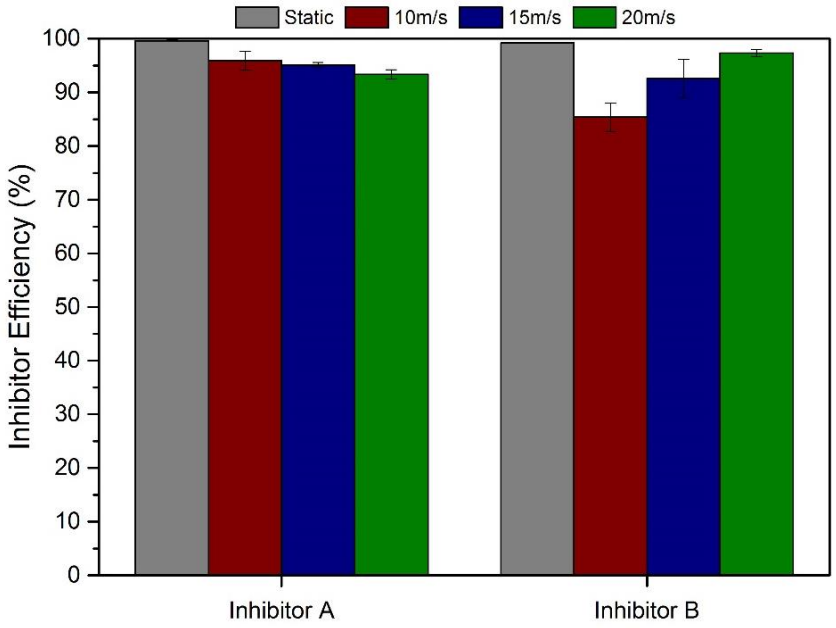

Figure 5.17 Efficiency of inhibitor A and inhibitor B at the end of tests after 250 ppm of inhibitor was added in static cell tests in a 2% NaCl, 60°C, pH 4.7, CO_2-saturated, 1 L solution and flow-induced corrosion SIJ tests in a 2% NaCl, 60°C, pH 4.7, CO_2-saturated solution at flow velocities of 10 m/s, 15 m/s and 20 m/s

The inhibitor efficiency was also calculated from the first measurement after the initial addition of corrosion inhibitor to the solution in static tests and flow-induced corrosion SIJ tests, shown in Figure 5.18. The corrosion inhibitor was added after the first measurement was completed and OCP was allowed to stabilise for a period of 4 minutes before the next measurement of corrosion rate was completed. The efficiency of both inhibitors in static conditions was high after they were initially added to the solution, with efficiencies exceeding 95%. The corrosion inhibitors were much less efficient at the start of the test than at the end of the test, showing the length of time required for the inhibitor to adsorb to and protect the surface sufficiently.

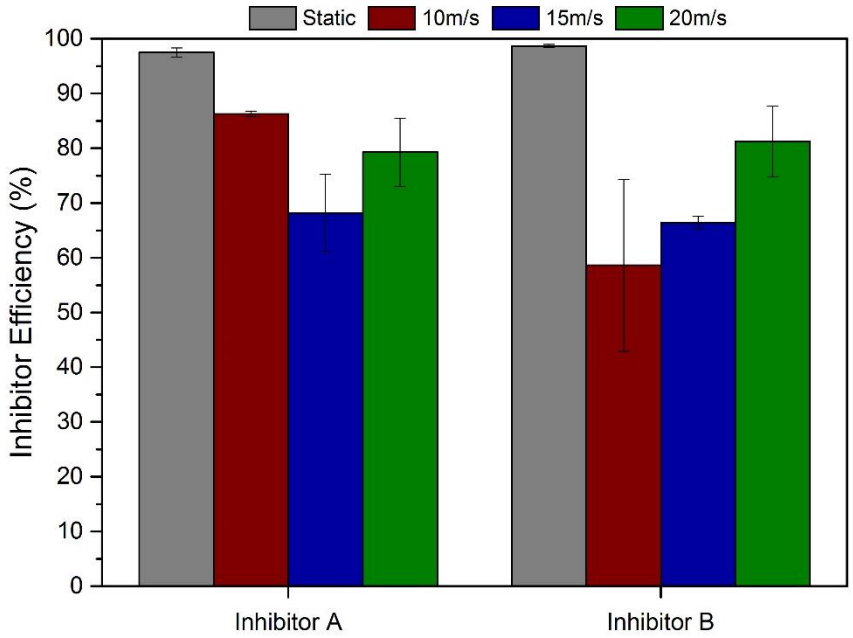

Figure 5.18 Efficiency of inhibitor A and inhibitor B approximately 4 minutes after 250 ppm of inhibitor was added in static cell tests in a 2% NaCl, 60°C, pH 4.7, CO_2-saturated, 1 L solution and flow-induced corrosion SIJ tests in a 2% NaCl, 60°C, pH 4.7, CO_2-saturated solution at flow velocities of 10 m/s, 15 m/s and 20 m/s

5.4 Erosion-Corrosion

Erosion and erosion-corrosion tests were completed in the SIJ using the same conditions as flow-induced corrosion tests and following the detailed methodology described in the previous chapter. Erosion-corrosion tests were completed in a CO_2-saturated, 2% NaCl, pH 4.7, 60°C solution, whilst erosion tests were completed in a N_2-saturated, pH 7 solution without the addition of NaCl. Erosion tests were completed at a different pH and in N_2-saturated conditions to avoid corrosion of the X65 specimens. The concentration of H^+ in the solution at pH 7 was insignificant, ensuring that the hydrogen evolution cathodic reaction, Equation (3.5), would not occur. It has been shown that at pH ≥ 6, the hydrogen evolution cathodic reaction does not have a significant influence on material degradation, but would have been significant at pH 4.7 if conditions from erosion-corrosion tests were replicated [30]. A calibrated quantity of sand was added to the reservoir to produce a concentration at the nozzle exit of 500 mg/L and 1000 mg/L.

5.4.1 Erosion and Erosion-Corrosion of X65 Carbon Steel

By definition in Equation (2.1) for total erosion-corrosion material loss, the static corrosion rate is used for the pure corrosion component of degradation. To differentiate between enhanced rates of corrosion caused by flow and sand the corrosion rates measured in erosion-corrosion conditions were compared with flow-induced corrosion rates. An average static corrosion rate of 4.32 ± 0.25 mm/yr was determined from Figure 5.1, where the corrosion rate was relatively constant over the 120-minute test and was highly repeatable. Mass loss measurements in erosion and erosion-corrosion SIJ tests at 500 mg/L sand concentration are shown in Table 5.5.

Table 5.5 Mass loss of X65 carbon steel during a 240-minute test period for blank erosion-corrosion SIJ tests in a 2% NaCl, 60°C, pH 4.7, CO_2-saturated solution and erosion SIJ tests in a 60°C, N_2-saturated solution at flow velocities of 10 m/s, 15 m/s and 20 m/s containing 500 mg/L of sand

	Δm (mg)	
U (m/s)	EC_{TML}	E_0
10	19.4 ± 1.37	1.90 ± 0.75
15	24.0 ± 3.85	5.75 ± 0.46
20	30.0 ± 6.13	13.3 ± 0.40

Each of the terms in Equation (2.1) for total erosion-corrosion material loss are plotted for 500 mg/L sand concentration erosion and erosion-corrosion tests in Figure 5.19. 'E-C TML' represents the total erosion-corrosion material loss measured from mass loss tests. 'C_{EC}' represents the corrosion rate of X65 measured using electrochemistry in erosion-corrosion conditions. 'E_0' is the pure erosion rate measured from erosion tests in N_2-saturated conditions using the SIJ for the same flow velocities and sand concentrations used in erosion-corrosion tests. 'ΔC_E' represents the erosion-enhanced corrosion rate of X65 measured by deducting corrosion rates measured using electrochemistry in flow induced corrosion conditions from corrosion rates measured in erosion-corrosion conditions. 'ΔE_c', the corrosion enhanced erosion rate, was determined by rearranging the erosion-corrosion Equation (2.1), as this was the only remaining term in the equation that was unknown.

High total erosion-corrosion degradation rates of greater than 10 mm/yr were observed at all flow velocities, showing the significance that erosion-corrosion can have on carbon steel degradation. The increase in flow velocity resulted in both an increase in the corrosion and erosion components of degradation.

Erosion appeared to increase more significantly with flow velocity than the corrosion terms. At a sand concentration of 500 mg/L and these flow velocities, the corrosion contribution to total material degradation was greater than the erosion contribution. A small increase in corrosion due to erosion mechanisms was observed compared with flow-induced corrosion rates, and some corrosion-enhanced erosion contributions were observed.

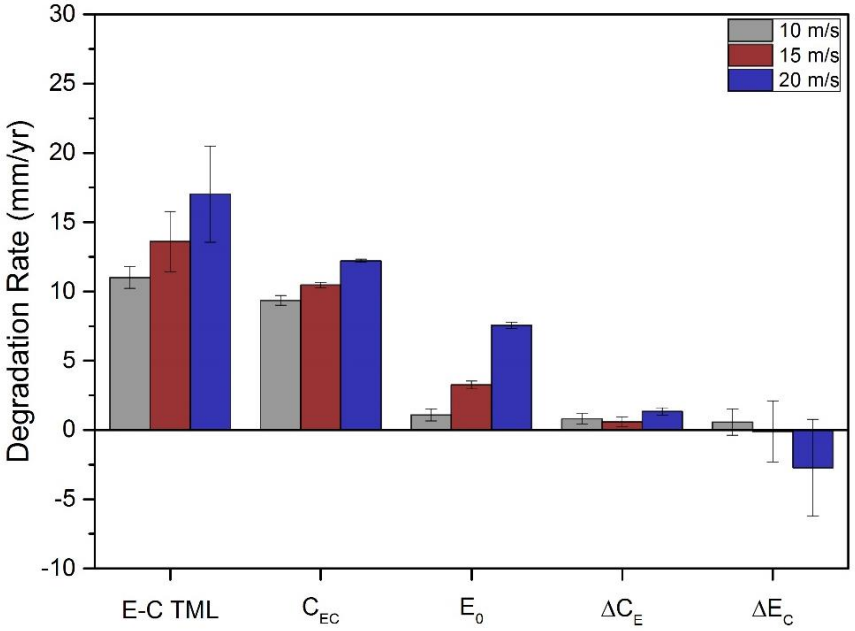

Figure 5.19 Contribution of flow-induced corrosion, pure erosion and erosion-corrosion interactions to total erosion-corrosion degradation in SIJ flow-induced corrosion tests in a 2% NaCl, 60°C, pH 4.7, CO_2-saturated solution at flow velocities of 10 m/s, 15 m/s and 20 m/s, erosion-corrosion SIJ tests in the same conditions containing 500 mg/L of sand and pure erosion SIJ tests in 60°C, pH 7, N_2-saturated conditions containing 500 mg/L of sand

At a sand concentration of 1000 mg/L, shown in Figure 5.20, the degradation rates were much more significant than 500 mg/L of sand due to an increased number of particle impacts on the surface of the X65 sample. Mass loss measurements in erosion and erosion-corrosion SIJ tests at 1000 mg/L sand concentration are shown in Table 5.5. Erosion was a much more significant component of the total material loss at a sand concentration of 1000 mg/L. Corrosion-enhanced erosion consisted of significant amounts of error, however, it did appear that corrosion-enhanced erosion accounted for a more significant proportion of degradation at 20 m/s. There did not appear to be a significant difference between corrosion rates in flow-induced corrosion conditions and erosion-corrosion conditions. The results of the interactions between erosion and corrosion for both sand concentrations are discussed in more detail later in the chapter.

Table 5.6 Mass loss of X65 carbon steel during a 240-minute test period for blank erosion-corrosion SIJ tests in a 2% NaCl, 60°C, pH 4.7, CO_2-saturated solution and erosion SIJ tests in a 60°C, N_2-saturated solution at flow velocities of 10 m/s, 15 m/s and 20 m/s containing 1000 mg/L of sand

	Δm (mg)	
U (m/s)	EC_{TML}	E_0
10	21.1 ± 4.51	3.17 ± 0.83
15	26.2 ± 4.84	9.57 ± 0.14
20	45.8 ± 2.63	15.2 ± 0.33

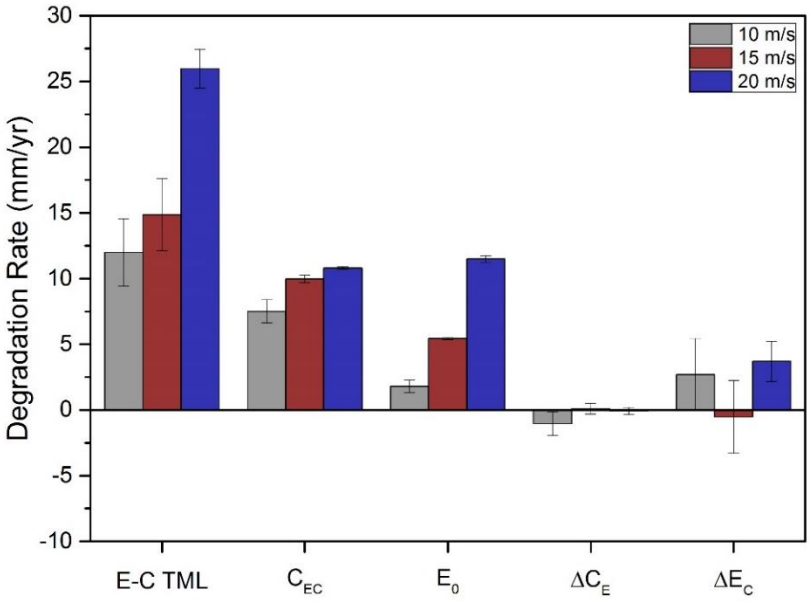

Figure 5.20 Contribution of flow-induced corrosion, pure erosion and erosion-corrosion interactions to total erosion-corrosion degradation in SIJ flow-induced corrosion tests in a 2% NaCl, 60°C, pH 4.7, CO_2-saturated solution at flow velocities of 10 m/s, 15 m/s and 20 m/s, erosion-corrosion SIJ tests in the same conditions containing 1000 mg/L of sand and pure erosion SIJ tests in 60°C, pH 7, N_2-saturated conditions containing 1000 mg/L of sand

5.4.2 Evaluation of Corrosion Inhibitor A & Inhibitor B

Both corrosion inhibitors were evaluated in erosion-corrosion conditions using the same method as used in the flow-induced corrosion tests, to investigate the effects of sand on the performance of the inhibitors. Inhibitor A tests were not completed due to adsorption of the corrosion inhibitor to sand particles. It has been shown that some corrosion inhibitors can adsorb to the surface of sand particles, resulting in reduced availability of corrosion inhibitor in the

solution [35, 191, 192]. Inhibitor A adsorbed to sand particles and caused them to stick to the sides of the SIJ reservoir. No erosion was observed on the surface of the samples, so it appeared that the majority of the sand particles were stuck to the sides of the SIJ and not flowing through the nozzle. Therefore, further testing of this inhibitor in erosion-corrosion conditions was not completed as it was unknown exactly how much, if any, sand was impacting on the surface of the X65 samples.

No noticeable effects of adsorption of inhibitor B to sand particles were observed. Figure 5.21 shows the contribution of individual components to total erosion-corrosion degradation in SIJ tests after 250 ppm of inhibitor B was added to a solution containing 500 mg/L of sand. The terms on the x-axis represent the same parameters as the previous graphs in blank conditions. The pure erosion rate, E_0, was determined from the previous erosion tests without inhibitor in N_2-saturated conditions. Overall erosion-corrosion degradation rates were reduced by the presence of the corrosion inhibitor on the X65 surface. This reduction was seen entirely in the corrosion rate with no reduction in erosion rate observed.

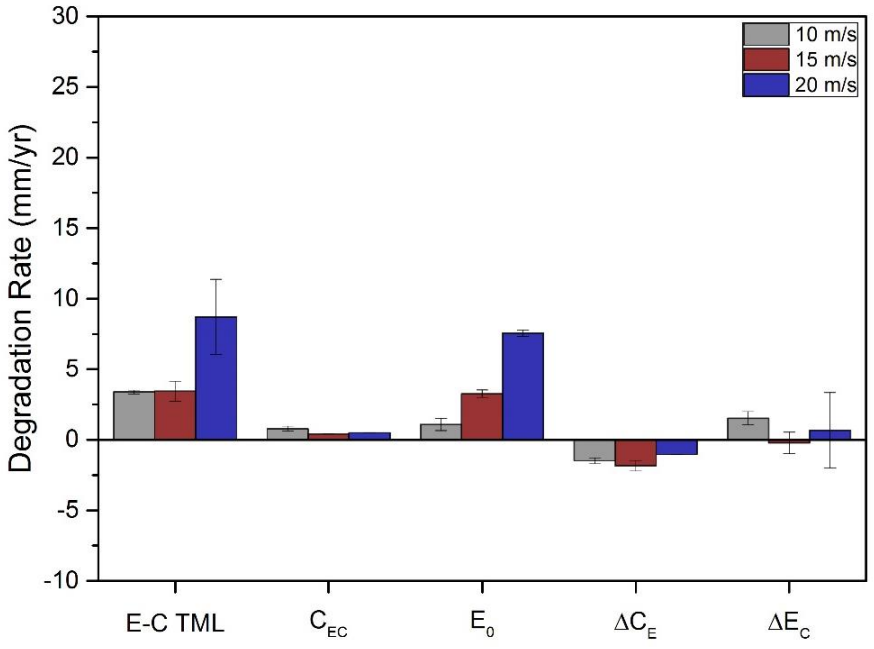

Figure 5.21 Contribution of flow-induced corrosion, pure erosion and erosion-corrosion interactions to total erosion-corrosion degradation in SIJ flow-induced corrosion tests in a 2% NaCl, 60°C, pH 4.7, CO_2-saturated solution at flow velocities of 10 m/s, 15 m/s and 20 m/s after the addition of 250 ppm of inhibitor B, erosion-corrosion SIJ tests in the same conditions containing 500 mg/L of sand after the addition of 250 ppm of inhibitor B and pure erosion SIJ tests in blank, 60°C, pH 7, N_2-saturated conditions containing 500 mg/L of sand

A slight reduction in the corrosion rate was observed in erosion-corrosion conditions compared with the flow-induced corrosion conditions. This was also seen when 1000 mg/L of sand was added to the solution, shown in Figure 5.22. Similar results were seen at 1000 mg/L, however, the erosion components were more significant. Despite the use of a corrosion inhibitor, degradation rates were still significantly high, due to the significance of erosion on the total material loss, with erosion wear accounting for more than 90% of the total degradation in inhibited conditions at 15 m/s and 20 m/s.

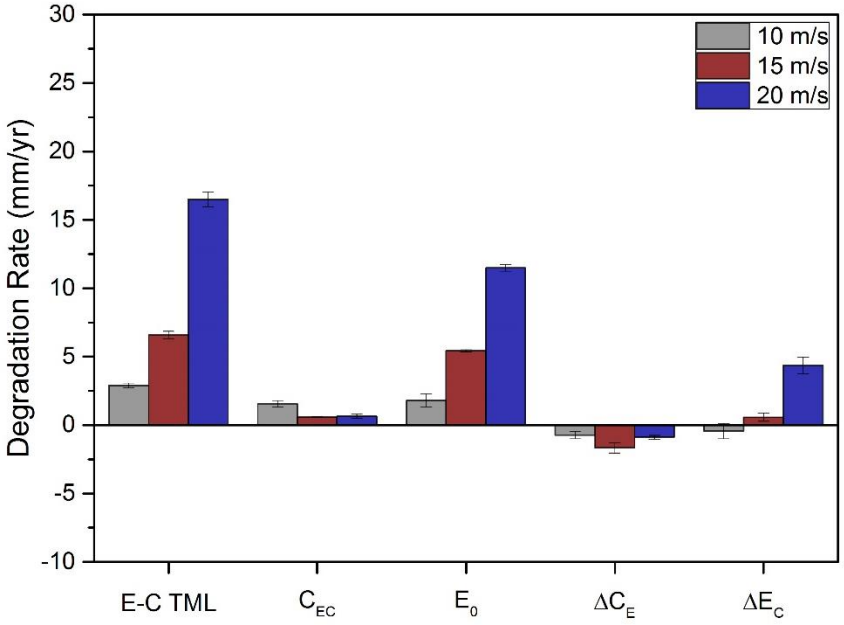

Figure 5.22 Contribution of flow-induced corrosion, pure erosion and erosion-corrosion interactions to total erosion-corrosion degradation in SIJ flow-induced corrosion tests in a 2% NaCl, 60°C, pH 4.7, CO_2-saturated solution at flow velocities of 10 m/s, 15 m/s and 20 m/s after the addition of 250 ppm of inhibitor B, erosion-corrosion SIJ tests in the same conditions containing 1000 mg/L of sand after the addition of 250 ppm of inhibitor B and pure erosion SIJ tests in blank, 60°C, pH 7, N_2-saturated conditions containing 1000 mg/L of sand

5.4.3 Erosion-Corrosion Interactions

The erosion-enhanced corrosion, ΔC_E, components for conditions with and without corrosion inhibitors in 500 mg/L and 1000 mg/L are compared for each flow velocity in Figure 5.23. In blank conditions with a 500 mg/L sand concentration, corrosion was enhanced. However, when 1000 mg/L of sand was added there appeared to be no significant change in corrosion rate, except at 10 m/s where the corrosion rate decreased. There appeared to be some inconsistency and no direct correlation between the sand concentration

and the enhanced corrosion rate. Further investigation of the mechanisms contributing to erosion-enhanced corrosion was required, and it was uncertain why the increase in corrosion was not as significant at 1000 mg/L.

Another observation from Figure 5.23 was that after inhibitor B was added to the 500 mg/L sand-laden solution, the corrosion rate was reduced. This was observed for each of three flow velocities and both sand concentrations. Due to the much lower corrosion rates measured when an inhibitor was used in flow-induced corrosion conditions compared to blank corrosion rates, the changes in corrosion rates were much more significant. Typically it would be expected that corrosion rates would be higher in sand-containing flows, due to the removal of inhibitor from the surface of the steel as a result of particle impingement, seen previously in erosion-corrosion inhibitor tests [6, 35, 62]. Therefore, the reasons for the decrease were unknown.

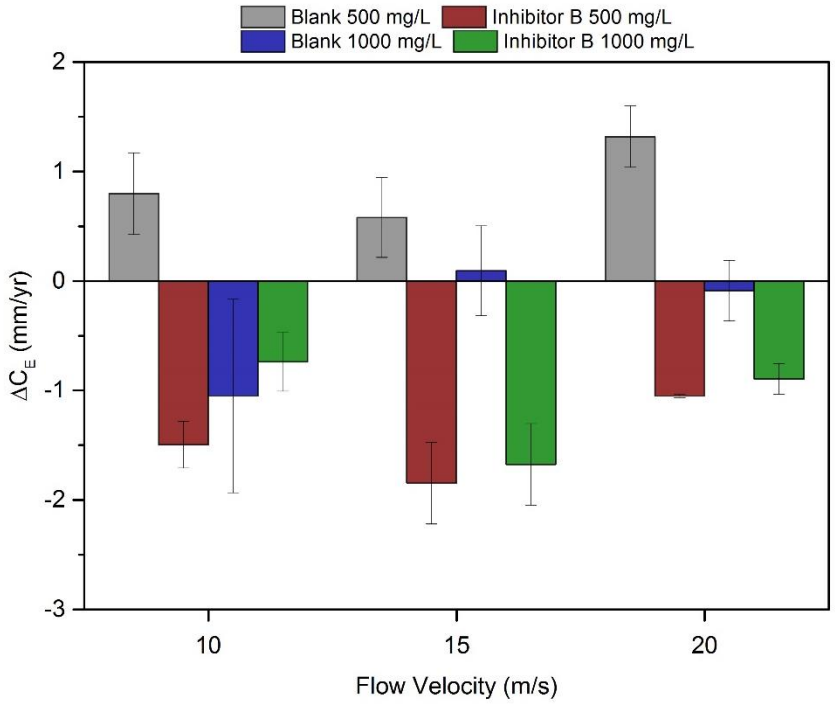

Figure 5.23 Comparison of erosion-enhanced corrosion measured using EIS in SIJ erosion-corrosion tests in blank conditions and after the addition of 250 ppm of inhibitor B in a 2% NaCl, 60°C, pH 4.7, CO_2-saturated solution at flow velocities of 10 m/s, 15 m/s and 20 m/s containing 500 mg/L and 1000 mg/L of sand

Corrosion-enhanced erosion is compared in blank and inhibited conditions in Figure 5.24. Error was significant in the results due to the propagation of error in the calculation of corrosion-enhanced erosion but in tests completed with a 1000 mg/L sand concentration there did appear to be an increase in erosion as a result of corrosion. Corrosion-enhanced erosion also became more significant as flow velocity was increased in blank and inhibitor tests with a

1000 mg/L sand concentration. Similar behaviour was observed in blank conditions and inhibited conditions, despite the reduced corrosion when the inhibitor film was present.

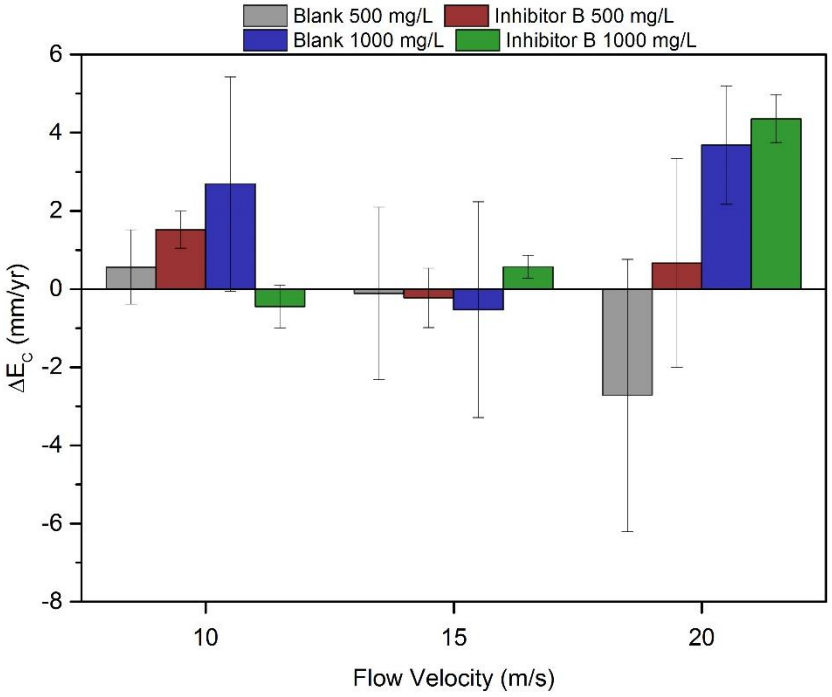

Figure 5.24 Comparison of corrosion-enhanced erosion calculated using Equation (2.1) in SIJ erosion-corrosion tests in blank conditions and after the addition of 250 ppm of inhibitor B in a 2% NaCl, 60°C, pH 4.7, CO_2-saturated solution at flow velocities of 10 m/s, 15 m/s and 20 m/s containing 500 mg/L and 1000 mg/L of sand

5.5 Summary and Conclusions

Flow-induced corrosion and erosion-corrosion tests were completed using an SIJ in conditions representative of field conditions to understand the influence flow and sand have on X65 and the performance of two corrosion inhibitors. Conditions in the SIJ were determined to replicate conditions in the fields analysed, with flow velocities, NaCl, sand concentration, temperature and inhibitor concentration replicated from field conditions. Three different flow velocities, two sand concentrations and two different corrosion inhibitors were compared to understand the conditions in the field and the effects on X65 and the inhibitors. The main conclusions from this chapter were:

- Flow-induced corrosion results showed, as expected, that the corrosion rate increased when flow velocity was increased;

- Corrosion inhibitors were evaluated in flow-induced corrosion conditions, showing high efficiency at reducing the corrosion rate. However, efficiency was lower than efficiency in static conditions but due to high rates of degradation in the SIJ and the relatively short test duration, this decrease in efficiency was not significant;
- Erosion-corrosion tests in conditions without inhibitor showed that erosion rates and erosion-corrosion rates increased with increasing sand concentration and increasing flow velocity as expected;
- Interactions were observed, with corrosion enhancing erosion in some conditions and erosion enhancing corrosion. Further work was required to understand the mechanisms for these interactions;
- Corrosion inhibitors were affected by the presence of sand particles in erosion-corrosion conditions. Corrosion inhibitor A did not perform effectively in sand-containing flows, as it adsorbed to the sand particles and caused them to adhere to the sides of the SIJ reservoir. Therefore, further testing was not completed in erosion-corrosion conditions with inhibitor A;
- Inhibitor B did perform better in sand containing conditions as no adsorption to sand particles was observed. The inhibitor did not reduce any of the erosion components of total erosion-corrosion degradation, and overall degradation rates remained high. However, corrosion rates were decreased when sand was present. Further work was required to understand the causes of this.

Chapter 6
Erosion-Corrosion Interactions of X65 Carbon Steel in CO_2 Oil & Gas Environments

Erosion and corrosion have been shown to interact causing enhanced rates of degradation of carbon steel [34, 35, 140]. Erosion-corrosion interactions were observed in Chapter 5 and further investigation to understand the mechanisms of erosion-enhanced corrosion and corrosion-enhanced erosion of carbon steel was the aim of this chapter. CFD was used to define the flow conditions and particle motion in the SIJ to provide more understanding of the erosion-corrosion conditions during tests. Knowledge of the conditions in erosion-corrosion tests has been shown to be important due the influence of flow and particle impingement angles on the mechanisms of corrosion and erosion. Erosion-corrosion tests were completed using the SIJ at a high flow velocity and high sand concentration with a range of surface analysis techniques utilised to investigate the causes of interactions and the effects they have on the surfaces of X65 carbon steel.

6.1 Introduction

The causes of corrosion-enhanced erosion and erosion-enhanced corrosion are not fully understood and were the subject of study in this chapter through the application of the SIJ. Erosion-corrosion interactions have been shown to account for a significant proportion of total erosion-corrosion degradation of carbon steel on several occasions in sand-containing corrosive flows [138, 140, 149]. However, the causes of the interactions between erosion and corrosion are not fully understood for active materials, such as carbon steel. This chapter investigated the interactions to provide an insight into the mechanisms of corrosion-enhanced erosion and erosion-enhanced corrosion.

The hydrodynamic conditions and erosive conditions in the SIJ flow-induced corrosion and erosion-corrosion tests completed in Chapter 5 were not fully understood and were difficult to measure due to the significant variation in conditions over the surface of the test sample [35, 105]. Tests completed in the previous chapter were completed at flow velocities of 10 m/s, 15 m/s and 20 m/s and sand concentrations of 500 mg/L and 1000 mg/L with a nominal sand impact angle of 90°. In reality, the conditions in the SIJ were much more complex than this with a wide range of hydrodynamic conditions experienced

on the sample and significant differences in particle impact velocities and impact angles [120].

To understand the flow conditions and erosion conditions in the SIJ, CFD was used to determine flow through the SIJ nozzle and to determine the trajectories of particles as they flow through the nozzle and impinge onto the surface of a carbon steel sample. An understanding of the erosion conditions in the SIJ was important to gain further understanding about the mechanisms of the erosion-corrosion interactions and to determine how particle impingements influenced the interactions. Properties of the surface were analysed after flow-induced corrosion, erosion and erosion-corrosion tests, including measurements of the surface roughness and hardness, to identify any effects corrosion-enhanced erosion and erosion-enhanced corrosion had on the carbon steel surfaces.

The objectives of this chapter were to:

- Predict the hydrodynamic conditions in the SIJ using CFD by developing a model of the flow through the SIJ nozzle;
- Predict the trajectories of sand particles as they flow through the SIJ nozzle and impinge onto the surface of a carbon steel sample located at a fixed distance from the exit of the nozzle;
- Complete flow-induced corrosion, erosion and erosion-corrosion tests in the SIJ to investigate how corrosion, erosion and interactions contribute to total erosion-corrosion degradation over different time periods in blank conditions;
- Complete surface analysis of samples after flow-induced corrosion, erosion and erosion-corrosion tests to understand the mechanisms of erosion-enhanced corrosion and corrosion-enhanced erosion;
- Investigate the interactions observed in Chapter 5 that showed increased inhibitor efficiency when sand particles were present in the flow compared to flow-induced corrosion conditions.

6.2 Experimental Methodology

Flow-induced corrosion, erosion and erosion-corrosion tests were completed using the SIJ to measure how each of the wear mechanisms contributed to erosion-corrosion of carbon steel. The same methodology used in Chapter 5 and explained in Chapter 4 was used for the tests in this chapter. Test conditions were kept the same with a 60°C, 2% NaCl tap water solution

saturated with CO_2 used for corrosion tests and a 60°C tap water solution saturated with N_2 used for erosion tests. In the previous chapter, flow velocity and sand concentration were varied to assess the effects of the parameters on erosion-corrosion of carbon steel. The most extreme conditions were used in this chapter, as degradation rates were highest at a flow velocity of 20 m/s and a sand concentration of 1000 mg/L. Rather than varying parameters, the test duration was varied to investigate how the contribution of erosion, corrosion and interactions to total erosion-corrosion degradation varied over time. 30, 60, 120 and 240-minute length tests were therefore completed and several properties of the surface, including hardness and roughness, were measured. 1, 5 and 10 minute tests were also conducted to measure the rate of work-hardening of the samples in erosion conditions and in CO_2 corrosion conditions to measure the rate at which work-hardened layers were removed. The average Vickers hardness of the samples, measured at various locations on the surface after being wet-ground to a surface roughness (S_a) of 0.15 µm ± 0.02 µm before testing, was 202 H_V ± 10 H_V.

To determine erosion-enhanced corrosion rates, electrochemistry measurements were completed in flow-induced corrosion and erosion-corrosion conditions to measure the difference in corrosion rate when sand was present in the flow. A standard three-electrode cell was used, consisting of the X65 sample as the working electrode, a Pt counter electrode and an Ag/AgCl reference electrode. EIS measurements and Tafel plots completed in Chapter 5 were used to determine the corrosion rates.

6.3 Prediction of Flow in the SIJ

Due to the lack of understanding about the flow and erosion conditions in Chapter 5, understanding of erosion-corrosion and erosion-corrosion interactions was limited, meaning that few complete conclusions could be made about the effects of sand particles on the degradation of X65 carbon steel. Therefore, further work was required to define the conditions in the SIJ. Flow through the SIJ nozzle was difficult to characterise experimentally, due to the complexity and lack of availability of measuring equipment to determine parameters such as shear stress on the surface of the sample [28]. Measuring particle trajectories and impacts on the surface was even more challenging due to greater complexity in measurements in high flow velocity flows and sand concentrations, and limitations of the techniques currently available to measure particle motion [4].

CFD has been used previously to predict the fluid flow and particle trajectories through the SIJ [35, 105]. A similar methodology for predicting the fluid flow and particle flow was used in conditions relevant to the field conditions analysed in this thesis. Some mathematical solutions exist, discussed in more detail later, that can be used to calculate flow parameters in axisymmetric jets; however, these equations are limited in the conditions that they can be used in, discussed later in this chapter [64, 212]. No method of predicting particle trajectories through an axisymmetric jet nozzle exists without the use of CFD. Therefore, using CFD was essential to gain further insight into the erosion-corrosion conditions in the SIJ.

6.3.1 Theory of Turbulent Axisymmetric Jet Flow

Before particle trajectories could be predicted, fluid flow was required to be predicted first. Due to the high flow velocity and high Reynolds number of flow through an SIJ nozzle, the flow through it was turbulent [35, 105]. The SIJ nozzle is an example of axisymmetric jet flow. In turbulent axisymmetric jet flow, fluid flows through a nozzle producing a jet of fluid as the flow spreads from the nozzle [64]. When a target, such as the X65 carbon steel samples used in this work, is positioned in the path of the flow, a stagnation point on the sample is produced in the centre of the nozzle [64, 211-213]. Highly turbulent flow develops as the flow spreads from the centre of the nozzle, before gradually decreasing in velocity [212]. A diagram representing the fluid flow out of the SIJ nozzle is shown in Figure 6.1.

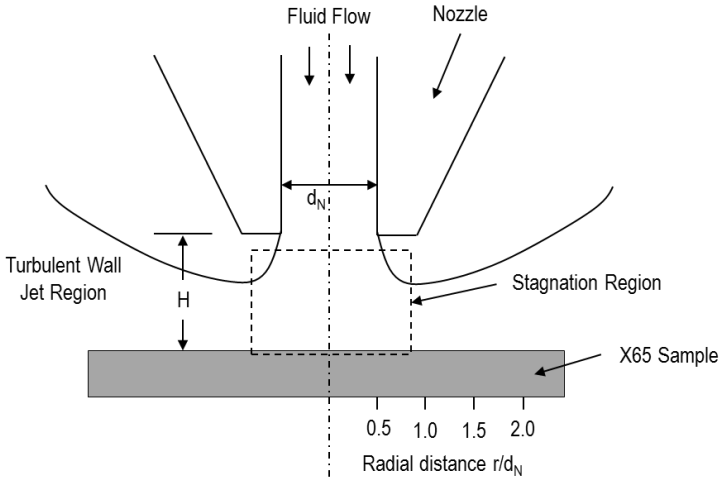

Figure 6.1 Fluid flow through a turbulent axisymmetric impinging jet representative of fluid flow through the SIJ nozzle, where $\boldsymbol{d_N}$ is the nozzle diameter, $\boldsymbol{H}$ is the distance from the exit of the nozzle to the sample and $\boldsymbol{r}$ is the radial distance from the centre of the sample, adapted from [28, 211]

Giralt and Trass [213] developed an equation for predicting the shear stress in an axisymmetric jet, Equation (6.1):

$$\tau_w = 0.0447 \rho_f U^2 Re_J^{-0.182} \left(\frac{r}{d_N}\right)^{-2} \quad (6.1)$$

where τ_w is the wall shear stress, ρ_f is the fluid density, U is the mean nozzle flow velocity, r is the radial distance from the centre of the sample and d_N is the nozzle diameter. The jet Reynolds number, Re_J, is defined as:

$$Re_J = \frac{\rho U d_N}{\mu} \quad (6.2)$$

Equation (6.1) has been used previously to calculate shear stress in SIJ flow [35, 51]. However, this equation only applies when the ratio of distance from the nozzle to the sample (H) to the nozzle diameter (d_N), H/d_N, is equal to 8 and when the Reynolds number of the flow is between 22,900 and 152,000 [213]. The flow-induced corrosion tests in this work were completed at H/d_N = 1.25, therefore this equation could not be applied to tests completed in this thesis. Erosion-corrosion tests have been completed using an SIJ with H/d_N ratios ≤ 1.25 in this thesis and in other erosion-corrosion research [34, 35, 145]. To achieve the higher ratio used in the Giralt & Trass [213] equation, the distance from the nozzle to the sample would have been required to be increased, which could have significantly changed the erosion conditions. Therefore, it was chosen to use the same H/d_N ratio of 1.25 used previously to investigate the interactions measured in the conditions in Chapter 5.

Tests completed in the previous chapter were completed with a solution at a temperature of 60°C, with water at this temperature having a dynamic viscosity of 4.67 x 10^{-4} Pa.s and density of 983.2 kg/m^3 [100]. For flow velocities of 10 m/s, 15 m/s and 20 m/s with a nozzle diameter of 4 mm, Reynolds numbers in the SIJ ranged from approximately 84,000 to 168,000.

Poreh et al. [65] developed an equation for calculating the shear stress in an axisymmetric jet in a particle free environment, summarised by Phares et al. [212], Equation (6.3), to calculate the shear stress in an axisymmetric nozzle. This model was developed to predict the shear stress in the turbulent jet region, r/d_N > 2, therefore could not be used to predict the shear stress over the entirety of the sample in the SIJ. 25 mm diameter samples were used in SIJ tests, with a 4 mm diameter nozzle meaning that the shear stress could not be calculated over the majority of the sample used for the SIJ setup in this work.

$$\frac{\tau_w Re_J^{1/2} \left(\frac{H}{d_N}\right)^2}{\rho_f u^2} = 0.34 Re_J^{1/5} \left(\frac{r}{H}\right)^{-2.3} \quad (6.3)$$

Figure 6.2 summarises the conditions in which Equation (6.1) and Equation (6.3) can be applied in an axisymmetric impinging jet flow.

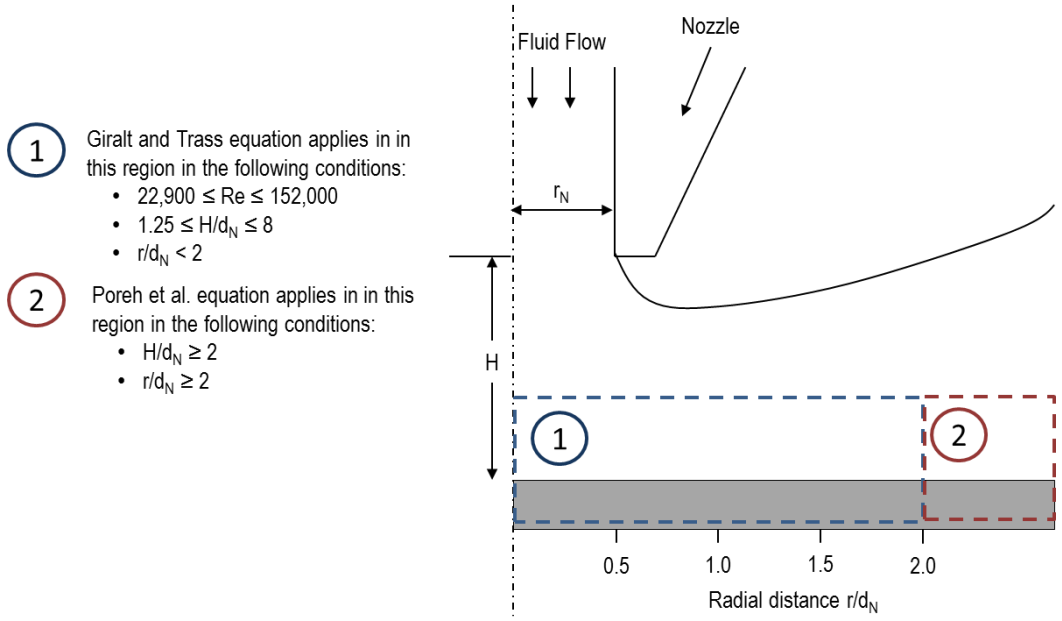

Figure 6.2 Regions on a sample surface in axisymmetric impinging jet flow where expressions developed by Giralt and Trass [213] and Poreh et al. [65] used to calculate wall shear stress can be applied, and the conditions under which they can be applied in

Gulbrandsen and Grana [51] compared Equation (6.1) and Equation (6.3) to predict the shear stress over a sample in an axisymmetric jet. Equation (6.3) predicted a higher shear stress for the same conditions than Equation (6.1). It was clear that there is not a complete understanding of the hydrodynamic conditions in axisymmetric jet flow, and that the SIJ setup used for flow-induced corrosion tests in the previous chapter could not be calculated using the analytical solutions. Therefore, CFD was used to predict the hydrodynamic conditions on the sample surface, with the analytical solutions described used for validation of the model in the conditions where these equations applied to give confidence in the accuracy of the CFD model.

6.3.2 Model Description

The SIJ model was developed using COMSOL Multiphysics 5.2a as a 2D axisymmetric nozzle. A representation of the model of the SIJ nozzle is shown in Figure 6.3.

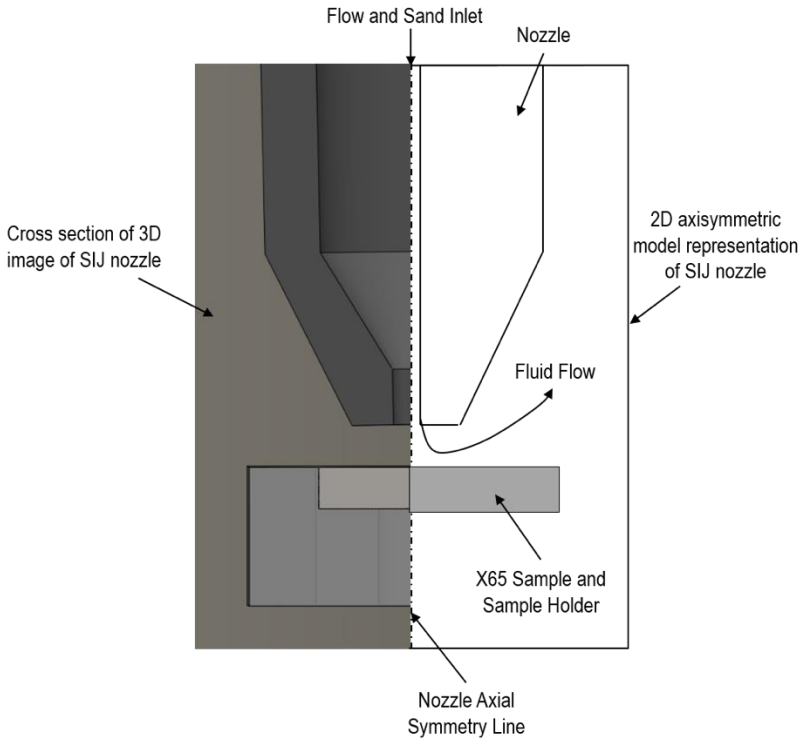

Figure 6.3 Representation of 2D axisymmetric model of SIJ nozzle developed for CFD predictions of fluid flow and particle trajectories

Defining the geometry of the SIJ nozzle as a 2D axisymmetric model significantly reduced the computational demands of the model and reduced the time taken to solve the model, without any effect on the accuracy of the prediction. The symmetry axis went through the centre axis of the nozzle, as shown in Figure 6.3. A 25 mm diameter sample was also modelled, with an additional width added to account for the size of the sample holder used to support samples in the SIJ, to accurately represent the flow in this region. The sample was assumed to be flat, which would not be representative of a sample after erosion testing, where a significant wear scar is observed on the surface of samples. However, validation of a model containing a changing surface representing an erosion-worn surface would be challenging, therefore the model was simplified to predictions on a flat surface only.

A similar methodology was used by Barker [35] and Gnanavelu [105] to develop CFD models of an SIJ nozzle. Due to the high Reynolds number in the SIJ, the flow was turbulent, therefore, an appropriate turbulence model was required. Barker [35] and Gnanavelu [105] used the k-ϵ turbulence model for their SIJ models, explained in Chapter 4.2.3; however, this turbulence model tends to over predict the spreading rate of turbulence in axisymmetric jets, thus over predicting parameters such as the shear stress on the sample

[13]. Therefore, the k-ω model was used in the development of this model, which has been reported to predict axisymmetric jet flow more accurately [13].

The no slip condition was applied at all of the boundary walls and a total of 82,969 elements were used in the mesh. The mesh consisted of triangular elements in the bulk of the fluid flow domain with rectangular boundary elements used adjacent to the walls to accurately resolve near to the wall. First order elements were used to predict the pressure and velocity terms in the fluid flow. The density of the water was assumed to be 983.2 kg/m^3 with a dynamic viscosity of 4.67 x10^{-4} Pa.s representative of water at a temperature of 60°C [100]. Defining the turbulent length scale and turbulent intensity boundary conditions at the flow inlet can be challenging due to a lack of knowledge of these parameters for the specific application used [27]. However, an input of these values is required for turbulence modelling. A turbulent length scale of 0.075 of the nozzle diameter and a turbulent intensity of 0.05 was used, typical values for axisymmetric jet flow [13, 27]. Results were not sensitive to changes in these parameters.

6.3.3 Mesh Sensitivity Study & Model Validation

Accuracy of CFD models can vary significantly based on the inputs specified by the user of the model, such as the number of elements used in the mesh and the use of turbulence models [13]. Shear stress was the parameter chosen to validate the CFD model, with the CFD output of shear stress compared with the results of the calculation using the Poreh et al. [65] model, Equation (6.3). Shear stress is defined by Equation (6.4) [100]:

$$\tau_w = \mu \frac{\partial U}{\partial z} \tag{6.4}$$

where U is the flow velocity and z is the distance from the wall. Wall shear stress is calculated using this method when the turbulence model fully resolves the flow down to the wall, such as the SST model. The use of turbulence models with wall functions means that empirical functions are used to predict the flow near to the wall. When wall functions are used, shear stress is calculated more accurately using friction velocity, Equation (6.5) [13, 214]:

$$\tau_{wy} = \rho_f u_\tau \frac{u_y^T}{u^+} \tag{6.5}$$

where τ_{wy} is the wall shear stress in the y-direction, u_τ is the friction velocity, defined by Equation (4.31), u_y^T is the tangential velocity in the y-direction (or any direction required to calculate the shear stress in) and u^+ is the

dimensionless velocity, defined by Equation (4.30). As was highlighted earlier, the Giralt and Trass [213] equation and Poreh et al. [65] equation only apply to certain conditions. Therefore, a 4 mm diameter nozzle was modelled, with the distance from the nozzle to the sample increased to 8 mm, giving an r is the radial distance from the centre of the sample ratio of 2 so that the Poreh et al. [65] equation could be used. A flow velocity of 8 m/s was simulated and the shear stress on the sample in the region from r/d_N of 2.5 to 3.1 was determined, representing the region on a sample in the SIJ from 20 mm to 25 mm diameter.

Several turbulence models were compared in Figure 6.4. The use of the k-ω model reduced the accuracy near to the wall, but significantly reduced computational demand. The SST model is an extension to the k-ω model but does not use wall functions, and fully resolves down to the wall [13]. The k-ω and the k-ϵ model gave similar results, with the k-ϵ model over predicting the shear stress in this region, as explained by the reported over prediction of turbulence spreading using this model for axisymmetric impinging jets [13]. Both turbulence models were a slight over prediction compared to the Poreh et al. [65] equation. The SST model reduced the difference between the model predicted shear stress and the Poreh et al. [65] analytical solution. However, the increased computational time was not justified given that only approximately a 2% change in results was observed between the k-ω and SST models. The improved accuracy of the SST model is explained by more refined performance in the near-wall region as empirical wall functions are not used, which are used for near-wall predictions using the k-ω and k-ϵ turbulence models [13].

For the purpose of this work, use of the SST model was not justified for such a small increase in accuracy, due to the significantly increased solving time when using the turbulence model. A mesh sensitivity study was also completed to ensure that results were not sensitive to the number of elements in the mesh, shown in Figure 6.5, using the k-ω turbulence model. The mesh sensitivity study in Figure 6.5, showed no significant change in results when 47,566 elements and 246,147 elements were used, and all other meshes used. Using fewer elements was therefore logical, to reduce computational demand. A total of 82,969 elements were used for the prediction of the rest of the results. There was some slight variation in the number of elements used in the mesh when different nozzle diameters were used due to the change of geometry. The use of first order elements provided sufficient accuracy.

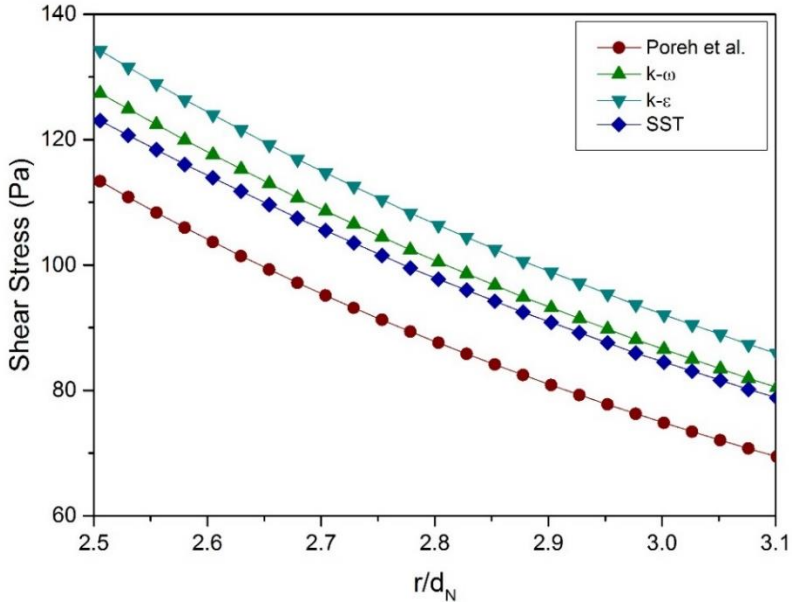

Figure 6.4 CFD prediction of wall shear stress on a sample surface in SIJ nozzle flow comparing different turbulence models with the analytical solution of Poreh et al. [65] at a flow velocity of 8 m/s, solution temperature of 60°C and $\boldsymbol{H/d_N}$ ratio of 2

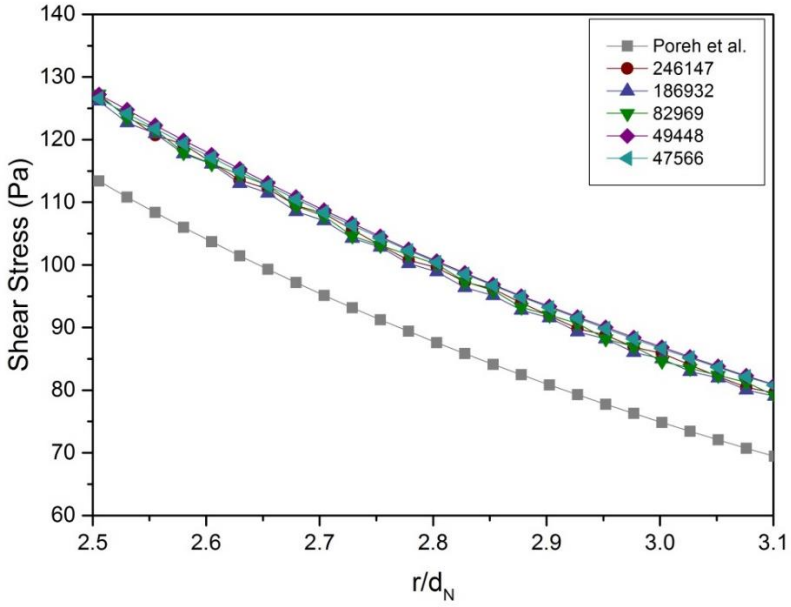

Figure 6.5 Mesh sensitivity study of CFD prediction of wall shear stress on a target in SIJ nozzle flow using the $\boldsymbol{k\text{-}\omega}$ turbulence model compared with the analytical solution of Poreh et al. [65] at a flow velocity of 8 m/s, solution temperature of 60°C and $\boldsymbol{H/d_N}$ ratio of 2

To ensure that the model was accurately resolved at the wall and that wall functions could be applied, the dimensionless wall distance, y^+, was used, defined in Equation (4.32). When wall functions are used in the model, a y^+ value between 30 and 500 is required to ensure that the mesh is refined sufficiently at the wall [13]. The y^+ parameter was calculated at the wall representing the sample surface in the SIJ for flow through the 4 mm diameter

nozzle used in the SIJ in tests in this chapter. An inlet flow velocity of 20 m/s and a water temperature of 60°C through the nozzle was predicted in Figure 6.6.

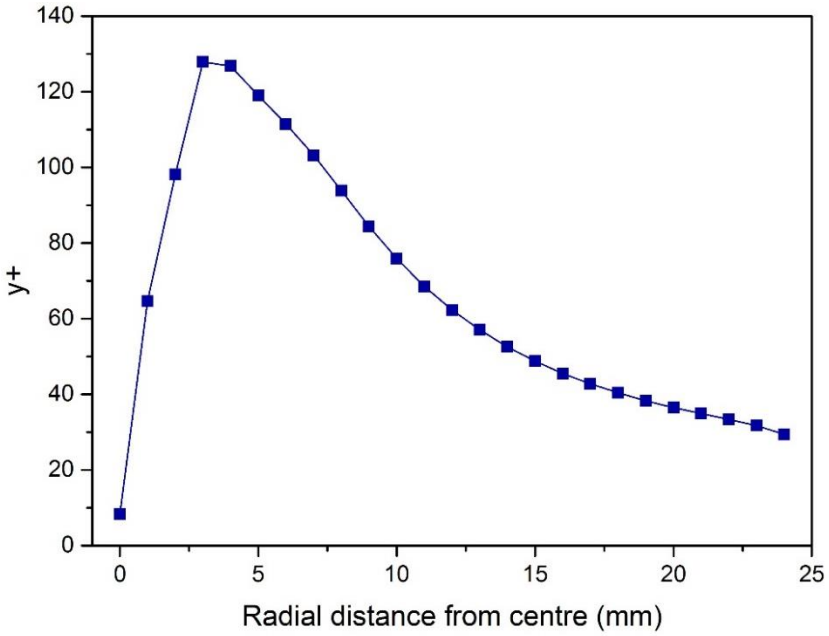

Figure 6.6 Calculation of $\boldsymbol{y^+}$ from CFD prediction of shear stress using the $\boldsymbol{k}$-$\boldsymbol{\omega}$ turbulence model over the target surface representing the sample surface in the SIJ nozzle at a flow velocity of 20 m/s, solution temperature of 60°C and $\boldsymbol{H/d_N}$ ratio of 1.25

The calculation of y^+ over the wall representing the sample surface showed that this criterion of y^+ values was met over the majority of the sample, with the exception of the initial value directly in the centre of the sample. The methods used to validate the CFD model of the SIJ nozzle showed that the model was accurate for the conditions validated for. A lack of theory and experimental data exist to validate the CFD model for all specifications of SIJ nozzle and the setup used in the erosion-corrosion tests in this work. However, the method used for all CFD predictions of SIJ nozzle flow was the same, giving confidence in the reliability of results in all conditions modelled.

6.3.4 Prediction of Flow through SIJ Nozzle

The test conditions and SIJ nozzle specification used (H/d_N = 1.25) in the flow-induced corrosion and erosion-corrosion tests in Chapter 5 at a flow velocity of 20 m/s were simulated using CFD, shown in Figure 6.7. A stagnation point was observed in the centre of the sample, with a higher velocity, higher turbulence region observed as the flow spread from the centre of the nozzle. The flow velocity reduced as it spread towards the edge of the

sample holder and gradually reduced to a fairly low velocity in the SIJ reservoir. The turbulent kinetic energy is also shown in Figure 6.7. A region with a high turbulent kinetic energy, k, was observed on the surface of the sample as the flow spread from the centre.

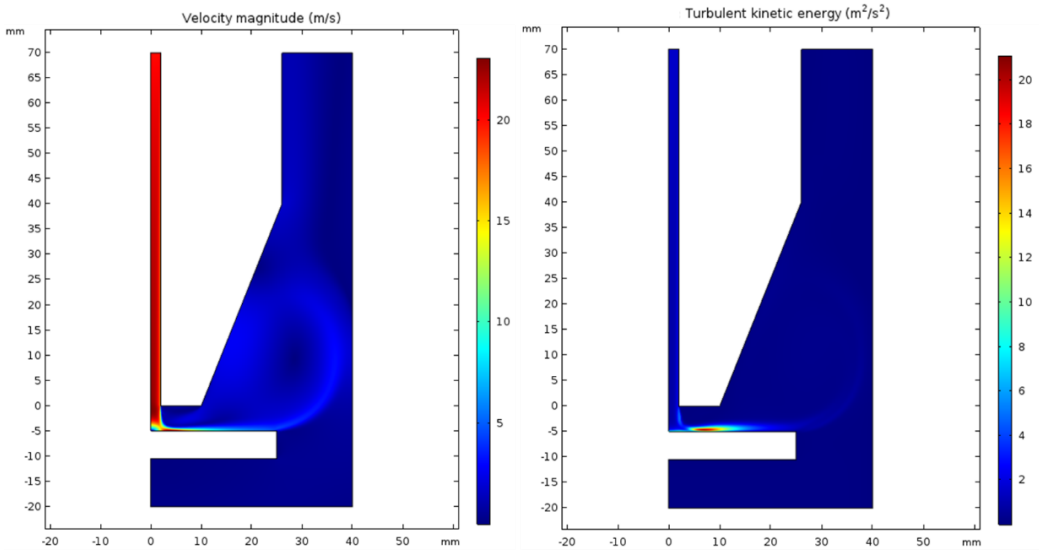

Figure 6.7 CFD prediction using the k-ω turbulence model of 60°C water flow through an SIJ nozzle with a nozzle diameter of 4 mm, distance to sample of 5 mm and an inlet flow velocity of 20 m/s showing (a) flow velocity and (b) turbulent kinetic energy, k

The predicted flow velocity over the surface of the X65 sample at an inlet flow velocity of 20 m/s is shown in Figure 6.8. The flow velocity at the first node adjacent to the surface is shown as, by definition, the flow velocity at the sample wall is equal to zero.

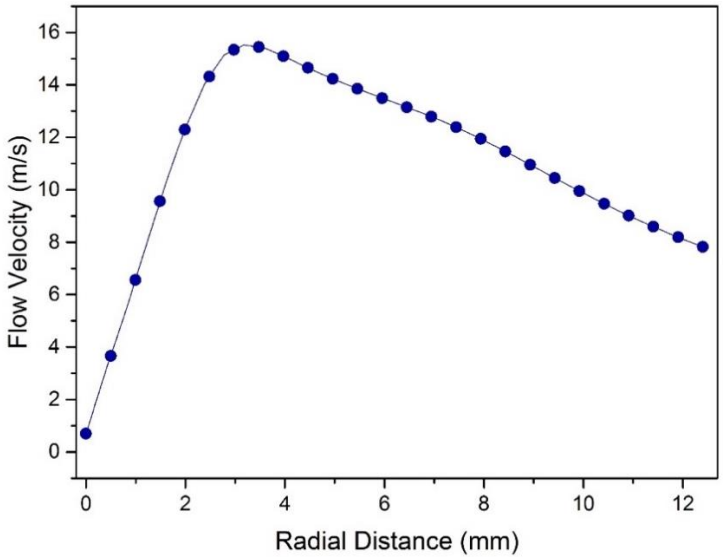

Figure 6.8 CFD prediction using the k-ω turbulence model of flow velocity adjacent to the X65 sample surface for 60°C water flow through an SIJ nozzle with a diameter of 4 mm, distance to sample of 5 mm and at a flow velocity of 20 m/s

A high flow velocity is observed in the high turbulence region, with a much lower velocity in the stagnation region in the centre of the sample. A nominal flow velocity was reported for the SIJ tests in Chapter 5. However, the variation in flow was much more complex over the surface than the simple nominal value implied.

6.4 Prediction of Particle Trajectories in the SIJ

The full range of sand particle impact angles and velocities were unknown in the SIJ erosion-corrosion tests completed in Chapter 5, limiting the conclusions that could be drawn from the effects of particle impacts on erosion-corrosion results. CFD has been used on several occasions to predict the trajectories of sand particles through various different geometries and has been used to predict particle impact angles, impact velocities, location of impacts on target surfaces and erosion rates [2, 35, 60, 105, 110, 116, 120-124]. The flow model developed for the SIJ nozzle was used to predict the trajectories of sand particles, with sand entering the top of the nozzle in the same location as the flow inlet, as shown in Figure 6.9.

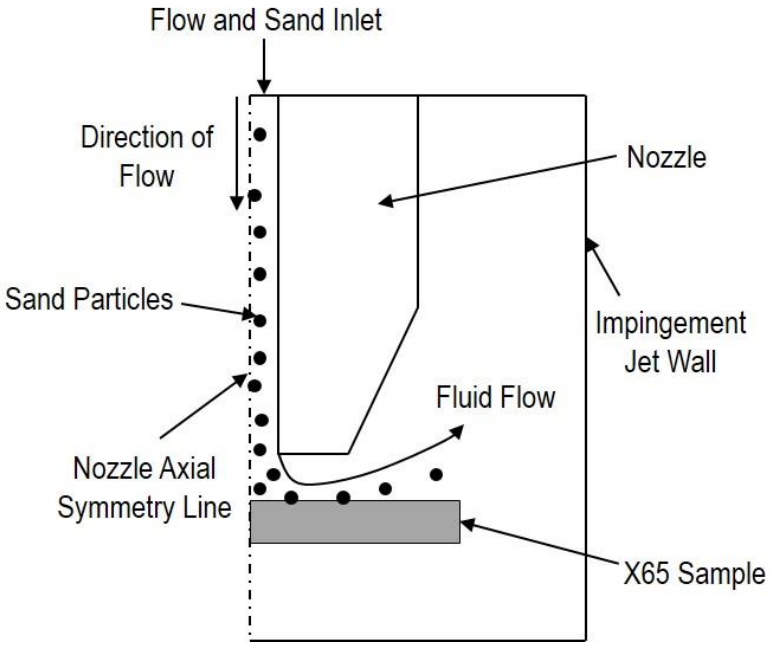

Figure 6.9 Representation of 2D axisymmetric model of SIJ nozzle developed to predict particle trajectories

Gnanavelu et al. [120] and Mansouri et al. [122] predicted the trajectories of sand particles through SIJ nozzles. Their results showed that impingement angle and material removal from particle impingement varied across the surface of a sample in the SIJ. However, their results could not be applied to

the SIJ used in this thesis due to different conditions simulated. Therefore, particle trajectories were required to be predicted using CFD for the nozzle diameter and test conditions used in this thesis, using the flow model developed in this chapter.

Once the fluid flow model was developed, particle trajectories were predicted through the nozzle. Several assumptions were made to simplify the particle trajectories prediction:

- Particles were assumed to be spherical in shape with a diameter of 250 µm. HST60 sand particles were used experimentally with an average diameter of 250 µm and distribution as shown in Chapter 4. The particles had diameters in the range of 100 µm to 500 µm, with approximately 70% of the particles in the size range from 180 µm to 320 µm. The influence of the size of the particles was investigated in more detail later in this chapter
- All surfaces were assumed to be smooth due to the low surface roughness of samples used experimentally. The surface texture was also expected to change during testing, as erosion had been shown to increase surface roughness of metal specimens [17].
- All particles were assumed to have a density of 2650 kg/m^3.
- The surface of the sample was assumed to remain flat throughout a test. Test duration was short enough to ensure that wear scars on the surface of the sample did not get so large to significantly change impact angles and velocities. Gnanavelu [105] showed that the particle impact angles and impact velocities did not vary significantly on a flat surface compared to a typical surface profile measured after an erosion test with a 60 µm maximum wear depth. This effect was investigated in more detail later in the chapter.
- Particles were assumed to be evenly distributed over the entire width of the nozzle inlet diameter, when entering the nozzle. Due to the random nature of the sand particle trajectories as they enter the nozzle and inability to validate their position, it is unknown exactly how the particles enter the nozzle. The simplest assumption that particles were evenly distributed over the inlet was used as no evidence exists to suggest the particles enter the nozzle in any other manner.
- Particles did not influence the fluid flow due to the low volume percentage of particles in the flow. This assumption was only valid for low sand concentrations [95]. The threshold for sand concentrations where particles influence fluid flow is discussed in this chapter.

- Particle-particle interactions were also considered negligible, an acceptable assumption due to the low sand concentration [4].
- Particles were assumed to have a starting velocity equivalent to the flow velocity at the inlet of 20 m/s. Particles have previously been assumed to start with no initial velocity [120], but it is often not stated what initial velocity is used for the particles in CFD models. This effect was investigated in more detail later in the chapter.
- Particles were assumed to only impact on the surface once and no effects of repeated impacts were considered. The influence of coefficients of restitution were investigated further.

These assumptions are common in CFD erosion models for sand flow through different geometries [2, 35, 105, 120]. Due to the difficulty in validating or disproving these assumptions, the same method was used for the CFD model developed in this work. Due to the assumptions involved, using CFD to predict particle trajectories has some limitations. Therefore, the model was intended to be used as a method of improving the general understanding of the impingements of particles on the surface in SIJ erosion and erosion-corrosion tests, rather than being used to calculate erosion rates or impact angles and impact velocities at precise locations on the surface, where the limitations of the assumptions become more significant. For example, by defining a general impact angle in a region on the surface, the erosion wear mechanism, cutting or indentation, could be defined in that region, without requiring precise values and high levels of accuracy from the CFD model. This made the CFD model more reliable for its intended use.

The Lagrangian approach, rather than Eulerian approach, was used to predict the trajectories of the particles due to the low sand concentration and small sized particles used in erosion and erosion-corrosion SIJ tests [4, 215]. The following equation of particle motion was used, based on Newton's laws of motion [125]:

$$m_p \frac{dv_p}{dt} = F_d + F_p + F_b + F_a \tag{6.6}$$

where m_p is the mass of an individual particle, dv_p/dt is the rate of change of particle velocity. The forces on the right-hand side of the equation consist of a drag force, F_d, the force due to the pressure gradient, F_p, the buoyancy force, F_b, and the force due to the added mass of the particle, F_a. This equation and the calculation of the individual forces in the equation have been used regularly in CFD particle trajectory prediction models [2, 35, 105, 120, 121]. The drag force, F_d, is defined by Equation (6.7):

$$F_d = C_D \frac{\pi d_p^2}{8} \rho_f (U - v_p)|U - v_p| \tag{6.7}$$

where C_D is the drag coefficient, defined by Equation (6.8), d_p is the particle diameter, U is the fluid velocity and v_p is the particle velocity.

$$C_D = \frac{24}{Re_p}\left(1 + 0.15 Re_p^{0.687}\right) \tag{6.8}$$

where Re_p is the particle Reynolds number defined by Equation (6.9).

$$Re_p = \frac{\rho_f}{\mu}|U - v_p| d_p \tag{6.9}$$

The pressure gradient force, F_p, exists as a result of local pressure gradients in the flow. The force is produced in the direction of the pressure gradient and is calculated using Equation (6.10):

$$F_p = \frac{1}{4}\pi d_p^3 \nabla p \tag{6.10}$$

where ∇p is the divergence of pressure. It was assumed that the pressure gradient was constant over the volume of the particle.

The buoyancy force, F_b, is the force acting upward on the particle due to the fluid pressure opposing the weight of the particle, defined by Equation (6.11):

$$F_b = \frac{1}{6}\pi d_p^3 (\rho_p - \rho_f) g \tag{6.11}$$

where g is the acceleration due to gravity.

An added mass force, F_a, is applied as an accelerating or decelerating particle in a fluid has to displace some of the surrounding fluid for it to move, calculated using Equation (6.12) [216]:

$$F_a = -\frac{1}{12}\pi d_p^3 \rho_p \frac{dv_p}{dt} \tag{6.12}$$

Particle dispersion in flow fields is effected by the turbulent nature of the flow [217]. To account for the effects of turbulence on the dispersion of particles in the flow, stochastic models are applied. Turbulent dispersion was used in the model developed by Chen et al. [2] and several other models developed at the E/CRC [121, 135] but was not used in the model developed by Gnanavelu [105], justified because of the use of large diameter particles used in the prediction. Discrete random walk, a stochastic model to represent the random nature of the effects of turbulence on the dispersion of the particles, is often used to predict the turbulent dispersion of particles in the flow, defined by Equation (6.13) [2, 121, 134, 135]. Similarly to the assumptions used in the development of the particle trajectory model, this effect was very difficult to

validate or disprove, but was used due to its use in literature for other particle trajectory models. The effect of this parameter was assessed later in this chapter.

$$u' = \xi \sqrt{\frac{2k}{3}} \tag{6.13}$$

where u' is the change in velocity of the particle as a result of turbulence, ξ is a normally distributed random number and k is the turbulent kinetic energy.

A turbulence model with wall functions, such as the k-ω turbulence model, was appropriate to use, rather than a turbulence model that fully resolves to the wall, such as the SST turbulence model, for predictions of fluid flow in the particle tracking CFD model used in this thesis. Mansouri et al. [121] compared the use of the k-ϵ turbulence model, which also uses wall functions to predict fluid flow, with a low Reynolds k-ϵ turbulence model, which fully resolves flow at the wall to investigate if the use of a more robust turbulence model had any significance on the accuracy of particle trajectory predictions. They showed that for particles of large diameter, equal to 256 μm, the fluid flow model solved using the k-ϵ turbulence model gave very similar results for erosion rate predictions when compared with erosion rate predictions using the fluid flow model solved with the low Reynolds k-ϵ turbulence model. These results were also validated with experimental results. When smaller particles were used, with a diameter equal to 25 μm, erosion rate predictions were highly inaccurate using a fluid flow simulation solved using the k-ϵ turbulence model, suggested to be due to the small sized particles being smaller than the thickness of the viscous sub-layer [121]. Sand particles with a diameter of 250 μm were used in the CFD particle trajectory model developed in this thesis, therefore, the k-ω turbulence model was accurate for the fluid flow model used for particle trajectory predictions.

6.4.1 Mesh Sensitivity Study

The mesh sensitivity study completed for the flow model showed that the shear stress prediction was relatively insensitive to changes in the number of elements in the mesh. A separate mesh sensitivity study was completed to determine how sensitive the particle impact data was to changes in the number of elements in the mesh. The particle impact velocities are compared for different meshes in Figure 6.10 and the effect of changing the mesh on particle impact angles are shown in Figure 6.11.

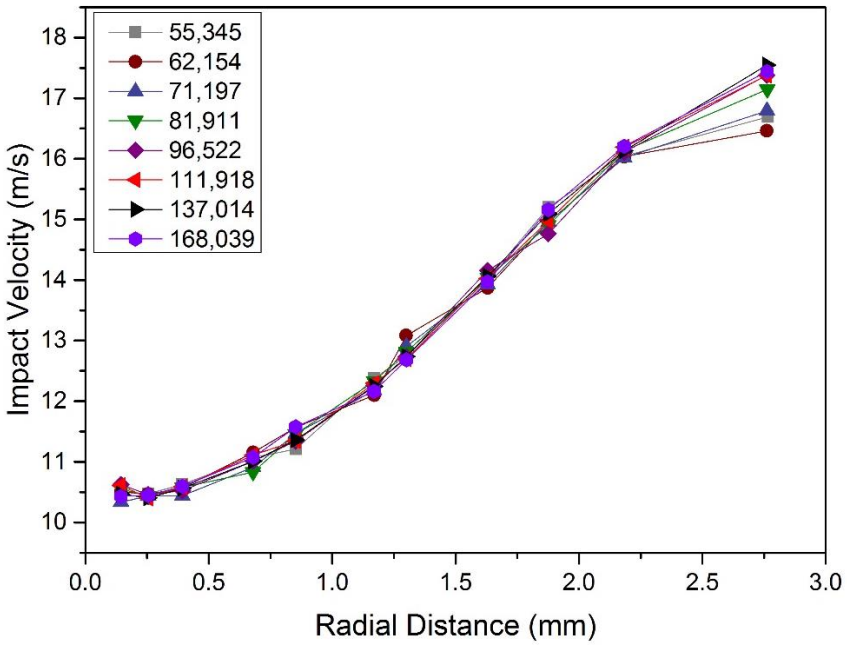

Figure 6.10 Mesh sensitivity study of CFD prediction of particle impact velocities on a target surface in an SIJ nozzle, with a diameter of 4 mm and distance to sample of 5 mm, using the k-ω turbulence model to predict fluid flow through the SIJ nozzle at a flow velocity of 20 m/s and solution temperature of 60°C, containing 250 µm diameter sand particles

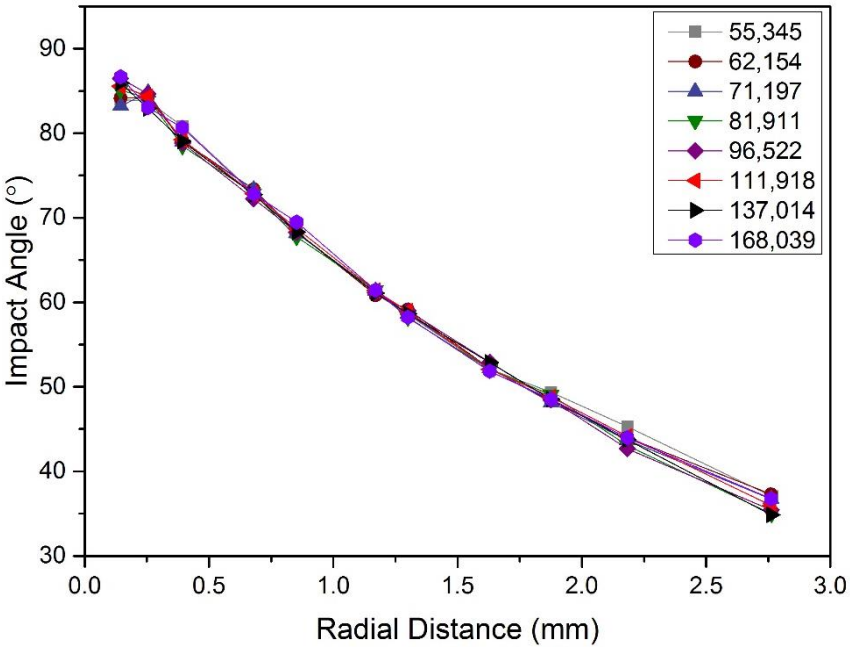

Figure 6.11 Mesh sensitivity study of CFD prediction of particle impact angles on a target surface in an SIJ nozzle, with a diameter of 4 mm and distance to sample of 5 mm, using the k-ω turbulence model to predict fluid flow through the SIJ nozzle at a flow velocity of 20 m/s and solution temperature of 60°C, containing 250 µm diameter sand particles

Particle impact velocities were slightly more sensitive to the number of elements in the mesh than shear stress, shown previously. At the point plotted

furthest from the centre of the sample at approximately 2.8 mm, impact velocity was most sensitive to changes in the number of elements in the mesh, varying by approximately 6% for the range of meshes analysed. At all other points, impact velocities were very similar. The mesh of 81,911 elements, shown previously to be appropriate for the flow model, was also shown to be an appropriate number of elements in the mesh for the predictions of impact angles and impact velocities due to the lack of variation in results caused by changing the mesh.

6.4.2 Prediction of Particle Trajectories

The particle trajectories predicted at a flow velocity of 20 m/s are shown in Figure 6.12. The 250 µm diameter sand particle trajectories were predicted by replicating erosion and erosion-corrosion tests completed in this chapter. The flow model was solved prior to adding particles into the flow using 81,911 elements.

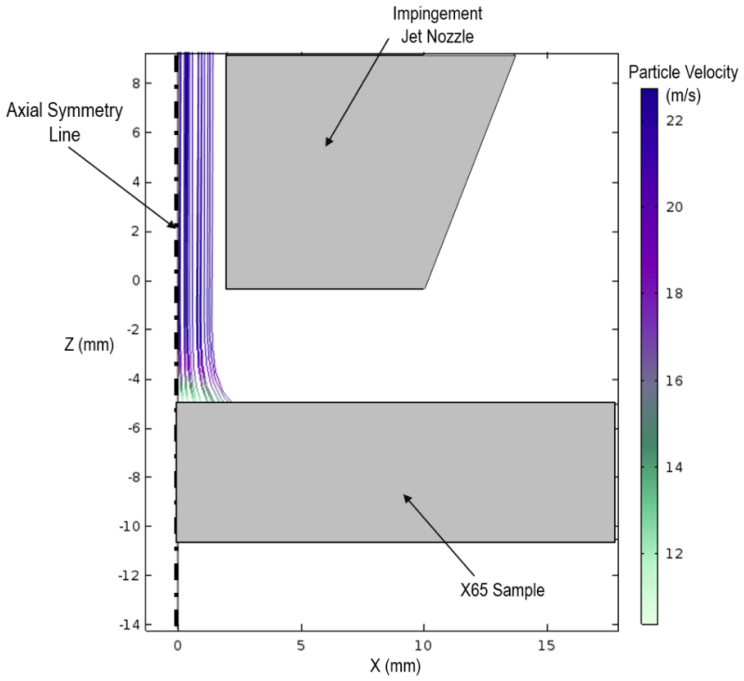

Figure 6.12 CFD prediction of particle trajectories in an SIJ nozzle, with a diameter of 4 mm and distance to sample of 5 mm, using the k-ω turbulence model to predict fluid flow through the SIJ nozzle at a flow velocity of 20 m/s and solution temperature of 60°C, containing 250 µm diameter sand particles

Particle trajectories were then predicted once the flow model was solved. A total of 50,000 particles were released through the nozzle in the model, to give a good statistical range of impacts on the sample surface, enabling a more reliable calculation of average impact angles and average impact velocities in

different regions across the sample surface. A wide range of particle impact angles from approximately 35° to 90° were predicted on the surface of the sample, shown in Figure 6.13. Impact velocities were also predicted in Figure 6.13 that showed the opposite trend to impact angle, with impact velocity increasing across the sample. Almost all of the particle impacts occurred within 3 mm from the centre of the sample.

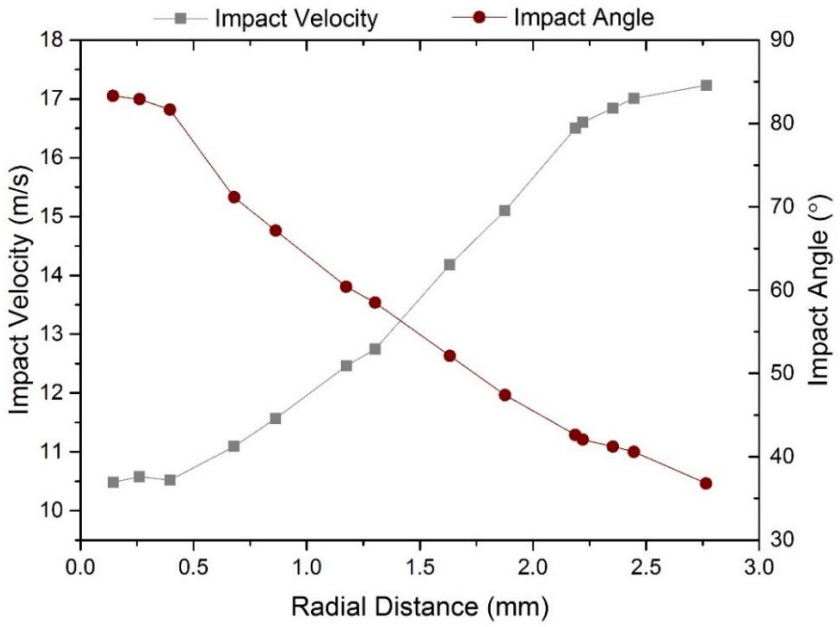

Figure 6.13 CFD prediction of particle impact velocities and impact angles on a target surface in an SIJ nozzle, with a diameter of 4 mm and distance to sample of 5 mm, using the k-ω turbulence model to predict fluid flow through the SIJ nozzle at a flow velocity of 20 m/s and solution temperature of 60°C, containing 250 µm diameter sand particles

6.4.3 Influence of Particle Size on Prediction

The significance of the assumptions on the prediction of particle impingements on the X65 surface was analysed to determine how much influence they had on the results. Ideally, experimental validation of these results would have been completed but this was not possible due to lack of available measurement techniques. One of the assumptions was that all particles had a diameter of 250 µm, but a significant distribution of particle sizes was measured in the sand used experimentally, and erosion rates typically increase when larger particles are present in the flow, suggesting different rates of degradation on the surface could be observed [75, 218].

Lynn et al. [83] showed how changes in particle size had a significant influence on measured erosion rates, but less significance on the impact velocity.

Erosion rates have been reported to be proportional to impact velocity with an exponent of between 2.3 and 2.7 depending on conditions, indicating how erosion rates can vary significantly from small changes in particle velocity [79]. However, the CFD model was not used to determine erosion rates, but to define the general mechanisms of material removal from particle impingement in regions on the sample. The impact velocity, Figure 6.14, and impact angle, Figure 6.15, for a particle diameter of 100 µm and a maximum diameter of 500 µm, measured as the maximum and minimum of the size distribution of the particles, were compared with the results for 250 µm diameter particles.

Less than 0.1% of the particles were measured to have a diameter of less than or equal to 100 µm and less than 0.4% had a diameter of greater than or equal to 500 µm. Predictions for the different sized particles were made using the same mesh of 81,911 elements that was used for the original prediction of impact velocities and impact angles when 250 µm diameter particles were used. The use of smaller particles generally showed a lower velocity and lower impact angle for the particle impacts across the sample surface, and impacts were predicted further from the centre of the sample. However, the trend across the sample for all three sizes of particle was very similar and it was expected that general mechanisms of wear in regions on the surface, in terms of cutting or plastic deformation, would not be effected based on this prediction.

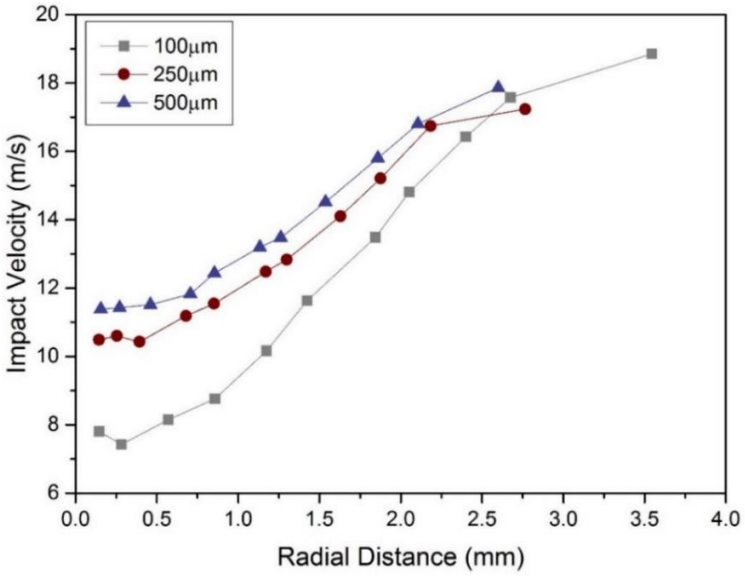

Figure 6.14 CFD prediction of particle impact velocities on a target surface in an SIJ nozzle, with a diameter of 4 mm and distance to sample of 5 mm, using the k-ω turbulence model to predict fluid flow through the SIJ nozzle at a flow velocity of 20 m/s and solution temperature of 60°C, comparing 100 µm, 250 µm and 500 µm diameter sand particles

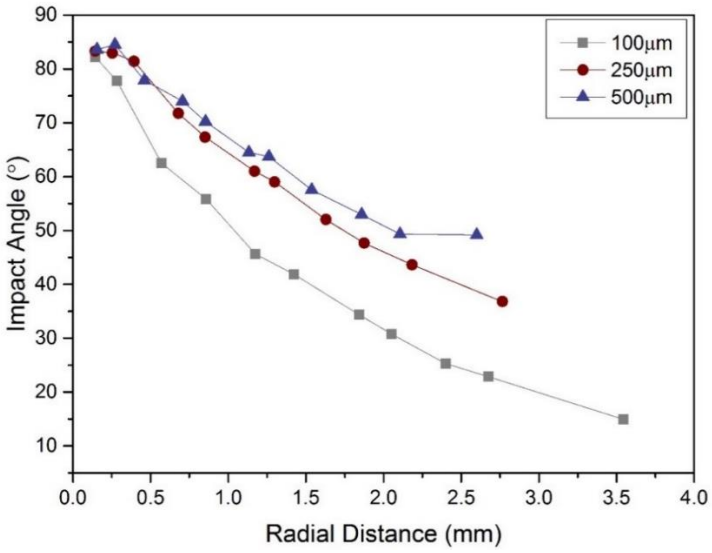

Figure 6.15 CFD prediction of particle impact angles on a target surface in an SIJ nozzle, with a diameter of 4 mm and distance to sample of 5 mm, using the k-ω turbulence model to predict fluid flow through the SIJ nozzle at a flow velocity of 20 m/s and solution temperature of 60°C, comparing 100 µm, 250 µm and 500 µm diameter sand particles

6.4.4 Influence of Surface Profile on Prediction

The surface of X65 samples was assumed to remain flat throughout erosion and erosion-corrosion tests; however, erosion can produce significant wear scars on the surface of samples changing the shape of the sample and effecting the flow locally in this region [34, 60, 105, 120, 122]. Gnanavelu [105] showed that the change in profile did not significantly change the impact angles and impact velocities on the surface in SIJ erosion tests.

A 6 mm diameter wear scar with a maximum depth of 120 µm was measured after 240-minute erosion-corrosion tests at a flow velocity of 20 m/s in a solution containing 1000 mg/L of sand, shown later in Section 6.5. This geometry was modelled to compare impact conditions. To simplify the geometry, an ellipse with a major axis width of 6 mm and minor axis width of 240 µm was modelled to remove a 3 mm wide, 120 µm deep wear scar from the surface of the flat sample in the 2D axisymmetric model. The flow model was required to be solved again due to the change in geometry.

The effect on impact velocity, Figure 6.16, and impact angle, Figure 6.17, were compared for a flat surface and a surface with a 120 µm wear scar. 250 µm diameter particles were used in the prediction. There was no significance of this effect on the impact angle and impact velocity due to the change in profile. Despite a large amount of material being removed from the surface to produce

this wear scar, the majority of the sand particles were larger in diameter than the depth of the wear scar showing how insignificant the depth of the wear scar was by comparison.

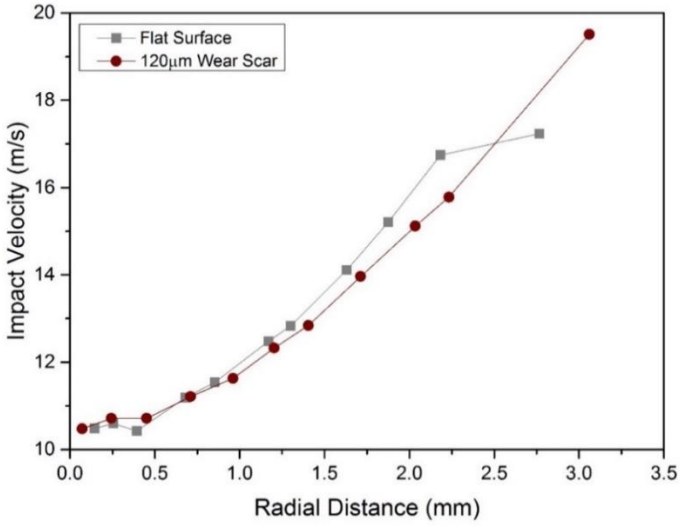

Figure 6.16 CFD prediction of particle impact velocities on a target surface in an SIJ nozzle, with a diameter of 4 mm and distance to sample of 5 mm, using the k-ω turbulence model to predict fluid flow through the SIJ nozzle at a flow velocity of 20 m/s and solution temperature of 60°C, containing 250 µm diameter sand particles, comparing a flat surface and a surface with a wear scar with a maximum depth of 120 µm, representing wear after a 240-minute erosion-corrosion test with 1000 mg/L of sand at a flow velocity of 20 m/s

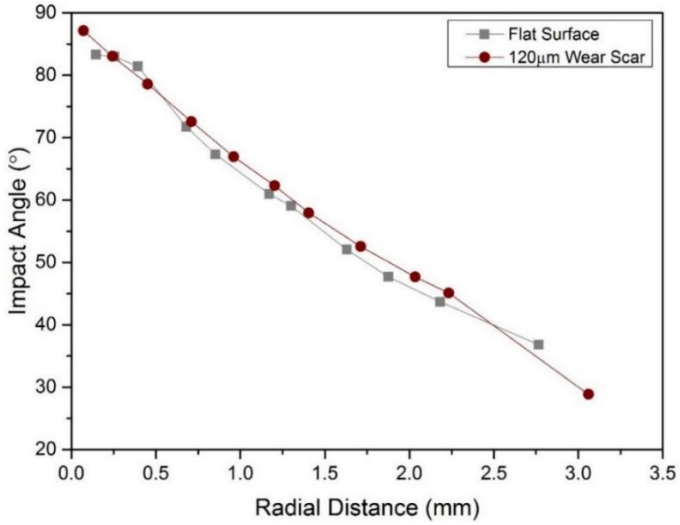

Figure 6.17 CFD prediction of particle impact angles on a target surface in an SIJ nozzle, with a diameter of 4 mm and distance to sample of 5 mm, using the k-ω turbulence model to predict fluid flow through the SIJ nozzle at a flow velocity of 20 m/s and solution temperature of 60°C, containing 250 µm diameter sand particles, comparing a flat surface and a surface with a wear scar with a maximum depth of 120 µm, representing wear after a 240-minute erosion-corrosion test with 1000 mg/L of sand at a flow velocity of 20 m/s

6.4.5 Influence of Repeated Particle Impacts on Prediction

To ensure that the assumption that only initial impacts of the particles on the surface needed to be considered, the rebound of particles at the sample wall were modelled using the statistical coefficients of restitution determined by Grant and Tabakoff [136] and a systematic variation of coefficients of restitution from 0 (an inelastic collision) to 1 (a perfectly elastic collision) in steps of 0.1 to determine if there were multiple impacts on the surface. The Grant and Tabakoff [136] equations, Equation (6.14) and (6.15), were used to calculate the normal and tangential coefficients of restitution as a function of the impingement angle. However, it was unknown how relevant these equations were to fluid flow and sand particle impacts on carbon steel, due to the different experimental conditions the equations were derived from.

$$e_N = 0.993 - 1.76\theta_p - 1.56\theta_p^2 - 0.49\theta_p^3 \quad (6.14)$$

$$e_T = 0.988 - 1.66\theta_p + 2.11\theta_p^2 - 0.67\theta_p^3 \quad (6.15)$$

where e_N is the coefficient of restitution normal to the surface, e_T is the tangential coefficient of restitution, θ_p is the particle impact angle of incidence at the surface. This method of determining the coefficient of restitution was used in the CFD models developed by Chen et al. [2] and Mansouri et al. [121]. Forder et al. [137] developed equations to calculate the coefficients of restitution, but it was not clear under what conditions they were determined from. No other appropriate method was available in the literature for determining coefficients of restitution due to the material specific nature of the coefficients.

The particle trajectories for different coefficients of restitution are shown in Figure 6.18. It was found that for all values of coefficient of restitution, no secondary impacts were observed on the surface of the sample based on the predictions completed, therefore only analysis of single impacts on the sample surface was completed. Figure 6.18 showed that particles impacted on the sample and then rebounded either in the stagnation region of the flow or turbulent jet region of the flow, depending on where the particles impacted on the sample surface. Particles were transported away from the sample and radially towards the edge of the sample. This is explained by the high radial component of flow velocity as flow spreads from the impinging jet nozzle towards the edge of the sample, transporting the particles in this direction.

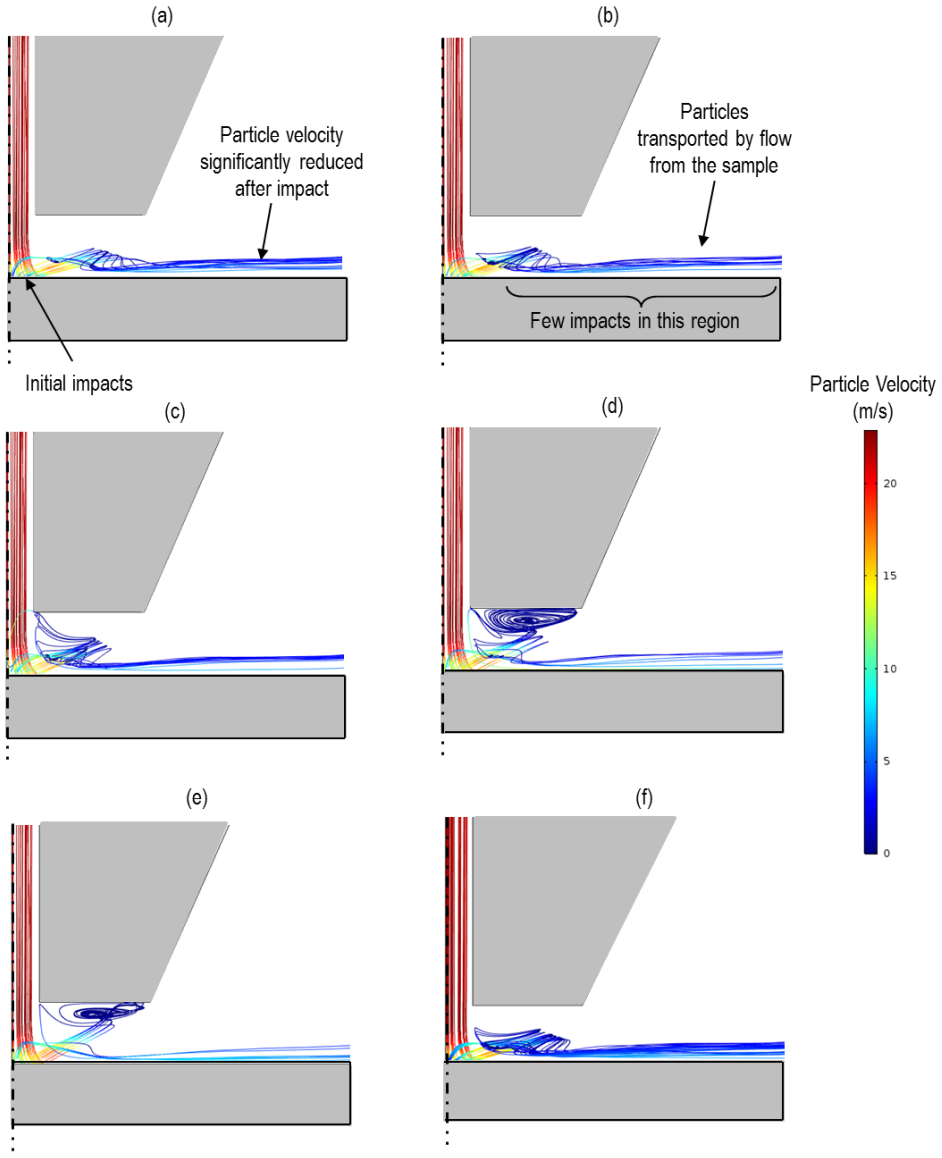

Figure 6.18 CFD prediction of particle trajectories in an SIJ nozzle, with a diameter of 4 mm and distance to sample of 5 mm, using the k-ω turbulence model to predict fluid flow through the SIJ nozzle at a flow velocity of 20 m/s and solution temperature of 60°C, containing 250 µm diameter sand particles, comparing particle rebounds using coefficient of restitution of (a) 0.2, (b) 0.4, (c) 0.6, (d) 0.8, (e) 1.0 and (f) coefficients calculated using the Grant & Tabakoff [136] equations

With a much smaller, potentially negligible, vertical component of flow velocity, fluid drag acting on the particles in the vertical direction would be significantly reduced, limiting the vertical motion of the particle back towards the sample surface after rebound. Therefore, there was no component of the fluid velocity that could cause the particles to impact on the surface. Smaller sized particles with lower equilibration numbers would be more influenced by random fluctuations in the flow as a result of turbulence in the turbulent jet region, potentially creating more vertical drag force that could lead to further particle impacts [4]. It is also possible that sand particles rebounding from the surface

could rebound into the path of other particles being transported to the surface from the nozzle, influencing their trajectories. However, low sand concentrations used in SIJ erosion and erosion-corrosion tests meant that particle-particle interactions could be assumed to be negligible, therefore this was not expected to be a significant influence [4].

Whilst it is accepted that assumptions limit the reliability of this prediction and that it, therefore, did not prove that repeated particle impacts on the sample surface did not occur experimentally, it did give a good indication that there wouldn't be a significant quantity of repeated impacts and that particle velocities would be significantly reduced after the first impact, reducing the potential degradation that could occur from multiple impacts. Hutchings [73] reported that at least 90% of the energy would be absorbed during impact, significantly reducing the rebound velocity of the particle. Okita et al. [88] reported that erosion as a result of repeated particle impacts was not as significant for liquid flow as for gas flow. It is accepted that more research is required into the effects of particle rebounds, but based on the expectation of a significantly reduced velocity after initial impact, it was assumed that any secondary impacts were not as significant from a material removal perspective as initial impacts.

6.4.6 Influence of the Squeeze Film on Prediction

Despite the limitations of the theory of squeeze films suggested by Clark and Burmeister [77], highlighted in Section 3.3.2, no further studies exist that are relevant to this work to confirm or disprove the theory of reduced particle impact velocity as a result of a squeeze film. The effects of squeeze films, however, were not thought to influence the particle impacts in the conditions in this work due to the significantly lower viscosity of the solutions being tested in. Equation (6.16) was used by Clark and Burmeister [77] and developed by Wenglarz [219] to calculate the particle stopping distance, S, equivalent to the thickness of squeeze film required to prevent impact on a surface.

$$S = \frac{v_o d_p^2 \rho_p}{18\mu} \tag{6.16}$$

where v_o is the velocity of the particle as it enters the boundary layer. The particle velocity from CFD predictions showed a range of values across the surface. At a nozzle flow velocity of 20 m/s, a range of flow velocities were predicted using the CFD model, with the lowest particle impact velocity on the sample predicted to be approximately 10.9 m/s, in the central stagnation

region on the sample. This particle impact velocity was used in Equation (6.16) to give a value of S of 0.2 m, assuming a 250 µm diameter particle. The boundary layer thickness, δ, was reportedly 0.1 mm by Wenglarz [219], used in the calculation completed by Clark and Burmeister [77]. A ratio of δ/S > 0.4 was reported as a threshold above which the boundary layer effects the particle motion close to the surface. Therefore, the squeeze film was expected to have no influence on impacts in the conditions modelled in this thesis, as the ratio of δ/S was significantly lower than the reported threshold value.

Acoustic emission monitoring was used to determine particle impacts at the surface of carbon steel surfaces in SIJ erosion tests at flow velocities from 7 m/s to 15 m/s by Ukpai et al. [145] that showed that the quantity of measured particle impacts agreed with the theoretical number of expected impacts, suggesting that the effect of the squeeze film had not had any significant effects on reducing particle impacts.

6.4.7 Particle-Particle Interactions and Fluid Coupling

It was assumed that the sand particles had no influence on the fluid flow and that there was no particle-particle interactions. This assumption was important to ensure that sand particles did not influence the flow, and to assume that there was no interactions between the particles and hence Lagrangian particle motion could be assumed. The assumption that particles did not interact with other particles applied when a mass loading ratio, γ, was less than 1, calculated using Equation (6.17) [4].

$$\gamma = \frac{M_p}{V_f \rho_f} \tag{6.17}$$

where M_p is the total mass of the sand particles in a volume of fluid, V_f, with density ρ_f. For a sand concentration of 1000 mg/L in a 50 L water solution at a temperature of 60°C, the mass loading ratio was equal to 0.001, significantly below the limit for particle-particle interactions to occur. Therefore, it was acceptable to assume that particle-particle interactions did not occur in flow through the SIJ nozzle at 20 m/s with a sand concentration of 1000 mg/L.

6.4.8 Influence of Particle Initial Velocity and Turbulent Dispersion

The assumption that the particles had an initial velocity equal to the velocity of the flow when the particles entered the nozzle was assessed. Gnanavelu [105] assumed that particles entered the SIJ nozzle with no initial velocity,

whilst it was assumed in the model in this work that the particle velocity was equal to the flow velocity. Figure 6.19 and Figure 6.20 showed that this assumption had no significant influence on the prediction and that the drag force exerted by the fluid was much more significant on the velocity of the particles than the initial velocity specified in the model inputs.

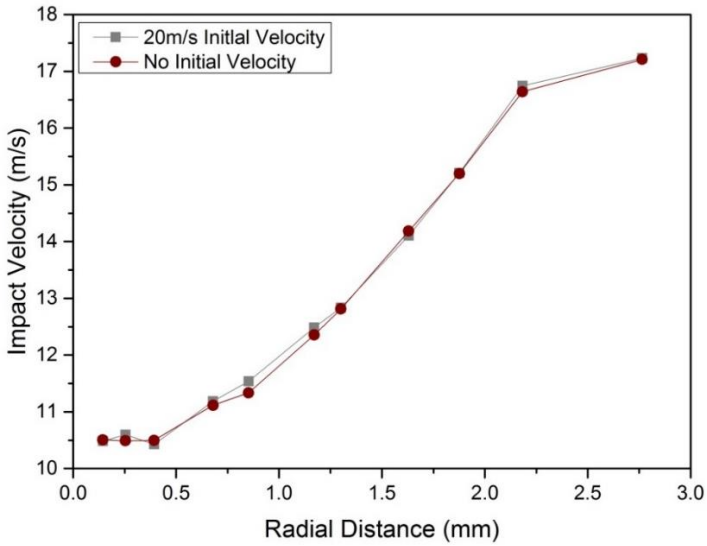

Figure 6.19 CFD prediction of particle impact velocities on a surface in an SIJ nozzle, with a diameter of 4 mm and distance to sample of 5 mm, using the k-ω turbulence model to predict fluid flow through the SIJ nozzle at a flow velocity of 20 m/s and solution temperature of 60°C, containing 250 µm diameter sand particles, comparing stationary particles at inlet and a particles with initial velocities equal to the fluid inlet velocity of 20 m/s

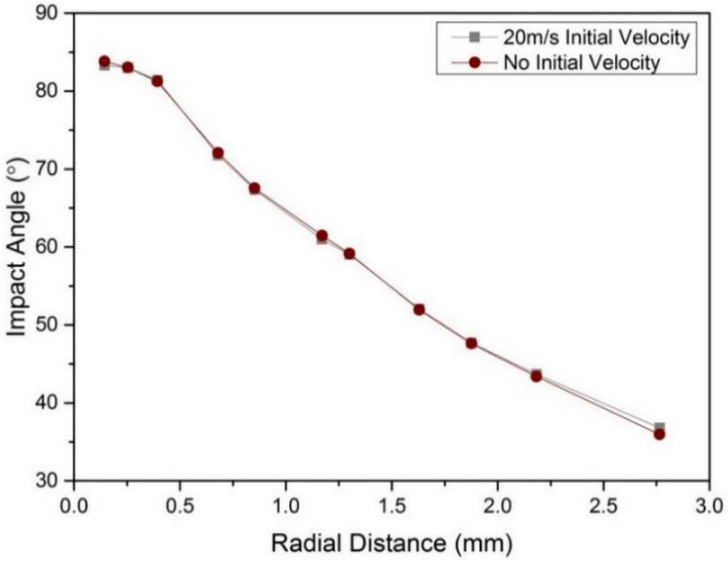

Figure 6.20 CFD prediction of particle impact angles on a surface in an SIJ nozzle, with a diameter of 4 mm and distance to sample of 5 mm, using the k-ω turbulence model to predict fluid flow through the SIJ nozzle at a flow velocity of 20 m/s and solution temperature of 60°C, containing 250 µm diameter sand particles, comparing stationary particles at inlet and a particles with initial velocities equal to the fluid inlet velocity of 20 m/s

The significance of turbulent dispersion on the particle trajectories was also analysed. A simulation completed with and without turbulent dispersion using the discrete random walk model was compared in Figure 6.21 and Figure 6.22. The effect of turbulent dispersion on the impact velocity of the particles at the specimen surface was negligible. The effect on particle impact angle was also negligible, expected due to the large particles used.

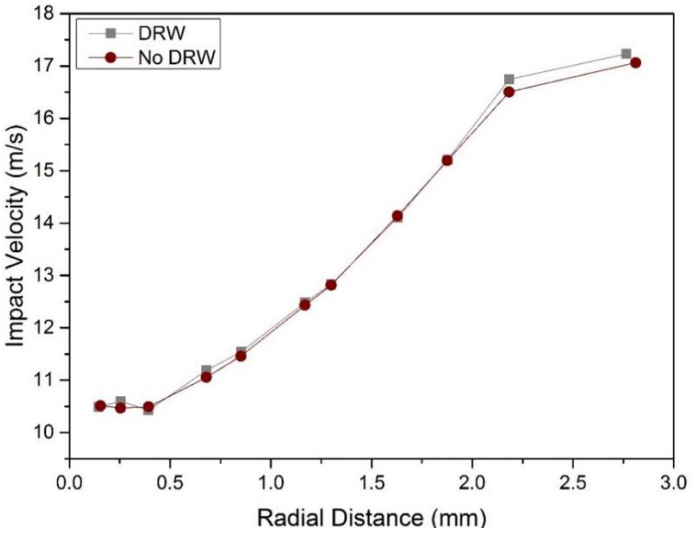

Figure 6.21 CFD prediction of particle impact velocities on a target surface in an SIJ nozzle, with a diameter of 4 mm and distance to sample of 5 mm, using the k-ω turbulence model to predict fluid flow through the SIJ nozzle at a flow velocity of 20 m/s and solution temperature of 60°C, containing 250 µm diameter sand particles, comparing the use of a discrete random walk (DRW) model to predict turbulent dispersion

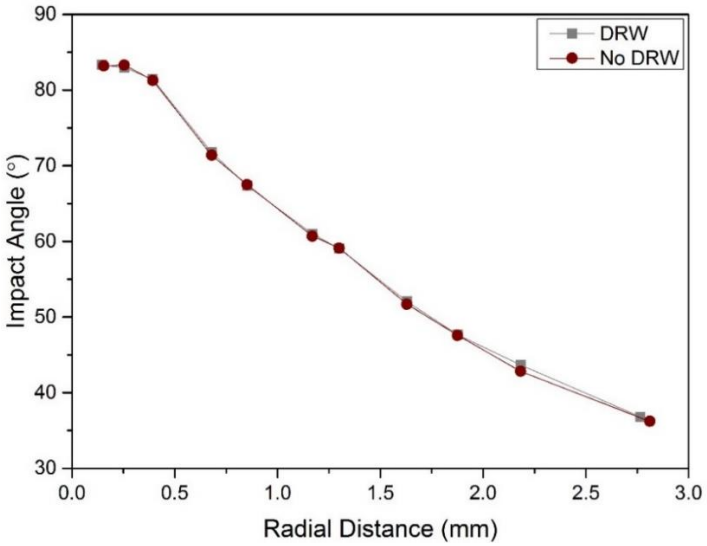

Figure 6.22 CFD prediction of particle impact angles on a target surface in an SIJ nozzle, with a diameter of 4 mm and distance to sample of 5 mm, using the $\boldsymbol{k}$-$\boldsymbol{\omega}$ turbulence model to predict fluid flow through the SIJ nozzle at a flow velocity of 20 m/s and solution temperature of 60°C, containing 250 µm diameter sand particles, comparing the use of a discrete random walk (DRW) model to predict turbulent dispersion

6.4.9 Comparison with Gnanavelu Model

Numerical or experimental validation of the particle trajectory predictions was difficult to the lack of availability of mathematical solutions and difficulties in experimental measurements of particle impact angle and impact velocity. However, the CFD model developed by Gnanavelu [105] was used as a comparison to demonstrate that the methodology used in this thesis agreed with the results predicted by Gnanavelu [105]. Gnanavelu [105] also validated the model by predicting the resulting surface profile after particle impacts and compared this with experimental results, and showed that very good agreement was measured between the prediction and experimental results. A nozzle diameter of 7 mm and height from nozzle to sample of 5 mm was used, with a flow velocity of 5 m/s and a temperature of 23°C to replicate the conditions modelled by Gnanavelu [105]. The comparison of predicted impact angle and impact velocity is shown in Figure 6.23. The use of the $\boldsymbol{k}$-$\boldsymbol{\omega}$ turbulence model, compared to the $\boldsymbol{k}$-ϵ turbulence meant that flow velocities were slightly different, with higher impact velocities predicted using the $\boldsymbol{k}$-$\boldsymbol{\omega}$ model in the stagnation region and lower impact velocities measured in the turbulent region towards the edge of the sample.

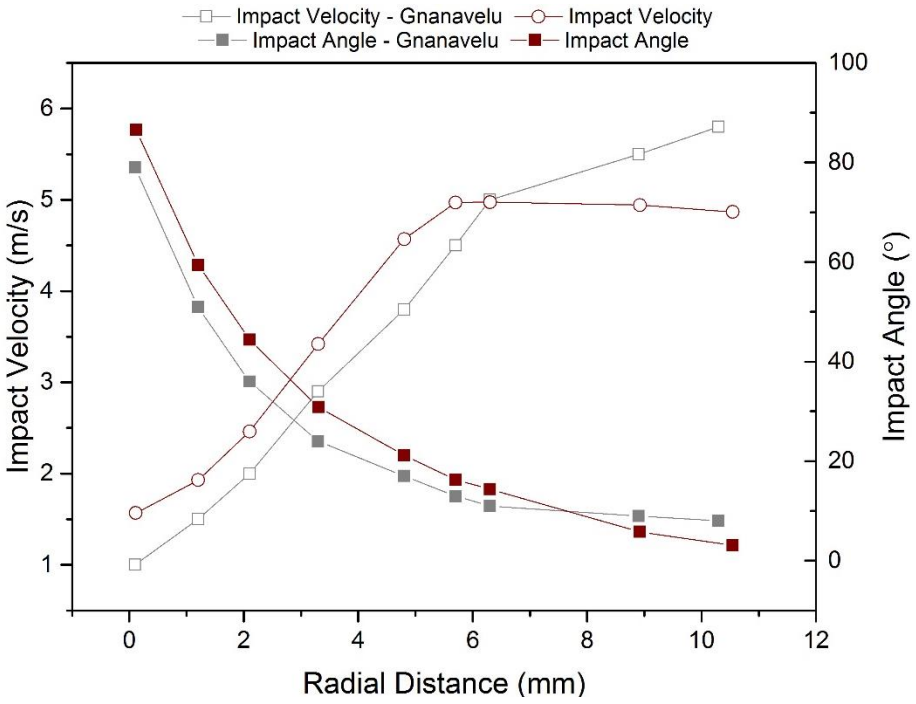

Figure 6.23 CFD prediction of particle impact velocities on a target surface in an SIJ nozzle, with a diameter of 7 mm and distance to sample of 5 mm, using the k-ω turbulence model to predict fluid flow through the SIJ nozzle at a flow velocity of 5 m/s and solution temperature of 25°C, compared with the model developed by Gnanavelu [105]

6.5 Measurement of Erosion-Corrosion and Interactions in SIJ Tests

The aim of the CFD model was to produce results that could be used to provide more information about the mechanisms of erosion wear on the surface of a sample used in erosion-corrosion SIJ tests, which was not fully explained in the tests completed in Chapter 5. CFD predictions in the first part of this chapter were used in combination with experimental results to gain further insight into erosion-corrosion mechanisms. Flow-induced corrosion, erosion and erosion-corrosion tests were completed using the SIJ to measure the contribution of each parameter to total erosion-corrosion material loss and investigate the interactions between erosion and corrosion in more detail.

6.5.1 Definition of Regions on the Surface of X65 Samples Used in the SIJ

To gain a better understanding of how particle impact angles and particle impact velocities affected the surface of carbon steel samples during erosion

and erosion-corrosion tests, different regions were chosen on the surface of the sample, Figure 6.24. The regions were determined through a combination of CFD and from a surface profile after an erosion-corrosion test measured using a Bruker NPFLEX white light interferometer. CFD predictions of impact angle and impact velocity, reported as average values in Figure 6.24, assumed that the surface was flat and were determined using the predicted results shown in Figure 6.13. The influence of wear scar geometry on the predictions of impact angle and impact velocity was shown not to have a significant influence on predictions and general wear mechanisms in the regions identified, as shown previously in Figure 6.16 and Figure 6.17.

Figure 6.24 shows a wear profile after a 240-minute erosion-corrosion test at 20 m/s, 60°C with a 1000 mg/L sand concentration, with the four regions identified. The particle impact data in each region is summarised in Table 6.1. The wear scar showed some very slight asymmetry, potentially due to slight misalignment of the specimen in the rig. However, this was not significant and it should be noted that the X-axis on the wear scar shown in Figure 6.24 is several orders of magnitude greater than the Y-axis, exaggerating any asymmetry observed in the wear scar.

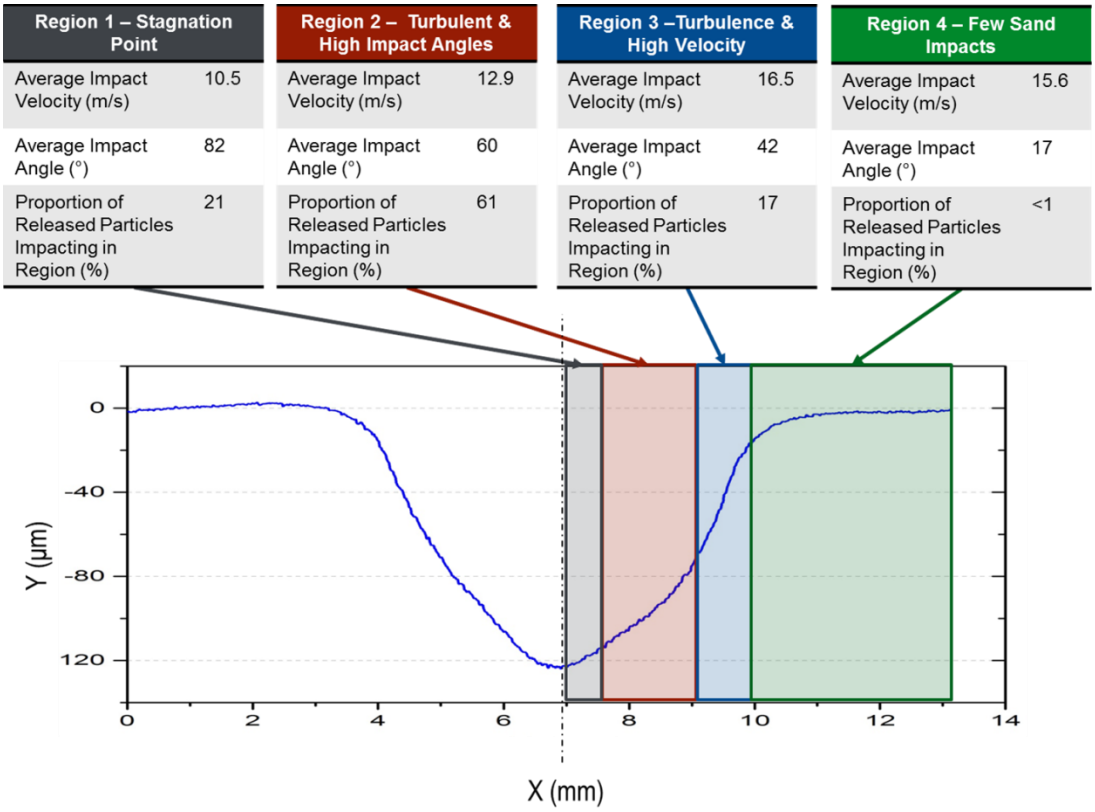

Figure 6.24 Identification of four regions on the profile of an X65 sample after a 240-minute erosion-corrosion test at 20 m/s, 60°C with 1000 mg/L of sand showing different erosion conditions in each of the regions as defined by CFD predictions of impact angle and impact velocity on a flat surface

Table 6.1 Particle impact data from CFD predictions of particle trajectories at a flow velocity of 20 m/s in the four regions identified on the surface of the SIJ sample, assuming a flat surface

Region	r (mm)	θ_p (°)	v_p (m/s)	Proportion of Impacts in Region (%)
1	$0 \leq r < 0.5$	82	10.5	21
2	$0.5 \leq r < 2$	60	12.9	61
3	$2 \leq r < 3$	42	16.5	17
4	$r \geq 3$	22	15.6	<1

Region 1 covered the width of the stagnation point and experienced high particle impact angles at relatively low speeds. In this region, most of the erosion wear was expected to be in the form of plastic deformation due to indentation from the particles at high impact angles [20]. Region 2 showed a turbulent region, with high impact angles but increased impact velocity compared to Region 1. Region 3 showed a highly turbulent region, with cutting wear of particle impacts expected due to lower impact angles [20]. Region 4 was expected to have very few particle impacts. Due to the limitations of the CFD model, because of the necessary assumptions, defining regions enabled a more general understanding of the erosion mechanisms on the surface to be identified, with average values defined rather than relying on precise outputs of impact angles and impact velocities from CFD.

6.5.2 Erosion-Corrosion and Erosion-Corrosion Interactions

Flow-induced corrosion, erosion and erosion-corrosion mass loss tests using the SIJ were completed. Figure 6.25 showed that each of the contributing parameters to total erosion-corrosion degradation changed linearly with time. All mechanisms showed a linear increase in mass loss, suggesting a constant degradation rate throughout the test. The contributions of erosion and corrosion were relatively similar throughout the test period in these conditions, and there was a significant contribution of corrosion-enhanced erosion.

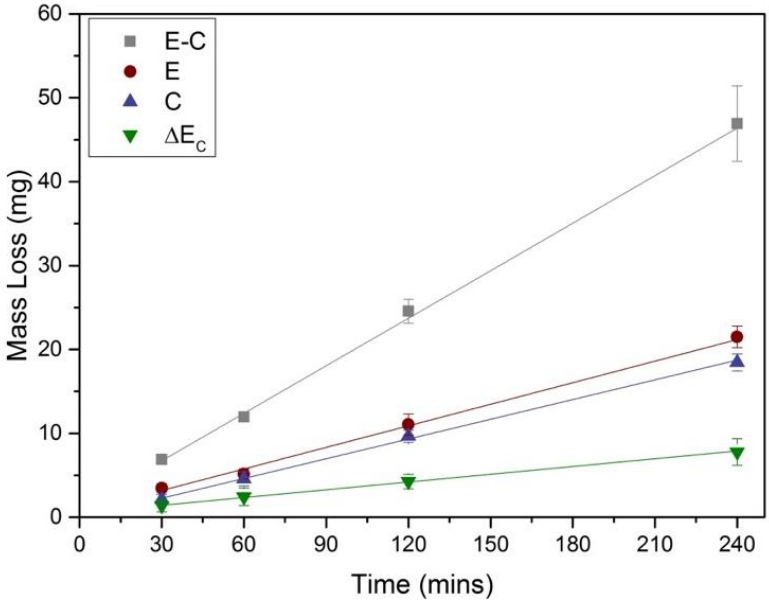

Figure 6.25 Contributions of erosion-corrosion components to total degradation over time in SIJ mass loss tests, where 'E-C' is erosion-corrosion degradation at a flow velocity of 20 m/s in a CO_2-saturated, 60°C, pH 4.7, 2% NaCl solution containing 1000 mg/L of sand particles with an average diameter of 250 µm; 'E' is pure erosion degradation at a flow velocity of 20 m/s in a N_2-saturated, 60°C, pH 7 solution containing 1000 mg/L of sand; 'C' is flow-induced corrosion degradation at a flow velocity of 20 m/s in a CO_2-saturated, 60°C, pH 4.7, 2% NaCl solution and 'ΔE_C' is corrosion-enhanced erosion calculated using Equation (2.1)

The electrochemistry measured corrosion rates for erosion-corrosion and flow-induced corrosion tests are compared in Figure 6.26. Similar corrosion rates were observed between the measured corrosion rates in flow-induced corrosion conditions and erosion-corrosion conditions. Mechanisms of pure corrosion in both environments were expected to be similar with flow accelerating the corrosion rates, compared to static environments, by increasing the transport of electrochemically active species to and from the carbon steel surface [3]. Both hydrogen evolution, Equation (3.5), and direct carbonic acid reduction, Equation (3.6), cathodic reactions were expected in the pH 4.7 conditions. Similarly to Chapter 5, these conditions prevented the formation of $FeCO_3$ layers on the surface of the samples. The mechanisms of flow-induced corrosion and transport of species to and from the sample surfaces were not expected to be influenced by the presence of sand particles, as the low sand concentration was expected to have no influence on the flow [4]. The similar corrosion rates in Figure 6.26 also indicated that corrosion mechanisms did not change between flow-induced corrosion and erosion-corrosion conditions.

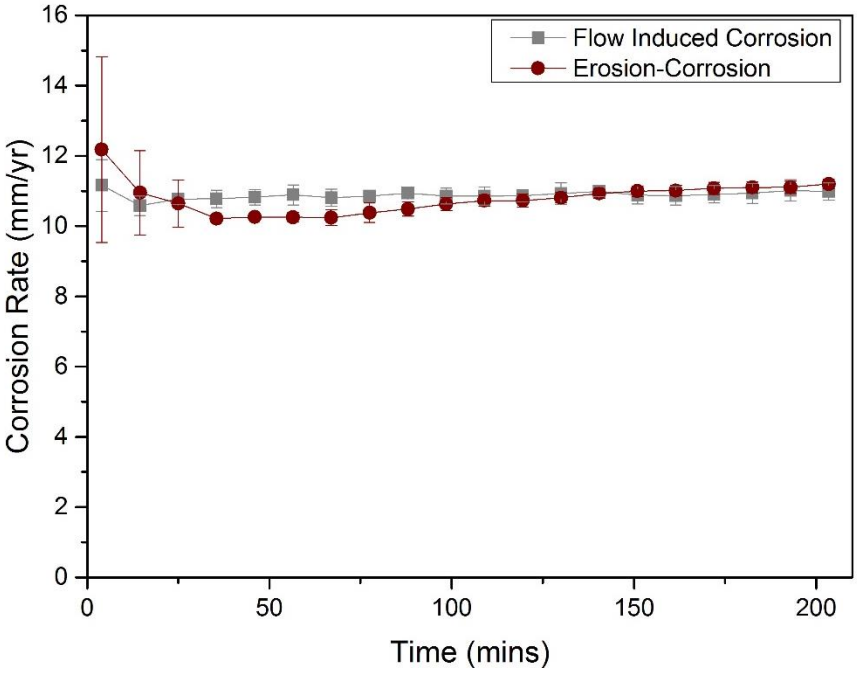

Figure 6.26 Comparison of in-situ corrosion rates measured using EIS in flow-induced corrosion tests at a flow velocity of 20 m/s in a CO_2-saturated, 60°C, pH 4.7, 2% NaCl solution and erosion-corrosion tests in the same conditions containing 1000 mg/L of sand

The influence of erosion on the carbon steel surface could potentially have influenced corrosion rates of carbon steel, resulting in erosion-enhanced corrosion [15]. A slight increase in corrosion rate was observed during the test in erosion-corrosion conditions, but this did not result in a significant difference when compared with flow-induced corrosion rates. Longer term tests may have shown that this increase might continue, but due to the increasing sample surface area from mechanical degradation during the test and potential degradation of sand particles, the conditions during longer term tests could change significantly from the tests completed over a 240-minute period, making a direct comparison between results difficult. Therefore, it was the assumed that erosion-enhanced corrosion was negligible for the comparison in these tests. As the increase in corrosion rate from the start of erosion-corrosion tests to the end was <1 mm/yr any erosion-enhanced corrosion effect over a 240-minute period was insignificant in comparison to the overall degradation rates measured in the tests shown in Figure 6.25.

The Tafel constants used to calculate the corrosion rates in Figure 6.26 were determined using the Tafel plots in Figure 6.27, with a Stern-Geary coefficient of 27.3 (β_a = 108 mV/decade, β_c = 151 mV/decade) for erosion-corrosion tests and 26.9 (β_a = 99 mV/decade, β_c = 165 mV/decade) calculated for flow-induced corrosion tests at a potential of OCP ± 50 mV.

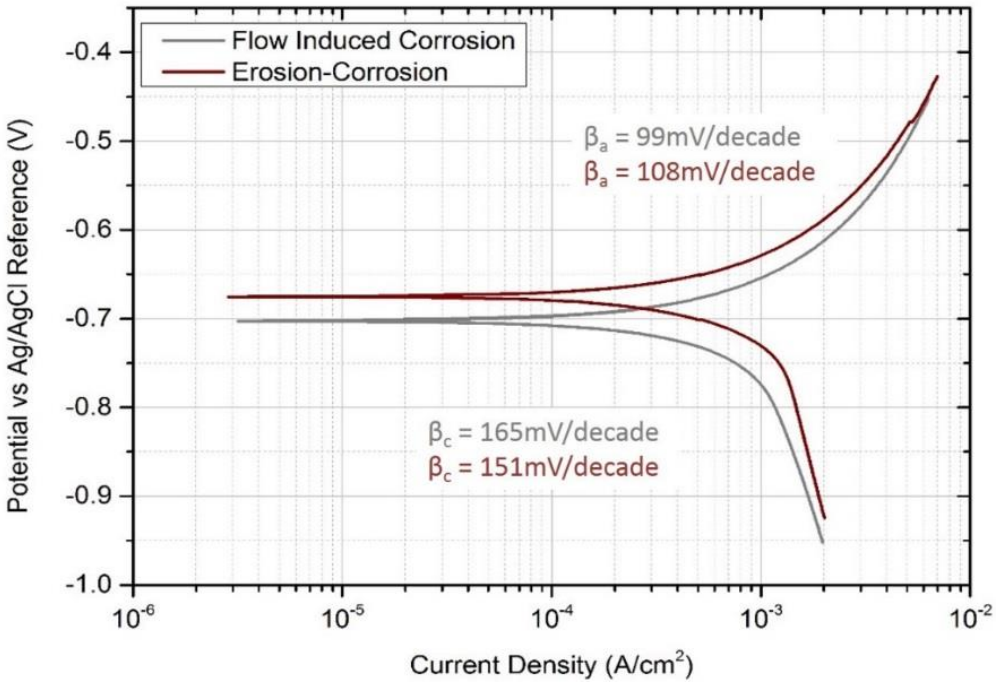

Figure 6.27 Tafel plots of X65 carbon steel samples measured using in flow-induced corrosion tests at a flow velocity of 20 m/s in a CO_2-saturated, 60°C, pH 4.7, 2% NaCl solution and erosion-corrosion tests in the same conditions containing 1000 mg/L of sand

The contribution of each degradation mechanism to total erosion-corrosion degradation is shown in Figure 6.28. Proportionally, erosion wear accounted for a smaller contribution to total erosion-corrosion degradation from 30 minutes onwards, dropping from approximately 50% to 43%-45%. A higher proportion of corrosion degradation was measured from this point onwards.

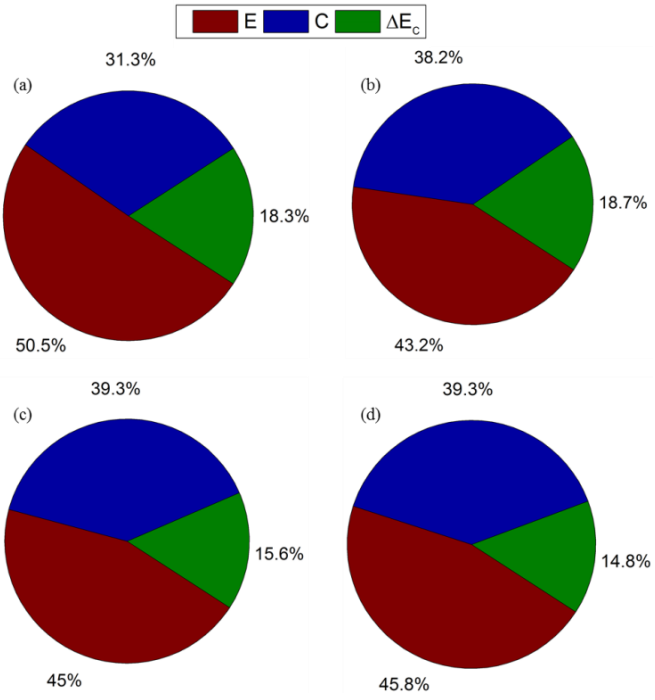

Figure 6.28 Contribution to total erosion-corrosion degradation of erosion (E), corrosion (C) and corrosion-enhanced erosion (ΔE_C) to total erosion-corrosion degradation in (a) 30-minute, (b) 60-minute, (c) 120-minute and (d) 240-minute SIJ tests

6.6 Analysis of Surfaces

Several surface analysis techniques were used to analyse the surfaces of the X65 samples in the 30, 60, 120 and 240 minute tests. Surfaces were profiled and properties such as the surface roughness and hardness were measured to investigate the causes of the interactions more thoroughly.

6.6.1 Surface Profiles

Surface profiles of the samples were measured using a Bruker NPFLEX interferometer. The surface was filtered to remove the form and tilt of the sample so that the 3D profiles could be extracted from a flat surface to distinguish between the form of the sample and the mechanical damage on the surface of the sample. 3D profiles were measured over the entire surface of the samples after erosion-corrosion and erosion tests, with 2D profiles through the centre of the wear scar extracted from the 3D profile to compare wear depth between the samples. Erosion and erosion-corrosion degradation profiles after 240 minutes are compared in Figure 6.29. Error bars shown in Figure 6.29 were determined based on a single profile measured from two samples for each erosion and erosion-corrosion specimens, with the average depth reported, measured through the centre of the wear scar.

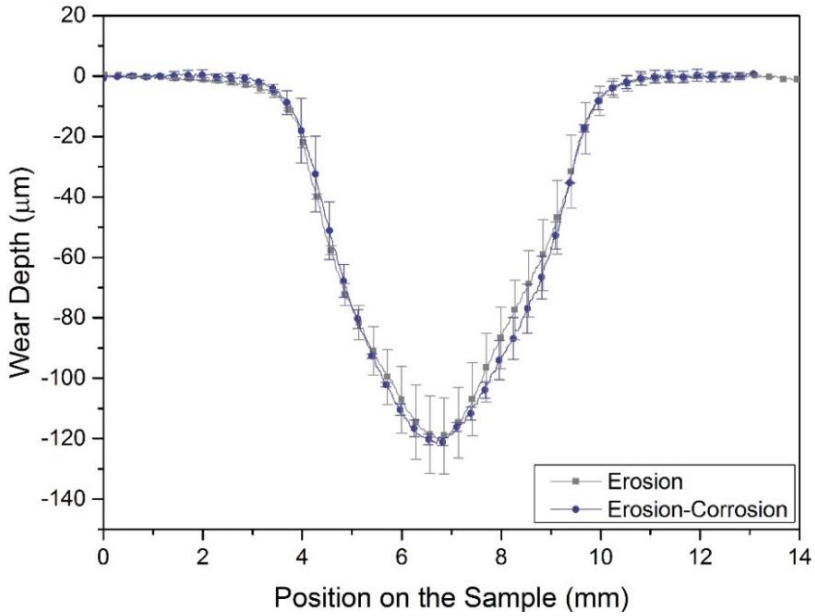

Figure 6.29 Surface profiles of surfaces after 240-minute SIJ erosion tests at a flow velocity of 20 m/s in a N_2-saturated solution at 60°C containing 1000 mg/L of sand and SIJ erosion-corrosion tests in CO_2-saturated conditions

Erosion-corrosion specimens appeared to be smoother, with less variation in results. This may have been as a result of enhanced corrosion removing surface features after particle impacts, such as lips, potentially making the surface smoother [15]. However, there was limited evidence to suggest this and it was also likely that general variation in experimental conditions could have contributed to this difference.

The 2D profiles, extracted from the 3D profiles, were shown through the centre of the wear scars on each of the samples, where the penetration depth was at a maximum on the surface. Similar profiles were observed between erosion and erosion-corrosion samples. These profiles partially validated the predictions of the CFD model, as no significant wear was observed towards the edge of the sample, outside of the wear scar, with the width of the wear scar being approximately 6 mm in diameter. This was shown in the CFD model, where almost all of the particle impacts occurred within a radial distance of 3 mm from the centre of the sample.

A ‘u-shaped’ wear scar was observed on both samples, with typical erosion wear scars showing a ‘w-shape’, with least degradation observed in the centre of the samples [120, 122]. However, the erosion SIJ tests completed by Mansouri et al. [122] and Gnanavelu et al. [120] were completed at lower flow velocities, with Gnanavelu et al. [120] reporting a particle impact velocity of 1 m/s in the centre of the sample. Impact velocities were in excess of 10 m/s, for the work completed in this thesis, in the stagnation region as shown in Figure 6.13. Therefore, degradation was expected to be much more significant in the central stagnation region, with high quantities of particle impacts predicted. Hu et al. [34] also observed ‘u-shaped’ wear scars in erosion SIJ tests at a flow velocity of 20 m/s, suggesting a transition from ‘w-shaped’ to ‘u-shaped’ wear scars as flow velocity increases.

6.6.2 Degradation of Sand Particles over Time

Sand particles were continuously recirculated during SIJ erosion and erosion-corrosion tests, therefore impinging onto the surface of the sample a significant quantity of times during a test. Potential degradation of these sand particles as a result of repeated impingement could have reduced their size, resulting in less erosive conditions towards the end of 240-minute tests

compared with 30-minute tests, making a direct comparison between erosion conditions difficult if the change was significant. A sample of sand particles was filtered after a 240-minute erosion test and measured using a Malvern Mastersizer 2000 particle sizer and compared with the size of sand particles measured prior to testing, shown in Figure 6.30. The analysis showed that there was almost no variation in the size of sand particles over time, therefore this effect was not significant in erosion and erosion-corrosion results.

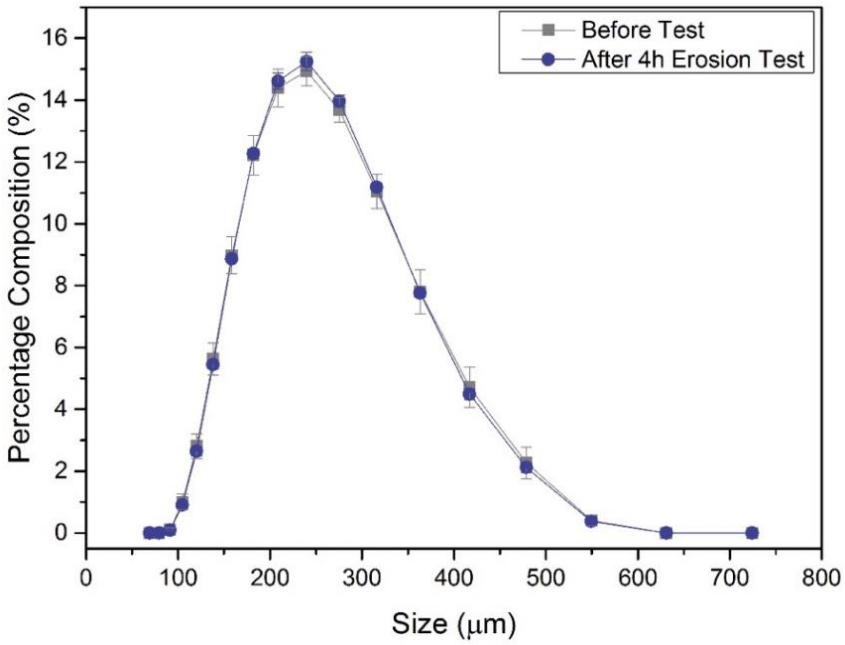

Figure 6.30 Change in size distribution of sand particles after a 240-minute erosion test in a N_2-saturated, 60°C solution containing 1000 mg/L of sand at a flow velocity of 20 m/s compared with sand size before the test

6.6.3 SEM Analysis of Surfaces

SEM images of each of the regions in Figure 6.31 of erosion and erosion-corrosion samples after 240 minutes confirmed that high amounts of plastic deformation occurred in region 1 due to high impact angles. Several impact zones could be seen in this region on both erosion and erosion-corrosion samples. In region 2 and region 3 more cuts were seen on the surface due to the low impact angle of the sand particles, with the surfaces of the samples visibly rougher in these regions. Region 4 showed no significant impacts on the surface. Similar surfaces were observed between erosion and erosion-corrosion samples in each of the four regions. Comparison with an untested surface can be made with the SEM image shown previously in Figure 4.3.

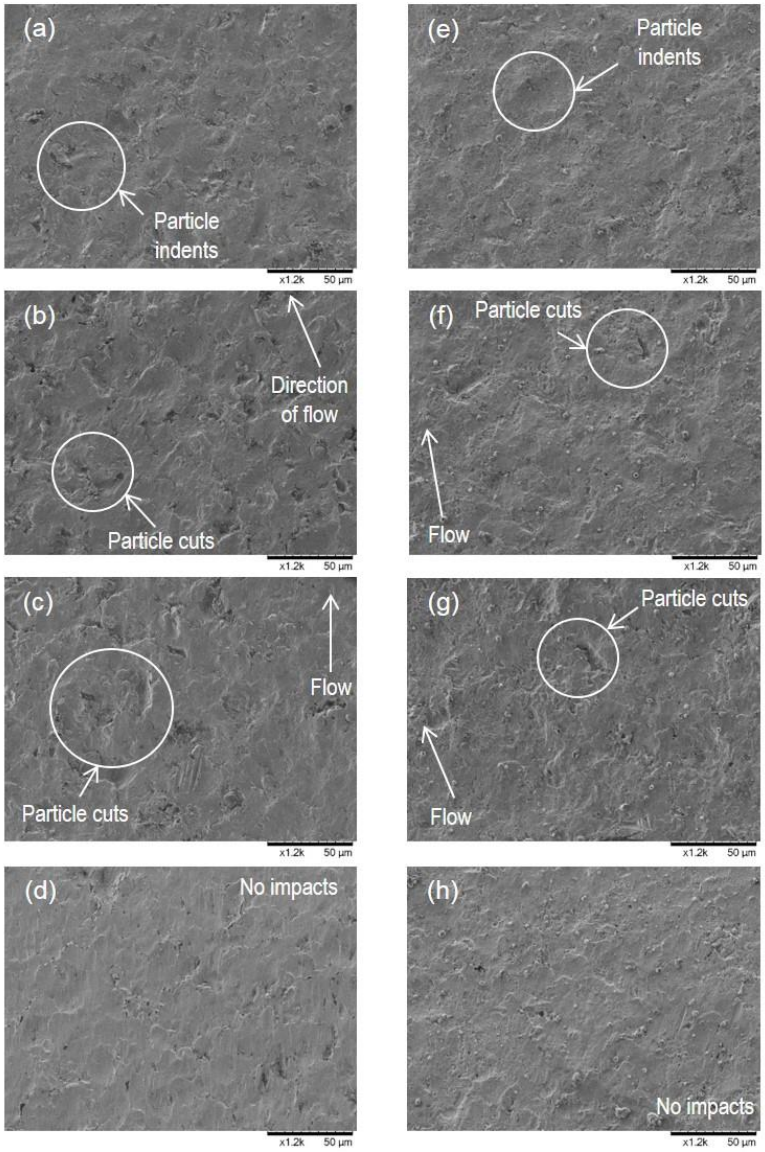

Figure 6.31 SEM images of erosion (a-d) and erosion-corrosion (e-h) samples after 240 minute tests in the SIJ at a flow velocity of 20 m/s in a solution at a temperature of 60°C containing 1000 mg/L of sand in region 1 (a, e), region 2 (b, f), region 3 (c, g) and region 4 (d, h)

The SEM images and surface profiles measured qualitatively validate the CFD model. As the CFD model was used to define impact conditions in different regions on the sample, rather than being used to calculate precise outputs of impact angle and impact velocity at specific locations on the surface, the general behaviour in those regions could be compared with the impacts in the regions and the expected mechanisms of wear in those regions. The most significant wear was expected in regions 1 and 2 where the majority of the particle impacts occurred which was seen from the surface profiles. Plastic deformation was observed in region 1 from the SEM images, expected at high impact angles. More cutting was observed in region 3 and surface roughening due to the lower impact angles and no significant degradation as a result of

particle impingement was observed in region 4, agreeing with expectations based on CFD predictions.

6.6.4 Surface Roughening and Erosion-Enhanced Corrosion

Surface roughness (S_a) of the samples in each of the four regions identified was measured using the NPFLEX with a 0.8 mm Gaussian cut-off filter applied to filter the general waviness and form of the samples. Changes in surface roughness were observed in each of the regions for erosion tests as shown in Figure 6.32. Surface roughness was highest in region 3 where high levels of cutting were experienced as predicted by the CFD model with impact angles in the range of 40°-50°. High rates of plastic deformation in region 1 caused some increase in surface roughness, but this was not as significant as the surface roughness increase in regions where cutting was the main mechanism of wear. Similar values of surface roughness were measured on erosion and erosion-corrosion samples in regions 1, 2 and 4, shown in Figure 6.33. A slightly higher surface roughness was observed on the erosion-corrosion samples in region 3 but there was no obvious reason for this difference. Despite the increase in surface roughness on the samples, the corrosion rate was not affected, suggesting the effect of erosion-enhanced corrosion was not a significant contributing factor to carbon steel erosion-corrosion degradation when no surface films were present in the conditions evaluated.

The increase in surface area of the samples as a result of the change in surface profile after 240 minutes of particle impacts in both erosion and erosion-corrosion conditions was measured to be less than 0.1%, using the NPFLEX. This calculation of surface area also accounted for the increase in surface roughness, showing that changes in surface area had no influence on the determination of degradation rates.

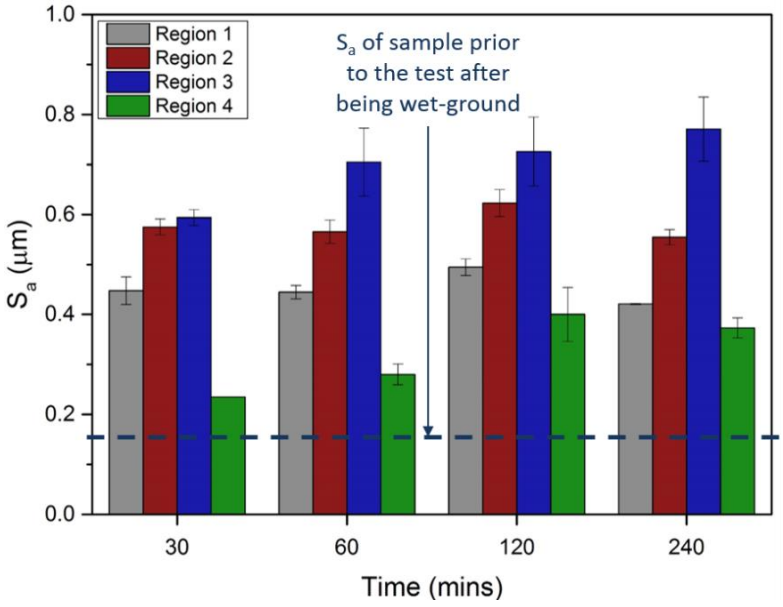

Figure 6.32 Measurement of X65 sample surface roughness (S_a) after pure erosion SIJ tests in a N_2-saturated 60°C solution containing 1000 mg/L of sand at a flow velocity 20 m/s

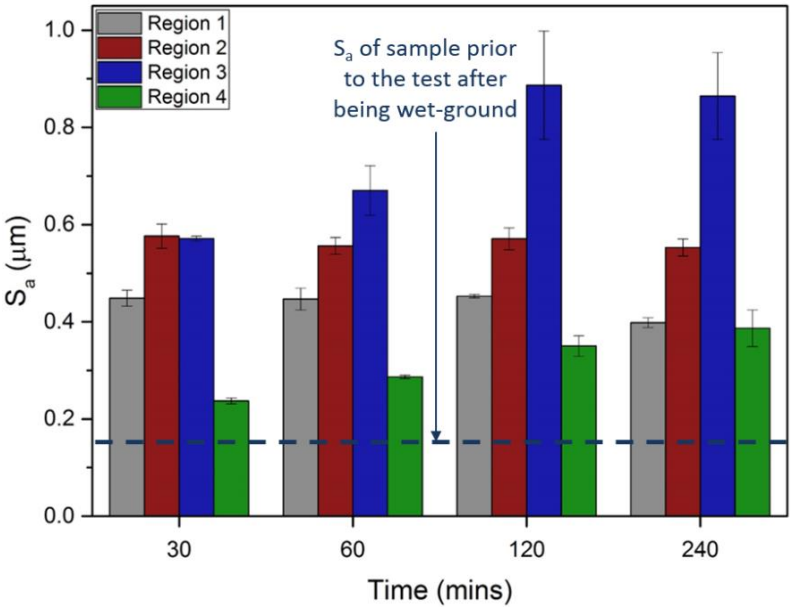

Figure 6.33 Measurement of X65 sample surface roughness (S_a) after erosion-corrosion SIJ tests in a CO_2-saturated 60°C, pH 4.7, 2% NaCl solution containing 1000 mg/L of sand at a flow velocity 20 m/s

The effect of surface roughness on corrosion rate was compared in Figure 6.34, in flow-induced corrosion SIJ tests at 20 m/s, with a sample that was wet-ground prior to starting the test using 1200 grit SiC polishing paper, to produce the same surface finish as the samples used in erosion-corrosion SIJ tests in this chapter, and 120 grit SiC polishing paper, equivalent to a surface roughness of 0.73 µm ± 0.06 µm. The Tafel plots shown in Figure 6.35 compared the plots for each of the four tests completed. Very similar

behaviour was seen between each sample, with Tafel constants determined at ±50 mV relative to OCP. Tafel plots were similar between rough and smooth samples, showing no obvious difference in corrosion rates or mechanisms.

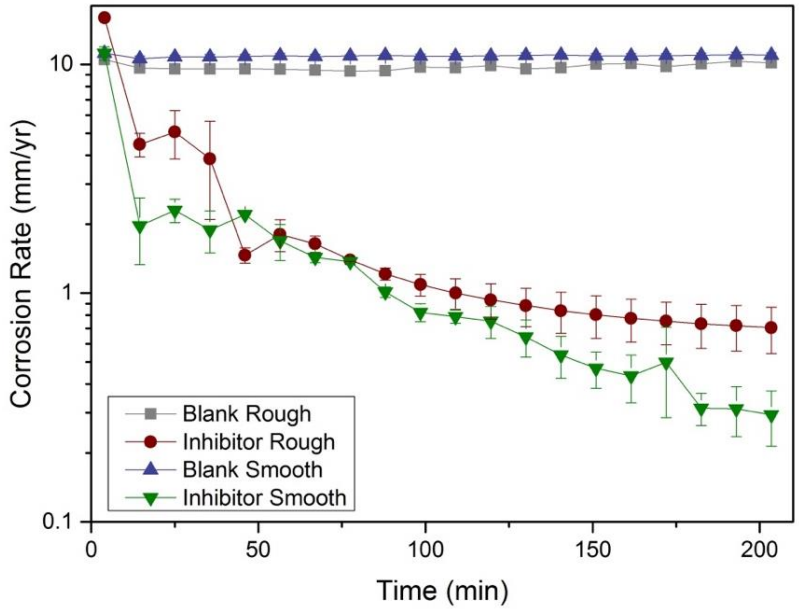

Figure 6.34 Comparison of in-situ corrosion rates of X65 carbon steel samples with a smooth surface of S_a = 0.15 µm ± 0.02 µm and a rough surface of S_a = 0.73 µm ± 0.06 µm in SIJ flow-induced corrosion tests in a CO_2-saturated, 2% NaCl, 60°C, pH 4.7 solution at a flow velocity of 20 m/s in blank conditions and after adding 250 ppm of inhibitor B

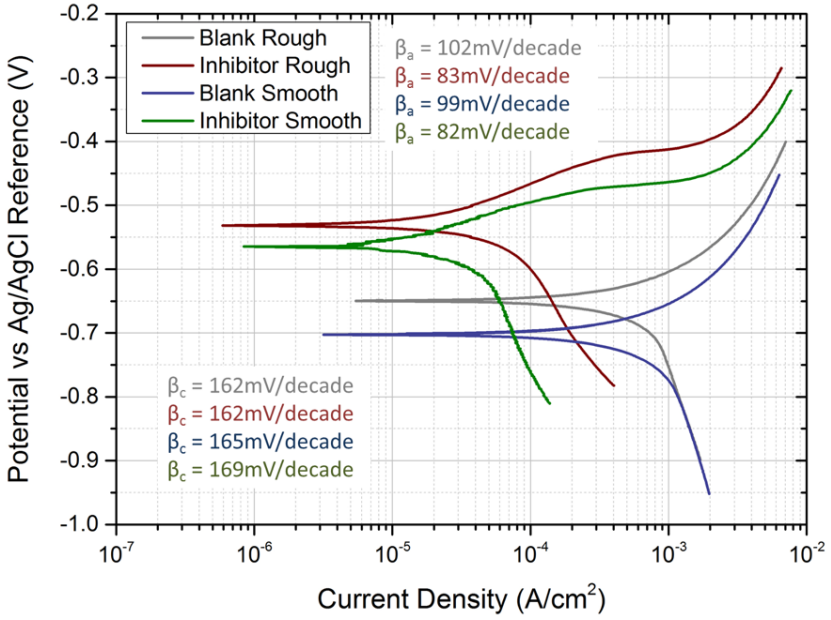

Figure 6.35 Comparison of Tafel plots measured using X65 carbon steel samples with a smooth surface of S_a = 0.15 ± 0.02 µm and a rough surface of S_a = 0.73 ± 0.06 µm in SIJ flow-induced corrosion tests in a CO_2-saturated, 2% NaCl, 60°C, pH 4.7 solution at a flow velocity of 20 m/s in blank conditions and after adding 250 ppm of inhibitor B

Similar flow-induced corrosion rates were measured in blank conditions, showing that the increase in surface roughness measured from particle impacts would not have a significant influence on corrosion rates. A concentration of 250 ppm of inhibitor B was also added and compared with a rough surface and smooth surface, as Chapter 5 showed that inhibitor B was more efficient in sand-containing flows. The effect of surface roughness on adsorption of inhibitor to the surface was therefore investigated, but showed no significant difference, with the rough surface producing a slightly higher corrosion rate. Corrosion rates were determined from EIS measurements and Tafel plots.

6.6.5 Work-Hardening, Removal of Work-Hardened Layers and Corrosion-Enhanced Erosion

Hardness of the X65 samples was compared after each of the erosion and erosion-corrosion tests using a Mitotoyo HM-122 micro-indenter. Vickers hardness (H_V) was measured with an indentation load of 4.9 N at multiple locations across the surface to give sufficient results to measure an average H_V in each of the regions. Work-hardening tendencies are influenced by material crystal structure, with dislocations moving through crystals when they yield after being subjected to strain [165]. Therefore, strain hardening was expected due to the repeated impacts of sand particles on the surface of the samples and this was seen in regions 1-3 after erosion tests, shown in Figure 6.36. It was observed that there was no influence of particle impact angle and impact velocity on work-hardening of the sample, with hardness being approximately the same in each of the three impact regions. Hardness across all regions increased compared to the hardness measured prior to tests of 202 $H_V \pm 10$ H_V.

Similar values of hardness were measured on the erosion and erosion-corrosion samples after 60 minutes onwards, shown in Figure 6.37. The hardness of erosion samples was greater after 30 minutes than erosion-corrosion samples. It was expected that the surfaces of erosion samples would be significantly harder, with corrosion of the work-hardened layers reducing the hardness of the samples in erosion-corrosion tests, but the difference was not significant.

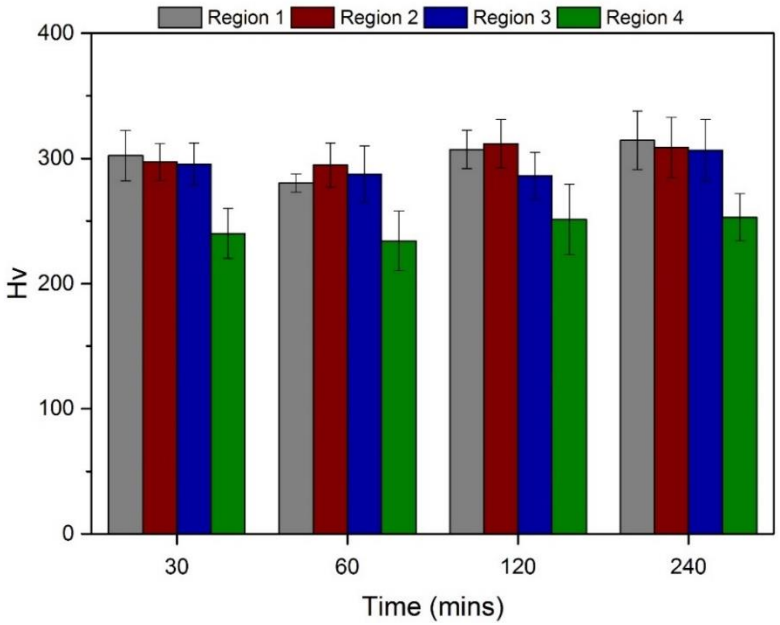

Figure 6.36 Measurements of Vickers hardness (H_V) after pure erosion SIJ tests in a N_2-saturated, 60°C solution containing 1000 mg/L of sand at a flow velocity 20 m/s

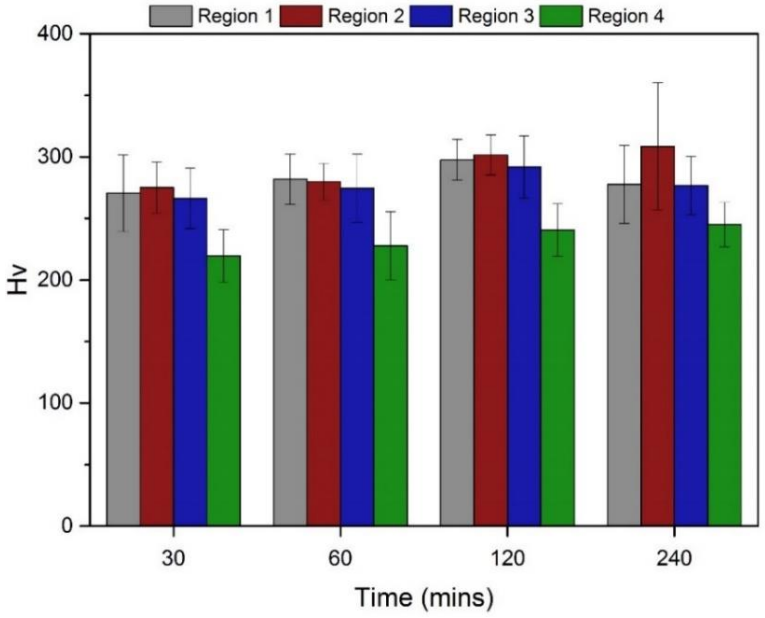

Figure 6.37 Measurements of Vickers hardness (H_V) after erosion-corrosion SIJ tests in a CO_2-saturated, 60°C, 2% NaCl, pH 4.7 solution containing 1000 mg/L of sand at a flow velocity 20 m/s

It was evident from these tests that there was no major differences between erosion and erosion-corrosion samples observed during this test period, explaining corrosion-enhanced erosion. Therefore, 1, 5 and 10 minute erosion tests were also completed to investigate the rate of work-hardening of the samples in the same erosion conditions as previous tests at 20 m/s with 1000 mg/L of sand, shown in Figure 6.38. A significant increase in hardness was measured after 1 minute, before reaching a peak hardness after

approximately 10 minutes. At this point no significant increase in hardness was observed despite high quantities of particle impacts. The removal of work-hardened layers in CO_2 corrosion conditions is also shown in Figure 6.38. Corrosion tests were completed using samples that were work-hardened in N_2 erosion conditions for a period of 120 minutes prior to the test. The aim of this was to measure the reduction in hardness of the samples as a result of corrosion of the work-hardened layers. Corrosion tests were completed in the same conditions as the previous CO_2 flow-induced corrosion tests at a flow velocity of 20 m/s in the SIJ. The hardness of the samples was reduced, but the rate of removal was much lower than the rate of work-hardening in erosion conditions. The hardness was not reduced to the original value of hardness measured prior to work-hardening and the hardness appeared to reach a constant value from 10-30 minutes.

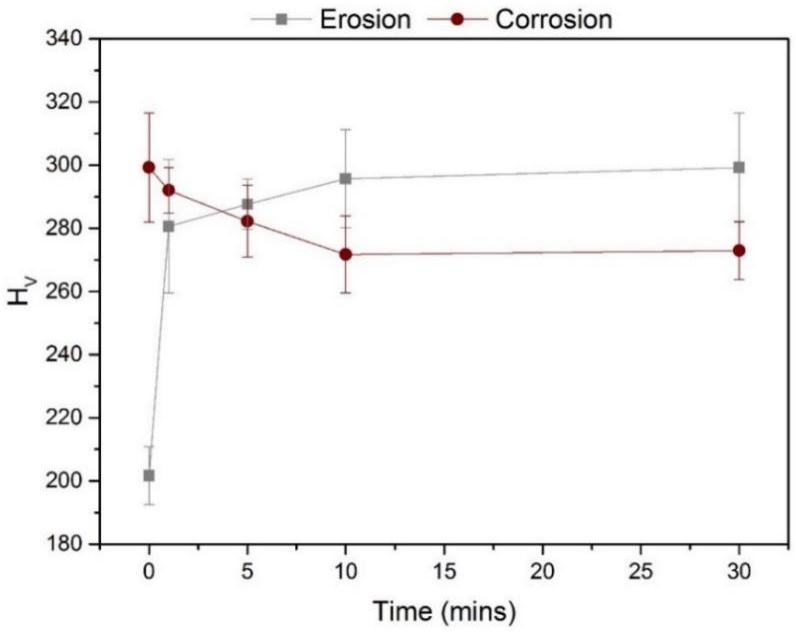

Figure 6.38 Measurements of the increase in Vickers hardness (H_V) after erosion tests in a N_2-saturated, 60°C solution containing 1000 mg/L of sand at a flow velocity 20 m/s and removal of work-hardened layers in pure corrosion tests at a flow velocity of 20 m/s in a 60°C, pH 4.7, 2% NaCl, CO_2-saturated solution using samples that had been work-hardened in pure erosion conditions for 120 minutes prior to the test

6.6.6 Analysis of Work-Hardened Layers

It was clear from the surface analysis completed up to this point that no obvious differences were apparent between erosion and erosion-corrosion samples to explain the causes of corrosion-enhanced erosion. Therefore further analysis of work-hardened layers was completed to compare the effects of work-hardening on micro-structural properties beneath the surface

of X65 samples after erosion and erosion-corrosion tests. Analysis of microstructures was completed using FIB-SEM.

FIB analysis of the work-hardened layers was completed on the erosion and erosion-corrosion samples as this utilised a technique that did not potentially influence the microstructure of the sample during sample preparation that, for example, cross sectioning the samples might. A small region in the centre of the wear scar on erosion and erosion-corrosion samples was milled using the ion beam to analyse the microstructure approximately 15 µm below the surface in that region of the sample. A sample was analysed prior to testing after being wet ground using 1200 SiC polishing paper to a surface roughness of 0.15 µm ± 0.02 µm, shown in Figure 6.39. A thin region of grain refinement, approximately 1 µm thick, was observed as a result of the wet grinding process. Larger grains were observed beneath this layer of grain refinement, typical of the grains expected in the majority of the X65 samples.

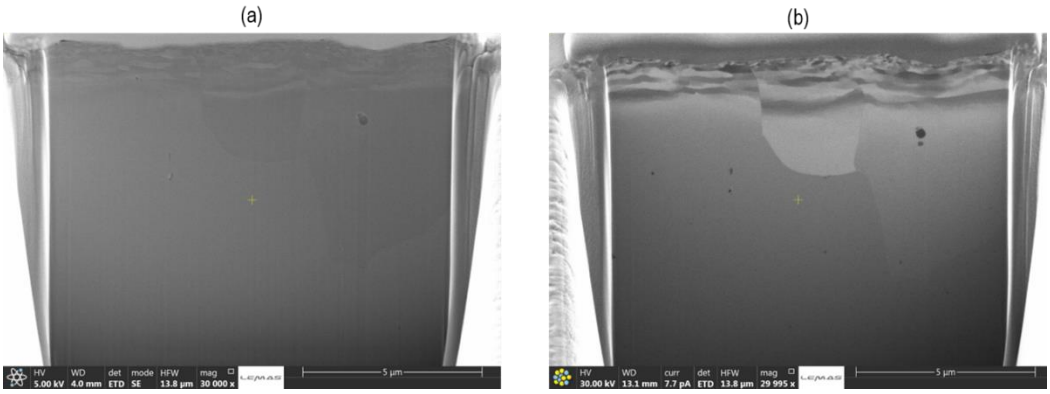

Figure 6.39 Cross sections of an X65 sample, prior to SIJ testing after being wet-ground to a surface finish of 0.15 ± 0.02 µm milled using FIB and imaged using (a) SEM at 30,000x magnification and (b) FIB etching

Four samples were analysed using FIB-SEM to compare erosion and erosion-corrosion effects. Erosion samples were compared with erosion-corrosion samples after 30 minutes and 240 minutes of testing. SEM images of the cross sections milled by the ion beam are shown in Figure 6.40. Several voids, thought to be cracks, were observed on the erosion-corrosion samples that were not observed on the erosion samples. These voids were much more significant on the erosion-corrosion samples after 240 minutes of testing compared with 30 minutes, with large voids observed across the entire width of the region analysed. These voids appeared across the nano-grain refinement layer, suggesting that the corrosion had some influence on the degradation mechanisms by accelerating the propagation of the crack. Rajahram et al. [108] showed that cracks growth was initiated in the regions where lips were formed after particle impact, with the crack being exposed at

the surface allowing corrosive species to be transported from the bulk solution to the crack in the surface. This was not observed in the cross-sections shown in Figure 6.40 as only a small section was analysed, but could have been present in other regions on the surface. These voids could have potentially reduced the erosion resistance of the sample in this region, contributing to the corrosion-enhanced erosion term measured in erosion-corrosion tests, as material could potentially have been more easily removed from above the void [108].

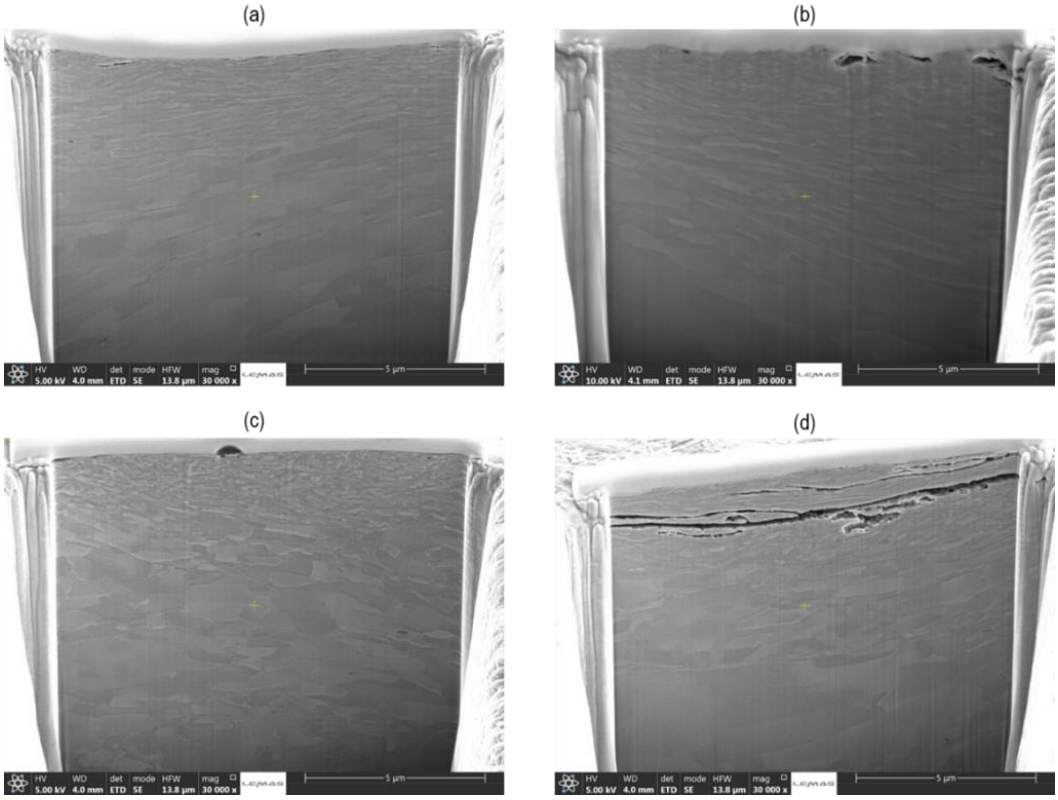

Figure 6.40 FIB-SEM images of cross sections in the centre of region 1 on the samples measured after (a) 30-minute erosion tests in a N_2-saturated, 60°C solution containing 1000 mg/L of sand at a flow velocity of 20 m/s, (b) 30-minute erosion-corrosion tests in a CO_2-saturated, 60°C, pH 4.7, 2% NaCl solution containing 1000 mg/L of sand at a flow velocity of 20 m/s, (c) 240-minute erosion tests and (d) 240-minute erosion-corrosion tests

Use of the ion beam to observe the microstructure beneath the sample surface is shown in Figure 6.41. Compared with the ion beam image of the sample prior to testing, in Figure 6.39, significant amounts of grain refinement were observed in the microstructure of each of the four samples analysed. A grain size in the range of 10 µm to 25 µm was observed on the specimens prior to testing, Figure 4.3. A very refined work-hardened layer, approximately 1 µm thick, was present closest to the surfaces of all samples. There also appeared to be two different regions of grain refinement, with a very fine microstructure

closest to the surface and a less dense region of grain refinement beneath. Underneath these layers, larger grains were observed, closer in size to the grains observed on the sample prior to testing. The thickness of these layers increased over time, but the overall thickness of the layers did not appear to be greater than the depth milled from the sample of approximately 15 µm. The comparison between erosion and erosion-corrosion samples showed that erosion work-hardened layers were much thicker than erosion-corrosion samples. It is possible that removal of material through corrosion resulted in less grain refinement being observed closest to the surface on the erosion-corrosion samples compared with erosion samples, potentially explaining why nano-grain layers on the erosion samples were slightly thicker, as shown in Figure 6.41. It has been reported that the nano-grain layer depth will increase as the total duration of impacts increases [108]. Therefore, enhanced removal of these layers as a result of erosion and corrosion mechanisms would have resulted in thinner regions of nano-grain refinement on erosion-corrosion samples compared to erosion samples.

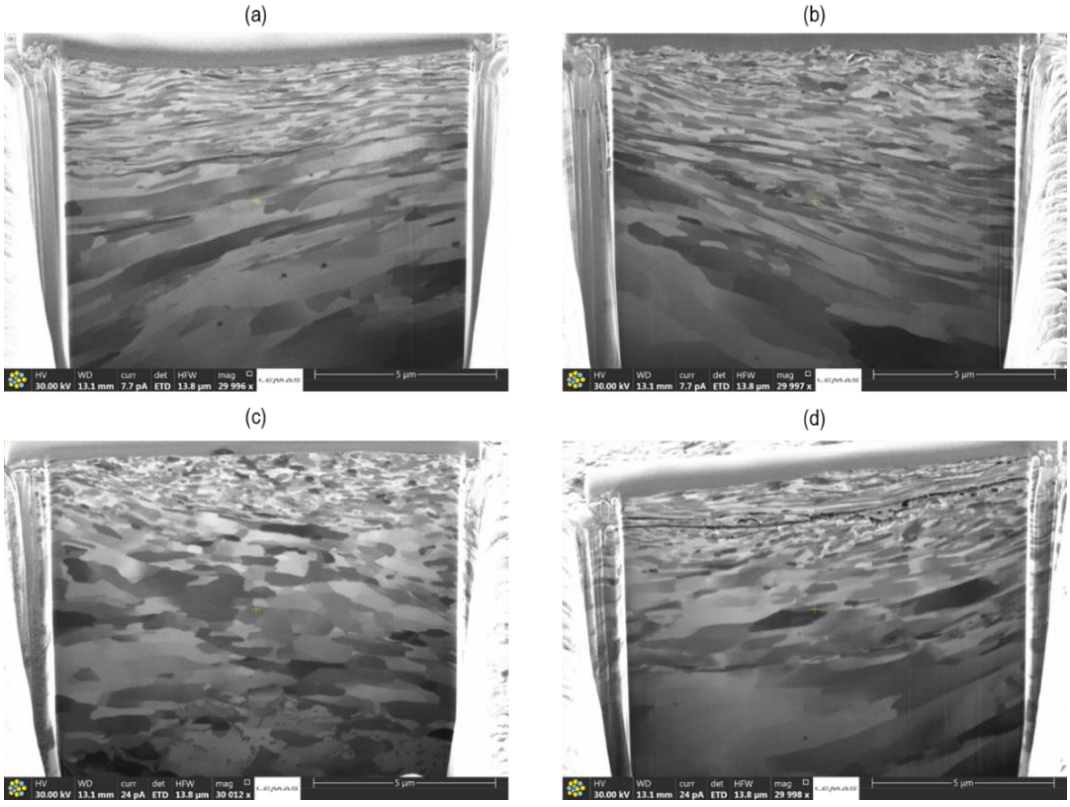

Figure 6.41 FIB images of cross sections in the centre of region 1 on the samples measured after (a) 30-minute erosion tests in a N_2-saturated, 60°C solution containing 1000 mg/L of sand at a flow velocity of 20 m/s, (b) 30-minute erosion-corrosion tests in a CO_2-saturated, 60°C, pH 4.7, 2% NaCl solution containing 1000 mg/L of sand at a flow velocity of 20 m/s, (c) 240-minute erosion tests and (d) 240-minute erosion-corrosion tests

6.7 Summary and Conclusions

Erosion-enhanced corrosion and corrosion-enhanced erosion was analysed on X65 carbon steel surfaces after erosion-corrosion, flow-induced corrosion and erosion tests using the SIJ. Combining experimental results with the CFD prediction of particle trajectories to define different regions on the surface of the X65 samples enabled a greater understanding of the conditions experienced in SIJ tests to be achieved. Several surface and subsurface analysis techniques including SEM and FIB were used to make comparisons between X65 carbon steel samples used in pure erosion tests and erosion-corrosion tests. The prediction of particle trajectories and a range of surface analysis techniques after corrosion, erosion and erosion-corrosion tests showed that:

- A wide range of particle impacts were expected on the surface of X65 samples in erosion and erosion-corrosion tests, with high impingement angles causing plastic deformation and lower impingement angles causing cuts on the sample, shown on SEM images of the surfaces after erosion and erosion-corrosion SIJ tests;
- All contributing factors to total erosion-corrosion degradation occurred at a constant rate, with a linear increase seen in erosion, corrosion, erosion-corrosion and corrosion-enhanced erosion mass loss degradation with time;
- Corrosion-enhanced erosion was the most significant enhancement of erosion-corrosion degradation. Corrosion of work-hardened layers and subsequent hardening of the sample at very high rates continuously exposed softer areas of material, accounting for the increased erosion wear;
- Work-hardened layers on erosion samples were thicker and more refined than the work-hardened layers measured after erosion-corrosion tests, suggesting that corrosion removed material from the work-hardened layers;

  Significant differences were observed in the subsurface microstructures of erosion-corrosion and erosion samples observed using FIB-SEM. Very refined work-hardened layers were present on erosion samples that were not as refined on the erosion-corrosion samples;
- Erosion-enhanced corrosion was not a significant contributing factor, despite the significant increase in surface roughness across the wear scar of the sample.

Chapter 7
Development of an Elbow for Erosion-Corrosion Evaluation of X65 Carbon Steel

The work completed in the previous chapters investigated the mechanisms of erosion-corrosion and the interactions between erosion and corrosion using the SIJ. The hydrodynamic conditions and particle trajectories were predicted in the SIJ using CFD. However, it was unknown how relevant to pipe flow conditions the SIJ geometry was from both an erosion and corrosion perspective. To investigate erosion-corrosion in pipe flow geometries, an elbow was designed and manufactured that could be used for erosion-corrosion testing of X65 carbon steel.

7.1 Introduction

The causes of erosion-enhanced corrosion and corrosion-enhanced erosion were investigated in Chapters 5 and 6 and it was observed that in high flow velocity conditions, corrosion-enhanced erosion was a significant contributor to total erosion-corrosion material degradation of carbon steel. However, the SIJ conditions used in Chapters 5 and 6 were not necessarily representative of the typical conditions that would be present in pipe flow in the field [49]. High particle impingement angles were predicted in the centre of the samples used in the SIJ and high velocity cutting impacts in the turbulent jet region of the flow. However, it was unknown how relevant these conditions were to pipe flow. Significant variation of impingement angles and impact velocities were also observed on the surface of the sample in the SIJ, making it difficult to prove what effects impact angles and impact velocities had on erosion-corrosion. The variation in hydrodynamic conditions on the surface of the sample also made it challenging to assess the influence of flow parameters on corrosion.

The SIJ was very effective for completing erosion-corrosion tests and could be easily modified to change conditions through the use of different nozzle diameters and varying the distance from the nozzle to the samples. Gnanavelu et al. [120] demonstrated how for a known impact angle and impact velocity, the sample thickness loss as result of pure erosion in the SIJ could be predicted, which could easily be related to other flow geometries. However, it was unknown if this methodology would be effective when applied in erosion-corrosion conditions and without a full knowledge of the conditions

in pipe flow and SIJ geometries, replicating the same conditions is challenging. It was therefore investigated how similar erosion-corrosion conditions in pipe flow geometries were to the SIJ through the design of a 90° elbow component.

Pipeline components that create disturbances in the sand-laden fluid flow are of particular importance for erosion-corrosion degradation, with a higher proportion of particle impingement expected than in straight sections of pipe [20, 49, 87]. Erosion in pipe elbows has been investigated by several researchers, typically combining CFD predictions of erosion with experimental results [2, 49, 123, 174]. However, erosion-corrosion research in elbows is lacking and limitations of the research completed in elbows has been discussed in Chapter 3. Therefore, an elbow was developed and used for erosion-corrosion evaluation of X65, detailed in this chapter along with CFD predictions of particle trajectories through the elbow. The objectives of this chapter were to:

- Design an elbow that could be used for erosion-corrosion evaluation of X65 carbon steel in pipe flow conditions;
- Manufacture the designed elbow using an appropriate material to be able to withstand the range of conditions required for erosion-corrosion testing;
- Create a flow loop using the elbow to enable erosion-corrosion testing to be completed in a representative flow environment;
- Complete flow-induced corrosion, erosion and erosion-corrosion tests using the elbow to measure the contribution of corrosion, erosion, erosion-enhanced corrosion and corrosion-enhanced erosion to total erosion-corrosion degradation at different locations in the elbow using mass loss and electrochemistry techniques.

7.2 Design Criterion

The main design aim was to develop a pipe component that could be used for erosion-corrosion testing of X65 carbon steel in a range of conditions more representative of pipe flow conditions than conditions in the SIJ. A 90° elbow component was chosen for this. The main features of the elbow design are discussed in this chapter. The elbow was designed so that multiple X65 samples could be located on the inner and outer radius for the purpose of measuring corrosion, erosion and erosion-corrosion at various locations. The

elbow was fitted into the pipework of the SIJ and erosion-corrosion experiments were completed. Mass loss measurements and electrochemistry measurement techniques were used to determine degradation rates in the elbow. Several requirements were specified from the design in order to meet the design aim stated above. An overview of the elbow design requirements is shown in Figure 7.1. The main requirements included being able to run flow-induced corrosion, erosion and erosion-corrosion tests using the elbow. This meant that the elbow component had to be able to withstand high flow rates and sand particle impacts.

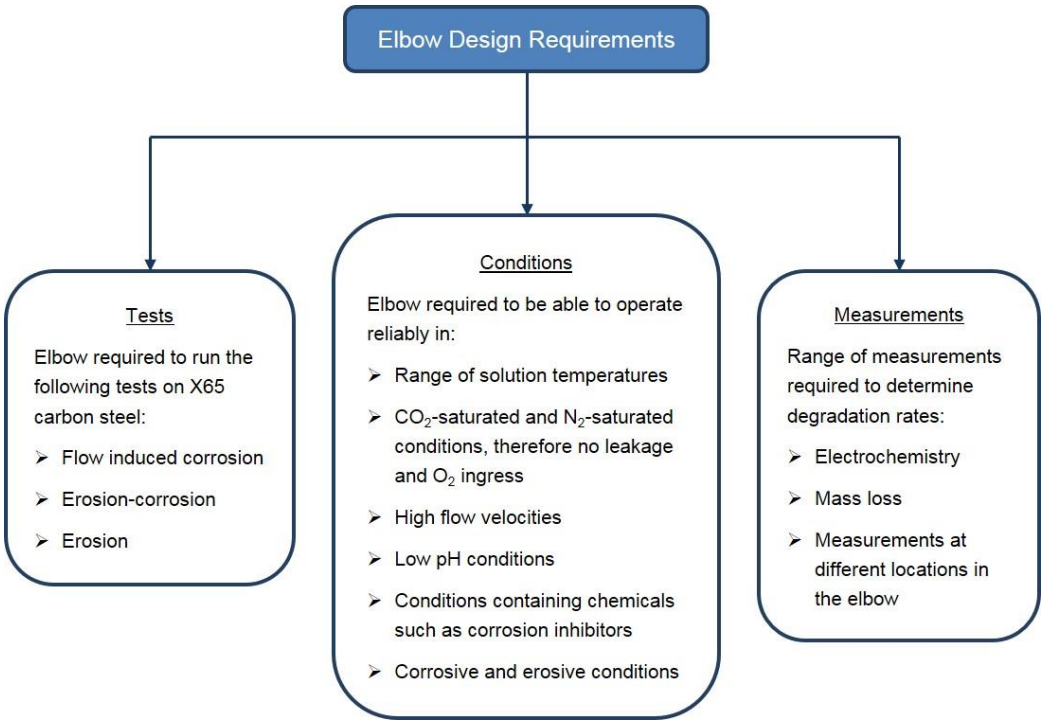

Figure 7.1 Overview of requirements that were considered for the development of the elbow to complete flow-induced corrosion, erosion and erosion-corrosion evaluation of X65 carbon steel

Various measurement techniques were required to determine material degradation rates in the elbow. Previous designs of elbows used thickness loss measurements only to determine degradation [2, 148]. However, thickness loss would not provide information about the contribution of each degradation component to total erosion-corrosion material loss. A non-conductive, corrosion resistant material was required for the body of the elbow so that electrochemistry measurements could be completed and to prevent degradation of the component. Multiple samples were fitted into the elbow to use as working electrodes in a three electrode cell setup. Being able to remove the samples to complete mass loss tests was also essential to individually determine the contribution from mechanical damage in addition to electrochemical dissolution in total erosion-corrosion degradation rates. It was

important that the samples were fitted securely into the elbow and shaped such that they were not protruding into the flow. This would have caused disturbances in the flow through the elbow which would not be present in normal pipe flow. It was highlighted in Chapter 3 how it was possible that elbow designed by Zeng et al. [174, 175] for erosion-corrosion testing could have experienced disruption to the flow through the elbow, affecting results. Preventing leakage of test solution and ingress of O_2 was also essential to complete tests in CO_2 and N_2 saturated conditions.

7.3 Elbow Design Detail

7.3.1 Design Overview

The fully assembled elbow design is shown in Figure 7.2, with a list of the labelled components shown in Table 7.1. The body of the elbow consisted of two components, an outer radius and an inner radius, with the elbow being split to ensure that samples could be accurately flush mounted prior to starting a test. Multiple X65 samples were fitted into the elbow at specific angles with an equal number of samples located on both the inner and outer radius of the elbow, enabling erosion-corrosion degradation rates to be determined at various locations.

Table 7.1 Description of components in the elbow shown in Figure 7.2

Component	Name	Description
1	Elbow Outer Radius	Outer half of the body of the elbow
2	Elbow Inner Radius	Inner half of the body of the elbow
3	X65 Samples	X65 samples fitted into the elbow
4	Sample Holders	Fixed samples in the elbow body and provided sealing pressure on o-rings fitted around samples
5	Flow Inlet/Outlet	Grooves in the body of inner and outer radius to secure elbow in SIJ pipes
6	O-ring seal	O-ring cord seal in the split of the two elbow halves to prevent leakage

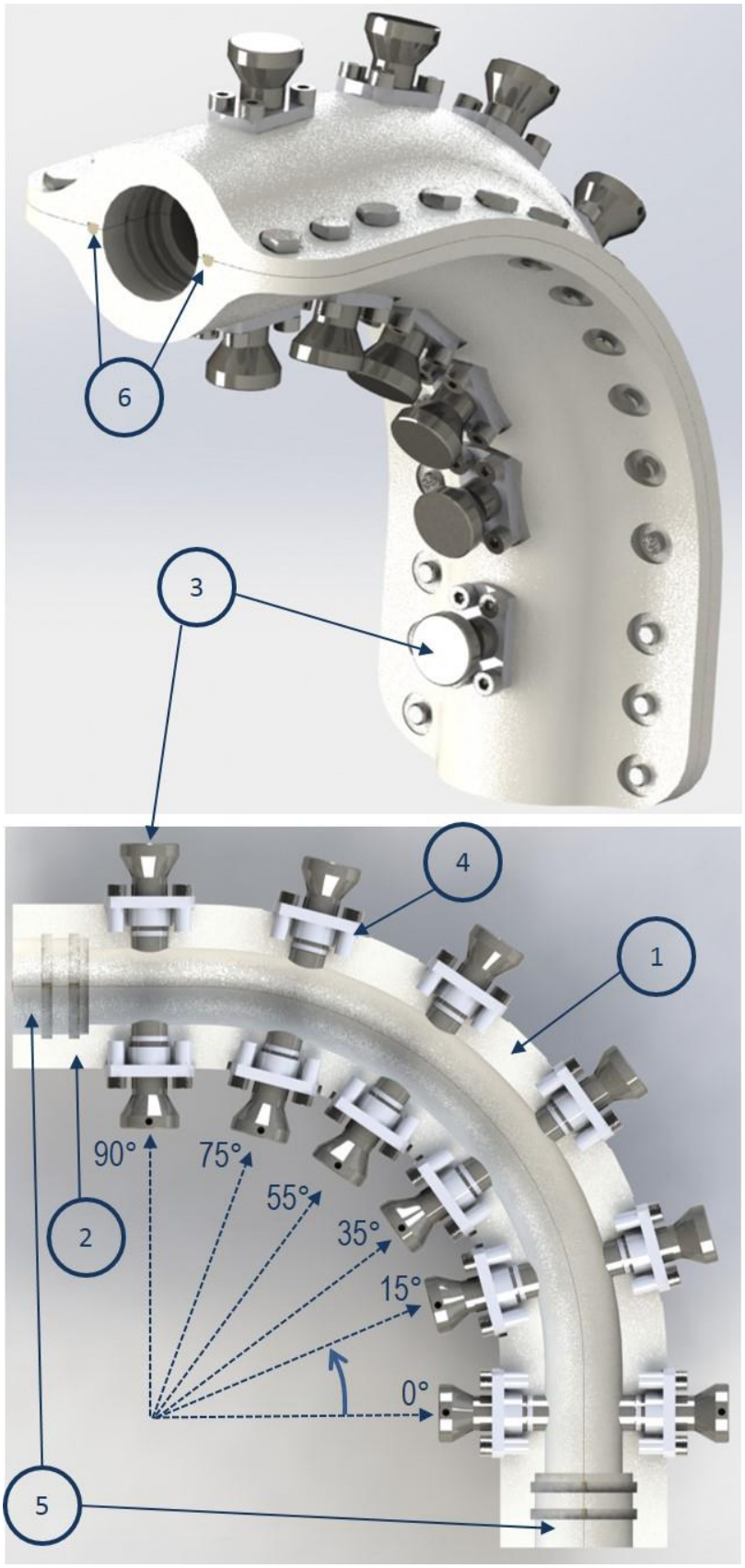

Figure 7.2 Fully assembled elbow design consisting of twelve X65 samples located on the inner and outer radius of the elbow

An internal diameter (D_p) of 25.4mm (1 inch) was used to maintain the same flow diameter as the inner diameter of the SIJ pipes in which the elbow assembly was fitted into to create a flow loop. The elbow radius, R_c, was equal to five times the internal diameter of the elbow (R_c/D_p = 5). This R_c/D_p ratio was chosen to be representative of elbows in field conditions. McLaury et al. [220] showed that erosion rates decreased as the R_c/D_p ratio increased. However, erosion was expected in an elbow with an R_c/D_p ratio of 5 [220].

Twelve samples were fitted into the SIJ at angles of 0°, 15°, 35°, 55°, 75° and 90°, with a sample located on both the inner and outer radius at each of these angles. This number of samples was chosen so that a sufficient number of points could be analysed in the elbow, within the geometrical limits of the design, whilst also ensuring that samples were of a sufficiently large diameter in order to complete reliable mass loss measurements. It is acknowledged that in the field, samples would not be isolated as an elbow would be one conductive component. However the use of multiple, isolated samples enabled individual degradation mechanisms to be determined at various locations in the elbow, providing a more detailed insight into erosion-corrosion degradation in pipe flow conditions.

By fitting the elbow into the SIJ, erosion-corrosion tests could be completed much more conveniently without the need for designing further components, such as pipes and a pump to recirculate the solution. The grooves in the elbow allowed the standard SIJ piping components to be securely fitted into the elbow, making it convenient and easy to fix the elbow into the SIJ pipework ensuring no leakage during the test. Prevention of leaks and O_2 ingress was essential for operating in N_2 and CO_2-saturated environments. O-ring cord was used in the split of the elbow to form a seal around the sides of the flow channel and to prevent leaks between the inner radius and outer radius components. Two o-rings were fitted around the X65 samples to prevent leaks around the sides of the samples. Pressure was applied to the o-rings through the sample holder components fitted and tightened using four screws into the elbow body around each of the samples. Two o-rings were fitted around each of the inlet and outlet SIJ pipes that could be positioned in the elbow body, before the inner radius and outer radius were fastened together around the sides of the elbow body. An epoxy glue layer was applied around the inlet and outlet pipes and the elbow body, before silicone sealant was applied to prevent leaks. This could be removed when the elbow was disassembled.

7.3.2 Manufacturing the Elbow

The elbow was 3D printed from a material with similar properties to acrylonitrile butadiene styrene (ABS). The use of 3D printing to manufacture prototype components provides a very quick and cost effective method of producing components [221]. The use of 3D printing also enabled the elbow to be manufactured quickly to preliminary test the components so that the design could be improved without significant expense and time. Due to the aggressive nature of the testing environment, elbow components could easily be replaced if they suffered any degradation from excessive use. The outer radius, inner radius and sample holders were 3D printed from the ABS material. ABS is a versatile thermoplastic polymer that is formable, has adequate strength and has good chemical resistance properties to cope with the erosion-corrosion test conditions [222]. The elbow components were 3D printed using a Stratasys Objet 1000 Plus 3D printer.

7.3.3 X65 Samples

X65 carbon steel samples were evaluated in erosion-corrosion conditions in the elbow. However, other materials could have easily been used, if required, for evaluation in relevant conditions. A cross section of the X65 samples as they were fitted in the elbow is shown in Figure 7.3. The surface exposed to the flow was required to be curved with the same radius as the radius of the flow channel in the elbow. A flat surface would have resulted in the samples protruding into the flow, causing disruptions the flow and resulting in a flow environment that was unrealistic and unrepresentative of pipe flow conditions.

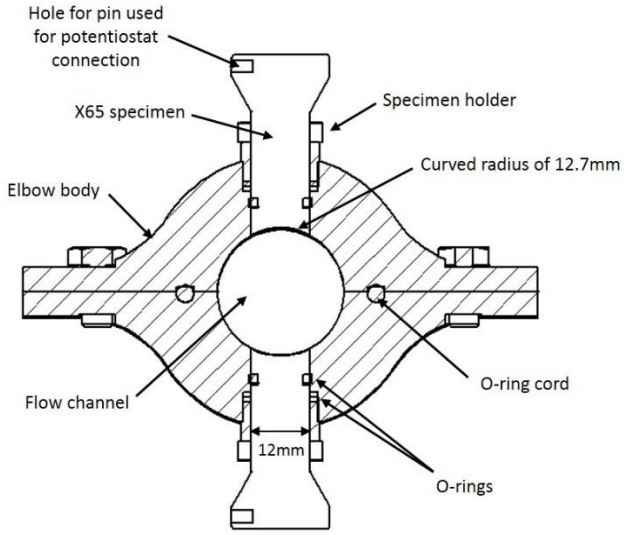

Figure 7.3 X65 carbon steel samples used in the elbow with a curved radius and a pin used as a connection for electrochemistry measurements

Samples could be fitted in and removed from the elbow to complete mass loss measurements to determine degradation rates. The procedure for fitting and removing the samples in the body of the elbow is shown in Figure 7.4. Electrochemistry could also be completed by using the samples as working electrodes. For convenience, carbon steel pins were inserted into the drilled holes in the sample so that wires from the computer controlled potentiostat could be connected.

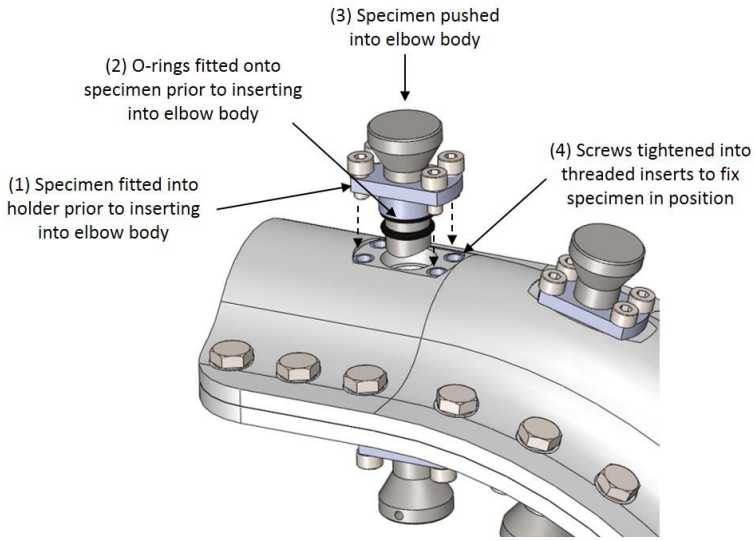

Figure 7.4 Procedure for inserting and securing samples in the elbow body. Removal of samples was completed in reverse order

A target minimum surface area of the face exposed to the flow of 1 cm^2 was used in the design stage so that sufficient mass loss would be measured without measurement error being a significant factor in the results, based on previous experimental experience using small surface area samples. It was also important that the surface area was not so large that local erosion-corrosion conditions, in terms of impingement angles, impingement velocities and flow parameters, varied significantly over the surface. Excessive variation in conditions over the surface would have made conditions at the sample surface difficult to define. Samples with a diameter of 12 mm were therefore used, resulting in a surface area of 1.16 cm^2 exposed to the flow. Samples were hand polished using 120, 600, 800 and 1200 grit SiC polishing paper to achieve a consistent surface. The curvature of the samples prevented reliable measurements of surface roughness from being made, but surface finish was expected to be similar to the surface finish of flat X65 samples used in SIJ tests which were polished using the same grades of polishing paper (0.15 µm ± 0.02 µm). Due to the size of the samples, a maximum of six could be fitted into each radius of the elbow and were located at angles of 0°, 15°, 35°, 55°, 75° and 90° to give an equal spacing between the samples in the sweep of

the elbow and to give four samples at the inlet (0°) and outlet (90°) of the elbow.

The tapered shape of the elbow samples was designed for the use of acoustic emission monitoring, using a sensor which required a diameter larger than 12 mm for the detection of acoustic energy. Acoustic emission monitoring was completed by Ukpai et al. [144, 145] to measure the impacts of sand particles on the surface of carbon steel samples in SIJ tests. Acoustic emission was not completed as part of the work in this thesis. However, samples were designed for the use of acoustic emissions in future projects.

7.3.4 Creating a Flow Loop Using the SIJ

A diagram showing how the elbow was located in the SIJ to create a flow loop is shown in Figure 7.5. The flow loop was used to recirculate the sand-laden fluid through the elbow continuously during a test. The SIJ had the main components required to provide a continuous flow of solution through the elbow, including a pump to recirculate the solution and a large reservoir to add the solution and sand particles to. The pipe work of the SIJ was also easily modified, with components easily removed or replaced to change the geometry of the flow.

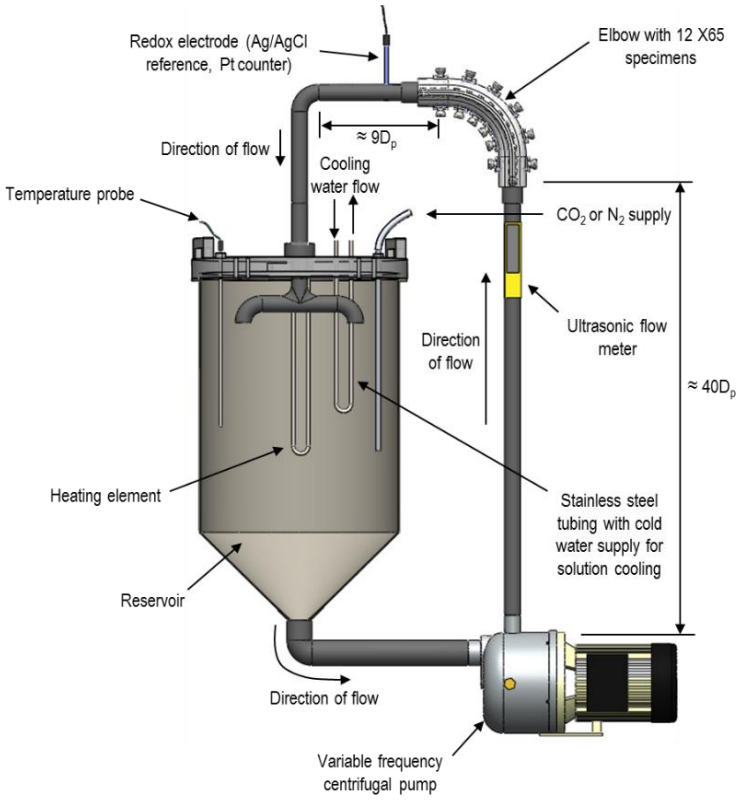

Figure 7.5 Diagram of the elbow used for flow-induced corrosion, erosion and erosion-corrosion tests fitted into the SIJ to create a flow loop

Sections of pipe from the SIJ were removed so that the elbow could be fixed into place securely. The pipe work in the SIJ consisted of 25.4 mm inner diameter, 32 mm outer diameter chlorinated polyvinyl chloride (PVC-C) pipes with different sections of pipe connected through PVC-C unions and fittings to change the geometry of the flow. PVC-C unions and fittings were cemented together to provide a seal and to fix components in position. Two short sections of PVC-C pipe were inserted into the inlet and outlet of the elbow so that the elbow could be fastened into the SIJ pipework, as shown in Figure 7.5. The elbow was positioned at a distance of approximately 40 internal diameters downstream of the pump so that the flow was fully developed when entering the elbow section. Nozzles were removed from the SIJ for elbow testing. A cooling tube was fitted into the SIJ to maintain solution temperature during testing. A redox Ag/AgCl reference electrode, incorporating a Pt counter electrode of the same specification as used in SIJ tests with a diameter of 12 mm, was fitted downstream of the elbow, so to not disturb the flow before the elbow for electrochemical measurements.

7.4 Evaluation of X65 Degradation in Pipe Flow Conditions

After the elbow was 3D printed, assembled and basic preliminary testing had been completed to demonstrate the reliability of the elbow to withstand test conditions, erosion-corrosion tests were completed. Flow-induced corrosion, erosion and erosion-corrosion tests were completed to measure the contribution of corrosion, erosion, corrosion-enhanced erosion and erosion-enhanced corrosion to total erosion-corrosion degradation at each location in the elbow, similar to the SIJ erosion-corrosion test methodology.

7.4.1 Experimental Procedure and Operating Conditions

Flow-induced corrosion, erosion and erosion-corrosion tests were completed in the elbow. Similar test conditions were used in the elbow to the conditions used SIJ tests reported in earlier chapters, where CO_2 was bubbled into the 50 L, 2% NaCl solution in the SIJ reservoir for corrosion and erosion-corrosion tests and N_2 was bubbled into the solution for erosion tests. Deionised water was used and was saturated with CO_2 to pH 4. The solution pH was lower for elbow tests than used in SIJ tests in Chapter 5 and Chapter 6 to maintain the field conditions in which the elbow was designed to replicate. This pH also meant that hydrogen evolution was the dominant cathodic reaction, therefore

allowing the hydrodynamic conditions to be more easily related to flow-induced corrosion, which could not be completed in Chapters 5 and 6 [30]. The solution was continuously recirculated during the bubbling period, before the elbow was fitted into the SIJ to ensure that conditions were consistent throughout the entire 50 L solution. Samples were polished by hand using 320, 600, 800 and 1200 grit polishing paper to achieve a consistent surface roughness across all samples during tests. The curved samples prevented the use of an automatic polisher/grinder machine, which required flat samples.

The solution was recirculated using the variable frequency pump at a flow velocity of 6 m/s, measured at the inlet of the elbow using a Micronics U-1000 ultrasonic flow meter, positioned on the PVC-C pipes upstream of the elbow, shown in Figure 7.5. The measurement of flow velocity as a function of input pump frequency is shown in Figure 7.6. A linear relationship between pump frequency and flow velocity was observed. Measurements could not be completed above a frequency of 45 Hz, due to excessive turbulence in the flow reducing the accuracy of measurements. Therefore a measurement at 42 Hz was completed, with a maximum linear velocity of 6 m/s achievable through the elbow.

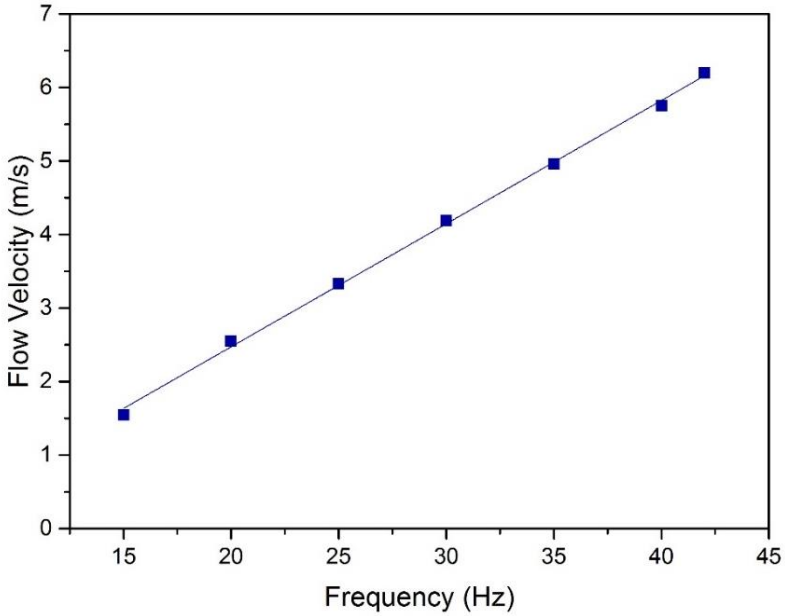

Figure 7.6 Calibration of pump frequency vs flow velocity measured using an ultrasonic flow meter at the inlet of the elbow

The solution temperature was maintained at 60°C during elbow tests. Tests were completed for 8 hours due to the low rates of degradation that were expected in elbow tests compared to the significantly higher rates of degradation measured in SIJ tests, due to the lower flow velocity. At high pump frequencies, the solution was heated by the pump causing some

increase in temperature during tests. This was not significant in shorter tests, but was more significant when longer tests were completed. Therefore, a cooling system was added to the SIJ reservoir to counteract the increase in solution temperature as a result of the high pump frequency, shown in Figure 7.5. The cooling system consisted of a stainless steel tube with an inlet hose connected to a cold water supply and an outlet hose which was used to drain the fluid. The flow rate of the water was set to maintain a constant temperature in the reservoir. The stainless steel tubing had similar dimensions to the heating element used in the SIJ and was fitted into the SIJ lid for elbow tests. Therefore, the temperature of the solution could be heated to the desired temperature using the heating element and the cooling system could maintain the temperature throughout the test.

HST60 sand particles were again added for erosion and erosion-corrosion tests. A similar pump frequency was used for 20 m/s SIJ erosion and erosion-corrosion tests, in which the sand concentration had previously been calibrated for. At this pump frequency it was found that the sand concentration added to the reservoir was equal to the sand concentration exiting the nozzle. Therefore, it appeared that sand settling was not an issue at this frequency so the same quantity of sand was added to elbow tests to give a sand concentration of 1000 mg/L through the elbow.

The mass of the samples was measured prior to starting tests and after completing tests to determine the mass loss of the samples. O-rings were removed from the samples prior to completing the measurements. To complete electrochemical measurements, wires from an ACM Gill 12-channel computer controlled potentiostat were connected to each of the X65 samples, used as working electrodes. Due to the distance between the working electrodes and the redox electrode, EIS measurements were completed using a single channel Solartron SI 1280 to determine the solution resistance for each of the twelve samples individually. The ACM Gill 12-channel could not be reliably used for AC measurements in these conditions, therefore an alternative potentiostat was used for EIS measurements. LPR measurements were therefore completed during the test to determine the corrosion rates of the samples and potentiodynamic sweeps were completed to produce Tafel plots, as EIS could not be used to determine corrosion rates for all 12 channels during a test. The same scan ranges and scan rates detailed in Section 4.5.5 were used for LPR measurements in the elbow. Measurements were completed sequentially, therefore a single LPR measurement was completed on each sample separately, starting at the inlet samples and ending at the

outlet samples, alternating between the samples on the inner and outer radius at each angle until all measurements were completed. The same measurements were completed in cycles, with one set of twelve measurements taking approximately 25-30 minutes to complete.

7.4.2 Erosion-Corrosion Tests

Erosion-corrosion tests were completed at a temperature of 60°C and a flow velocity of 6 m/s in the elbow. The comparison of degradation measured from mass loss in 8 hour flow-induced corrosion tests on the inner and outer radius is shown in Figure 7.7. Angle on the x-axis refers to the position in the elbow, not the particle impact angle. Degradation was high in the high flow velocity, high temperature, low pH conditions and was similar on the outer radius and inner radius. It did appear that degradation was slightly higher on the outer radius of the elbow, however, error was significant in some of the measurements and the difference in mass loss was small. There was some variation between the samples, but degradation was similar at all samples from the inlet up to the 75° sample. There did appear to be a slight increase in degradation at the 90° samples on both the inner and outer radius. However, error was significant in the measurements at this sample.

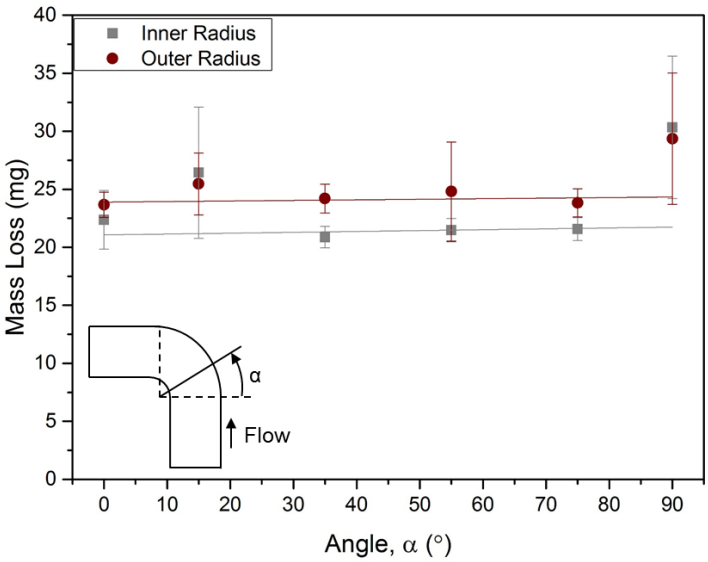

Figure 7.7 Degradation of X65 carbon steel samples on the inner radius and outer radius of an elbow in 8-hour flow-induced corrosion tests at a flow velocity of 6 m/s in a 2% NaCl, pH 4, CO_2-saturated solution at 60°C

Electrochemistry measured corrosion rates were sensitive to small errors due to the large solution resistances and very high corrosion rates measured. Solution resistances in excess of 100 $\Omega \cdot cm^2$ were measured, whilst charge transfer resistances were approximately in the range of 20 $\Omega \cdot cm^2$ to 30 $\Omega \cdot cm^2$,

as demonstrated in Figure 7.8 where a Nyquist plot is shown, measured for an X65 elbow sample on the inlet of the elbow at 0°, the furthest sample from the redox electrode, in the same experimental conditions as flow-induced corrosion tests. To calculate corrosion rates accurately, the solution resistance was required to be determined using the Solartron SI 1280 potentiostat for EIS measurements and then deducted from the polarisation resistance measured using the ACM Gill 12 LPR measurements, to give the charge transfer resistance, Equation (4.3). However, this resulted in error in solution resistance measurements having a very significant effect on corrosion rate calculations. Therefore, it was decided that electrochemistry-measured corrosion rates could not be used reliably for reporting corrosion rates. Small errors in the measurement of solution resistance had a much greater significance on the calculation of corrosion rate, limiting the success of the electrochemistry measurements completed.

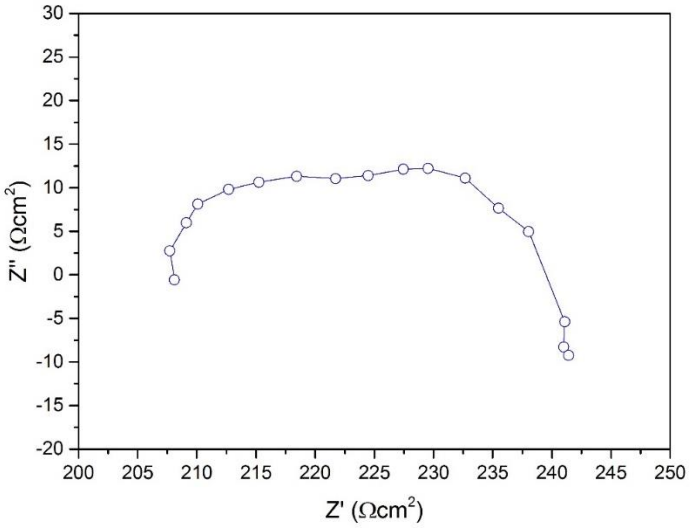

Figure 7.8 Nyquist plot from EIS measurements on the inner radius of the elbow on the sample positioned at 0° in 2% NaCl, pH 4, CO_2-saturated conditions at a temperature of 60°C

To demonstrate that corrosion rates remained constant during the test period and that mass loss measurements were therefore representative of constant degradation throughout a test, electrochemistry measured polarisation resistances are shown over the 8-hour test period on the inner and outer radius in Figure 7.9 and Figure 7.10. Polarisation resistance is measured during LPR electrochemistry measurements, as explained in Section 4.5.3, and is the sum of solution resistance and charge transfer resistance, Equation (4.3), so cannot be used to calculate corrosion rates. However, solution resistance remained constant during a test, as shown in Chapter 5, indicating that a constant polarisation resistance and constant solution resistance will

produce a constant corrosion rate. Therefore, these results are used to demonstrate that mass loss measurements give a reliable measurement of average degradation during flow-induced corrosion tests and that corrosion mechanisms would not change significantly during a test.

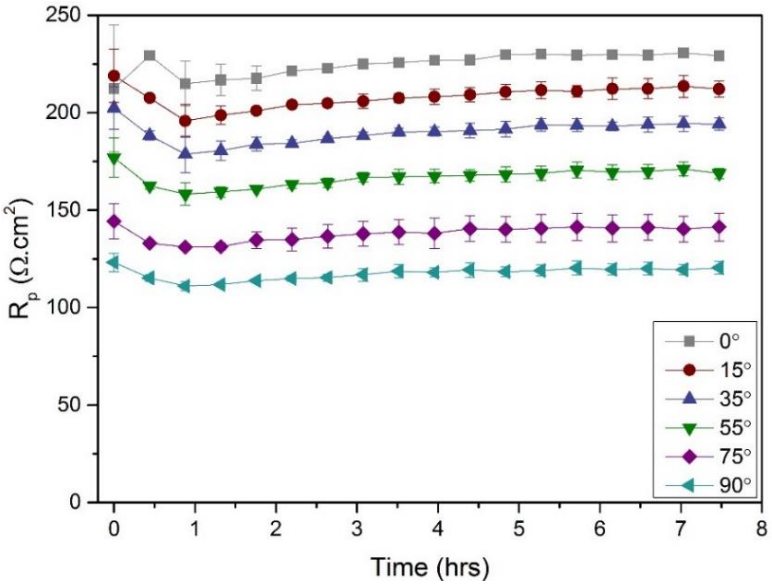

Figure 7.9 Comparison of polarisation resistance from LPR measurements on the inner radius of an elbow in flow-induced corrosion tests at a flow velocity of 6 m/s in a 2% NaCl, pH 4, CO_2-saturated solution at 60°C

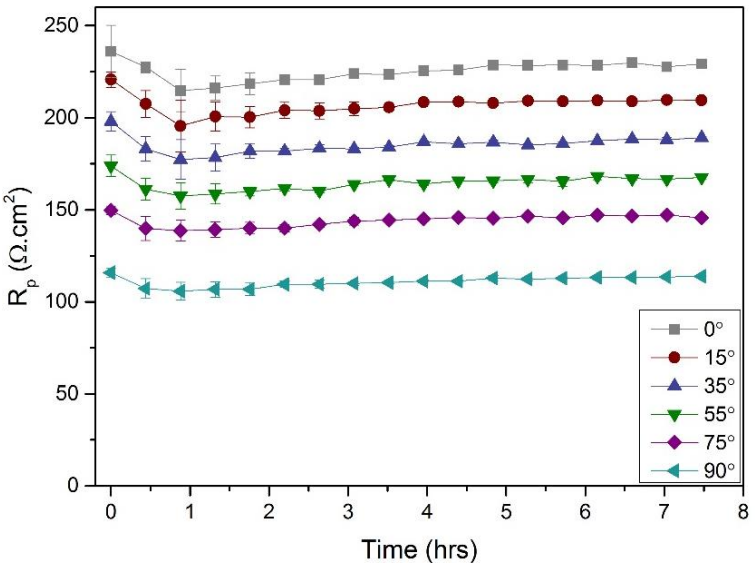

Figure 7.10 Comparison of polarisation resistance from LPR measurements on the outer radius of an elbow in flow-induced corrosion tests at a flow velocity of 6 m/s in a 2% NaCl, pH 4, CO_2-saturated solution at 60°C

The comparison of degradation of X65 measured from mass loss in flow-induced corrosion, erosion and erosion-corrosion tests on the inner radius and outer radius of the elbow are shown in Figure 7.11 and Figure 7.12. No erosion was measured on the inner radius of the elbow, with erosion-corrosion

degradation and flow-induced corrosion degradation similar. Error was significant in erosion-corrosion mass loss measurements and more significant than flow-induced corrosion degradation, but there did appear to be a slight increase in degradation in erosion-corrosion conditions when compared with flow-induced corrosion conditions on the outer radius. The most significant increase in degradation in erosion-corrosion conditions was observed at the 75° sample. A very small erosion contribution was measured.

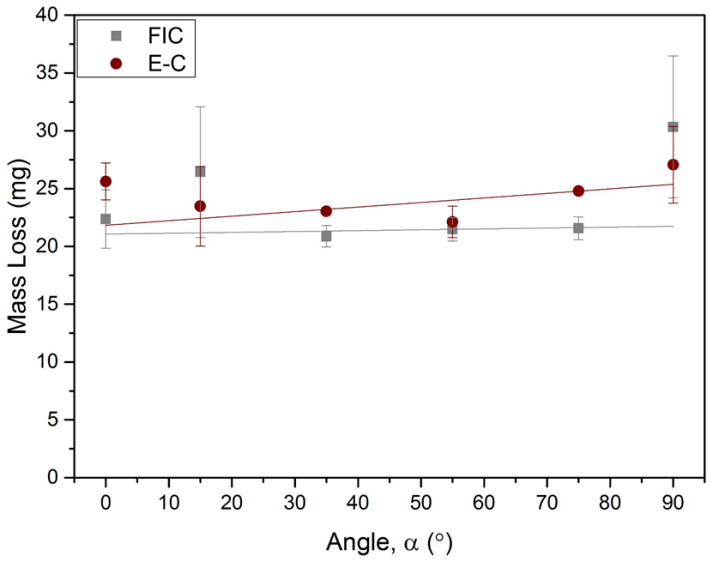

Figure 7.11 Mass loss degradation of X65 carbon steel samples on the inner radius of an elbow in 8-hour flow-induced corrosion tests at a flow velocity of 6 m/s in a 2% NaCl, pH 4, CO_2-saturated solution at 60°C and erosion-corrosion tests containing 1000 mg/L of sand

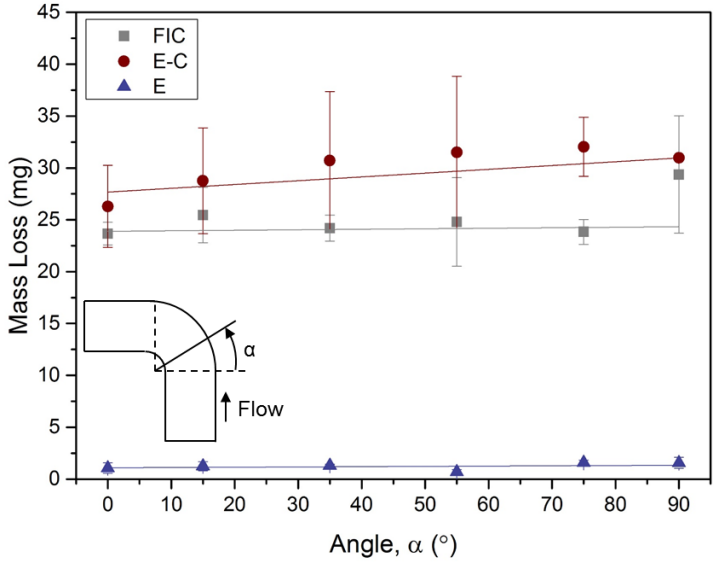

Figure 7.12 Mass loss of X65 samples on the outer radius of an elbow in 8-hour flow-induced corrosion tests at a flow velocity of 6 m/s in a 2% NaCl, pH 4, CO_2-saturated solution at 60°C; erosion tests containing 1000 mg/L of sand in N_2-saturated conditions and erosion-corrosion tests containing 1000 mg/L of sand in CO_2-saturated conditions

The contribution of the individual mechanisms to total erosion-corrosion degradation is shown in Figure 7.13 for the each of the six samples on the outer radius. The same terminology for the erosion-corrosion tests in this chapter was the same as previously used, where 'EC_{TML}' represents the total erosion-corrosion material loss measured from mass loss tests. 'C_{FIC}' represents the total flow-induced corrosion degradation measured from mass loss tests. 'E_0' is the pure erosion degradation measured from erosion tests in N_2-saturated conditions. '$\Delta C_E + \Delta \mathrm{E}_C$' represents the contributions of erosion-enhanced corrosion and corrosion-enhanced erosion.

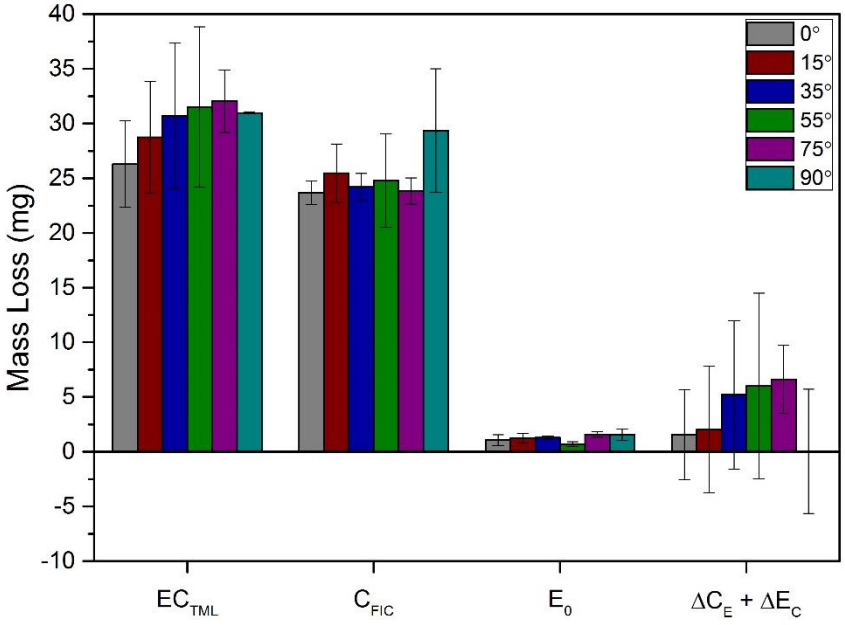

Figure 7.13 Contribution of corrosion ($\boldsymbol{C_{FIC}}$) in flow-induced corrosion elbow tests at a flow velocity of 6 m/s in a CO_2-saturated, 2% NaCl, pH 4, 60°C solution; pure erosion ($\boldsymbol{E_0}$) elbow tests at a flow velocity of 6 m/s in a N_2-saturated, 60°C solution containing 1000 mg/L of sand and interactions ($\boldsymbol{\Delta C_E + \Delta E_C}$) to total erosion-corrosion degradation ($\boldsymbol{\mathrm{EC}_{TML}}$) on the outer radius of the elbow at a flow velocity of 6 m/s in a CO_2-saturated, 2% NaCl, pH 4, 60°C solution containing 1000 mg/L of sand in 8-hour tests

Figure 7.13 highlighted how flow-induced corrosion dominated the overall degradation in these conditions. The contribution of erosion was much less significant and the contribution of the interactions to total erosion-corrosion degradation was small and errors were significant in the results. Due to the significance of error in the calculation of corrosion-enhanced erosion and the limitations in the electrochemistry results, explained previously, separating the two mechanisms could be not reliably completed to determine the contributions of enhanced corrosion and enhanced erosion individually.

7.5 Summary and Conclusions

An elbow was designed to complete flow-induced corrosion, erosion and erosion-corrosion tests. The key features of the design were explained in this chapter and erosion-corrosion tests were completed using the elbow to measure degradation of X65 carbon steel at different locations in the elbow in flow-induced corrosion and erosion-corrosion conditions to analyse degradation in conditions more representative of pipe flow. The main conclusions from the chapter were:

- An evaluation of X65 carbon steel in flow induced corrosion and erosion-corrosion conditions was completed using a newly-designed elbow at a flow velocity of 6 m/s in a solution at a temperature of 60°C;
- Mass loss in flow-induced corrosion tests at 6 m/s in a pH 4 solution saturated with CO_2 at a temperature of 60°C were very high. Degradation was slightly higher on the outer radius of the elbow and increased on both the inner radius and outer radius towards the outlet of the elbow. However, error was significant in the results;
- Error was significant in the erosion-corrosion results at 6 m/s, but there did appear to be an increase in degradation on the outer radius of the elbow compared to flow induced corrosion conditions. The most significance increase in degradation in erosion-corrosion conditions compared to flow induced corrosion conditions was observed on the outer radius on the sample located at 75°;
- Flow-induced corrosion degradation was the most significant contributing mechanism to total erosion-corrosion degradation in the conditions tested.

Chapter 8
Using CFD to Evaluate the Influence of Flow Parameters on Erosion-Corrosion Mechanisms

Flow has a significant influence on pure erosion, pure corrosion and erosion-corrosion degradation. The influence of flow on erosion and corrosion parameters is not always fully defined in geometries used for erosion-corrosion testing, limiting how widely applicable conclusions are from erosion-corrosion research. The influence of test conditions on erosion degradation, in terms of impact angles, number of impacts and impact velocities has been defined in the SIJ. This was extended to the elbow geometry in this chapter. To also understand how flow influenced corrosion in different geometries, mass transfer coefficients were predicted using CFD.

8.1 Introduction

Two geometries have been used for erosion-corrosion testing of X65 carbon steel in this thesis. SIJs have been used for erosion-corrosion evaluation on several occasions [6, 34, 58-62]. Whilst SIJs have provided significant understanding of erosion-corrosion, if the conditions are not fully understood or defined it can be difficult to translate understanding of mechanisms and conclusions into different flow geometries, for example, in pipe flow in the field. Due to the dependence of erosion on a number of parameters, including impact angle and impact velocity, and the variation in flow conditions over a sample surface in the SIJ, that could potentially influence corrosion rates, understanding the influence of flow on erosion-corrosion is essential to define material degradation mechanisms [10, 29]. The influence of flow on erosion-corrosion degradation is often not investigated in significant detail, which has potentially limited the understanding of erosion-corrosion, with erosion-corrosion mechanisms not fully understood and applicable to a general understanding of erosion-corrosion, with most research being relevant to specific applications [8].

A summary of the main flow parameters that have been considered to influence erosion-corrosion degradation in this thesis are shown in Figure 8.1, grouped into erosion and corrosion categories. Flow significantly influences particle trajectories and therefore impact angle and impact velocity, two essential parameters in erosion degradation, meaning erosion rates and mechanisms of erosion can be different in different flow conditions [4]. The

use of CFD to predict particle trajectories has been shown to be important in understanding erosion degradation on several occasions [2, 110, 116, 120, 122, 123]. Gnanavelu et al. [120] demonstrated how material thickness loss could be reliably predicted using CFD particle trajectory predictions to determine impact angles and impact velocities in SIJ pure erosion conditions. The use of CFD to determine impact angles and impact velocities in Chapter 6 of this thesis enabled erosion mechanisms to be characterised on the surface of the SIJ sample. This methodology was extended to determine erosion material removal mechanisms in the elbow in this chapter and to compare conditions in both geometries.

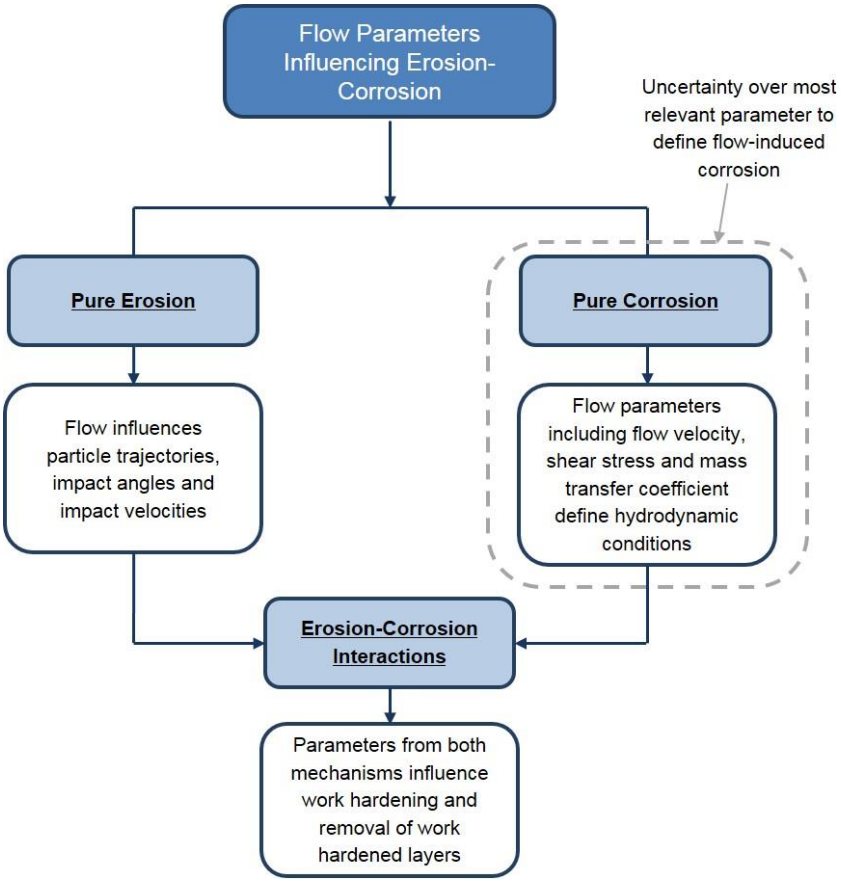

Figure 8.1 Flow parameters influencing flow-induced corrosion, erosion and erosion-corrosion degradation of carbon steel

More debate exists about the most relevant flow parameter that relates hydrodynamic conditions to corrosion rates. However, in flow-induced corrosion conditions at pH < 4, when no surface films are present, the mass transfer coefficient has been shown to be the most influential flow parameter on the corrosion rate [3, 30, 31]. The mass transfer coefficient defines the rate at which corrosive species are transported to a surface and has been shown to translate flow-induced corrosion conditions effectively between different flow geometries to produce the same corrosion rates [30, 31, 52]. Therefore,

mass transfer coefficients were assumed to be the most appropriate flow parameter to relate flow to corrosion rates and were predicted in the SIJ and elbow in this chapter using CFD to define the influence of flow on corrosion mechanisms.

Erosion-corrosion interactions, whereby particle impingement caused surfaces to work-harden and corrosion mechanisms removed work-hardened layers, shown in Chapter 6, would have been influenced by a combination of both erosion and corrosion mechanisms. Therefore, the influence of flow on erosion and corrosion was evaluated separately to define erosion-corrosion conditions in a flow environment. It was not the aim of this chapter to predict erosion-corrosion rates, but to develop a methodology for relating the flow conditions to erosion and corrosion mechanisms using CFD. The objectives of this chapter were to:

- Predict the flow of sand particles through the elbow using CFD to determine particle impact angles and impact velocities and compare with impact angles in the SIJ;
- Define the influence of flow on flow-induced corrosion conditions in the SIJ and elbow by predicting mass transfer coefficients in both geometries using CFD;
- Compare the influence of flow on erosion-corrosion conditions between the elbow and SIJ geometries in terms of mass transfer coefficients, impact angles and impact velocities;
- Identify if erosion-corrosion conditions could be translated between the elbow and SIJ geometries to demonstrate how flow conditions can be accounted for in erosion-corrosion conditions.

8.2 Prediction of Particle Trajectories in the Elbow

When comparing the elbow and SIJ test methodologies, the SIJ offers the benefits of quicker testing, due to shorter setup times, and more options for surface analysis due to the use of thin, flat surface X65 samples. Larger curved samples were used in the elbow which made surface analysis challenging. The elbow was also limited in the number of tests that could be completed using it, as investigations of a slightly different geometry would require new designs to be 3D printed, whilst the SIJ conditions could be changed much more easily. Therefore, there were benefits to using the SIJ for erosion-corrosion testing as opposed to using the elbow. However, it was

unknown how general conditions in the SIJ compared with conditions in the elbow and conditions in the field.

The influence of flow on erosion in a non-corrosive environment in the elbow was analysed first to make a comparison between particle impact angles and impact velocities with the SIJ impingement characteristics. Particle impact angles have been shown to be significant for characterising erosion material removal mechanisms [16-18]. Therefore, when making a comparison between field erosion-corrosion conditions and lab-based tests, it is important to consider if the mechanisms of erosion degradation are similar. CFD was used in Chapter 6 to define mechanisms of degradation in different regions of the sample surface in the SIJ. However, it was unknown which erosion material removal mechanisms were observed in the elbow and how impact angles compared between both geometries.

8.2.1 Elbow Model Description

A diagram of the elbow model identifying the inlet and outlet of the flow is shown in Figure 8.2. The elbow geometry was modelled in 3D using COMSOL Multiphysics 5.2a, rather than 2D used for the SIJ model in Chapter 6. Axisymmetric conditions could not be assumed for the elbow, due to the complexity of the geometry, so was modelled in 3D. To reduce computational time, only half of the elbow was modelled assuming symmetry in the XY plane through the centre of the elbow as shown in Figure 8.2. The same dimensions of the experimental elbow were input with an internal of 25.4 mm and radius equal to five times the internal diameter (R_c/D_p = 5).

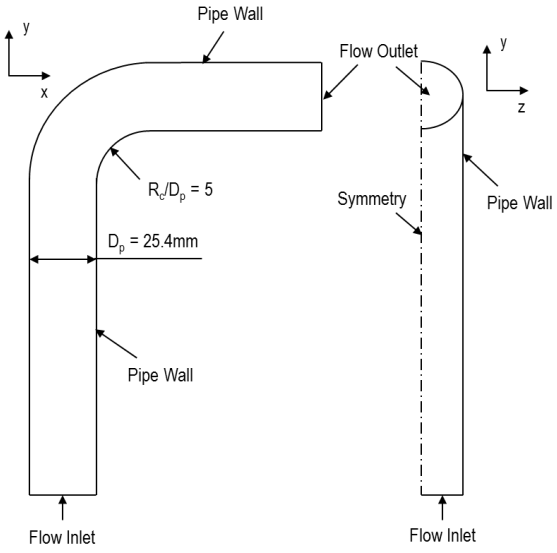

Figure 8.2 Geometry of the 3D 25.4 mm diameter pipe elbow CFD model

The k-ω turbulence model was used, which has been reported to be accurate for internal curved pipe flows [13, 223]. The input conditions were specified for 60°C water flow to replicate conditions in erosion-corrosion testing completed using the elbow in Chapter 7 (ρ = 983.2 kg/m^3, μ = 4.67 x10^{-4} Pa.s) [100]. An inlet flow velocity of 6 m/s was also specified to replicate the test conditions. Fully developed flow was modelled at the inlet by solving flow through a straight pipe length of 100 diameters in the same conditions. The fully developed velocity profile at the end of the straight pipe was specified as the inlet of the elbow. Experimentally, the elbow was positioned 40 internal diameters downstream of the pump, allowing the flow to develop prior to entering the elbow, with an entrance length of 10 diameters typically required in turbulent pipe flow [224]. The additional length of 100 diameters was modelled to ensure a fully developed flow profile was predicted, with the additional length not significantly increasing the time required for the model to converge. A total of 207,165 elements were used in the elbow mesh, consisting of hexahedral elements in the straight sections of pipe, tetrahedral elements in the elbow bend and hexahedral boundary elements close to the walls.

8.2.2 Validation and Prediction of Fluid Flow

The most effective method of validation for the elbow model developed was to compare the results with results of flow velocity through an elbow measured by Enayet et al. [225]. Flow velocities were measured in an elbow at different Reynolds numbers in a 48 mm diameter pipe and R_c/D_p ratio of 2.8. The flow velocity was measured across the diameter of the pipe at an angle of 30° from the inlet, as shown in Figure 8.13. The highest Reynolds number used in experiments completed by Enayet et al. [225] was 43,000, which was simulated using CFD with an inlet flow velocity of 0.98 m/s, assuming ambient fluid conditions.

The flow velocity was expressed as a ratio to the nominal inlet flow velocity across the pipe. A mesh sensitivity study was also completed in these conditions to assess how sensitive results were to changes in the number of elements in the mesh. The predicted flow velocity was very similar to the experimentally measured flow velocities and results were relatively insensitive to changes in the number of elements in the mesh. Over the bulk of the flow across the pipe diameter, the percentage difference between predicted and experimental results was less than 5% when comparing the prediction using 353,225 elements in the mesh. Closer to the walls there was more

discrepancy between experimental and computational results, but there was agreement between the general trend of experimental results and CFD predictions. This was possibly as a result of a low resolution turbulence model near to the wall. However, Edwards et al. [116] also showed that CFD predictions were less accurate closer to the wall, despite using a low Reynolds turbulence model with improved accuracy near to the wall. Experimental error could have also been more significant in the near wall region, potentially explaining the discrepancy. Edwards et al. [116] showed that erosion results validated CFD predictions of erosion in an elbow, suggesting that this effect was not significant on predictions. Whilst these results did not completely validate the model developed for the elbow used in this thesis, the method was shown to be accurate in predicting the behaviour of similar conditions within the literature.

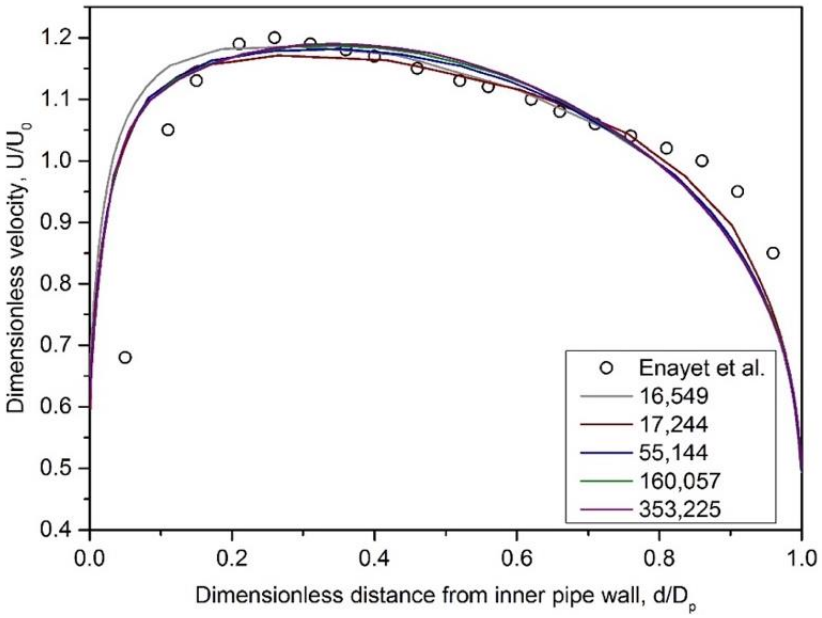

Figure 8.3 Dimensionless fluid velocity measured across the diameter of the pipe in a $\boldsymbol{R_c/D_p}$ = 2.8 elbow at 30° after the inlet for a fluid with Re = 43,000 by Enayet et al. [225] compared with CFD predictions using the $\boldsymbol{k}$-$\boldsymbol{\omega}$ turbulence model

The fluid flow simulation in the elbow at an inlet flow velocity of 6 m/s is shown in Figure 8.4, where the flow velocity through the centre plane of the elbow in the XY axis is shown. A higher flow velocity was generally observed towards the inner radius at the inlet of the elbow compared with the outer radius before the flow separated from the wall. Separation of the flow from the inner wall towards the exit of the elbow was represented as a low velocity region. A higher velocity was observed on the outer wall at this point.

Validation of this elbow model was difficult due to the lack of comparable experimental data. El Gammal et al. [68] completed CFD simulations and experimental analysis of fluid flow through a 1 inch diameter pipe elbow with an R_c/D_p ratio of 1.5 at a flow velocity equivalent to a Reynolds number of 40,000, that qualitatively showed similar results to the results shown in Figure 8.4, with a higher velocity shown towards the inner radius of the elbow and flow separation towards the exit of the elbow. CFD models of fluid flow through elbows developed at the E/CRC use erosion rate experiments to validate erosion rate predictions in elbows, but there are limitations of this method, that have been discussed previously, and it does not reliably validate fluid flow simulations [110, 120, 122].

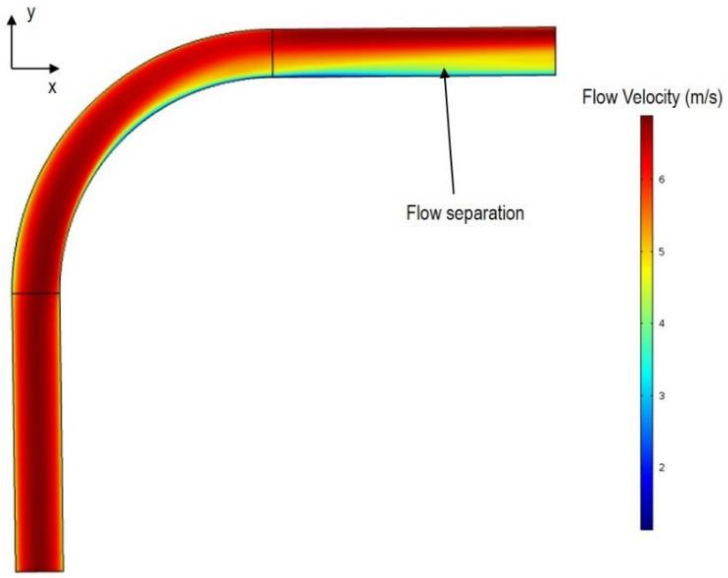

Figure 8.4 Prediction of flow velocity using the $\boldsymbol{k}$-$\boldsymbol{\omega}$ turbulence model through the central plane of a $\boldsymbol{R_c/D_p}$ = 5 elbow at an inlet flow velocity of 6 m/s and solution temperature of 60°C

8.2.3 Prediction of Particle Trajectories

The same methodology and assumptions used in Chapter 6 for the CFD simulation of particle trajectories through the SIJ nozzle was used to predict particle trajectories in the elbow. 50,000 particles were released at the inlet of the elbow and the trajectories of the sand particles as they flow through the elbow are shown in Figure 8.5 at an inlet flow velocity of 6 m/s in a 60°C solution. Particles were shown to flow through the elbow with similar velocities to the flow velocity, with the majority of particles flowing around and exiting the elbow without impacting on the surface. No impacts from sand particles were predicted on the inner radius of the elbow, in agreement with the

experimental results that showed no significant increase in degradation rates when sand was added in erosion-corrosion tests on the inner radius.

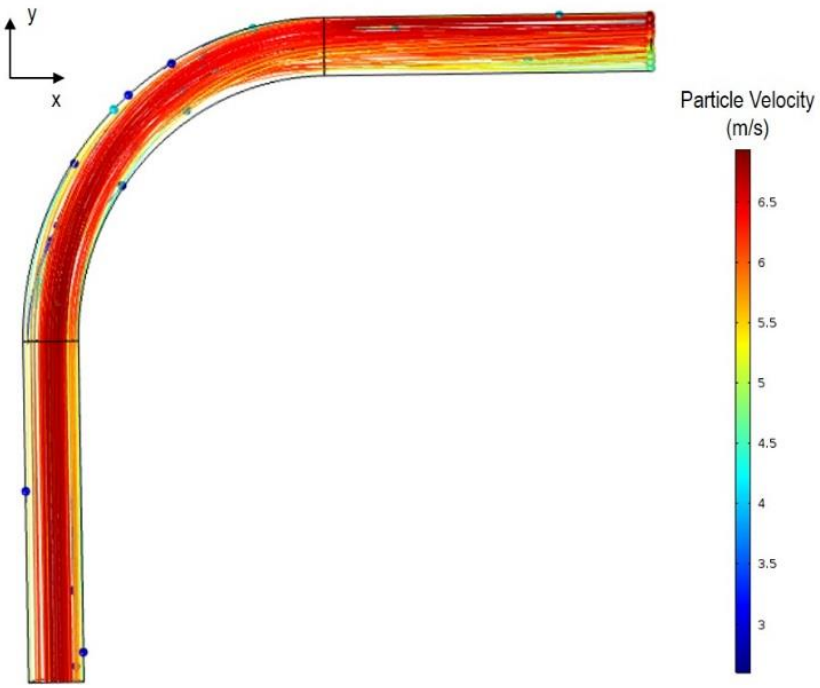

Figure 8.5 CFD prediction of 250 µm diameter sand particle trajectories through a $\boldsymbol{R_c/D_p}$ = 5 elbow at a flow velocity of 6 m/s and solution temperature of 60°C

The average particle impact angles and impact velocities over the surface area of the samples used experimentally were determined using the CFD model at each of the X65 samples on the outer radius of the elbow, shown in Table 8.1. Particles were predicted to not impact on the surface of the 0° sample at the inlet of the elbow on the outer radius. 95% of the particles were also predicted not to impact on the elbow surface and flowed through to the outlet of the elbow. Very low impact angles were predicted, as the particles generally followed the streamlines of the flow without significant deviation. Impact velocity was highest at the 15° samples and gradually reduced further towards the exit of the elbow. Impact angles were very low and less than 5° at each of the samples. This impact angle was significantly different to the range of impact angles predicted in the SIJ in Chapter 6 where, for a 4 mm diameter nozzle at a flow velocity of 20 m/s, impact angles in the range of 30° to 90° were predicted. Gnanavelu et al. [120] predicted impact angles as low as 5° in a SIJ with a 7 mm diameter nozzle at a flow velocity of 5 m/s, showing that reduced impingement angles could be achieved in the SIJ that were similar to the impact angles predicted in the elbow.

Table 8.1 CFD predicted number of particle impacts, impact angles and impact velocities at each of the six samples on the outer radius of the elbow at a flow velocity of 6 m/s and solution temperature of 60°C

Sample	Percentage of Particle Impacts (%)	v_p (m/s)	θ_p (°)
0°	0%	-	-
15°	0.5%	2.3	4.7
35°	1.1%	2.2	4.4
55°	1.0%	2.1	4.2
75°	0.9%	1.8	3.5
90°	1.1%	0.9	3.0

8.3 Influence of Flow on Corrosion

The influence on erosion has been shown to be important for defining particle impact angles and impact velocities and hence erosion mechanisms and degradation. To define how flow parameters influence flow-induced corrosion conditions in the SIJ and elbow, without the presence of sand particles in the flow, mass transfer coefficients were predicted in both geometries using CFD. The predictions were made assuming that sand had no influence on flow and mass transfer coefficients when applied in erosion-corrosion conditions, which was a valid assumption due to the low sand concentration in the erosion-corrosion tests completed in this thesis.

8.3.1 Mass Transfer and Corrosion

Pure corrosion contributes to the total erosion-corrosion degradation of carbon steel and can enhance erosion rates. Therefore, defining how flow influences corrosion mechanisms was essential to understanding the contribution of corrosion to erosion-corrosion degradation. When solution pH is less than 4, the mechanism of corrosion is diffusion controlled, where the dominant mechanism of corrosion is the reduction of H^+ ions [3]. Therefore, at low pH, the flow-induced corrosion rates are defined by the rate at which H^+ ions are transported to the surface [37]. At higher pH's, $4 < pH < 6$, the dissociation of carbonic acid provides an additional source of H^+ ions and an additional cathodic reaction, so the mechanisms are more complex than the diffusion controlled reactions at $pH < 4$ and it was uncertain how flow influences

corrosion rates in these conditions [3]. This rate is defined as the mass transfer coefficient and has been reliably used on a number of occasions to determine corrosion rates and to translate flow-induced corrosion conditions between different flow geometries [52]. The elbow tests in Chapter 7 were completed at pH 4 in a diffusion controlled environment. The mass transfer coefficient is defined using the Sherwood number, Equation (8.1) [226]:

$$Sh = \frac{k_m}{D/L} \tag{8.1}$$

where Sh is the Sherwood number, k_m is the mass transfer coefficient, D is the diffusion coefficient and L is a characteristic length. The numerator in the equation represents convective mass transfer and the denominator represents diffusion. In a diffusion-controlled electrochemical reaction, the mass transfer coefficient can be determined from a limiting current, as shown previously by Equation (3.12). When defined as a Sherwood number, Equation (8.1) becomes [37, 226]:

$$Sh = \frac{k_m}{D/L} = \frac{i_{lim}^d}{nFc_b}\frac{L}{D} \tag{8.2}$$

where n is the charge number. For the case of the transport of H^+ ions, the focus of this work, the charge number is equal to +1 [226].

The Berger and Hau [55] correlation and Eisenberg [56] correlation are examples of relationships that can be used to calculate the mass transfer coefficients in straight pipes and RCEs respectively. These mass transfer coefficient relationships are well defined and validated for straight pipes and RCEs, but mass transfer coefficients in some geometries cannot be calculated as easily. Silverman [52, 53] translated conditions between different flow geometries through the use of mass transfer coefficients, and defined the RCE angular velocity required to achieve the same mass transfer coefficient in the RCE that would be present in other geometries. One of the geometries compared was the SIJ, but this was only applicable for a very narrow range of nozzle diameters and nozzle to sample heights, so could not be universally applied to SIJs [53]. Therefore, prediction of mass transfer coefficients in the SIJ could not be easily completed.

Few correlations also exist for complex flow geometries, such as elbows. Wang et al. [67] developed an equation to predict the maximum mass transfer coefficient in a 90° pipe elbow using results from CFD predictions, Equation (8.3):

$$Sh_e = \frac{k_m}{D/D_p} = 0.0165Re^{0.86}Sc^{0.33}\left[0.68 + \{1.2 - 0.044\log(Re)\}e^{-0.065\frac{R_C}{D_p}} + \frac{0.58}{\log(Sc+2.5)}\right] \quad (8.3)$$

where Sh_e is the maximum Sherwood number in the elbow and Sc is the Schmidt number. This equation was combined with the straight pipe correlation of Berger and Hau [55] to predict the maximum mass transfer coefficient in the elbow using the mass transfer coefficient in a straight pipe of the same diameter. However, there were several limitations to this equation as it could only be used to predict the maximum mass transfer coefficient and did not provide information about the location in the elbow of the maximum mass transfer coefficient or how mass transfer coefficients varied in the elbow. Therefore, determining mass transfer coefficients in the SIJ and pipe elbow geometries was not possible through mathematical equations or empirical relationships, and required the use of CFD.

8.3.2 Theory of Species Transport in Turbulent Flow

In a fluid element, as defined in Chapter 2, the rate of mass of species a flowing into the element is equal to the sum of the mass flowing out of the element and the increase of mass within the element. The rate of increase of mass of species a is defined by [227]:

$$\frac{\partial(\rho_a)}{\partial t}\delta x\delta y\delta z \quad (8.4)$$

where ρ_a is the density of the species a and δx, δy and δz are the dimensions of the fluid element. The rate of addition of mass and rate of removal of mass across all of the boundaries in the fluid element is defined as [227]:

$$\begin{aligned}&\left(n_{a,x} - \frac{\partial(n_a)}{\partial x}\frac{1}{2}\delta x\right)\delta y\delta z - \left(n_{a,x} + \frac{\partial(n_a)}{\partial x}\frac{1}{2}\delta x\right)\delta y\delta z + \\ &\left(n_{a,y} - \frac{\partial(n_a)}{\partial y}\frac{1}{2}\delta y\right)\delta x\delta z - \left(n_{a,y} + \frac{\partial(n_a)}{\partial y}\frac{1}{2}\delta y\right)\delta x\delta z + \\ &\left(n_{a,z} - \frac{\partial(n_a)}{\partial z}\frac{1}{2}\delta z\right)\delta x\delta y - \left(n_{a,z} + \frac{\partial(n_a)}{\partial z}\frac{1}{2}\delta z\right)\delta x\delta y\end{aligned} \quad (8.5)$$

where n_a is the mass flux in kg/(m^{2}s). An additional term is utilised in chemical species transport, that was not used in fluid flow, whereby the mass of species a can change as a result of chemical reaction within the fluid element [227]:

$$r_a\delta x\delta y\delta z \quad (8.6)$$

where r_a is the mass of species a produced by chemical reactions. The continuity equation for species, similar to the fluid flow equation in Chapter 2,

is therefore defined by Equations (8.4), (8.5) and (8.6) after dividing by the element volume [227]:

$$\frac{\partial \rho_a}{\partial t} = -\left(\frac{\partial n_{ax}}{\partial x} - \frac{\partial n_{ay}}{\partial y} - \frac{\partial n_{az}}{\partial z}\right) + r_a \tag{8.7}$$

This equation can then be expressed in vector form:

$$\frac{\partial \rho_a}{\partial t} = -\nabla n_a + r_a \tag{8.8}$$

The continuity equation is often expressed in terms of molar concentration rather than mass and becomes:

$$\frac{\partial c_a}{\partial t} = -\nabla N_a + R_a \tag{8.9}$$

where c_a is the concentration of species a in mol/m^3, N_a is the flux of species a in mol/(m^{2}s). Mass of the species can be transported into and out of the fluid element through convection and diffusion. Therefore the flux term is defined by a convection term and a diffusion term [227]:

$$N_a = c_a \mathbf{U} + J_a \tag{8.10}$$

where $\mathbf{U}$ is the velocity vector, and J_a is the diffusive flux of species a, defined by Fick's first law of diffusion [228]:

$$J_a = -D_a \nabla c_a \tag{8.11}$$

where D_a is the diffusion coefficient of the species a. Fick's second law of diffusion is defined by [228]:

$$\nabla J_a = -D_a \nabla^2 c_a \tag{8.12}$$

Therefore, the continuity equation, Equation (8.9), can be rewritten as Equation (8.13), by substituting in Equations (8.10) and (8.12):

$$\frac{\partial c_a}{\partial t} = \nabla \cdot (c_a \mathbf{U}) - D_a \nabla^2 c_a + R_a \tag{8.13}$$

Equation (8.13) does not account for the effects of turbulent flow. Turbulence can have a significant effect on the transport of species [227]. Similarly to the definitions of turbulent flow in Chapter 4, where the flow velocity was defined as the mean velocity with an additional fluctuation term as a result of turbulence, the concentration of species is also defined by a mean concentration and a turbulence fluctuation term:

$$c_a = \bar{c_a} + c_a' \tag{8.14}$$

where $\overline{c_a}$ is the mean concentration and c_a' is the turbulent fluctuation of the concentration. By replacing the velocity and concentration terms in Equation (8.13) with the mean values and the fluctuations due to turbulence, and assuming that no chemical reactions occur within the element, the continuity equation becomes:

$$\frac{\partial c_a}{\partial t} = -\left(\frac{\partial}{\partial x}\bar{u}\overline{c_a} + \frac{\partial}{\partial y}\bar{v}\overline{c_a} + \frac{\partial}{\partial z}\bar{w}\overline{c_a}\right) - \left(\frac{\partial}{\partial x}\overline{u'c_a'} + \frac{\partial}{\partial y}\overline{v'c_a'} + \frac{\partial}{\partial z}\overline{w'c_a'}\right) + D_a\left(\frac{\partial^2\overline{c_a}}{\partial x^2} + \frac{\partial^2\overline{c_a}}{\partial y^2} + \frac{\partial^2\overline{c_a}}{\partial z^2}\right) \quad (8.15)$$

This equation has additional unknown terms of $\overline{u'c_a'}$, $\overline{v'c_a'}$ and $\overline{w'c_a'}$ that represent the effects of turbulence on the transport of species. The turbulent flux is therefore defined as Equation (8.16) in the x-direction [227]:

$$\overline{J_a} = \overline{u'c_a'} \quad (8.16)$$

By analogy with Fick's first law of diffusion [227]:

$$\overline{u'c_a'} = -D_t\frac{\partial c_a}{\partial x} \quad (8.17)$$

where D_t is the turbulent mass diffusivity, defined by Equation (8.18) [227]:

$$D_t = \frac{\mu_t}{\rho Sc_t} \quad (8.18)$$

where μ_t is the turbulent viscosity term defined previously Sc_t is the turbulent Schmidt number. The turbulent Schmidt number is difficult to define, with a value of 0.71 typically assumed in CFD simulations of diffusion [229]. However, it has been shown that this value can be inaccurate and that turbulent Schmidt number is significantly influenced by the flow geometry and the distance from the wall, potentially leading to inaccuracies in the prediction of mass transfer coefficients [229, 230]. Turbulent Schmidt numbers were not reported in the mass transfer CFD models developed by Srinavanasan [70], Keating and Nesic [66] and Wang et al. [67]. Nesic et al. [128] and Wang et al. [231] used a turbulent Schmidt number of 0.9 for liquid pipe flow, but no justification was given for the use of this value. The turbulent Schmidt number is analogous to the turbulent Prandtl number used in heat transfer predictions, which has been reported to range from 0.5 to 0.9 for flow in pipes and jets [227]. It has also been shown that a value of 0.7 for the turbulent Schmidt number is accurate for predictions in axisymmetric jet flow [229]. The effect of turbulent Schmidt number on mass transfer coefficients was investigated.

8.3.3 CFD Prediction of H^+ Mass Transport

CFD was used to predict mass transfer coefficients in the SIJ and elbow geometries used in the erosion-corrosion tests in previous chapters. CFD has been used previously to predict mass transfer coefficients in different pipe flow geometries [67, 70, 179]. The use of turbulence models that fully resolve to the wall are required to predict mass transfer coefficients, due to the mass transfer boundary layer being well within the viscous sub-layer in the range of $y^+ < 0.5$ [70, 209]. Wall functions cannot solve to this level of accuracy [13].

In low pH conditions, it is assumed that all H^+ ions are consumed at the surface, therefore the concentration at the wall is zero, and the mass transfer coefficient is defined by Equation (8.19) [228]:

$$N = k_m(c_b - c_w) = k_m c_b \tag{8.19}$$

where c_b is the concentration of the H^+ ions in the bulk solution in mol/m^3 and c_w is the concentration of the H^+ ions at the wall in mol/m^3. The concentration of H^+ ions in the bulk can be determined from the pH of the solution, using Equation (8.20) [30]:

$$c_{b[H^+]} = 10^{-pH} \tag{8.20}$$

where pH is the pH of the bulk solution. The diffusion coefficient of H^+ ions in water solution at a temperature of 25˚C is 9.31 x 10^{-9} m^2/s [232]. The variation of the diffusion coefficient with temperature and viscosity is defined by the Stokes-Einstein equation, Equation (8.21) [228]:

$$D = D_0 \frac{T}{T_0} \frac{\mu_0}{\mu} \tag{8.21}$$

where D_0 is the diffusion coefficient in ambient conditions, T_0 is the ambient temperature (25°C) and μ_0 is the dynamic viscosity of the water in ambient conditions (8.9 x 10^{-4} Pa.s) [100]. At a solution temperature of 60°C used for predictions of mass transfer coefficients in the SIJ and elbow, the diffusion coefficient of H^+ ions in water solution was calculated to be 1.98 x 10^{-8} m^2/s using Equation (8.21). The flux of H^+ could be determined at the boundary of the wall using CFD by measuring the concentration gradient. From this flux, the mass transfer coefficient could then be calculated.

8.4 Validation of Methodology for Predicting Mass Transfer Coefficients Using CFD

CFD predictions of mass transfer coefficient in the SIJ and elbow geometries, shown later, could not be fully validated due to a lack of available experimental data and mathematical solutions. Therefore, simulations of fluid flow through a straight pipe were completed to determine mass transfer coefficients and to demonstrate that the CFD approach was a reliable method of predicting mass transfer coefficients. Nesic et al. [30, 31] completed tests in a straight pipe to determine mass transfer coefficients and Berger and Hau [55] derived an equation that could be used to predict mass transfer coefficients in a straight pipe, providing two methods of validating the CFD model.

8.4.1 Straight Pipe Model Description

The straight pipe was modelled so that a comparison could be made between the well-defined conditions in straight pipes from the correlation developed by Berger and Hau [55] and the experimental results obtained by Nesic et al. [30], where mass transfer coefficients were measured in a straight pipe at flow velocities from 1 m/s to 11 m/s at ambient pressure with a solution temperature of 20°C, a fluid density of 998 kg/m^3 and a dynamic viscosity of 1.0 x 10^{-3} Pa.s [100]. The Berger and Hau [55] straight pipe correlation for predicting mass transfer coefficient is given in Equation (8.22):

$$Sh = \frac{k_m D_p}{D} = 0.0165 Re^{0.86} Sc^{0.33} \tag{8.22}$$

where Sh is the Sherwood number, D_p is the pipe diameter and Sc is the Schmidt number defined by Equation (8.23):

$$Sc = \frac{\mu}{\rho D} \tag{8.23}$$

A 2D axisymmetric model of a straight pipe with the same diameter was modelled using CFD. A diagram of the straight pipe model is shown in Figure 8.6. A mesh consisting of 437,532 rectangular elements was used, with a finer mesh at the pipe wall to resolve the transport of species to a high level of accuracy. The first layer of elements adjacent to the wall had a thickness equivalent to $y^+ \approx 0.1$. The equation defined in the previous section for calculating mass transfer coefficient, Equation (8.19), was used to determine the mass transfer coefficient along the pipe wall. The SST turbulence model was used rather than the $\boldsymbol{k}$-$\boldsymbol{\omega}$ model to fully resolve the flow at the wall, rather than using wall functions. A straight pipe with a length of 105 diameters was

modelled so that the flow was fully developed. Mass transfer coefficients reported were obtained at the pipe wall from an average in the region from 100 diameters to 105 diameters.

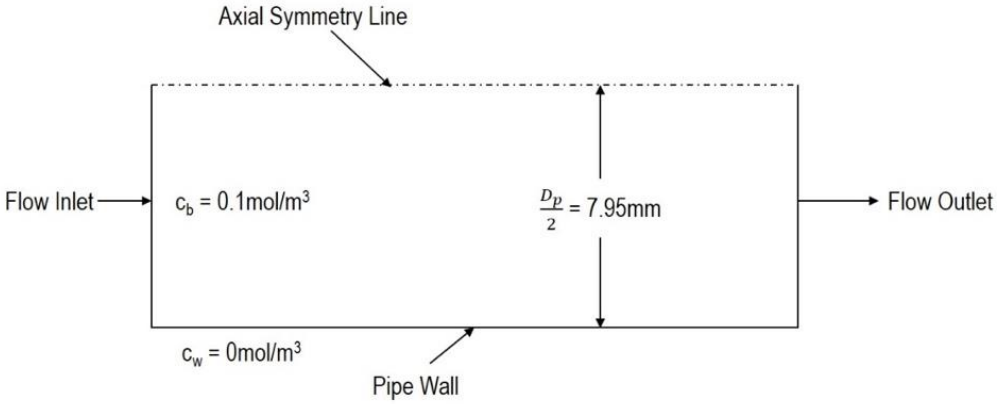

Figure 8.6 Geometry of the straight pipe 2D axisymmetric CFD model with a 15.9 mm diameter and H^+ bulk concentration of 0.1 mol/m^3, equivalent to pH 4

8.4.2 Model Sensitivity Study

A mesh sensitivity study was completed to investigate how sensitive predictions of mass transfer coefficient were to changes in the number of elements in the mesh, shown in Figure 8.7. The mesh sensitivity study showed that increasing the number of elements not only increased accuracy compared to the Berger and Hau [55] mass transfer coefficient predictions, but also showed more consistency across the length of pipe analysed. The use of 831,180 elements required significant computational resources and took a significantly long time to run the simulation. Therefore, 437,532 elements were used in the mesh for the predictions of mass transfer coefficient as this showed similar levels of accuracy to predictions made using 831,180 elements, without excessive computational demand, predicting mass transfer coefficients to within 8% of the Berger and Hau [55] mass transfer coefficient predictions. Some variation across the length of the pipe was observed in the coarser meshes so were not appropriate for accurate predictions of mass transfer coefficient.

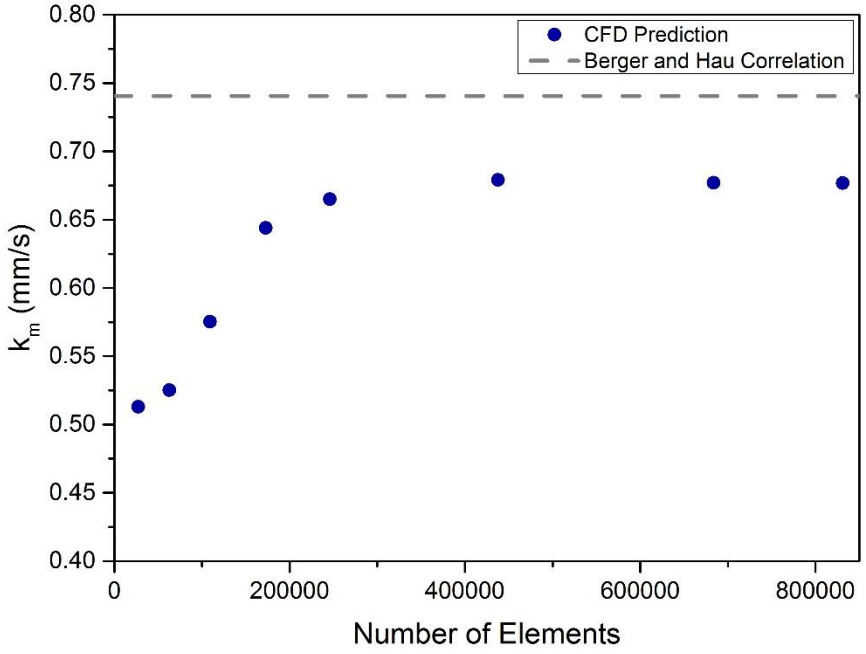

Figure 8.7 Sensitivity of CFD-predicted mass transfer coefficients using the SST turbulence model to changes in changes in the number of elements in the mesh for a straight pipe with diameter of 15.9 mm at an inlet flow velocity of 5 m/s, solution temperature of 25°C and $\boldsymbol{Sc_t}$ = 0.71

The sensitivity to the turbulent Schmidt number is shown in Figure 8.8 for an inlet flow velocity of 5 m/s using a mesh consisting of 437,532 elements at y^+ ≈ 0.1. The simulations in Figure 8.7 were completed using a turbulent Schmidt number of 0.71, the value typically assumed for CFD simulations of mass transport. A systematic variation of turbulent Schmidt number between a value of 0.1 and 1.0 was compared with the mass transfer coefficients predicted by the Berger and Hau [55] correlation to demonstrate the significance of the value of turbulent Schmidt number on mass transfer coefficient predictions. A turbulent Schmidt number of 0.5 appeared to be the most appropriate for the prediction of mass transfer coefficient in straight pipe flow. Without further evidence to change this value, it was assumed that 0.5 was the most appropriate turbulent Schmidt number for mass transfer in a straight pipe.

The sensitivity of the solution to changes in the thickness of the first cell adjacent to the wall was also investigated by changing the distance to the centre of the first cell, represented by y^+. For y^+ ≈ 0.1, significant refinement of the mesh was required to achieve this level of accuracy. However, a value of y^+ < 0.5 is often reported to be required for mass transfer solutions [70, 179]. The sensitivity of the mass transfer coefficient to changes in the y^+ value is shown in Figure 8.9.

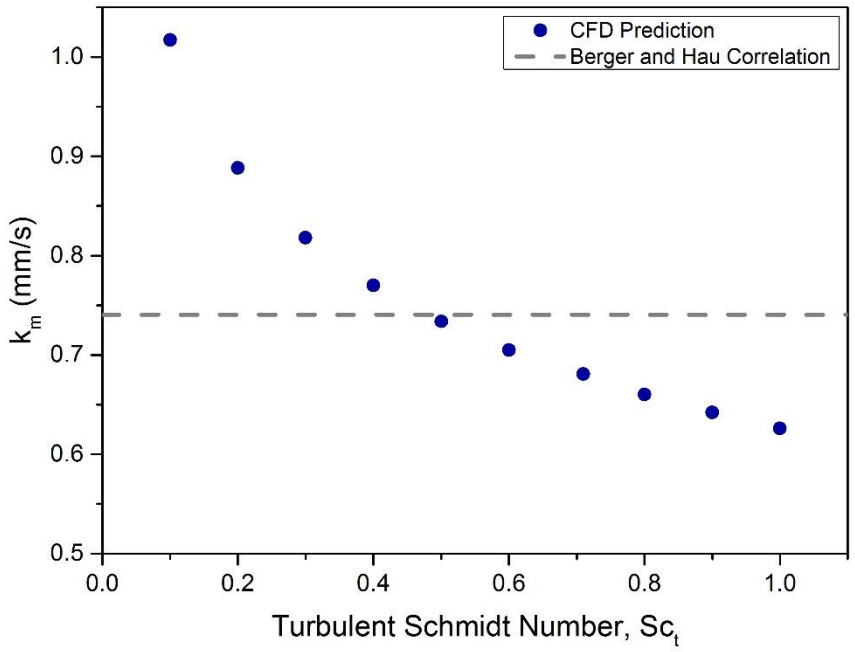

Figure 8.8 Sensitivity of CFD-predicted mass transfer coefficients using the SST turbulence model to changes in $\boldsymbol{Sc_t}$ for a straight pipe with diameter of 15.9 mm at an inlet flow velocity of 5 m/s and solution temperature of 25°C

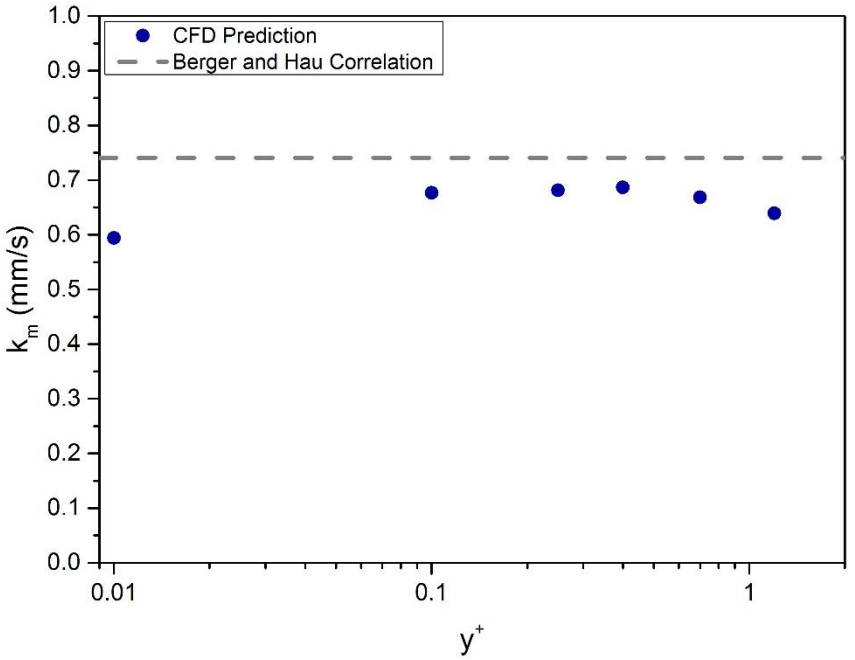

Figure 8.9 Sensitivity of CFD-predicted mass transfer coefficients using the SST turbulence model to changes in $\boldsymbol{y^+}$ of the first element centre thickness for a straight pipe with diameter of 15.9 mm at an inlet flow velocity of 5 m/s and solution temperature of 25°C

Some reduction in accuracy was expected at higher y^+ values because a less refined bulk mesh was required to achieve a higher y^+ at the wall. However, only a very small change was observed between mass transfer coefficient

predictions using a mesh with a first element thickness of $y^+ \approx 0.1$ and $y^+ \approx 0.7$. Therefore, there did not appear to be a significant dependence on the thickness of the first element to achieve an accurate mass transfer coefficient solution, for these conditions, if $y^+ < 0.7$. At $y^+ \approx 1.2$, the solution was slightly more inaccurate, with the difference between CFD predictions and predictions made using the Berger and Hau [55] correlation within 10% to 15%. The finest resolution of $y^+ \approx 0.01$ was compared to show that excessive refinement of the mesh could potentially reduce accuracy, giving the most inaccurate result in Figure 8.9, possibly due to poor transition between the very fine boundary mesh and bulk domain mesh. To ensure that the most accurate solution could be achieved, a target y^+ value of between 0.1 and 0.7 was used for all mass transfer models.

8.4.3 Prediction of Mass Transfer Coefficients & Validation

Mass transfer coefficients were predicted using CFD for the range of flow velocities from 1 m/s to 11 m/s that were experimentally determined by Nesic et al. [30, 31] for a straight pipe that compared well with the Berger and Hau [55] correlation. These conditions were predicted using the CFD model developed in this work to validate the methodology used for mass transfer coefficient prediction. A typical concentration of H^+ ions through the straight pipe in a region of fully developed flow is shown in Figure 8.10, at a flow velocity of 5 m/s. It was observed that the concentration was that of the bulk inlet concentration throughout the majority of the pipe.

To demonstrate how the concentration changed at distances very close to the wall, a comparison of the concentration gradient in the z-axis and the velocity profile is shown in Figure 8.11. The gradients have been shown in dimensionless form by dividing the concentration and velocity at each point by the nominal inlet concentration and flow velocity. The concentration increased to its maximum value consistent in the bulk flow at a distance much closer to the wall than velocity. The concentration changed significantly within 1 μm from the wall, showing that mass transfer boundary layer is well within the fluid boundary layer, requiring a high level of mesh refinement.

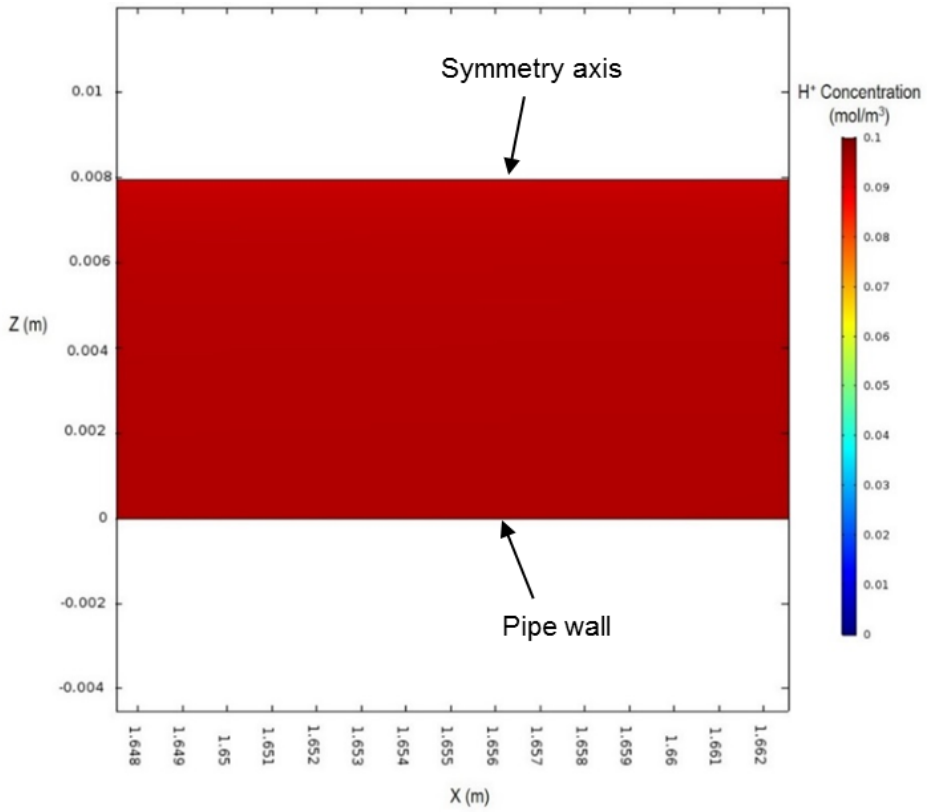

Figure 8.10 CFD prediction of H^+ concentration in a 15.9 mm diameter straight pipe using the SST turbulence model at a flow velocity of 5 m/s and solution temperature of 25°C

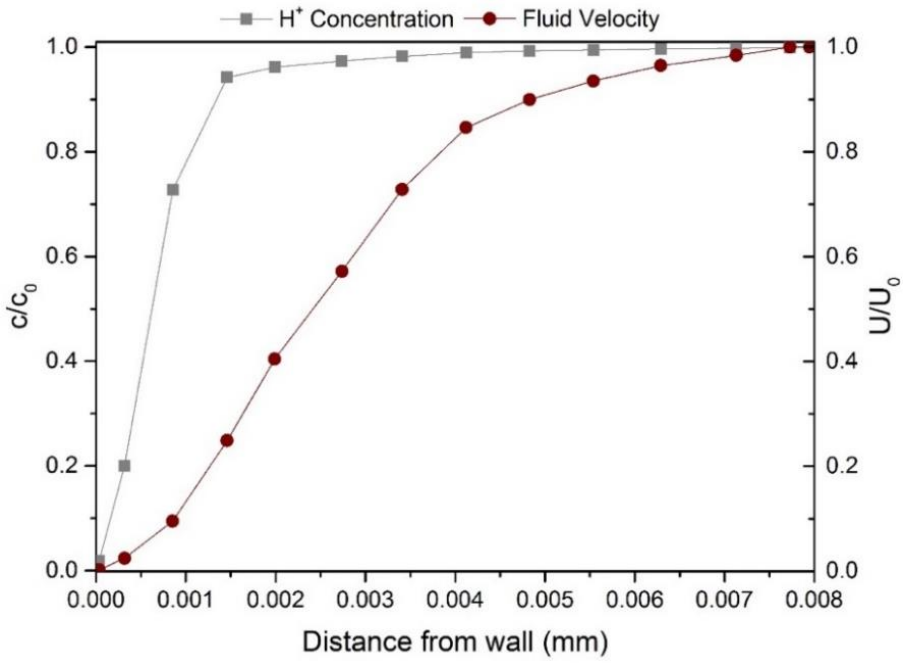

Figure 8.11 CFD prediction of H^+ concentration gradient and flow velocity profile in a 15.9 mm diameter straight pipe using the SST turbulence model at a flow velocity of 5 m/s and solution temperature of 25°C

The full prediction of mass transfer coefficients through the straight pipe at flow velocities from 1 m/s – 11 m/s is shown in Figure 8.12. The CFD

prediction of mass transfer coefficients was compared with the experimental mass transfer coefficients determined by Nesic et al. [30] and the Berger and Hau [55] correlation, showing relatively good agreement with both results for all flow velocities at a turbulent Schmidt number of 0.5. Using a turbulent Schmidt number of 0.71 under predicted the mass transfer coefficient compared to the Berger and Hau [55] correlation and Nesic et al. [30] experimental measurements of mass transfer coefficients in the pipe.

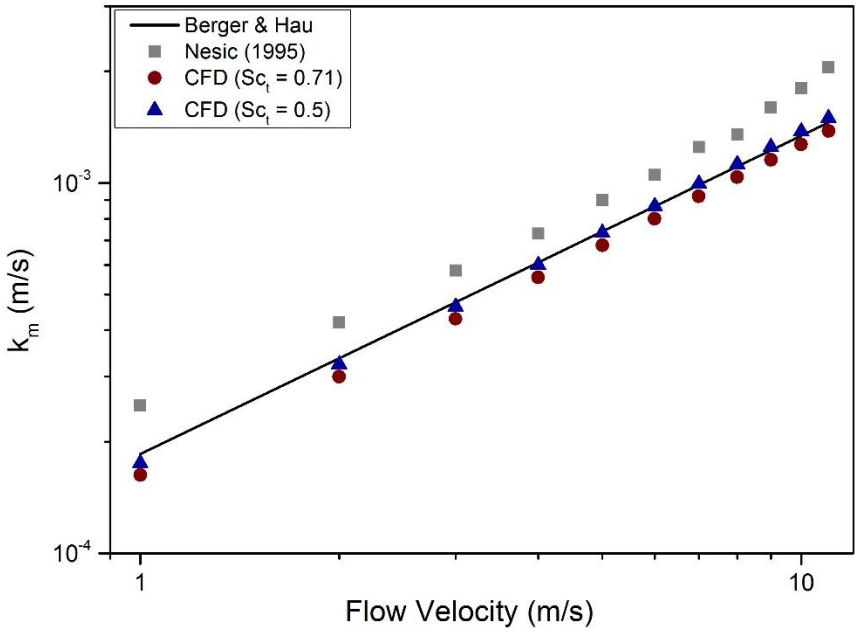

Figure 8.12 CFD prediction of mass transfer coefficients in a 15.9 mm diameter straight pipe using the SST turbulence model at flow velocities of 1 m/s - 11 m/s and a solution temperature of 25°C, compared with the Berger and Hau [55] correlation for mass transfer coefficients in a straight pipe and experimental mass transfer coefficients obtained by Nesic et al. [30]

8.5 Prediction of Mass Transfer Coefficients in the Elbow

After showing that CFD was an accurate method of predicting mass transfer coefficients in a simple geometry, mass transfer coefficient predictions in the more complex geometries used for predictions in the elbow. The same methodology was applied to the prediction of mass transfer coefficients in an elbow to fully define the erosion-corrosion conditions in the elbow geometry designed for erosion-corrosion testing of carbon steel in Chapter 7.

8.5.1 Model Description

The elbow model used for the particle trajectory predictions was adapted and used for the mass transfer coefficient predictions. However, simulations were completed using a 2D elbow model, rather than the 3D model used for particle trajectory predictions in the elbow. The 2D model of the elbow used for mass transfer predictions is shown in Figure 8.13. Excessive computational demand and solving time was required to obtain mass transfer coefficients with a sufficiently accurate resolution of the mesh near to the wall in 3D. For the results required in this thesis, the 2D model provided the necessary accuracy and enabled the mesh to be refined more accurately at the wall.

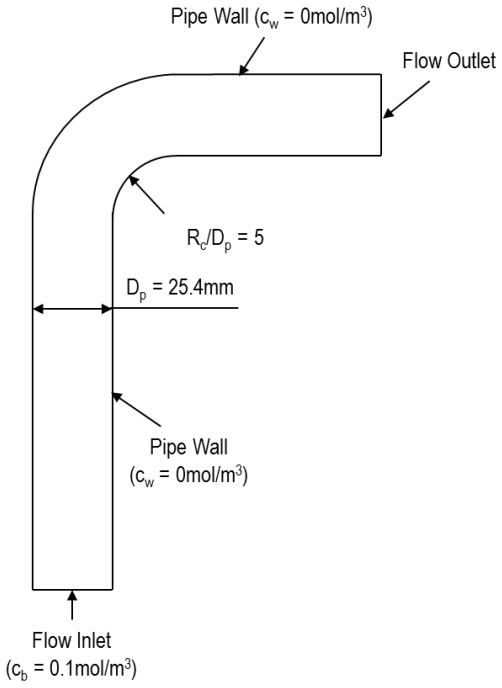

Figure 8.13 Geometry of the 2D elbow CFD model with a 25.4 mm diameter, $\boldsymbol{R_c/D_p}$ ratio of 5 and H^+ bulk concentration of 0.1 mol/m^3, equivalent to pH 4

The SST turbulence model was used for mass transfer predictions in the elbow. The inputs conditions were specified for a 60°C water flow and an inlet flow velocity of 6 m/s to replicate the test conditions in Chapter 7. A total of 326,442 elements were used in the elbow mesh, consisting of rectangular elements in the straight sections of pipe, triangular elements in the elbow bend and rectangular boundary elements close to the walls. The centre of the first element layer was specified to have a thickness of $y^+ \approx 0.1$ at the surface of the pipe walls.

8.5.2 Prediction of Mass Transfer Coefficients

The mass transfer coefficients on the inner and outer radius of the elbow at a flow velocity of 6 m/s in a 60°C solution are shown in Figure 8.14. The mass transfer coefficient varied through the elbow and were higher on the inner radius of the elbow than the outer radius. On the inner radius, the mass transfer coefficient was generally higher through the elbow than in the straight sections of pipe at 0° and 90°. A turbulent Schmidt number of 0.71 was used as no experimental data was available that confirmed a more appropriate number to use. A turbulent Schmidt number of 0.5 was shown to be more accurate in straight pipe flow, and it was possible that this would be acceptable in flow through an elbow. However, it was unknown how the disturbance in the flow through the elbow effected the turbulent Schmidt number. To partially validate the model, a maximum mass transfer coefficient of 2.17 mm/s was predicted using the Wang et al. [67] correlation, Equation (8.3). This value was approximately 5% greater than the maximum mass transfer coefficient predicted in Figure 8.14.

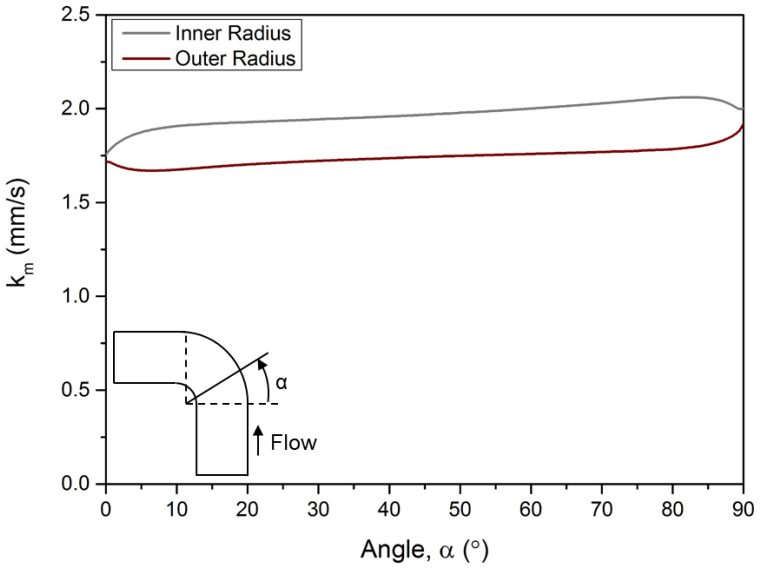

Figure 8.14 CFD prediction of mass transfer coefficients in a 90° elbow using the SST turbulence model for an elbow with an $\boldsymbol{R_c/D_p}$ ratio of 5, with an inlet flow velocity of 6 m/s at a temperature of 60°C, predicting the transport of H^+ ions

8.6 Prediction of Mass Transfer Coefficients in the SIJ

CFD predictions of mass transfer in the SIJ were completed to compare the hydrodynamic conditions in both geometries used for erosion-corrosion tests in this thesis. The SIJ geometry used for erosion-corrosion tests in Chapters

5 and 6 was modelled and the same methodology as straight pipe and elbow tests was used to determine the mass transfer coefficients on the surface of the sample in the SIJ.

8.6.1 Model Description

Mass transfer coefficients in the SIJ were predicted so that the conditions in the SIJ could be compared with conditions in the elbow geometry. The same model geometry used for the SIJ in Chapter 6 was used for the prediction of mass transfer coefficients. The SIJ nozzle was modelled as a 2D axisymmetric model, with H^+ ions entering through the top of the nozzle and transported to the X65 carbon steel sample located below the exit of the nozzle shown in Figure 8.15.

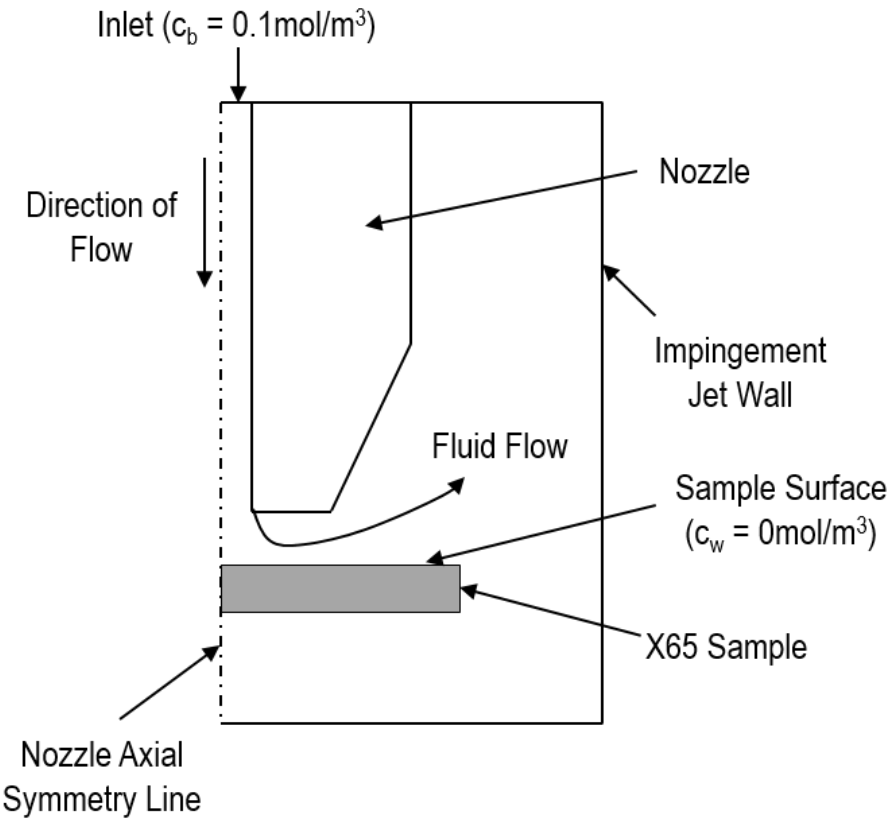

Figure 8.15 Geometry of the SIJ CFD model with an 8 mm diameter nozzle, distance from nozzle to sample of 5 mm and bulk H^+ concentration of 0.1 mol/m^3 equivalent to pH 4

Similarly to the straight pipe model, the centre of first element layer in the mesh at the surface of the X65 sample had a thickness equivalent to $y^+ \approx 0.1$ and the SST turbulence model was used to predict the fluid flow. This added a significant amount of complexity to the model of the SIJ previously used for flow and particle trajectory predictions and increased the time required for the

model to solve. A mesh consisting of 246,147 elements was used, consisting of triangular elements in the bulk domain and a finer rectangular mesh at the pipe wall to resolve the transport of species to a high level of accuracy. It was shown previously that this level of accuracy was sufficient for fluid flow predictions in the SIJ. This was the most refined mesh analysed in the mesh sensitivity study in Chapter 6. This level of accuracy was used for the bulk mesh as a more refined mesh was required at the wall. A nozzle diameter of 8 mm was used, rather than 4 mm nozzle used for erosion-corrosion tests in Chapter 5 and Chapter 6. The use of a larger diameter nozzle enabled lower velocities to be achieved in the SIJ [35]. A nozzle flow velocity of 6 m/s was predicted to make a direct comparison between the mass transfer coefficients in the SIJ and elbow at the same flow velocity. A solution temperature of 60°C was input into the model through the use of a density equal 983.2 kg/m^3 and dynamic viscosity of 4.67 x 10^{-4} Pa.s [100]. A turbulent Schmidt number of 0.71 was used.

8.6.2 Prediction of Mass Transfer Coefficients

The variation in mass transfer coefficient over the X65 sample surface in the SIJ at a flow velocity of 6 m/s is shown in Figure 8.16. The mass transfer coefficient in the stagnation region in the centre of the sample was lower than the mass transfer coefficient in the turbulent jet region. The mass transfer coefficient increased gradually across the sample before becoming relatively constant towards the outer edge of the sample. Mass transfer coefficients in the SIJ were larger than the mass transfer coefficients measured in the elbow for the same inlet flow velocity. The mass transfer coefficient in the SIJ was approximately double the mass transfer coefficients predicted on the outer radius of the elbow at a flow velocity of 6 m/s. Mass transfer coefficients were higher on the inner radius, however, particle impacts were only observed and predicted on the outer radius of the elbow. Therefore, to make a comparison with the samples subject to erosion-corrosion in the elbow, only the outer radius mass transfer coefficients were compared with the SIJ mass transfer coefficients. Mass transfer coefficients were also larger in the SIJ than were predicted on the inner radius, therefore the SIJ was expected to be a more aggressive environment for flow-induced corrosion than the elbow at pH < 4.

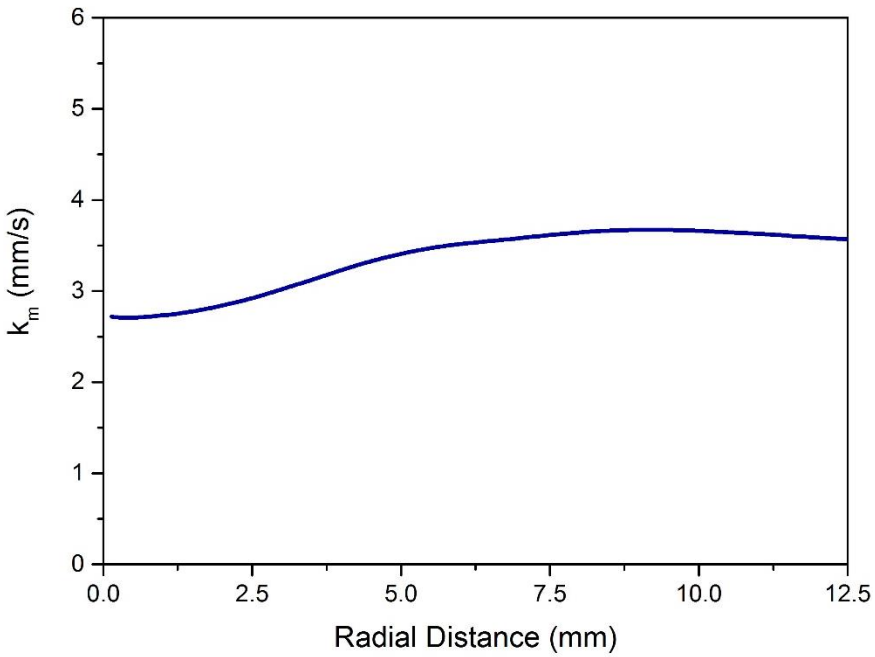

Figure 8.16 CFD prediction of mass transfer coefficients on an SIJ sample using the SST turbulence model for an SIJ nozzle diameter of 8 mm and distance to sample of 5 mm at a flow velocity of 6 m/s and solution temperature of 60°C, predicting the transport of H^+ ions

8.7 Summary and Conclusions

CFD was used to predict the mass transfer coefficient in different flow geometries used for erosion-corrosion testing of carbon steel. In low pH conditions, similar to the conditions tested in the elbow in Chapter 7, corrosion rates are controlled by the mass transport of H^+ ions to the carbon steel surface, when no surface are films are present, defined by the mass transfer coefficient. Therefore mass transfer coefficients were predicted using CFD in different flow geometries to define the flow-induced corrosion conditions in those geometries. Mass transfer coefficients were predicted in a straight pipe to validate the mass transfer coefficient method using CFD and in the SIJ and elbow geometries used for erosion-corrosion testing in Chapters 5, 6 and 7. Translating flow-induced corrosion conditions between different geometries through the use of mass transfer coefficient has been shown to be effective on several occasions [30, 31, 52]. The dependence of erosion on the impact angles and impact velocities on a surface has also been shown on several occasions [10, 17]. Therefore, conditions in the SIJ and elbow were compared using CFD predictions of mass transfer coefficient and predictions of impact

angles and impact velocities at the surface. The main conclusions from the chapter were:

- Mass transfer coefficients in the SIJ geometry were higher than mass transfer coefficients in an elbow at the same nominal inlet flow velocity, and vary over the surface of a typical sample used in flow-induced corrosion and erosion-corrosion testing;
- Predictions of particle trajectories showed that over 95% of particles did not impact on the surface of samples in the elbow;
- Low impingement angles, less than 5°, were predicted on the surfaces of samples and impact velocities decreased at samples closer to the exit of the elbow;
- Impact angles in the elbow were therefore much lower than the impact angles predicted in the SIJ geometry, potentially resulting in different mechanisms of erosion degradation;
- The SIJ used for erosion-corrosion testing in Chapters 5 and 6 does not produce the same erosion-corrosion conditions that were measured in the elbow designed in Chapter 7.

Chapter 9
Discussion of Erosion-Corrosion Mechanisms and Erosion-Corrosion in Complex Flow Geometries

The key findings from the results are discussed in this chapter to explain the mechanisms of erosion-corrosion degradation in complex flow geometries and to discuss an improved methodology for analysis of erosion-corrosion in flow environments. The effect of flow velocity, sand concentration, temperature and geometry on the erosion-corrosion of carbon steel have been investigated. The causes of erosion-corrosion and the interactions between erosion and corrosion in the different conditions and flow geometries are discussed in this chapter.

9.1 Introduction

SIJ and elbow tests have been completed to understand the erosion-corrosion of X65 carbon steel in conditions relevant to the oil and gas industry and to gain further insight into how corrosion inhibitors perform in high flow velocity, high sand concentration conditions. Enhanced rates of degradation of carbon steel were observed in erosion-corrosion conditions, with the mechanisms for this discussed in this chapter. Investigations of the mechanisms contributing to the interactions between erosion and corrosion were completed in Chapter 6, and differences between the subsurface microstructures of samples after erosion and erosion-corrosion tests were observed with the reasons for this discussed in this chapter. The discussion of results from Chapter 5 and Chapter 6 aimed to improve the understanding of erosion-corrosion interactions and mechanisms of erosion-corrosion degradation.

A 90° elbow was developed to complete erosion-corrosion studies in conditions more relevant to the conditions that would be expected in oil and gas pipe flow environments. To characterise the influence of flow on erosion-corrosion conditions in the SIJ and the elbow, CFD was used to predict mass transfer coefficients and particle impingement characteristics in both of the flow geometries. This chapter discusses how effective this method was to make a direct comparison between the two geometries and how this could potentially improve erosion-corrosion experimentation, prediction of erosion-corrosion and understanding of erosion-corrosion degradation mechanisms. The objectives of this chapter were to discuss:

- The significance of erosion-corrosion degradation and the interactions between erosion and corrosion leading to enhanced degradation of carbon steel;
- The effects that flow and sand have on the performance of corrosion inhibitors used to reduce erosion-corrosion degradation rates;
- The success of using CFD to predict particle trajectories in different flow geometries and if assumptions limit the effectiveness of using CFD to improve the understanding of erosion-corrosion;
- The mechanisms of erosion-enhanced corrosion and corrosion-enhanced erosion and the significance these mechanisms have on overall degradation;
- Erosion-corrosion evaluation using a newly designed elbow to understand the significance of erosion-corrosion in pipe flow conditions;
- The effectiveness of using CFD to predict mass transfer coefficients and erosion conditions in the elbow and SIJ to translate erosion-corrosion between different flow geometries;
- Suggestion of a refined methodology for improving the understanding of erosion-corrosion in flow environments using a combined experimental and computational approach.

9.2 Flow-Induced Corrosion and Erosion-Corrosion of X65

Flow-induced corrosion and erosion-corrosion tests were completed at a range of different flow velocities using an SIJ in Chapter 5. Tests were completed in a 2% NaCl solution at a temperature of 60°C and flow velocities of 10 m/s, 15 m/s and 20 m/s. For sand-containing tests, 500 mg/L and 1000 mg/L of sand, with an average particle diameter of 250 µm, was added to the solution. Mass loss and electrochemical techniques were used to determine the degradation rates of carbon steel and to quantify the individual contributions of corrosion, erosion, corrosion-enhanced erosion and erosion-enhanced corrosion to total erosion-corrosion degradation. These degradation rates are summarised for each of the conditions tested in Table 9.1 to show which conditions resulted in the highest rates of degradation.

High degradation rates were observed in most conditions, particularly at high flow velocities and high sand concentrations. In all cases, erosion-enhanced corrosion was very low with corrosion-enhanced erosion more significant at high flow velocities and high sand concentrations. Erosion rates increased

significantly with flow velocity and erosion-corrosion degradation rates were significant in most conditions. Inhibitor B significantly reduced flow-induced corrosion rates, and at low flow velocities, reduced erosion-corrosion degradation rates much closer to acceptable rates of degradation. However, at high flow velocities, the corrosion inhibitor was unable to reduce erosion rates, which contributed significantly to high rates of erosion-corrosion degradation.

Table 9.1 Degradation maps from degradation rates in mm/yr measured in 2% NaCl, 60°C solution at flow velocities of 10 m/s, 15 m/s and 20 m/s in (a) blank erosion-corrosion pH 4.7, CO_2-saturated conditions containing 500 mg/L of sand, (b) erosion-corrosion pH 4.7, CO_2-saturated conditions containing 500 mg/L of sand and 250 ppm of inhibitor B, (c) blank erosion-corrosion pH 4.7, CO_2-saturated conditions conditions containing 1000 mg/L of sand and (d) erosion-corrosion pH 4.7, CO_2-saturated conditions conditions containing 1000 mg/L of sand and 250 ppm of inhibitor B

	10 m/s	15 m/s	20 m/s
E-C	11.0	13.6	17.0
C_{FIC}	8.6	9.9	10.9
C_{EC}	9.4	10.4	12.2
E_0	1.1	3.3	7.5
ΔC_E	0.8	0.6	1.3
ΔE_C	0.6	-0.1	-2.7

(a)

	10 m/s	15 m/s	20 m/s
E-C	3.4	4.1	8.7
C_{FIC}	1.7	2.3	1.5
C_{EC}	0.8	0.4	0.5
E_0	1.1	3.3	7.5
ΔC_E	-1.0	-1.8	-1.1
ΔE_C	1.5	0.5	0.7

(b)

	10 m/s	15 m/s	20 m/s
E-C	12.0	14.9	26.0
C_{FIC}	8.6	9.9	10.9
C_{EC}	7.5	10.0	10.8
E_0	1.8	5.4	11.5
ΔC_E	-1.1	0.1	-0.1
ΔE_C	2.7	-0.5	3.7

(c)

	10 m/s	15 m/s	20 m/s
E-C	2.9	6.6	16.5
C_{FIC}	2.0	2.5	1.6
C_{EC}	1.5	0.6	0.6
E_0	1.8	5.4	11.5
ΔC_E	-0.5	-2.0	-1.0
ΔE_C	-0.4	0.6	4.4

(d)

Degradation Rates (mm/yr)

< 0.1 > 25

9.2.1 Corrosion Rate Measurements

The reliability of electrochemistry measurements and the corrosion mechanisms in the flow-induced corrosion SIJ tests completed are discussed first from the results in Chapter 5. The effects of flow clearly influenced the corrosion mechanisms due to the significantly increased corrosion rates in

flow-induced corrosion tests compared with static corrosion tests. EIS was used to determine the corrosion rates of X65 and to investigate the corrosion mechanisms. EIS was favoured over the use of LPR in Chapter 5 so that a direct comparison between corrosion mechanisms in blank and inhibited conditions could be made. High solution resistances in the SIJ required the use of EIS regardless to determine the solution resistance, which LPR could not be used to obtain. The use of two electrochemistry techniques would have contributed to more error in the calculation of corrosion rates. Therefore, it was chosen to use EIS to measure both solution resistance and charge transfer resistance.

Some slight fluctuation in the electrochemistry measured corrosion rates was observed during testing, accounting for some of the error in electrochemistry results. However, these fluctuations were not significant in the results. General conditions in the SIJ could also vary slightly at the start of tests which contributed to variations in the in-situ measured corrosion rates. It was possible that slightly different temperatures and pH conditions were observed at the bottom of the SIJ reservoir, as the solution was not mixed during the bubbling period, where the solution was bubbled for a minimum period of 12 hours prior to starting the test. Consistency in the solution was achieved, however, relatively quickly after starting the test, within approximately 10-20 minutes. These errors could have also contributed to corrosion rates measured from mass loss measurements, in addition to measurement error.

Average corrosion rates were determined using electrochemical measurements that showed corrosion rates were stable throughout the test. No significant change in corrosion rate was measured during the tests, with rates being fairly stable throughout the 240-minute test period. However, the calculation of corrosion rate assumed that Tafel constants did not vary over time. Tafel constants, summarised in Table 9.2 for flow-induced corrosion tests at 20 m/s were shown to remain approximately constant throughout a 240-minute test. Therefore, in flow-induced corrosion conditions it was shown that it was reasonable to assume an average corrosion rate over the duration of the test. Tafel plots showed diffusion controlled reactions, with Tafel constants being required to be measured in activation control [24]. However, at 50 mV where measurements were taken, a linear relationship was observed. Electrochemistry results were validated with mass loss measurements, showing close agreement.

In blank conditions, without inhibitor, the equivalent circuit used to represent the corrosion mechanism of carbon steel in the SIJ flow-induced corrosion

tests consisted of a resistor, representing the solution resistance, in series with a constant phase element to represent the capacitance of the EDL in parallel with another resistor to represent the charge transfer resistance. Farelas et al. [203] and Barker [35] observed a high frequency capacitive loop, representative of the capacitance of the EDL and a low frequency inductive loop in similar CO_2 corrosion conditions, suggested to be the revealing of an Fe_3C network on the surface. The impedance plots measured in the flow-induced corrosion tests in this thesis did not show an inductive loop, potentially due to higher flow velocities removing iron carbide from the surface.

Table 9.2 Tafel constants and Stern-Geary coefficients determined over a 240-minute test period in flow-induced corrosion tests completed at a flow velocity of 20 m/s in a 2% NaCl, 60°C, pH 4.7, CO_2-saturated solution

t (mins)	β_a (mV/decade)	β_c (mV/decade)	B
30	101	165	27.2
90	105	157	27.3
150	106	155	27.3
210	99	165	26.9

9.2.2 Flow-Induced Corrosion Mechanisms

It was shown in Table 9.1 that corrosion rates were significantly accelerated in flow conditions. Flow has been shown to increase rates of corrosion on several occasions and is widely regarded as a highly influential parameter on corrosion rates. Barker [35] and Efird [28] showed enhanced corrosion as a result of flow and the de Waard and Milliams [40, 176] and NORSOK [177] models each utilise a flow velocity term to predict corrosion rates. The increase in corrosion rate measured in SIJ tests at different flow velocities is shown in Figure 9.1.

In Figure 9.1 a linear relationship was observed in corrosion rate as flow velocity was increased from 10 m/s to 15 m/s and 20 m/s, which the static corrosion rate did not follow. Barker [35] compared corrosion rates of X65 in CO_2-saturated conditions using an SIJ with predictions using the de Waard and Milliams [40, 176] model and NORSOK model [177] that showed a logarithmic relationship between flow velocity and corrosion rate. Shear stress was used rather than flow velocity to predict corrosion rates using the

NORSOK model, defined by the following equation to determine corrosion rates of carbon steel in CO_2 conditions [177]:

$$CR = K_T f_{CO_2}^{0.6} f_{pH} \left(\frac{\tau_w}{19}\right)^{0.15+0.03\log(f_{CO_2})} \quad (9.1)$$

where K_T is a temperature-related constant, f_{CO_2} is the fugacity of CO_2, f_{pH} is a function related to the pH of the solution and τ_w is the wall shear stress. The constants for the model are provided by Halvorsen and Sontvedt [177].

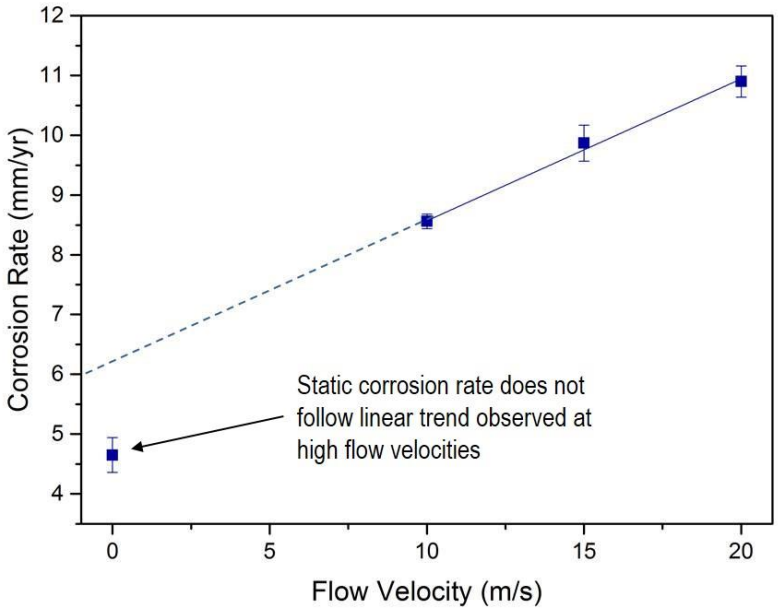

Figure 9.1 Effect of flow velocity on corrosion rates measured using electrochemical techniques in SIJ flow-induced corrosion tests compared with static 1 L tests in a 2% NaCl, 60°C, pH 4.7, CO_2-saturated solution

The relationship between shear stress and corrosion rate is shown in Figure 9.2 when predicted using the NORSOK model for the same conditions as flow-induced corrosion tests completed in Chapter 5. The maximum shear stress that the NORSOK model is validated for is 150 Pa, therefore, it could not be used to predict the corrosion rates in SIJ flow-induced corrosion tests at flow velocities from 10 m/s to 20 m/s, with shear stresses expected to be much higher on the surface of the test sample used in the SIJ [51]. However, this plot was shown to demonstrate that a logarithmic relationship was observed between corrosion rate and shear stress, showing that corrosion rates increased significantly from approximately no shear stress to 20 Pa of shear stress, before the increase became less significant as shear stress increased. This explained why the static corrosion rate shown in Figure 9.1 did not follow the linear trend shown by flow velocity and corrosion rate. Static corrosion rates could not be predicted using the NORSOK model, however, the

difference between corrosion rate measured in Figure 9.1 and the shear stress of 1 Pa predicted using Equation (9.1) was approximately 2%, validating the corrosion rates measured in static conditions in this thesis. It is also unlikely that conditions would have been ideally static in the test cell, with very low wall values of shear stress produced from stirring the solution at low velocities.

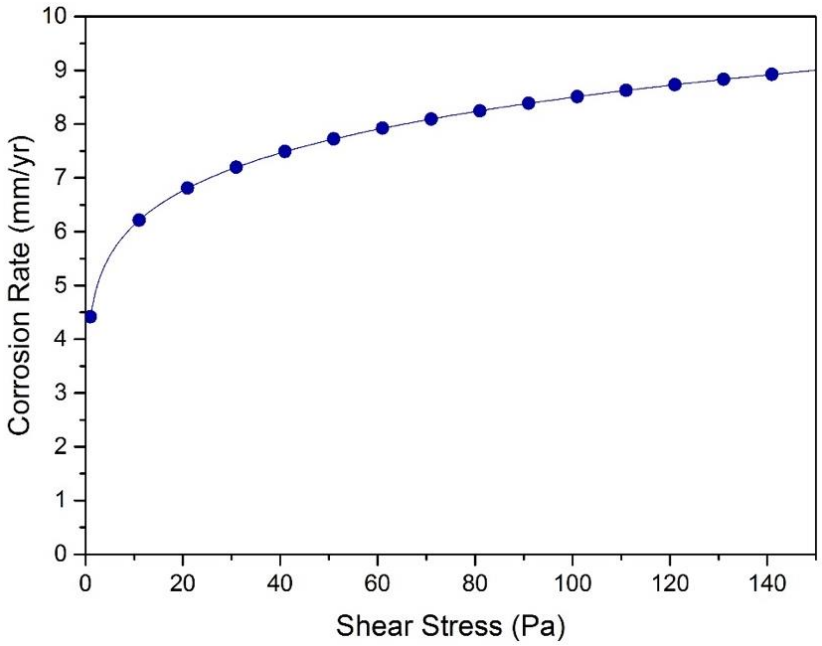

Figure 9.2 Relationship between shear stress and CO_2 corrosion rates predicted using the NORSOK model in a pH 4.7 solution at a temperature of 60°C [177]

It is likely that the predictions from the NORSOK model would overestimate the corrosion rate measured in the SIJ, if extrapolated, as the corrosion rate at 150 Pa was predicted to be higher than the corrosion rate measured at 10 m/s in SIJ flow-induced corrosion tests. However, it has been shown that there is a significant variation in flow conditions over the surface of the sample used in an SIJ test [28, 35, 51, 105]. Gulbrandsen and Grana [51] showed that conditions varied from approximately no shear stress in the centre of the sample, to shear stresses in excess of 1500 Pa at other locations on the surface at flow velocities of 20 m/s with a H/d_N nozzle ratio of 5. Therefore, determining the most influential flow parameter and how this parameter directly influenced the corrosion rate of carbon steel was not easy due to the variation across the sample surface. However, the increase in flow velocity clearly caused an increase in the corrosion rate and profiles of X65 samples measured using the NPFLEX after SIJ tests in flow-induced corrosion conditions showed no variation across the surface, indicating that the flow conditions caused a uniform rate of corrosion in the SIJ tests completed.

9.2.3 Effects of Sand Particle Impingement on X65 Degradation

Erosion-corrosion tests were completed at three different flow velocities of 10 m/s, 15 m/s and 20 m/s in a 2% NaCl, 60°C solution containing 500 mg/L and 1000 mg/L of sand using the SIJ. Erosion and erosion-corrosion degradation rates were determined from mass loss measurements and reported with the units of mm/yr. It is acknowledged that thickness loss would not be uniform across the surface in erosion and erosion-corrosion conditions in the SIJ, as was shown by wear profiles after particle impingement in Chapter 6, but these units enabled a direct comparison to be made with flow-induced corrosion conditions.

The effect of flow velocity on the degradation caused by the impingement of sand particles in erosion and erosion-corrosion tests is shown in Figure 9.3, from results in Section 5.4. The erosion-corrosion degradation and erosion degradation were approximately proportional to the flow velocity squared. It has been shown that the erosion is proportional to velocity with an exponent in the range of 2.3 to 2.7 [4, 18]. This was explained by the relationship between the kinetic energy of the particle and further removal of material due to particle rotation and cutting at low impact angles [79]. The value of the exponent relating the velocity to erosion rate in Figure 9.3 was also approximately 2.7 for both 500 mg/L and 1000 mg/L.

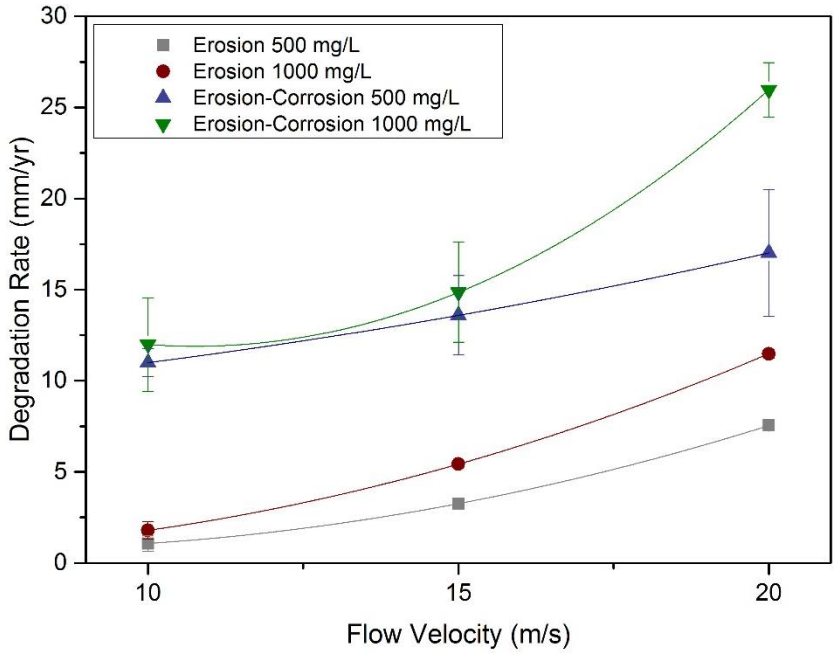

Figure 9.3 Effect of flow velocity on erosion and erosion-corrosion rates of X65 carbon steel measured from SIJ erosion tests in an N_2-saturated, 60°C solution containing 500 mg/L and 1000 mg/L of sand and SIJ erosion-corrosion tests in an CO_2-saturated, 60°C, pH 4.7, 2% NaCl solution containing 500 mg/L and 1000 mg/L of sand

An increase in flow velocity and sand concentration caused an increase in degradation rate and influenced the contribution of corrosion and erosion mechanisms to total erosion-corrosion degradation. Stack et al. [151, 153, 155] used erosion-corrosion wear maps that defined transitions between erosion-corrosion regimes. Using the method suggested by Stack et al. [160], discussed in Section 3.5.1, the ratio of corrosion degradation ($C + \Delta C_E$) to erosion degradation ($E + \Delta E_C$) is shown in Table 9.3 for each flow velocity and sand concentration. Clearly flow velocity and sand concentration had an influence on the erosion-corrosion regime, with erosion-corrosion dominated regimes observed at high velocities and high sand concentrations. Corrosion dominated regimes were observed at lower flow velocities and sand concentrations. At a sand concentration of 500 mg/L for all flow velocities, corrosion was dominant. With increasing flow velocity, erosion became more significant but degradation was still in the corrosion-dominated regime with some influence of erosion. At a sand concentration of 1000 mg/L, erosion was much more significant. The transition between an erosion-corrosion dominated regime and a corrosion-dominated regime is a ratio of 1. Therefore, at 20 m/s conditions were in an erosion-corrosion dominated regime, where erosion and corrosion contributions to total erosion-corrosion degradation were of a similar magnitude.

Table 9.3 Ratio of corrosion degradation ($\boldsymbol{C + \Delta C_E}$) determined from the sum of EIS-measured flow-induced corrosion rates and EIS-measured erosion-enhanced corrosion to erosion degradation ($\boldsymbol{E + \Delta E_C}$) determined from the sum of erosion rates measured from mass loss erosion tests and corrosion-enhanced erosion, calculated using Equation (2.1), measured in flow-induced corrosion tests in a CO_2-saturated, pH 4.7, 2% NaCl, 60°C solution; erosion tests in a N_2-saturated, 60°C solution containing 500 mg/L and 1000 mg/L of sand and erosion-corrosion SIJ tests in a CO_2-saturated, pH 4.7, 2% NaCl, 60°C solution containing 500 mg/L and 1000 mg/L of sand at flow velocities of 10 m/s, 15 m/s and 20 m/s

	$\frac{C + \Delta C_E}{E + \Delta E_C}$	
	Sand Concentration (mg/L)	
U (m/s)	500	1000
10	5.71	1.68
15	3.31	2.03
20	2.53	0.71

9.2.4 Interactions between Erosion and Corrosion

It has been shown on several occasions that there are interactions between erosion and corrosion that result in enhanced rates of total erosion-corrosion degradation [34, 49, 140]. Interactions between erosion and corrosion were observed in the tests completed in this thesis. However, there was no obvious conclusions or trends that could be made from the results in Chapter 5. Some increase in corrosion was observed at lower sand concentrations but erosion enhanced-corrosion rates were low in comparison to flow-induced corrosion rates. Corrosion-enhanced erosion was a significant proportion of total erosion-corrosion degradation at high flow velocities and high sand concentrations, but this was not consistent across all sand concentrations and flow velocities tested, and error was significant in some of the results.

Enhanced degradation rates were observed as a result of interactions between erosion and corrosion. The significance of the interactions for each of the conditions tested are shown in Figure 9.4 and Figure 9.5 for 500 mg/L and 1000 mg/L sand concentrations, respectively. Average electrochemistry measured corrosion rates were used to determine enhanced corrosion rates in erosion-corrosion conditions through comparison with flow-induced corrosion rates.

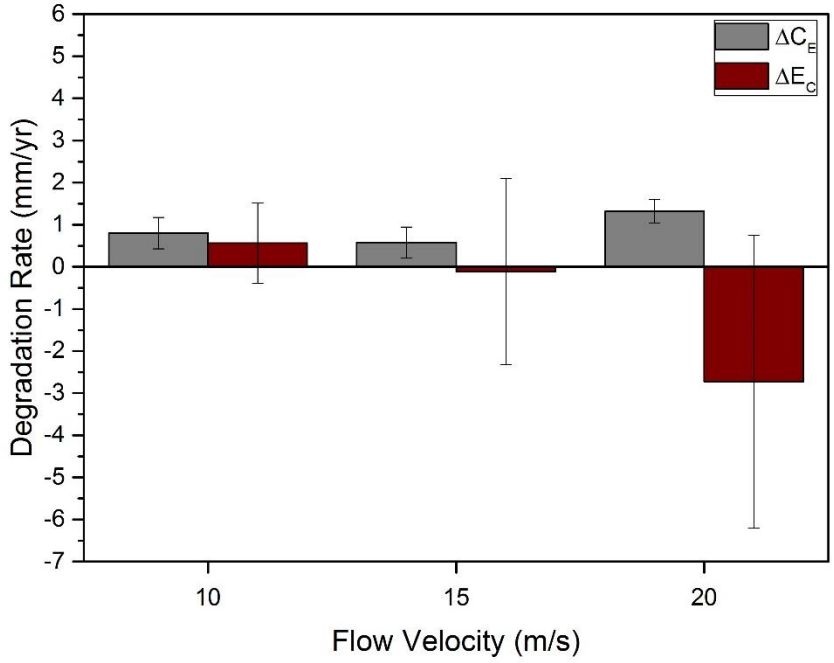

Figure 9.4 Corrosion-enhanced erosion and erosion-enhanced corrosion of X65 carbon steel measured from SIJ tests in 500 mg/L sand concentration erosion-corrosion tests in a 2% NaCl, 60°C, pH 4.7 solution at flow velocities of 10 m/s, 15 m/s and 20 m/s

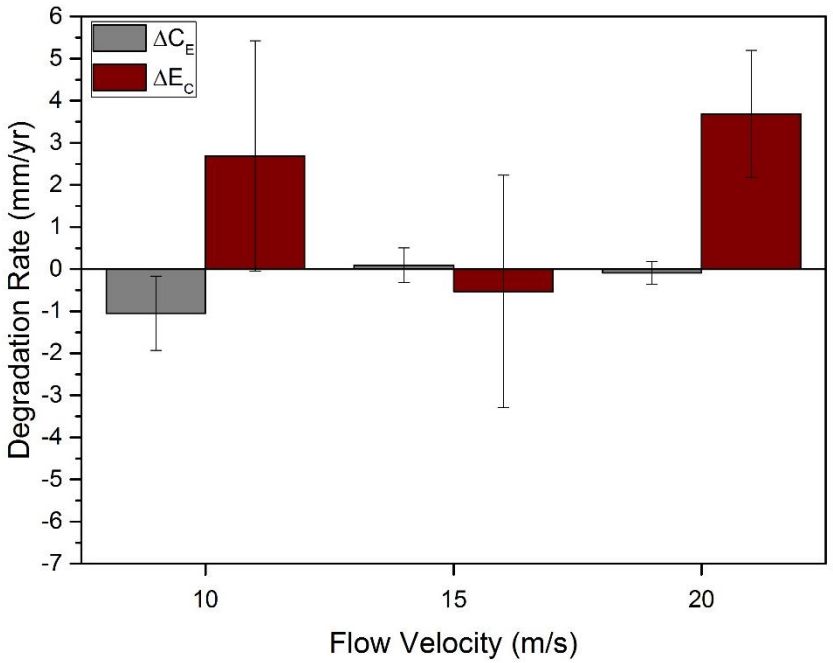

Figure 9.5 Corrosion-enhanced erosion and erosion-enhanced corrosion of X65 carbon steel measured from SIJ tests in 1000 mg/L sand concentration erosion-corrosion tests in a 2% NaCl, 60°C, pH 4.7 solution at flow velocities of 10 m/s, 15 m/s and 20 m/s

Equation (2.1) defined erosion-corrosion as consisting of a pure static corrosion rate, with enhanced degradation rates being measured in either flow or sand-containing conditions. To make a direct comparison between the conditions with and without sand, on enhanced degradation rates, it was assumed that any enhancement from the effects of flow were equal in both flow-induced corrosion conditions and erosion-corrosion conditions, and that the flow was not influenced by the presence of sand. The low sand concentration used in SIJ tests allowed the assumption that particles did not influence the flow in CFD particle trajectory predictions, suggesting that it was reasonable to assume sand did not influence the flow contribution to enhanced degradation rates.

Corrosion rates of carbon steel increased due to erosion interactions more significantly at 500 mg/L sand concentration than at 1000 mg/L of sand concentration. However, enhanced corrosion rates were less than 2 mm/yr in all cases and experimental error was significant in the measurements. Erosion-corrosion tests completed by Hu and Neville [34] and Malka et al. [49] also showed that erosion-enhanced corrosion was not as significant as corrosion-enhanced erosion as a contributing factor to total erosion-corrosion degradation rate. Concluding from the range of conditions evaluated in this work and other research, it is likely that erosion-enhanced corrosion is

typically not a significant contributing factor in the erosion-corrosion degradation of carbon steel in oil and gas CO_2 conditions.

Corrosion-enhanced erosion was significantly affected by error, as it was required to be calculated, rather than measured, using Equation (2.1). Calculation of corrosion-enhanced erosion, rather than measurements during tests, was required by using the results gained from the other contributions to total erosion-corrosion degradation. Equation (2.1) was rearranged and ΔE_C was calculated by deducting flow-induced corrosion degradation, pure erosion degradation and erosion-enhanced corrosion degradation from total erosion-corrosion degradation. The error from each of these measurements propagated in the calculation of the corrosion-enhanced erosion rate and became highly significant in the results. Results at higher flow velocities and sand concentration, where corrosion-enhanced erosion degradation rates were highest, were effected less significantly by the magnitude of the error, due to the large degradation rates measured.

Due to the lack of available techniques for measuring corrosion-enhanced erosion directly, this associated error is a significant limitation of the results. However, it did appear that erosion rates were enhanced by the corrosion mechanisms. Hu and Neville [34] showed a significant proportion of corrosion-enhanced erosion in the degradation rate of X65 in carbon steel that accounted for approximately 50% of the total degradation, much higher than the rates measured in this work. Aminul Islam and Farhad [149] and Malka et al. [49] showed that corrosion-enhanced erosion also accounted for a significant proportion of erosion-corrosion degradation of carbon steel. However, from the results in this thesis and results available in literature, there did not appear to be a consistent relationship between enhanced degradation rates and flow velocity or sand concentration, possibly due to the significance of error in the corrosion-enhanced erosion rates.

9.2.5 Influence of Flow and Sand on Corrosion Inhibitors

One of the methods commonly used to protect carbon steels from erosion-corrosion degradation is the use of corrosion inhibitors [62]. Inhibitor A and inhibitor B, two commercially available inhibitors used in the field, were compared in this work by completing SIJ tests in flow-induced corrosion and erosion-corrosion conditions to understand how flow and sand influenced the performance of corrosion inhibition. Flow-induced corrosion testing of X65 showed that corrosion rates were significantly reduced in the 240-minute tests

after the addition of inhibitors A or B. Corrosion rates continued to drop throughout tests, potentially due to continued transport of inhibitor to the surface, continuously increasing inhibitor surface coverage during the test. Corrosion inhibitors performed effectively in both static conditions and in flow-induced corrosion conditions, but efficiency was slightly reduced when comparing static to flow-induced corrosion conditions.

Wall shear stress has been suggested as a flow mechanism causing removal of inhibitor films and other protective films [7, 62, 183]. However, the shear stress present in typical pipe flows is of the order of 10^2 - 10^3 Pa, and therefore much less than the shear stress required to remove inhibitors from the surface, reported to be of the order 10^6 Pa [188]. The shear stress in an SIJ geometry was calculated by Gulbrandsen and Grana [51]. They showed that shear stresses exceeded 1400 Pa in the SIJ at a flow velocity of 20 m/s and that inhibitor efficiency was not reduced when shear stress was increased. High inhibitor efficiency measured at 10 m/s to 20 m/s in SIJ flow-induced corrosion tests in Chapter 5, for both inhibitor A and inhibitor B, suggested that shear stress did not remove inhibitor from the surface and that the inhibitors would be efficient in the field, due to the higher shear conditions in SIJ tests than typically seen in pipe flow. The efficiency of inhibitor B was also higher in the higher shear stress conditions at a flow velocity of 20 m/s than 10 m/s.

Corrosion rates after the addition of inhibitors were also only measured over a relatively short period of 240 minutes and corrosion rates were continuing to drop when the test was stopped. Therefore, it was expected that corrosion rates would continue to decrease, further increasing inhibitor efficiency. However, tests were intentionally kept short for the purpose of direct comparison with erosion-corrosion tests. Changes in surface roughness and profile during erosion and erosion-corrosion tests, shown previously in SIJ erosion and erosion-corrosion tests, meant that long term tests could significantly change the hydrodynamic conditions near the surface of the sample, making direct comparison between erosion-corrosion results and flow-induced corrosion results difficult.

EIS results were used to plot equivalent circuits to investigate the mechanisms of corrosion when an inhibitor was present on the surface. Two capacitance loops were observed in corrosion inhibitor EIS measurements completed by Tan et al. [182], where the second capacitance loop represented the capacitance of the inhibitor film in addition to the EDL capacitance. Inhibitor A and inhibitor B used in flow-induced corrosion tests showed only one capacitance loop. Chen et al. [233] also showed that a single capacitance loop

was observed after EIS tests on the performance of an inhibitor, suggesting that the inhibitor formed a monolayer and that the high rates of turbulent flow in the system caused the inhibitor film to be porous. This could have potentially been the case in the flow-induced corrosion tests in the SIJ because of the highly turbulent nature of the flow.

The effect of sand on the performance of the inhibitors was also assessed. Inhibitor A could not be tested as it adsorbed to the surface of sand particles, preventing the flow of sand through the SIJ nozzles. Adsorption of chemical inhibitors to sand particles is a commonly seen occurrence [6, 35, 191]. The chemical composition of inhibitors A and B was not reported, therefore, a comparison of particular components in the inhibitor could not be made with literature to determine if particular chemicals adsorb to sand particles. This may be of future interest in corrosion inhibitor evaluation.

Inhibitor B efficiency at each of the three flow velocities in erosion-corrosion SIJ tests containing different sand concentrations is shown in Figure 9.6. Sand has been reported to remove inhibitor films from the surface, contributing to enhanced corrosion rates in erosion-corrosion conditions [15, 194]. Removal of the inhibitor from the surface did not appear to be significant in the conditions tested, as it was shown that inhibitor efficiency was not significantly reduced by the presence of sand. Inhibitor efficiency actually increased when sand was added in some of the conditions shown in Figure 9.6.

At a sand concentration of 1000 mg/L and flow velocity of 10 m/s inhibitor efficiency was lowest. A higher quantity of sand was added to erosion-corrosion tests at 10 m/s than at 15 m/s and 20 m/s because sand was found to settle in the SIJ at the lower flow velocity. Any adsorption of inhibitor to sand particles was most likely to occur in the tests, potentially explaining the lower efficiency. Inhibitor efficiency was approximately the same in conditions with and without sand at 15 m/s and 20 m/s. However, the 20 m/s tests showed the highest efficiency and efficiency remained high when sand was added at a flow velocity of 15m/s. One possible explanation for the reduced corrosion rate in sand-containing flow is that the increase in surface roughness caused by the impacts of sand particles, reported by Bitter [20] and shown in Chapter 6, could increase local turbulence at the surface of the sample, potentially increasing the transport of inhibitor to the surface. It was shown that at 20 m/s inhibitor efficiency was increased in flow-induced corrosion conditions, therefore increased flow and turbulence appeared to improve the adsorption of inhibitor to the surface. However, it was also shown in Chapter 6 that roughened surfaces did not significantly change the inhibitor efficiency.

Therefore, it was unknown if this was the reason for the change in inhibitor efficiency.

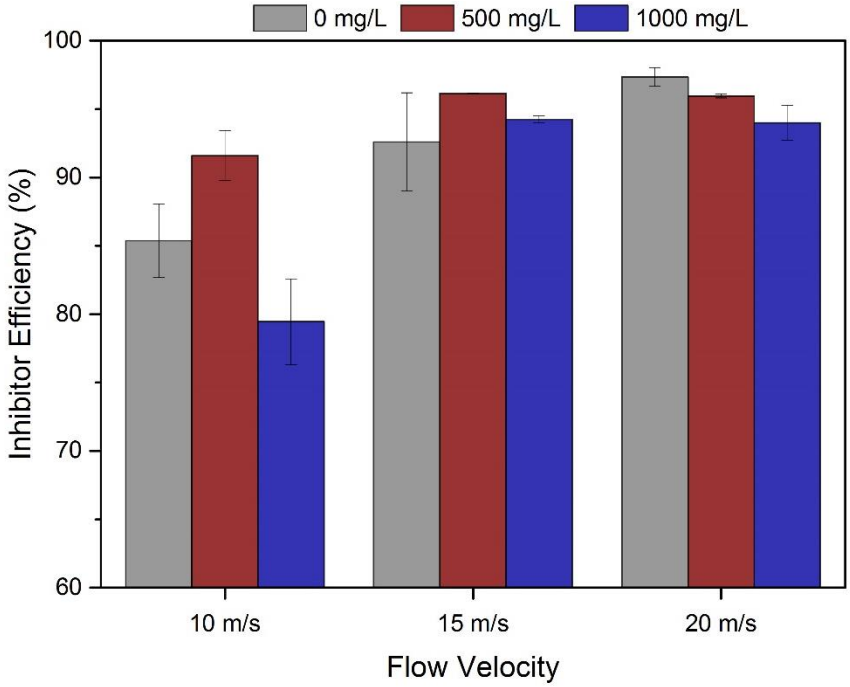

Figure 9.6 Effect of sand concentration on the efficiency of 250 ppm of inhibitor B in erosion-corrosion SIJ tests at flow velocities of 10 m/s, 15 m/s and 20 m/s in a 2% NaCl, 60°C, pH 4.7, CO_2-saturated solution containing 500 mg/L and 1000 mg/L of sand

Erosion-corrosion tests completed by Barker [35], showed that some corrosion inhibitors reduced erosion wear components in addition to inhibiting corrosion, thought to be due to a damping effect provided by the inhibitor film adsorbed to the surface, resulting in either a significantly reduced particle velocity upon impact or no impacts at all. This was not the case for inhibitor B used in this thesis, as erosion and corrosion-enhanced erosion accounted for a significant proportion of total erosion-corrosion degradation.

9.3 Mechanisms of Erosion-Corrosion Interactions

Several areas of further research were highlighted from the literature review and from the results in Chapter 5, where erosion-corrosion was investigated. It was observed that there were interactions between the erosion and corrosion mechanisms, but the reasons for these interactions could not be confirmed based on this analysis alone. There was some uncertainty about what caused the interactions between erosion and corrosion of carbon steel, in particular corrosion-enhanced erosion, and how influential these effects

were, as there was significant quantities of error in the calculation of corrosion-enhanced erosion. However, it was clear from the results that some interactions between the two mechanisms were present.

Therefore, further investigation of the mechanisms of erosion-corrosion and the interactions between erosion and corrosion was completed in Chapter 6, where SIJ erosion-corrosion tests were completed over a range of test durations in high flow velocity, high sand concentration conditions. Experimental results were combined with the results from CFD predictions of particle impact angle and velocity to define the material removal mechanisms from the surface of the sample in the SIJ. As explained previously, the effects of erosion-enhanced corrosion were not thought to be significant in the conditions tested. Corrosion-enhanced erosion, however, was a more significant issue, as it was shown to account for approximately 20% of the total degradation in erosion-corrosion conditions at a flow velocity of 20 m/s containing 1000 mg/L of sand.

9.3.1 Erosion-Enhanced Corrosion

Erosion-enhanced corrosion has been shown to be negligible in this thesis. However, this section discusses the typical parameters that influence erosion-enhanced corrosion to investigate if these parameters, such as surface roughness, changed significantly during a test and how this could have influenced erosion-enhanced corrosion. Several parameters were analysed on the surfaces of X65 samples after erosion and erosion-corrosion tests to determine the mechanisms of enhanced degradation. Surface roughening and increased local turbulence has been suggested as a cause of erosion-enhanced corrosion [15]. The comparison of different values of surface roughness and its effect on corrosion rate showed that this effect was not significant at a flow velocity of 20 m/s, as no significant increase in corrosion rate was measured in erosion-corrosion tests.

However, the influence of particle impacts on surface roughness was investigated despite the lack of significance on erosion-enhanced corrosion. Surface roughness measured after erosion and erosion-corrosion tests is shown in Figure 9.7 in each of the four regions defined on the SIJ sample surface after CFD analysis. A similar surface roughness was measured on erosion and erosion-corrosion samples. A slightly higher roughness was measured in region 3 on the erosion-corrosion samples compared to the erosion samples. This could have potentially have been due to increased local

turbulence in the region, increasing the rate of corrosion and increasing material removal [15]. However, it was unknown how corrosion influenced surface roughness. It was also likely that error in the measurement of surface roughness would have caused some differences in results, as region 3 was a small area on the surface of the samples.

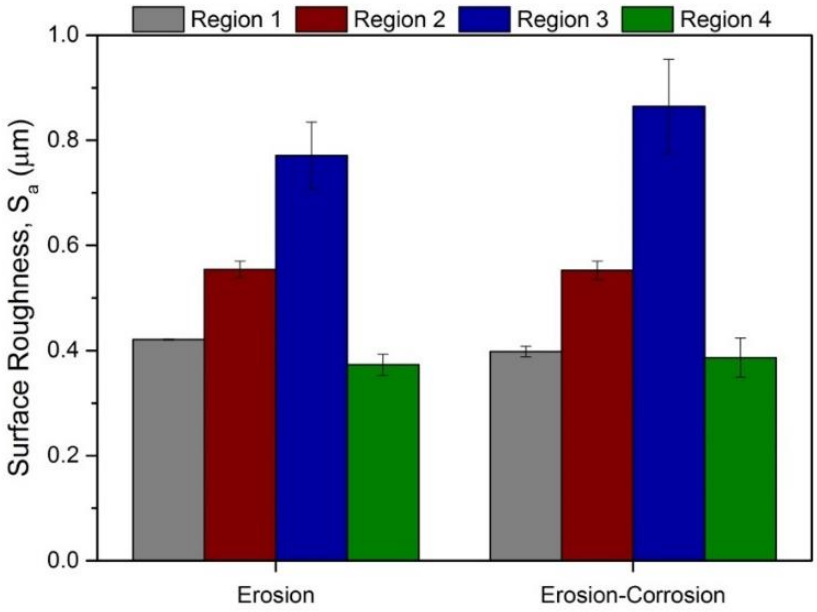

Figure 9.7 Comparison of surface roughness (S_a) measured in different regions of X65 samples after 240-minute erosion SIJ tests at a flow velocity of 20 m/s in a N_2-saturated, 60°C solution containing 1000 mg/L of sand and 240-minute erosion-corrosion SIJ tests at a flow velocity of 20 m/s in a CO_2-saturated, 60°C, pH 4.7, 2% NaCl solution containing 1000 mg/L of sand

The variation in surface roughness with impact angle is shown in Figure 9.8. The impact angle was determined from the CFD prediction of impacts on the surface of the SIJ sample, with the average values in regions 1-4 shown. Therefore, it was expected that there would be some variation in actual impact angle in the regions identified due to the use of an average value. However, it did appear that surface roughness was highest at an angle of approximately 45°, correlating with the most significant expected increase in surface roughness, suggested by Bitter [20]. Figure 9.8 also showed a very similar trend to the typical erosion degradation trend seen as a function of impact angle for ductile materials, with a higher rate of degradation typically observed at impact angles in the range of 20° to 45° before decreasing at impact angles towards 90°. It should be noted that more impacts were observed in some regions and regions were not of equal size. Impact velocity also varied between the different regions and therefore could have influenced surface

roughness. However, there did appear to be an influence of impact angle on surface roughening.

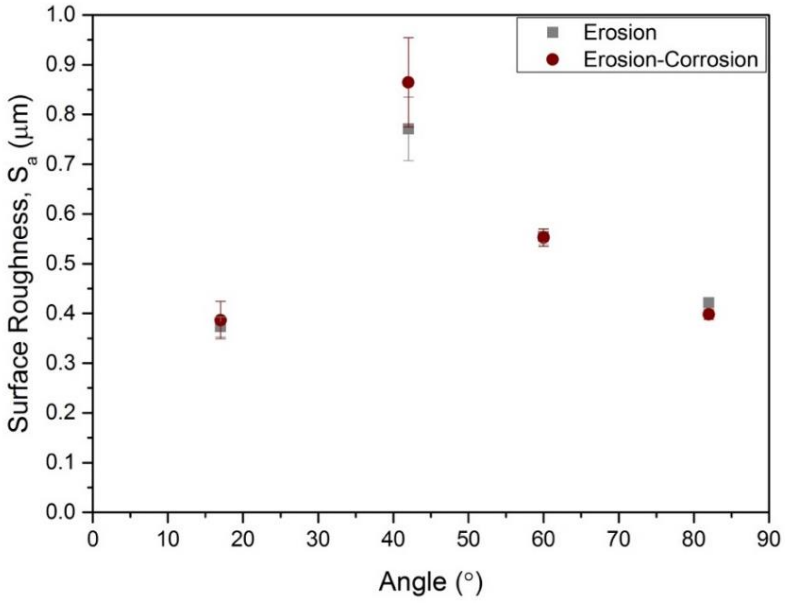

Figure 9.8 Variation of surface roughness with CFD predicted particle impact angles of X65 samples measured after 240-minute erosion SIJ tests at a flow velocity of 20 m/s in a N_2-saturated, 60°C solution containing 1000 mg/L of sand and erosion-corrosion 240-minute SIJ tests at a flow velocity of 20 m/s in a CO_2-saturated, 60°C, pH 4.7, 2% NaCl solution containing 1000 mg/L of sand

9.3.2 Corrosion-Enhanced Erosion

The corrosion of work-hardened layers, exposing softer material is often suggested as a cause of corrosion-enhanced erosion [15, 149, 164]. Despite the fact this reason is commonly given, the causes of corrosion-enhanced erosion on carbon steel have rarely been shown and proven to be caused by this. Work-hardening was observed on the surface of the samples measured using a micro-indenter after erosion-corrosion and erosion SIJ tests in this thesis. Work-hardening of steel has been observed after particle impacts on several occasions [58, 72, 76]. Therefore, it was expected that the X65 surfaces would work-harden after particle impact. Guo et al. [164] showed that work-hardened layers could be removed in a corrosion environment, but it was unknown how the corrosion and erosion mechanisms would interact with the removal of work-hardened layers in erosion-corrosion environments.

Comparison of the Vickers hardness on the samples, measured inside the wear scar of samples by averaging the hardness measured in regions 1, 2 and 3, is shown in Figure 9.9. No influence of impact angle and impact velocity

on hardness was observed, as was seen in other erosion-corrosion tests using an SIJ by Barik et al. [59], where hardness measured inside the wear scar was relatively constant. Therefore, hardness in regions 1-3 was averaged to make a comparison between the erosion and erosion-corrosion samples. Few impacts were observed in region 4, with a much lower hardness measured, so were not included in the average. It was originally assumed that the hardness of samples after SIJ erosion tests would be greater than the hardness measured on erosion-corrosion samples, if work-hardened layers were removed. However, it was shown that the hardness between erosion and erosion-corrosion samples measured was very similar, suggesting other mechanisms were occurring on the surface of the sample rather than a simple removal of work-hardened layers resulting in lower hardness of erosion-corrosion samples.

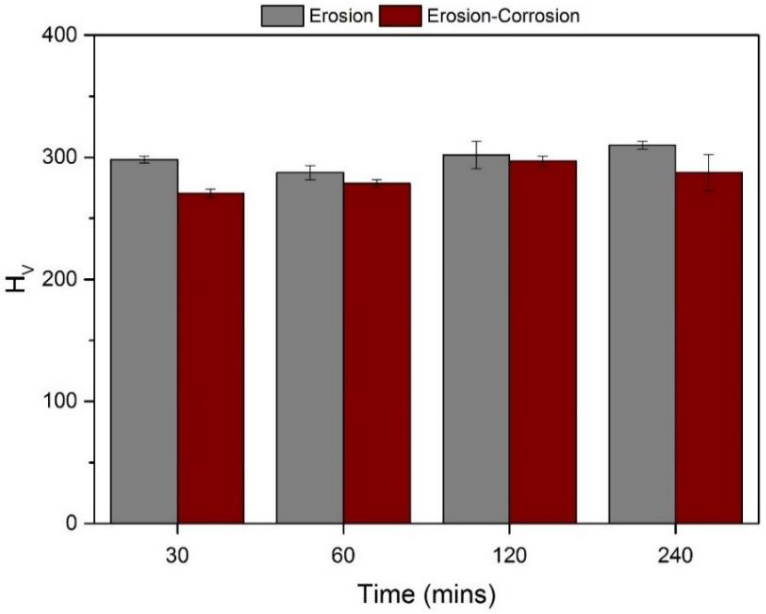

Figure 9.9 Comparison of Vickers hardness measured in the wear scar of erosion and erosion-corrosion samples by averaging hardness in regions 1 - 3 after 30, 60, 120 and 240-minute erosion SIJ tests at a flow velocity of 20 m/s in a N_2-saturated, 60°C solution containing 1000 mg/L of sand and 240-minute erosion-corrosion SIJ tests at a flow velocity of 20 m/s in a CO_2-saturated, 60°C, pH 4.7, 2% NaCl solution containing 1000 mg/L of sand

SIJ erosion tests completed over shorter time periods showed that the hardness of samples increased rapidly after relatively few particle impacts. Naim and Badahur [166] showed how hardness of brass samples increased after only a few impacts before reaching a constant value where no further increase in hardness was observed, despite further particle impacts. This was conducted using much larger diameter particles and on a different material

than was used in the SIJ tests, but similar results were seen. It was also observed in erosion and erosion-corrosion tests in this thesis that hardness reached a constant value and no significant change in hardness was observed after a 30-minute period.

Whilst the work-hardening behaviour was analysed, and it was clear that particle impacts increased the hardness of X65, there was still no obvious explanation for the enhanced rate of erosion observed in SIJ tests as a result of corrosion. Therefore, FIB-SEM analysis was completed to investigate the subsurface microstructure in the regions of interest on the samples used in SIJ erosion and erosion-corrosion tests. Rajahram et al. [108, 139] completed FIB analysis of stainless steel samples after erosion-corrosion testing to analyse the effects of work-hardening on passive materials. The results were used as a comparison with the FIB analysis completed in Chapter 6, to observe if there were similarities between the material removal mechanisms of both materials. A comparison between the 30-minute and 240-minute X65 samples used in erosion tests is shown in Figure 9.10. Three distinct regions of grain refinement were observed, with a very fine crystal structure closest to the surface and a less refined region beneath. After longer tests, bulk grains began to deform deeper into the sample.

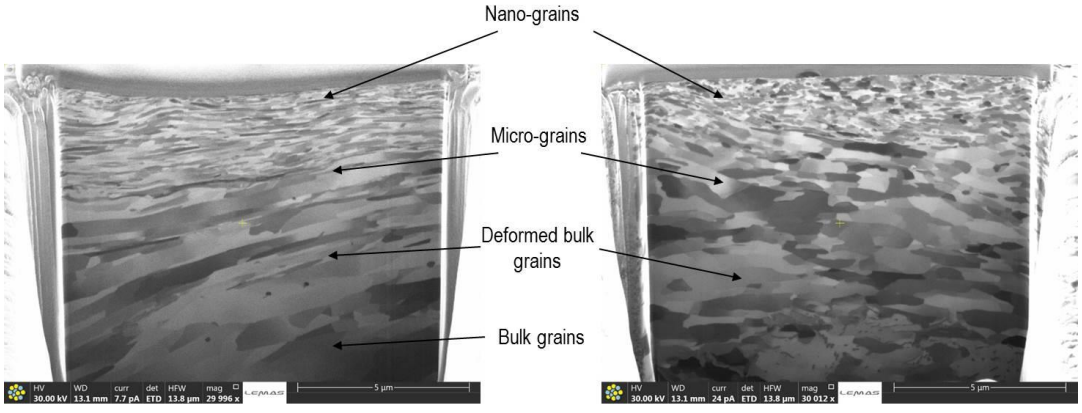

Figure 9.10 FIB analysis of X65 carbon steel samples after (a) 30-minute and (b) 240-minute erosion SIJ tests at a flow velocity of 20 m/s in a N_2-saturated, 60°C solution containing 1000 mg/L of sand showing the different grain sizes as a result of work-hardening

The very refined work-hardened layer, consisting of nano-grains and approximately 1 µm thick, was present closest to the surfaces of all samples. Underneath the nano-grain layer, grain refinement was still observed but the grains were slightly larger in size. Large grains, similar in size to the grains observed in the bulk of the sample prior to testing, were present beneath these two refined layers, with some deformation of the bulk grains observed. This

possibly explained why no significant difference in Vickers hardness was measured between erosion and erosion-corrosion samples, as the penetration depth of the indenter was potentially greater than the thickness of the work hardened layers.

A representation of the mechanisms of work-hardening of carbon steel samples is shown in Figure 9.11. A similar mechanism of grain refinement was also observed by Rajahram et al. [108], where it was suggested that nano-grains were formed closest to the surface due to the kinetic energy of initial particle impacts. Load was transmitted to bulk grains from subsequent particle impacts in the work-hardened region, causing micro-grains to form beneath the nano-grain layer and subsequently causing deformation of the bulk grains [108]. The thickness of both the nano-grain layer and micro-grain sub-layer increased over time on the erosion samples. It was expected that the nano-grain layer at the surface would have a higher hardness than the larger grains beneath this layer [165].

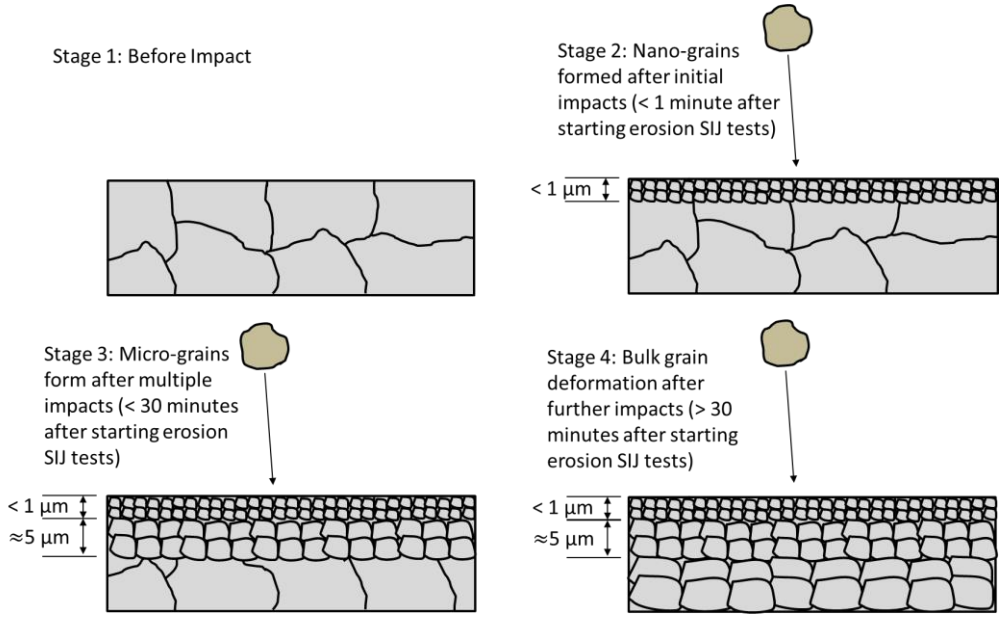

Figure 9.11 Mechanisms of work-hardening of carbon steel after particle impingement in different stages as determined from FIB analysis of erosion samples after SIJ erosion tests at a flow velocity of 20 m/s in a N_2-saturated, 60°C solution containing 1000 mg/L of sand

The comparison of the erosion and erosion-corrosion samples showed that there was differences in the subsurface microstructure of the two samples after 240-minute tests, shown in Figure 9.12. The work-hardened layers were thicker on erosion samples than erosion-corrosion samples. This was most obvious in the comparison between the samples after 240-minutes of testing, where nano-grain layers were slightly thicker and micro-grain layers were significantly thicker on the sample subject to erosion. Nano-grains also

appeared to be more refined on the erosion samples than on the erosion-corrosion samples.

In erosion-corrosion conditions, the corrosion of the X65 surface continuously exposed softer material, by removing nano-grain layers closest to the surface. However, nano-grain layers were still observed on erosion-corrosion samples, therefore suggesting this layer formed at very high rates after very few particle impacts. The high rates of work-hardening in the high flow velocity and sand concentration used in this work, shown previously in Figure 6.38, showed that the hardness increased significantly after one minute of erosion testing. However, the continuous dissolution of nano-grain layers meant that micro-grain layers were not as thick, probably due to fewer particle impacts in the same locations on the surface, meaning load from particle impacts was not transmitted to bulk grains beneath the nano-grain layer to the same extent as erosion samples, where less overall material removal occurred [139]. The lack of a thick micro-grain layer on erosion-corrosion samples likely contributed to erosion-enhanced corrosion as softer grains in the micro-grain layer were more likely to be exposed after corrosion, with the harder nano-grain layer removed by electrochemical dissolution.

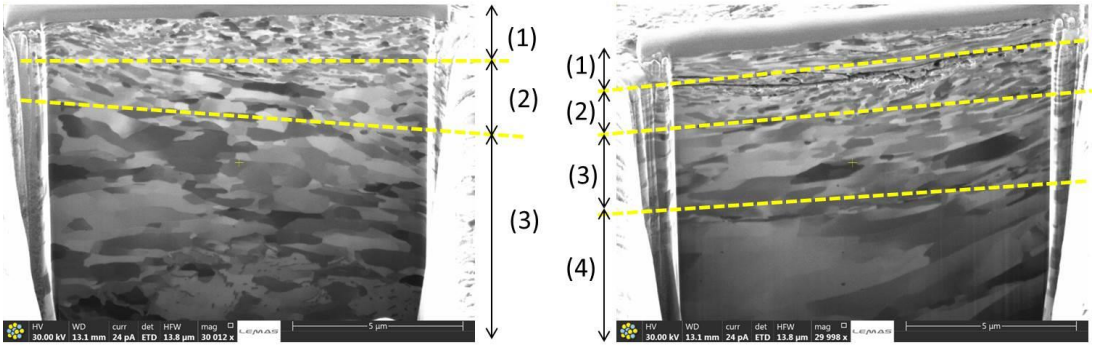

Figure 9.12 FIB analysis of X65 samples after 240-minute (a) erosion SIJ tests at a flow velocity of 20 m/s in a N_2-saturated, 60°C solution containing 1000 mg/L of sand and (b) erosion-corrosion SIJ tests at a flow velocity of 20 m/s in a CO_2-saturated, 60°C, pH 4.7, 2% NaCl solution containing 1000 mg/L of sand, showing the (1) nano-grain layer, (2) micro-grain layer, (3) deformed bulk grains and (4) bulk grains

The presence of a thick micro-grain layer on erosion samples also explained why the corrosion of the work-hardened layers did not reduce sample hardness to pre-test levels, when corrosion of work-hardened layers was tested in CO_2-saturated conditions using samples that had been work-hardened for 120 minutes prior to testing. An approximate corrosion rate determined from mass loss measurements of 4.59 mg/hr ± 0.38 mg/hr was

measured, which, if assumed to be constant over the surface area of the sample, was equivalent to a thickness loss of 1.24 µm/hr ± 0.10 µm/hr. Therefore, in a 30-minute period, it was estimated that approximately 0.6 µm to 0.7 µm of material would have been removed by corrosion, meaning that some of the nano-grain layer probably remained, with the micro-grain layer beneath remaining unaffected.

Large voids were observed in the subsurface of erosion-corrosion samples that were not observed on the erosion samples, thought to be subsurface cracks. Some very fine cracks appeared to be present in the subsurface of the erosion samples, but these cracks had not propagated significantly into the sample. It should be noted that FIB analysis is completed on a very small scale. It could be argued that the large voids on the surface were observed because of overlapping material, such as lips, formed from particle impacts close to the region analysed. However, smaller cracks were also observed that initiated within the region of the analysed subsurface region and the cracks did appear in a similar region to the subsurface cracks seen in FIB analysis completed by Rajahram et al. [139] after erosion-corrosion tests, where a crack was observed between the nano-grain and micro-grain layers, shown in Figure 9.13. It is possible that cracks had begun to form on erosion samples in regions that were not analysed, but there was no mechanism to accelerate the growth of the crack. Corrosion mechanisms were expected to accelerate the growth of the crack, meaning that any cracks in erosion samples would not have propagated at the same rate [169].

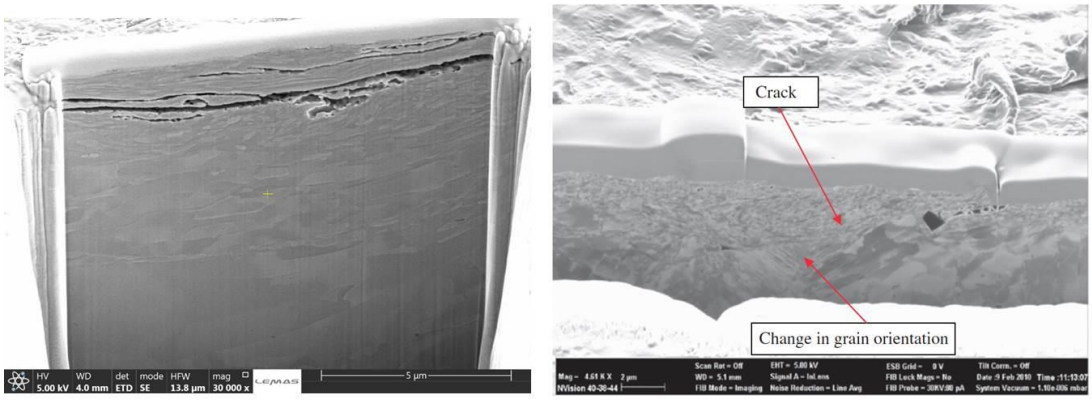

Figure 9.13 FIB-SEM images of X65 carbon steel samples after 240-minute erosion-corrosion SIJ tests at a flow velocity of 20 m/s in a CO_2-saturated, 60°C, pH 4.7, 2% NaCl solution containing 1000 mg/L of sand compared with the FIB analysis of UNS S31603 completed by Rajahram et al. [139]

Several theories exist that explain subsurface cracking of steels as a result of particle impacts. Levy [76] observed subsurface cracks on pearlitic carbon steels, thought to be due to fracture of brittle cementite regions after particle impacts. Repeated impacts and the formation of nano-grains can also cause the nano-grain layer to become brittle [165]. The erosion behaviour of ductile materials and brittle materials vary significantly, with high impact angles causing the highest rates of degradation of brittle materials [162]. The impact of particles on brittle materials can cause fracture, where material is removed by the formation and intersection of cracks [16]. Jiang et al. [170] also suggested that repeated particle impacts on a surface caused a low cycle fatigue degradation mechanism, resulting in the initiation of cracks at lips formed from impact craters after particle indents, as shown by Rajahram et al. [139], thought to be the cause of the subsurface cracking observed in this thesis. An overview of the proposed mechanism of subsurface cracking is explained in the schematic diagram shown in Figure 9.14.

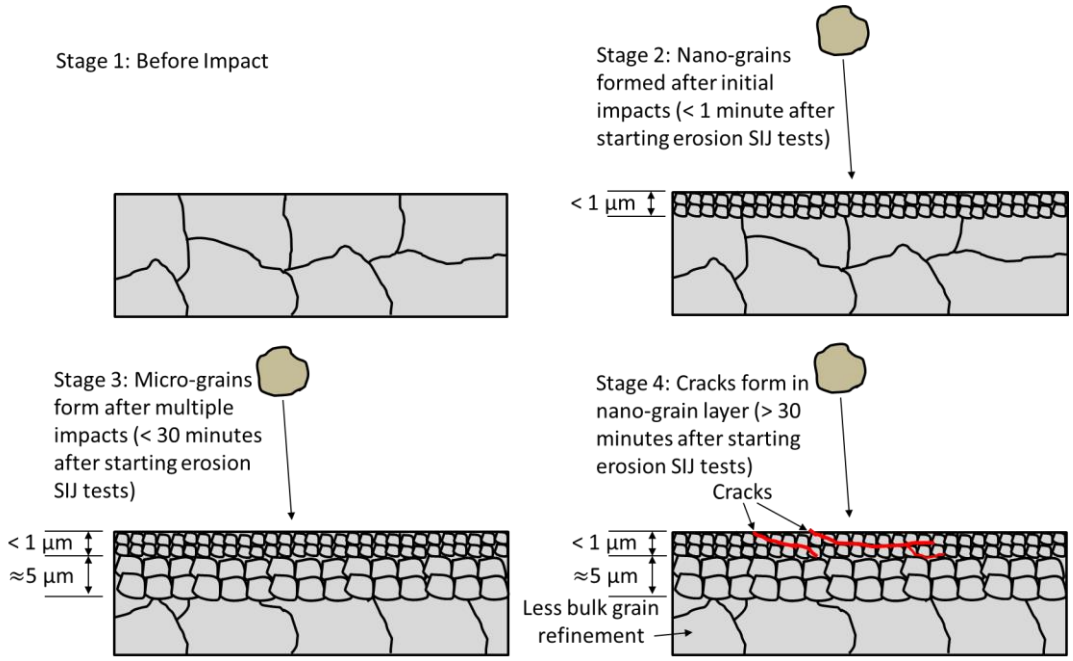

Figure 9.14 Propagation of cracks in the nano-grain work-hardened layer of carbon steel samples in erosion-corrosion SIJ tests at a flow velocity of 20 m/s in a CO_2-saturated, 60°C, pH 4.7, 2% NaCl solution containing 1000 mg/L of sand

The presence of thicker work-hardened layers on the erosion samples may also have been more effective at absorbing energy upon the impact of a particle and transferring it to bulk grains [108]. As cracks were observed between the nano-grain and micro-grain layers on the erosion-corrosion samples, impact energy may not have been transmitted as effectively to the bulk grains, explaining why less bulk grain refinement was observed in

erosion-corrosion samples compared to erosion samples. Cracks were only observed in the nano-grain region and in the region of the transition between the nano-grain layer and the micro-grain sub-layer, where embrittlement was most likely to be possible, due to the very fine grain structure [165]. The growth of cracks could potentially loosen the material between the grain boundaries, resulting in material removal after fewer particle impacts [15].

9.4 Using CFD to Improve the Understanding of Material Removal Mechanisms after Particle Impingement

One of the limitations of the findings and discussion of erosion-corrosion results in Chapter 5 was that the full range of impact conditions on the surface of the samples in the SIJ were unknown. A nominal impact angle of 90° was given to describe the impacts of particles on the surface. In reality a significant range of impact angles were expected on the surface of the sample, as was shown in the CFD predictions of particle flow through the SIJ nozzle, which resulted in different rates of degradation across the surface and enabled a much more detailed evaluation of erosion-corrosion interaction mechanisms to be completed in Chapter 6. However, several assumptions were made to predict particle trajectories and the accuracy of the model is discussed to demonstrate the benefits of using CFD in analysis of erosion and erosion-corrosion.

9.4.1 Significance of Assumptions in CFD Simulations

A CFD model was developed in Chapter 6 to simulate the particle trajectories through an SIJ nozzle. Whilst there were some limitations in the CFD model developed, due to the assumptions made, these assumptions would not significantly affect the useful results gained from the simulation used to improve the understanding of erosion-corrosion. Analysis of the assumptions in Chapter 6 showed that most of the assumptions did not have a significant effect on results. Gnanavelu et al. [120], Mansouri et al. [122] Chen et al. [110] and Vieira et al. [123] all showed, using the same methodology as used in this thesis, that CFD was accurate and effective in the analysis of erosion.

One of the most significant assumptions in CFD particle trajectory models is the assumption of a single particle size. However, experimentally, a range of sizes were measured in the sand particles used that were representative of sand particles present in oil and gas pipelines. Different particle sizes were

shown by Lynn et al. [83] to produce different impact velocities on the surface of a specimen in slurry pot testers and Humphrey [4] reported how the trajectory of a particle was influenced by its' size. To demonstrate the significance of particle size on impact velocity and erosion rate for the particle size range used in this thesis, the range of particle sizes is compared with results obtained by Lynn et al. [83], shown in Figure 9.15. Particle size had two effects on erosion rate as larger particles caused increased rates of material removal and particle velocity increased with increasing size, also increasing erosion rates. The impact velocity approximately doubled over the range of sizes, but the erosion rates were almost ten times greater for the largest particle size compared to the smallest particle size in the range.

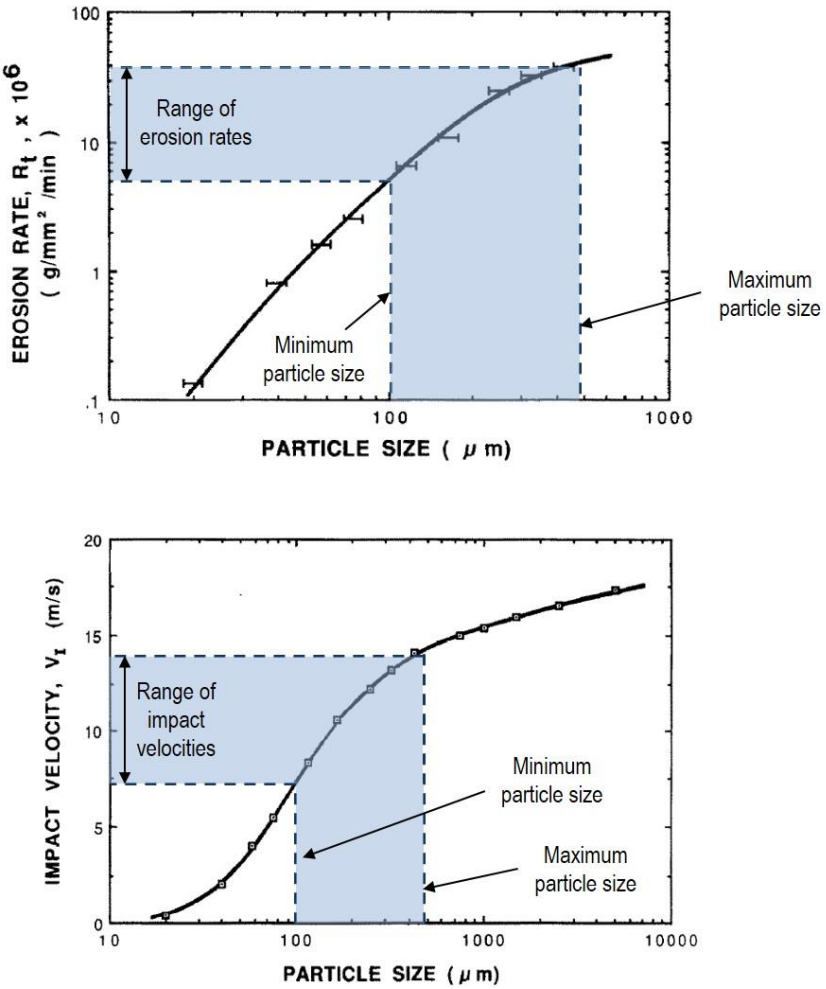

Figure 9.15 Variation of impact velocity and erosion rate for varying particle sizes as shown by Lynn et al. [83] compared with the range of sizes of particles used in erosion and erosion-corrosion SIJ tests in this thesis

Therefore, it is suggested that assuming one particle size can significantly limit the accuracy of erosion rate predictions, if there is a wide size distribution of particles used experimentally. If the size range is narrow, this assumption will be much less significant, as shown in the validated results completed by

Gnanavelu et al. [120], where a narrower range of particle sizes were used for erosion SIJ erosion experiments than were used in this thesis. When a large range of sizes is used, it is suggested that it is more appropriate to use CFD to define impact angles and impact velocities and characterise average conditions in regions on a surface, as was completed in Chapter 6, rather than to predict erosion rates, which would be more significantly affected by the assumption of one particle size, as shown in Figure 9.15.

9.4.2 Validation of CFD Model and Recommended Methodology

Erosion material removal mechanisms are highly dependent on impact angle, with cutting at low impact angles and plastic deformation at high impact angles [16]. The SEM images from each of the regions defined on the surface are compared with the impact angle in Figure 9.16. No precise threshold values for impact angles are available in the literature that define when the material removal mechanism changes from plastic deformation to cutting. However, the material removal mechanisms, observed using an SEM in each of the regions, agreed with the mechanisms expected from CFD predictions of impact angle. High impact angles resulted in plastic deformation, showing impact craters on the surface of the sample in region 1, and cuts were observed in regions 2 and 3, allowing the definition of a plastic deformation-dominated region, a mixed deformation and cutting region and a cutting-dominated region. Few impacts were observed on the surface of region 4.

It is, therefore, also suggested that the assumption of one particle size does not significantly limit the conclusions from the CFD model because the wear mechanism in the regions identified would not be expected to change, despite the variation in particle size. The significance of the changes in size, and hence impact velocity and impact angle, would have a much greater influence on the prediction of erosion rate. Models of erosion through different geometries completed by Chen et al. [2, 110], Vieira et al. [123], Gnanavelu et al. [120] and Mansouri et al. [122] were used to predict erosion rates or changes of geometry on metal samples. Models were then validated by measuring the erosion rates in the same conditions experimentally. The significant variations and uncertainties in predictions of particle trajectories mean that erosion rates can be significantly affected, limiting the reliability of the above models, unless a narrow range of particle sizes is used.

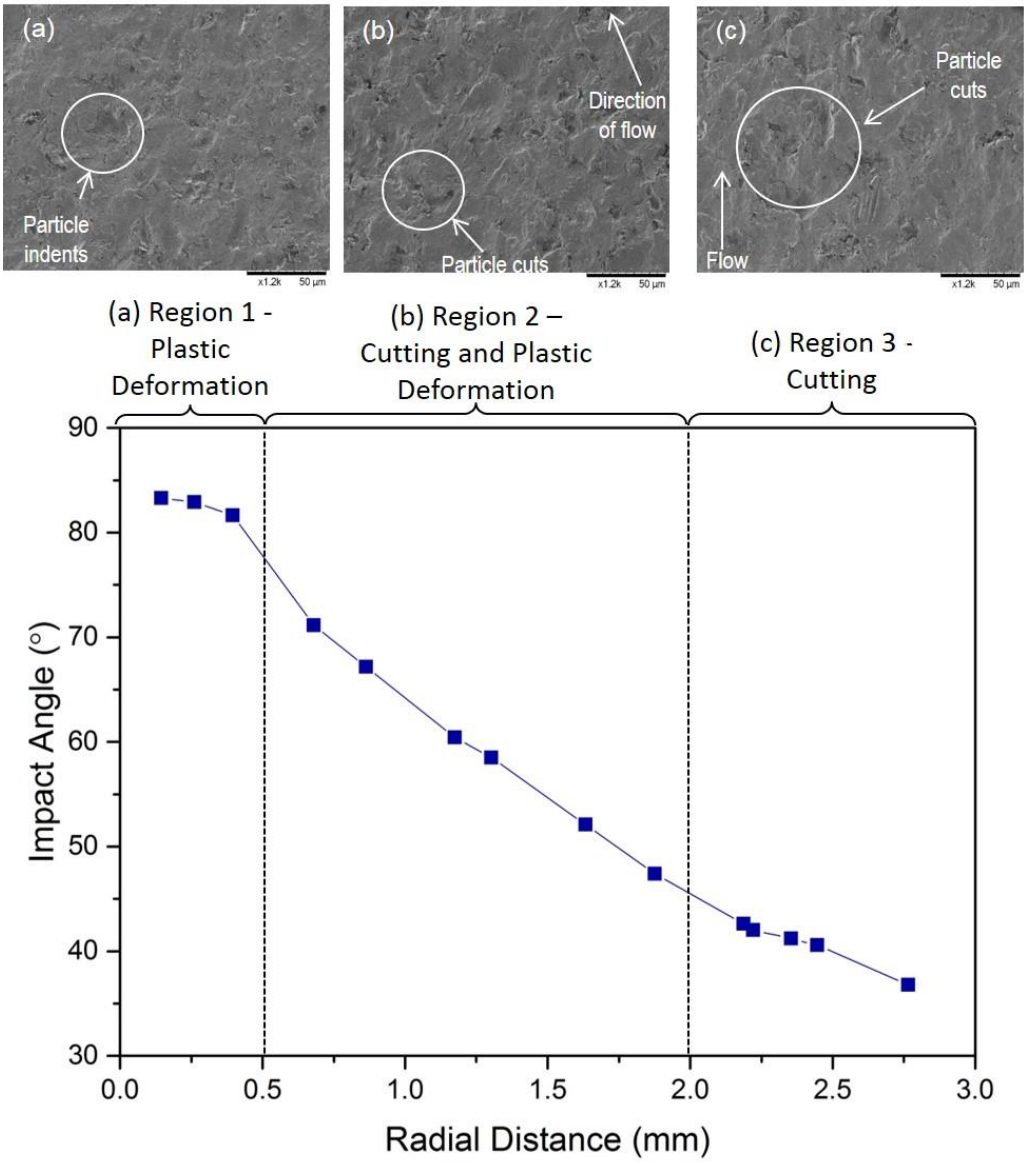

Figure 9.16 Comparison of CFD predicted impact angles over the different regions of an X65 sample compared with SEM images of the three regions experiencing particle impact after completing 240-minute erosion SIJ tests at a flow velocity of 20 m/s in a N_2-saturated, 60°C solution containing 1000 mg/L of sand

9.4.3 Influence of Particle Impingement Parameters

Knowledge of the particle impact velocity enables the calculation of several impact parameters at the surface that may be more relevant to explaining material removal mechanisms from particle impingement. Particle impact velocity is regularly used as an input parameter for prediction of erosion rates [10]. However, the impact velocity does not directly relate the particle impact to material removal mechanisms and the use of impact energies or strain rates may be more appropriate. Impact energy has been suggested as a parameter

that related impact velocity to erosion rates and impact energy has been discussed in the mechanisms of work-hardening after particle impingement [18, 108]. However, erosion degradation has been shown to be proportional to impact velocity with an exponent in the range of 2.4 and 2.7, as impact energy did not fully account for material removal mechanisms during impact and from repeated impacts [4, 18].

Hutchings [16] proposed that the mean strain rate, calculated using Equation (9.2), was a useful parameter for determining erosion, defining a minimum strain rate typically required for deformation of material after particle impact.

$$\dot{\epsilon} \approx \frac{2^{3/2} v_p^{1/2}}{5\pi r_p} \left(\frac{3H}{2\rho_p}\right)^{\frac{1}{4}} \tag{9.2}$$

where $\dot{\epsilon}$ is the strain rate, H is the hardness of the material and r_p is the radius of the particle. This equation is an approximation of the strain rate at high impact angles, assuming a spherical particle, and is dependent on particle size which varies in experimental erosion conditions. However, it was used to give an approximation of strain rate from particle impacts across the surface of the sample used in the SIJ, shown in CFD predictions at 20 m/s using the model developed in Chapter 6 in Figure 9.17. One value of hardness was assumed, determined from the measured hardness after work-hardening in erosion and erosion-corrosion tests, of approximately 300 H_v. Very high strain rates were observed in the order of 10^5 s^{-1}, with Hutchings [16] suggesting that a minimum strain rate of approximately 10^6 s^{-1} is required to cause material deformation from particle impact.

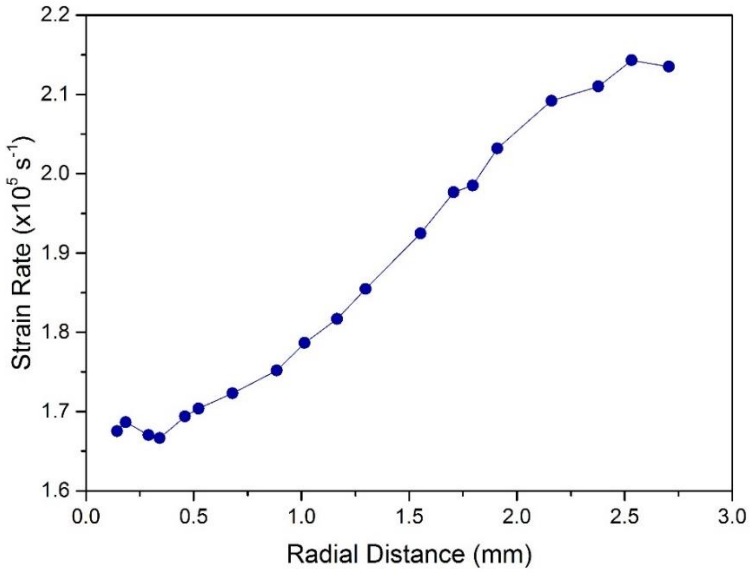

Figure 9.17 Strain rate predictions using CFD across the surface of the sample in the SIJ after particle impingement at a flow velocity of 20 m/s in a 60°C solution

Strain rates can also be converted to strain caused by particle impact by assuming a time duration of particle impact, which Hutchings [234] suggested varied dependent on particle size. Several theories have been suggested for material removal after particle impact, including the removal of material after a critical strain is achieved, accumulated after repeated impacts, or a low cycle fatigue mechanism where repeated impacts strain the material [10, 16]. FIB-SEM analysis of the X65 subsurface after erosion-corrosion tests, shown earlier in this chapter, suggested that a low cycle fatigue mechanism was occurring due to cracks present in the subsurface. Therefore, use of strain rate could be a more reliable parameter than impact velocity from CFD predictions to explain degradation mechanisms.

The use of a strain parameter from a particle impact also relates the impact of particles to work-hardening of the material. Naim and Badahur [166] showed the relationship between accumulated strain and hardness of the material and showed that hardness increased very quickly after strain accumulated caused by particle impacts, before material was removed after a critical fracture strain was reached. Barik et al. [59] observed no obvious relationship between hardness and strain rate in SIJ erosion tests, but it was suggested that the work-hardened layer was thinner than the indentation depth, potentially influencing results. The use of a strain parameter may be more relevant, and easily determined using CFD, to relate the effects of particle impacts to material removal mechanisms. However, it is less clear how particle impact angle influences the plastic strain, as Equation (9.2) is used for high impact angle deformation.

9.5 Erosion-Corrosion of Carbon Steel in Pipe Flow

The SIJ was used to investigate the mechanisms of erosion-corrosion and quantify the contribution of corrosion, erosion, erosion-enhanced corrosion and corrosion-enhanced erosion to total erosion-corrosion degradation in conditions representative of oil and gas conditions. However, it was shown that impact angle and impact velocity have a significant influence on degradation rates and mechanisms, so it was unknown if SIJ results were representative of the conditions that would typically be seen in pipe flow. Corrosion rates of carbon steel can also vary between different geometries for the same flow velocity [30, 52]. Therefore, it is also assumed that the erosion-enhanced corrosion is influenced by flow conditions and geometry. Stack et al. [112, 152, 156, 157] showed that different erosion-corrosion regimes occur

dependent on the conditions present. Understanding the significance of flow conditions, controlled by the flow geometry, is essential to understanding erosion-corrosion.

9.5.1 Comparison of Erosion Conditions in the Elbow and SIJ

Erosion-corrosion research has been completed in different geometries to determine the contribution of corrosion and erosion components to total erosion-corrosion degradation, often without defining the conditions, other than providing a nominal impact angle and flow velocity [34, 62, 149]. To investigate the significance of flow geometry on erosion-corrosion of carbon steel, analysis in conditions more representative of oil and gas pipe flow was completed by designing an elbow for erosion-corrosion evaluation of X65.

A CFD model of the elbow was also developed to predict the particle impact angles and impact velocities expected at the surfaces of X65 samples in the elbow. When comparing the range of particle impact angles in the elbow and the SIJ determined using both CFD models, a much wider range was predicted in the SIJ. To demonstrate the significance of a wide range of impact angles, the SIJ and elbow impact angles are shown on a typical erosion degradation plot for a ductile material in Figure 9.18, where it can be seen that the SIJ impact angles occur over a wide range of angles, resulting in very different erosion conditions over the entire surface, making it essential to factor this into investigations of erosion-corrosion using SIJs. The elbow had a much smaller range of angles, with less direct impingement observed and lower angles of cutting.

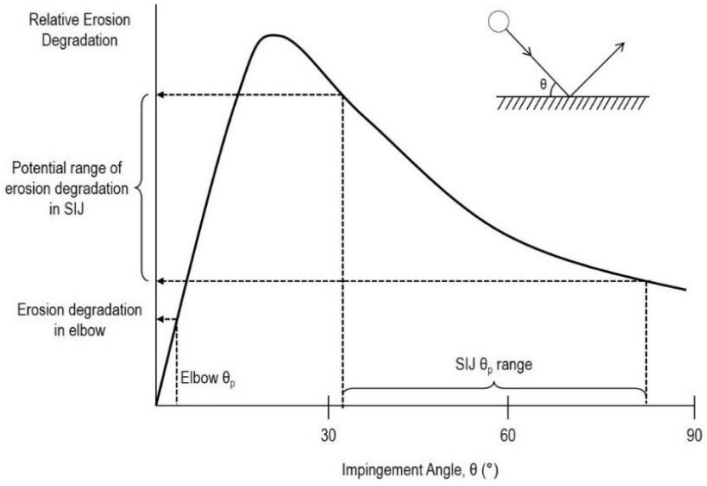

Figure 9.18 Range of impact angles predicted using CFD in the SIJ at a flow velocity of 20 m/s and in the elbow at a flow velocity of 6 m/s when compared with erosion degradation typical of ductile materials adapted from [17]

9.5.2 Erosion-Corrosion Evaluation of X65 Using an Elbow

Flow-induced corrosion degradation was high in the low pH conditions and similar on both the inner and outer radius of the elbow. Nesic et al. [37] measured corrosion rates of X65 in pH 4 solution at 50°C of approximately 5 mm/yr and in excess of 8 mm/yr at 80°C at a Reynolds number of 30,000. The Reynolds number in elbow tests in this thesis at 6 m/s and 60°C was much higher, in excess of 320,000. Therefore, the flow was highly turbulent in these conditions. It was also shown by Nesic et al. [37] that corrosion rates in pH 4 solutions were more than four times greater at 80°C than at 20°C. Therefore, it was expected that degradation rates in the elbow would be high. However, there were some errors present in results as there was a significant amount of variation in measured degradation at 6 m/s in 60°C flow-induced corrosion tests. Some limitations of the elbow design, which could be modified in future versions, could have potentially contributed to error in the results. Crevice corrosion around the sides of the X65 samples could have accelerated corrosion rates, as the corrosive solution could be in contact with the samples up to the position of the o-ring. This also made it challenging to calculate corrosion rate reliably, as solution would have been contact with a greater surface area on the sample than intended. Experimental error, such as slight changes in solution pH or temperature could have also had a significant influence on corrosion rates, due to the high degradation measured, and less consistency in surface finish was probably achieved, due to the method of polishing by hand.

Corrosion rates tended to increase towards the exit of the elbow, measured at the 90° specimens, compared with samples at the inlet of the elbow. Zeng et al. [174] reported similar increased corrosion rates at the outlet in experiments completed in an elbow at a flow velocity of 4 m/s in a 60°C, CO_2-saturated solution, at pH 5.4, but a slightly greater difference in corrosion rates on the inner and outer radius was observed than seen in the results in this thesis. Degradation was lower in the elbow results reported by Zeng et al. [174] than in the elbow in this thesis. However, pH was much higher, with Nesic et al. [37] showing that corrosion rates were three times greater at pH 4 than pH 5 at 50°C.

In erosion-corrosion conditions, particle impacts were observed on the outer radius of the elbow in tests completed at a flow velocity of 6 m/s and solution temperature of 60°C. Pure corrosion accounted for the majority of total degradation at all samples on the outer radius. A comparison of the ratio of total erosion-corrosion degradation to pure flow-induced corrosion

degradation from results in this thesis is made with erosion-corrosion research of carbon steel in CO_2 environments available in literature in Figure 9.19. The conditions tested in for each of the results shown in Figure 9.19 are detailed in Table 9.4. Elbow results from Chapter 7 were compared with SIJ results in Chapter 6, SIJ results reported by Hu and Neville [34] and results downstream of a rapid expansion reported by Malka et al. [49].

Experimental conditions had a significant effect on the ratio of erosion-corrosion degradation to flow-induced corrosion degradation, shown in Figure 9.19. Variation was observed in the elbow, highlighting how conditions can change within a flow geometry despite the same conditions present. A comparison of SIJ results from Chapter 6 completed in similar conditions to Hu and Neville [34], showed that degradation in erosion-corrosion conditions was much greater than in flow-induced corrosion conditions. Similar conditions were tested in both tests, however, pH was likely to have been higher in tests completed by Hu and Neville [34] as test conditions were reported to be in conditions favourable to iron carbonate growth. Iron carbonate did not precipitate in the tests reported by Hu and Neville [34], but these conditions would typically produce a lower corrosion rate [37]. Hu and Neville [34] reported that corrosion-enhanced erosion was the most significant proportion of overall degradation, and higher than the SIJ results in this thesis, despite a much higher sand concentration used in this thesis.

Table 9.4 Experimental conditions used for the comparison of the ratio of erosion-corrosion degradation to flow-induced corrosion degradation of carbon steel in CO_2-saturated conditions shown in Figure 9.19

Test	Geometry	T (°C)	U (m/s)	d_p (μm)	Sand Conc. (mg/L)	pH
a	0° elbow sample (Chapter 7)	60	6	250	1000	4
b	75° elbow sample (Chapter 7)	60	6	250	1000	4
c	SIJ (Chapter 6)	60	20	250	1000	4.7
d	SIJ (Hu and Neville [34])	60	20	250	200	Not reported
e	After rapid expansion (Malka et al. [49])	34	2	275	20,000	4

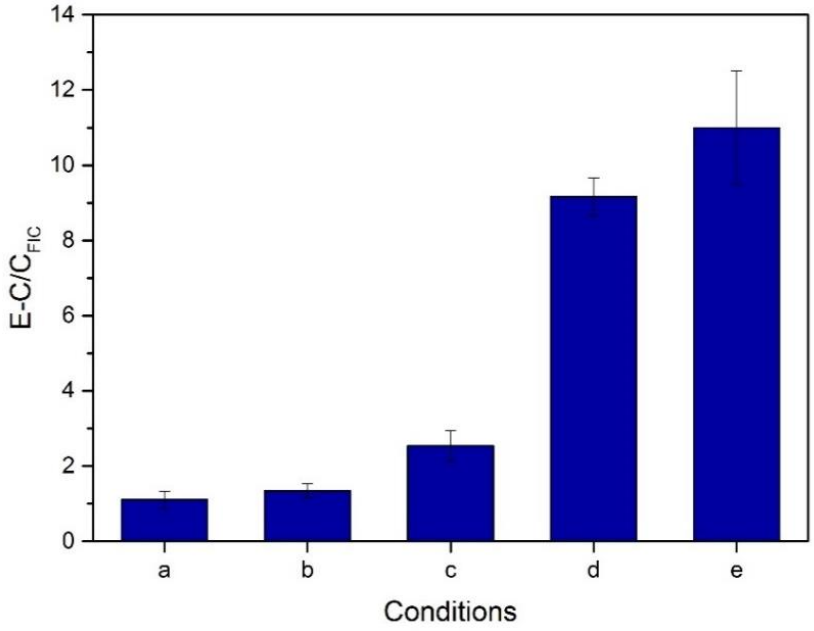

Figure 9.19 Comparison of the ratio of erosion-corrosion degradation to pure flow-induced corrosion degradation for the conditions shown in Table 9.4

The results in a rapid expansion reported by Malka et al. [49] showed that erosion-corrosion degradation was much greater than flow-induced corrosion degradation. Erosion conditions in the rapid expansion were less severe than the other test conditions, due to the much lower flow velocity and temperature, resulting in a higher solution viscosity which reduces particle impact velocity [75]. Very high quantities of sand were added, but CFD analysis of the elbow showed that not all particles impact on the wall in a pipe flow geometry. CFD simulations of particle trajectories was not completed by Malka et al. [49], so it could either be assumed that not all sand particles impacted at this location in the rapid expansion, similarly to the elbow, or a much higher proportion of the particles impacted at this point, highlighting how flow geometry has significance on the particular erosion-corrosion degradation.

When comparing the results in this thesis with the results obtained by Malka et al. [49] and Hu and Neville [34], it was clear that several factors, including test geometry, resulted in different results on some occasions and similar results on other occasions, with no apparent trend observed in results. The similarities between the high synergistic components of overall degradation observed by Malka et al. [49] and Hu and Neville [34] could also be misleading as material removal mechanisms could vary significantly. Therefore, it is essential that the conditions in the specific erosion-corrosion application being analysed are fully understood when completing laboratory-based erosion-corrosion tests that attempt to replicate conditions.

It should also be noted that electrochemical isolation of the X65 samples in the elbow used for erosion-corrosion analysis might not be representative of a carbon steel pipe manufactured from one carbon steel component. This may result in different corrosion mechanisms and possibly localised corrosion in regions of the pipe experiencing higher quantities of particle impingement as a result of local acidification in erosion craters formed from particle impacts, as reported by Wood and Hutton [15]. However, for the purpose of this work, isolating the samples enabled a much greater insight into individual degradation mechanisms at multiple locations in the elbow.

9.6 An Improved Methodology for Erosion-Corrosion Testing

An improved methodology for defining and translating erosion-corrosion conditions in different flow geometries in low pH conditions is proposed using CFD simulations of mass transfer coefficients and particle trajectories. Conclusions from the results obtained in this thesis would be significantly limited if flow conditions were not fully defined. For example, FIB-SEM analysis of the subsurface after erosion and erosion-corrosion tests was completed in a region of high angle particle impacts where plastic deformation is the dominant mechanism of wear. Different mechanisms may occur at cutting angles of impact at other locations on the sample surface. Therefore, simply defining a nominal impact angle for those tests conditions would not fully explain the corrosion-enhanced erosion mechanisms. CFD was used to improve erosion-corrosion experimentation.

9.6.1 Suggested Approach to Erosion-Corrosion Testing

Erosion-corrosion research has often overlooked how significant the influence of flow is on conditions. Research has been completed, often only reporting a nominal impact angle and nominal flow velocity, as was completed in Chapter 5 of this thesis, which did not account for the full range of conditions that would be present on a test specimen surface [6, 34, 51, 61, 62, 120, 122]. This could result in incorrect conclusions being made from results as erosion mechanisms can vary significantly for different impact angles. It is suggested that flow and erosion conditions need to be defined more thoroughly to fully understand erosion-corrosion.

Conclusions made regarding corrosion-enhanced erosion mechanisms in this thesis would be significantly weakened if it was unknown what particle impact

angles were in the regions analysed. Higher mass transfer in the SIJ than the elbow would also significantly influence the dissolution of work-hardened layers. A lower corrosion rate could, for example, remove less of the nano-grain layer formed after particle impacts leading to a more refined work-hardened layer and significantly less corrosion-enhanced erosion for the same particle impact angles and impact velocities. A lack of definition of conditions in Chapter 5 would lead to conclusions from nominal velocities of 10 m/s, 15 m/s and 20 m/s and a nominal impact angle of 90°. However, another application at the same flow velocity, but much lower mass transfer coefficients and actual particle impact angles of 90°, could produce considerably different degradation rates and mechanisms, explaining why significantly different contributions to total erosion-corrosion degradation were observed in Figure 9.19. Therefore, it is essential to the understanding of erosion-corrosion that conditions are fully defined.

A new approach is suggested that defines the flow conditions more thoroughly to either replicate conditions from a particular application or improve the explanation of degradation mechanisms, as was completed in this thesis in Chapter 6. A summary of the approach using the SIJ or another lab-based test geometry, to replicate field conditions, is shown in Figure 9.20. The first stage is to define conditions in the particular application more accurately. There are limitations in how accurately conditions can be replicated, as, for example, achieving the same multi-phase flow conditions or replicating precise brine compositions can be complicated. However, simple parameters, such as flow geometry and mass transfer coefficients, can be replicated in simple lab geometries. Particle impingement characteristics and flow can be predicted using CFD to define the degradation mechanisms, in geometries such as elbows in oil and gas pipe flows. After particle impact angles, impact velocities and mass transfer coefficients have been defined, conditions can then be replicated more accurately in lab-based test geometries. Different mass transfer coefficients on the SIJ sample can be achieved by varying the height of the sample from the nozzle [235]. Alternatively, a new pipe geometry could be designed and 3D printed, similar to the elbow designed in this thesis that could replicate conditions more accurately. The potential benefits of using this method and limitations under which conditions this approach can be used are discussed in the following sections.

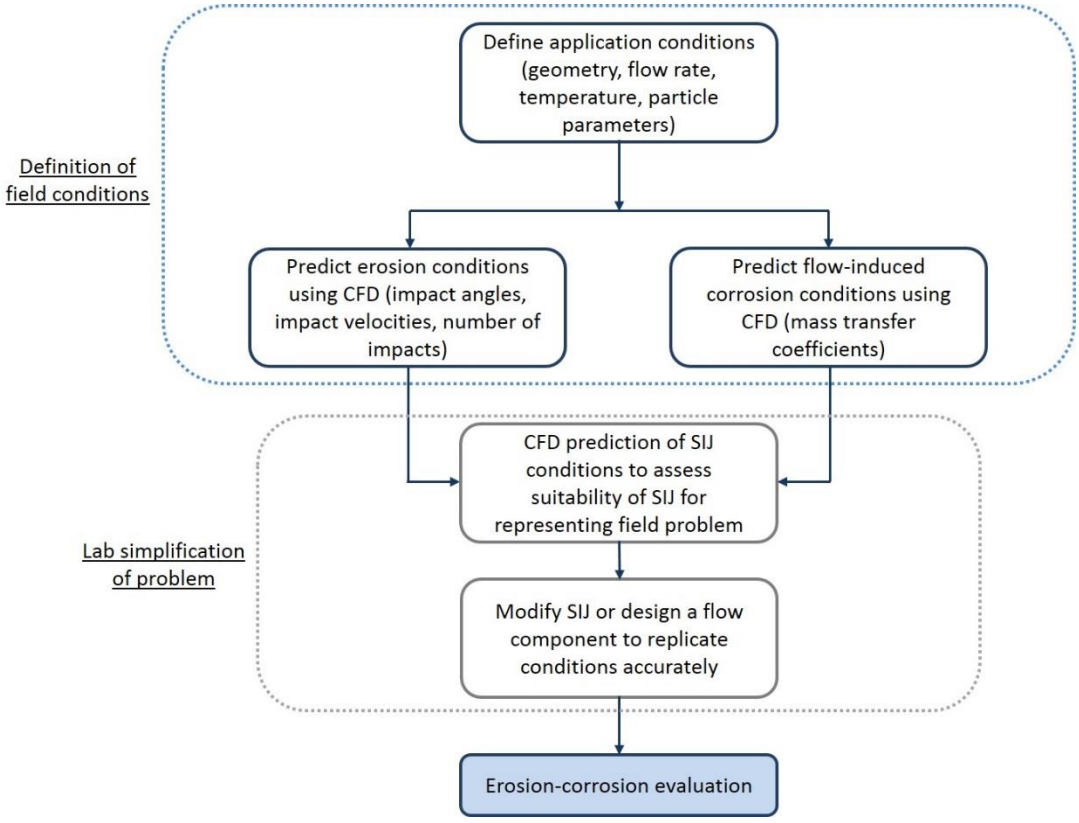

Figure 9.20 Framework for improved approach to erosion-corrosion evaluation of field problems and applications

9.6.2 Using CFD Particle Trajectory and Mass Transfer Predictions to Define Erosion-Corrosion Conditions

Mass transfer coefficients and particle trajectory predictions from CFD simulations were used to define erosion-corrosion conditions. The main parameters that were suggested to influence erosion were impact angle and impact velocity, whilst corrosion in low pH can be defined using mass transfer coefficients when no surface films are present [30]. It is unknown if flow has any specific influence on erosion-corrosion interactions. However, it is unlikely that flow would only influence an erosion-corrosion interaction mechanism, as mechanisms of work-hardening and removal of work-hardened layers, contributing to corrosion-enhanced erosion, would be defined by particle impingement and corrosion rates, both defined by flow parameters. Therefore, it is a logical assumption that flow influences corrosion and erosion mechanisms, which contributes to erosion-corrosion interactions.

Replicating impact angles, impact velocities and mass transfer coefficients in the SIJ to match conditions in the particular application of interest, should theoretically produce similar degradation rates and the same mechanisms of degradation. Gnanavelu et al. [120] showed how pure erosion rates could be

predicted using CFD simulations of particle impact angle and impact velocity, and these parameters are regularly included in erosion models [10, 18, 118]. Other parameters included in erosion rate calculations are typically material, fluid and particle properties. Therefore, by using the same particles and material in different flow geometries, erosion rates should be constant if the fluid properties, particle impact angle and particle impact velocity are identical.

Nesic et al. [30] showed how an increase in mass transfer coefficient in different geometries contributed to increases in corrosion rate of carbon steel, and it is generally accepted that increasing mass transfer coefficient in low pH conditions, when no inhibitor film is present, increases corrosion rates of carbon steel. It has also been shown that mass transfer coefficients can be used reliably to translate flow-induced corrosion conditions between different geometries [30, 52, 53]. Mass transfer coefficients were predicted in the SIJ and elbow, with mass transfer coefficients being much higher in the SIJ geometry than in the elbow at the same flow velocity of 6 m/s. Therefore higher corrosion rates were expected in the SIJ conditions than in the elbow. Results in Chapter 5 and 6 were obtained in SIJ erosion-corrosion tests at flow velocities of 10 m/s, 15 m/s and 20 m/s. A comparison of the mass transfer coefficients in each of the three flow geometries at those flow velocities from CFD predictions, using the models developed in Chapter 8, is shown in Figure 9.21. Maximum mass transfer coefficients in each of the flow geometries are reported. Mass transfer coefficients were much higher in the SIJ than the pipe geometries at the same flow velocities. Therefore, SIJ tests completed in Chapter 5 and Chapter 6 would have been completed in a more corrosive environment than would be present in the field.

Comparing the mass transfer coefficients in Figure 9.21 it was clear that flow geometry can significantly influence mass transfer coefficient for tests completed using the same corrosive fluid properties and flow velocity. Conditions in the SIJ can be changed, by varying nozzle diameter and nozzle heights, to produce different mass transfer coefficients on the surface of samples in the SIJ. Therefore, the SIJ could be used and changed to replicate pipe flow conditions and translate conditions between different flow geometries accurately in CO_2-saturated conditions at low pH. The mass transfer coefficient in the SIJ also varies across the surface, meaning that samples of different dimensions can be used to investigate different conditions in the flow.

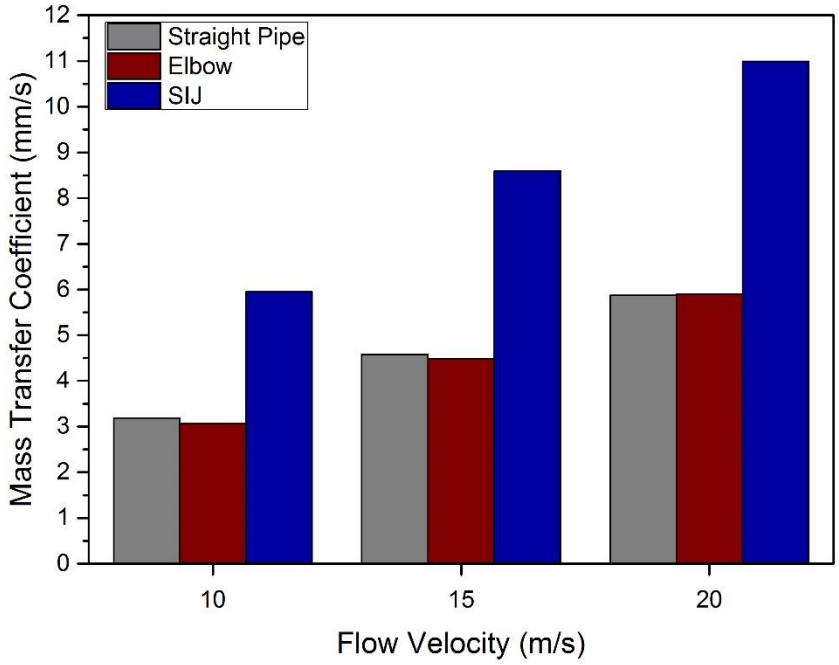

Figure 9.21 Comparison of CFD predicted mass transfer coefficients in different flow geometries at flow velocities of 10 m/s, 15 m/s and 20 m/s at a solution temperature of 60°C

Validation of mass transfer coefficients in the elbow and SIJ geometries was limited, due to a lack of available experimental data and models in the literature. However, the methodology used to determine mass transfer coefficients was shown to be accurate in the straight pipe CFD model developed. The comparison of maximum mass transfer coefficient in the elbow with the correlation derived by Wang et al. [67] showed that CFD simulations of mass transfer in the elbow in this thesis were accurate. Full validation of mass transfer coefficients in the SIJ and elbow was required to prove that this methodology was reliable across a wide range of conditions. Therefore, definition of mass transfer coefficients, particle impact angles and particle impact velocities in an erosion-corrosion environment allows for a much more detailed analysis of erosion-corrosion material removal mechanisms and potentially allows erosion-corrosion conditions to be translated accurately between different flow geometries.

9.6.3 Potential for Erosion-Corrosion Model Development

SIJ testing offers the benefit of being able to change flow and erosion conditions very easily, where different nozzles can be used at different heights from the metal sample. In the elbow, any change required to test slightly different conditions would require a redesign and manufacture of a new component. Surface analysis of samples used in SIJ tests is also easier due

to the flat geometry of the specimens used in SIJ tests opposed to the curved geometry required in elbow testing. Therefore, the SIJ provides many benefits over the use of an elbow for erosion-corrosion tests, and could also be used effectively in the development of a model for predicting erosion-corrosion degradation rates of materials. Erosion-corrosion degradation rates of X65 in low pH, CO_2-saturated conditions are suggested to be a function of the following parameters, based on conclusions from this work and commonly used parameters in flow-induced corrosion, pure erosion and erosion-corrosion analysis [10, 18, 176, 177]:

$$\begin{gathered} E = fn\left(\theta_p, v_p, \dot{\epsilon}, F_p, F_{m,e}\right) \\ C = fn\left(k_m, F_{m,c}, F_C\right) \\ E - C = fn\left(E, C\right) \end{gathered} \tag{9.3}$$

where θ_p, v_p and $\dot{\epsilon}$ define the particle impingement characteristics, significantly influenced by the flow, F_p is a function of particle properties, such as the diameter, density, hardness and shape and $F_{m,e}$ is a function of erosion-relevant target material properties, such as the hardness and work-hardening exponent. Each of these terms define erosion rates and the contribution of erosion mechanisms to erosion-corrosion degradation and have been used previously in erosion models [10, 18, 109, 177]. Mass transfer coefficients, k_m, define the flow-induced corrosion rates as a function of the flow properties and flow velocity in different geometries, $F_{m,c}$ are corrosion-relevant material properties and F_C is a function of solution corrosion chemistry, accounting for the significance of pH and partial pressure. Particle properties, solution chemistry and material properties can easily be replicated between different test conditions, and are not influenced by flow. Therefore, particle impact angles, impact velocities, mass transfer coefficients and strain rates are the remaining properties that characterise erosion-corrosion in a flow environment.

Gnanavelu et al. [120] developed a methodology for predicting wear depth across the surface of an SIJ sample from a particle impact angle and impact velocity input in pure erosion conditions. This method could be extended to erosion-corrosion conditions by including the prediction of mass transfer coefficients across the surface of the SIJ sample, to determine thickness loss as a function of impact angle, impact velocity and mass transfer coefficients, as demonstrated in Figure 9.22.

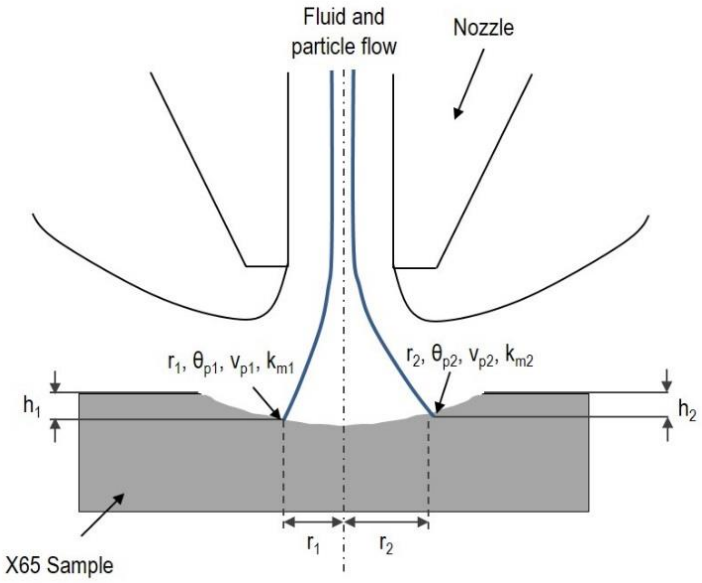

Figure 9.22 Key flow parameters that can be predicted using CFD on the surface of an SIJ sample to determine thickness loss, $\boldsymbol{h}$, as a function of impact angle, impact velocity and mass transfer coefficient

For a range of conditions, impact angles, impact velocities and mass transfer coefficients, thickness loss could be measured by profiling samples after tests. This could lead to the development of a basic model for erosion-corrosion degradation in a wide range of conditions. There are some limitations in the use of CFD, as have been discussed previously, but it has been shown on several occasions to be an accurate and reliable tool for erosion analysis [2, 116, 120-123]. Further to this, modelling corrosion-enhanced erosion could be improved by calculating strain rates, work-hardening exponents and expected thickness loss of work-hardened layers in corrosion conditions. However, more analysis is required to improve the understanding of work-hardening mechanisms and the removal of work-hardened layers in a range of environmental conditions.

Chapter 10
Conclusions from Erosion-Corrosion Analysis of Carbon Steel, Industrial Relevance and Future Work

Erosion-corrosion evaluation of carbon steel has been completed in different flow geometries to replicate the erosion-corrosion conditions in oil and gas carbon steel pipelines, in a range of environmental conditions. The contribution of flow-induced corrosion, erosion and erosion-corrosion interactions to total erosion-corrosion were quantified at different flow velocities and sand concentrations. The mechanisms of these interactions between erosion and corrosion were investigated in more detail to understand why enhanced rates of wear were measured in erosion-corrosion tests. A pipe elbow was designed to complete erosion-corrosion tests in a complex flow geometry to compare the erosion-corrosion conditions in the SIJ with conditions in more relevant geometries to the field. The main conclusions from the work and future work suggestions are given in this chapter.

10.1 Conclusions

A case study was completed in Chapter 5 to investigate the significance of erosion-corrosion of X65 carbon steel in conditions replicated from North Sea oil and gas pipelines, where sand production was found to be a significant issue. To replicate the conditions from the field as closely as possible in lab conditions, an SIJ was used with a 2% NaCl, 50 L solution maintained at a temperature of 60°C and flowing through the SIJ nozzle at velocities of 10 m/s, 15 m/s and 20 m/s in CO_2-saturated conditions for flow-induced corrosion tests. 500 mg/L and 1000 mg/L of sand particles, with an average diameter of 250 µm, were added to the solution to create erosion-corrosion conditions. The contributions of corrosion, erosion, erosion-enhanced corrosion and corrosion-enhanced erosion were measured at each sand concentration and flow velocity. Two corrosion inhibitors were compared with the results in blank conditions to determine how flow and the presence of sand particles affected the performance of corrosion inhibitors. The conclusions from Chapter 5 after completing erosion-corrosion tests were:

- Flow-induced corrosion results showed, as expected, that the corrosion rate increased when flow velocity was increased, showing a logarithmic relationship between flow velocity and corrosion rate;

- Corrosion inhibitors were evaluated in flow-induced corrosion conditions, showing high efficiency at reducing the corrosion rate, in excess of 85%. However, efficiency was lower than efficiency in static conditions, which was approximately 99%, but due to high rates of degradation in the SIJ and the relatively short test duration, this decrease in efficiency was not significant;
- Erosion-corrosion tests in conditions without inhibitor showed that erosion rates and erosion-corrosion rates increased with increasing sand concentration and increasing flow velocity as expected, with erosion-corrosion degradation rates in excess of 25 mm/yr at a flow velocity of 20 m/s and sand concentration of 1000 mg/L;
- Interactions were observed, with corrosion enhancing erosion in some conditions and erosion enhancing corrosion. However, erosion-enhanced corrosion rates were less significant. Further work was required to understand the mechanisms of these interactions, which was completed in Chapter 6;
- Corrosion inhibitors were affected by the presence of sand particles in erosion-corrosion conditions. Corrosion inhibitor A did not perform effectively in sand-containing flows, as it adsorbed to the sand particles and caused them to adhere to the sides of the SIJ reservoir. Therefore, further testing was not completed in erosion-corrosion conditions with inhibitor A;
- Inhibitor B did perform better in sand containing conditions as no adsorption to sand particles was observed. The inhibitor did not reduce any of the erosion components of total erosion-corrosion degradation, and overall degradation rates remained high, in excess of 15 mm/yr at a flow velocity of 20 m/s and sand concentration of 1000 mg/L. However, corrosion rates were decreased when the inhibitor was added.

These tests were useful for highlighting the significance of each of the contributing parameters to total erosion-corrosion degradation of carbon steel and identifying areas of further research. However, several limitations and unknowns existed from the first chapter of SIJ results, Chapter 5, as particle impact angles and impact trajectories were unknown, two significantly important parameters in erosion. Mechanisms of degradation could also not be explained from the results. CFD prediction of the trajectories of particles through the SIJ nozzle and onto a target specimen was completed to determine the impact angles and impact velocities of the particles on the surface of the X65 carbon steel samples. Further experimental SIJ work was

completed at a flow velocity of 20 m/s and sand concentration of 1000 mg/L, similar to the tests completed in Chapter 5, with different test durations to determine how mechanisms of degradation varied over time. Analysis of surfaces after each of the tests was completed using SEM, interferometry, micro-indentation and FIB-SEM to investigate the mechanisms of wear. The conclusions from the CFD model, erosion-corrosion tests and surface analysis in Chapter 6 were:

- A wide range of particle impact angles were predicted using CFD on the surface of X65 samples in erosion and erosion-corrosion tests, ranging from 35° to 85°, with high impingement angles causing plastic deformation and lower impingement angles causing cuts on the sample, shown on SEM images of the surfaces after erosion and erosion-corrosion SIJ tests;
- All contributing factors to total erosion-corrosion degradation occurred at a constant rate, with a linear increase seen in erosion, corrosion, erosion-corrosion and corrosion-enhanced erosion;
- Corrosion-enhanced erosion was the most significant enhancement of erosion-corrosion degradation. Corrosion of work-hardened layers and subsequent hardening of the sample at very high rates continuously exposed softer areas of material, accounting for the increased erosion wear;
- Work-hardened layers on erosion samples were thicker and more refined than the work-hardened layers measured after erosion-corrosion tests, suggesting that corrosion continuously removed material from the work-hardened layers, preventing thick, refined layers from forming on erosion-corrosion samples;
- Significant differences were observed in the subsurface microstructures of erosion-corrosion and erosion samples observed using FIB-SEM. Very refined work-hardened layers were present on erosion samples that were not as refined on the erosion-corrosion samples;
- Subsurface cracking was observed in the nano-grain layer of erosion-corrosion samples, contributing to corrosion-enhanced erosion. This was thought to be caused by a low cycle fatigue mechanism from repeated particle impacts, with corrosive species accelerating the propagation of the crack;
- Erosion-enhanced corrosion was not a significant contributing factor, despite the significant increase in surface roughness across the wear scar of the sample.`

The SIJ tests improved the understanding of the mechanisms of corrosion-enhanced erosion and the effect of particle impacts on the surface of X65 carbon steel. However, the aim of this work was to understand the mechanisms of erosion-corrosion in pipe flow conditions, with it being unknown how representative SIJ conditions were of pipe flow conditions, in terms of particle impact angles and impact velocities. Therefore, a 90° elbow was designed to evaluate erosion-corrosion degradation of X65 at multiple locations in the elbow. The following conclusions were made from the results of the erosion-corrosion tests completed in Chapter 7:

- An evaluation of X65 carbon steel in flow induced corrosion and erosion-corrosion conditions was completed using a newly-designed elbow at a flow velocity of 6 m/s in a solution of temperature 60°C;
- Mass loss in flow-induced corrosion tests at 6 m/s in a pH 4 solution saturated with CO_2 at a temperature of 60°C was very high. Degradation was slightly higher on the outer radius of the elbow and increased on both the inner radius and outer radius towards the outlet of the elbow. However, error was significant in the results;
- Error was significant in the erosion-corrosion results at 6 m/s, but there did appear to be an increase in degradation on the outer radius of the elbow compared to flow induced corrosion conditions. The most significance increase in degradation in erosion-corrosion conditions compared to flow induced corrosion conditions was observed on the outer radius on the sample located at 75°;
- Flow-induced corrosion degradation was the most significant contributing mechanism to total erosion-corrosion degradation in the conditions tested.

To improve the understanding of the influence of flow on erosion-corrosion mechanisms, CFD was used to define flow conditions in erosion-corrosion conditions in both geometries. CFD was used to predict impact angles and impact velocities to determine the influence of flow on erosion conditions and mass transfer coefficients were predicted to characterise the influence of flow on corrosion. The combination of the CFD analysis in erosion and corrosion conditions was suggested to define erosion-corrosion conditions in different geometries. The conclusions from Chapter 8 were:

- Mass transfer coefficients in the SIJ geometry were higher than mass transfer coefficients in an elbow at the same nominal inlet flow velocity,

and vary over the surface of a typical sample used in flow-induced corrosion and erosion-corrosion testing;

- Predictions of particle trajectories showed that over 95% of particles did not impact on the surface of samples in the elbow;
- Low impingement angles, less than 5°, were predicted on the surfaces of samples and impact velocities decreased at samples closer to the exit of the elbow;
- Impact angles in the elbow were therefore much lower than the impact angles predicted in the SIJ geometry, potentially resulting in different mechanisms of erosion degradation;
- The SIJ used for erosion-corrosion testing in Chapters 5 and 6 does not produce the same erosion-corrosion conditions that were measured in the elbow designed in Chapter 7.

10.2 Industrial Relevance and Novelty of Work Completed

The novelties from the erosion-corrosion research completed, the elbow design and the methodology for predicting erosion-corrosion conditions are discussed. The industrial relevance of the work is also highlighted.

Novelty 1: corrosion-enhanced erosion was shown to be caused by the corrosion of work-hardened layers and subsurface cracking

Corrosion-enhanced erosion was measured in SIJ tests and was much more significant than erosion-enhanced corrosion in the conditions investigated, something that has also been observed on other occasions in erosion-corrosion research. This thesis provided much more understanding about the mechanisms of the interactions between erosion and corrosion, as relatively little research has been completed that has fully investigated the mechanisms of corrosion-enhanced erosion of active materials. Work-hardened layers produced after particle impact were much thicker in erosion conditions than in erosion-corrosion conditions, as removal of the layers through corrosion mechanisms limited the growth and refinement of nano-grain and micro-grain layers. This exposed underlying softer material with less erosion resistance, increasing erosion rates. Subsurface cracks were also observed in the nano-grain layers of erosion-corrosion samples. It was likely that cracks were formed either as a result of embrittlement of nano-grain layers, through a low cycle fatigue degradation mechanism or a combination of both. The cracks

prevented the growth of work-hardened layers. Erosion rates could have also been enhanced by cracking due to weakening of the grains near the surface.

Reducing the effects of erosion is critical for industry in high velocity, high sand concentration pipe flows. Erosion components were shown to have a significant influence on degradation rates. Corrosion inhibitors have been shown to be very effective at reducing corrosion rates. One possible method to reduce erosion-corrosion rates is to use corrosion inhibitors that reduce the material removal caused by particle impacts in addition to corrosion inhibition. The inhibitors tested in this thesis did not show particularly effective performance in sand-containing flows, in terms of reducing erosion damage, whilst other inhibitors reported in literature have shown to reduce erosion rates. Reducing the contribution of erosion wear would also likely reduce the contribution of corrosion-enhanced erosion to total degradation rates.

Novelty 2: design of an elbow for erosion-corrosion tests

The elbow designed was useful for completing erosion-corrosion testing in a more relevant flow geometry to oil and gas pipe flow. Particle impact angles on the surface of a sample in the SIJ did not fully represent conditions in the designed elbow. The elbow could be used for a range of tests in different conditions, more relevant to the industrial problem of erosion-corrosion. The design could also easily be modified to test in different conditions, if required, due to the use of 3D printing to manufacture the elbow. Some limitations of the current design were reported, as electrochemistry measurements contained error that was significant in the results gained in the conditions tested and surface analysis could not be completed as easily due to the sample geometry. The use of the SIJ can overcome these issues and conditions in the SIJ can easily be changed. However, if field conditions cannot easily be replicated in the SIJ, it is highly recommended that a more representative geometry is designed, using the methodology reported in this thesis for erosion-corrosion evaluation.

Novelty 3: development of a new methodology for erosion-corrosion analysis

CFD was used to predict mass transfer coefficients, particle impact angles and impact velocities in the SIJ and the elbow. Whilst CFD has been used on some occasions before to predict mass transfer coefficients, the success of the models was limited by the methodology used. Prediction of particle trajectories has also been completed before to predict erosion rates in different flow geometries. However, despite some limitations in using CFD for

particle trajectory predictions, due to the significance of the assumptions required when modelling, it has been shown to be accurate and reliable for erosion analysis. Particle impact angles and particle impact velocities were predicted, rather than erosion rates, to define the general conditions in regions of test specimens in the SIJ and elbow and mass transfer coefficients were predicted successfully in different geometries. The aim for the future would be to use this methodology to accurately represent a particular erosion-corrosion problem in the field. For example, the particle impact angles and impact velocities could be replicated more precisely using the SIJ to provide a representative understanding of erosion-corrosion mechanisms that would occur in the field. Erosion-corrosion tests completed that compare parameters such as flow velocity and nominal impact angle are useful, but it is difficult to make comparisons between applications if they are not fully understood or defined. Therefore, a more general understanding of erosion-corrosion could be achieved by defining erosion-corrosion conditions thoroughly using the methodology suggested. This method could also be extended to the development of erosion-corrosion models in the future, as for a known impact angle, impact velocity and mass transfer coefficient in the SIJ, a thickness loss can be determined.

10.3 Future Work

Four key areas of future work are recommended to improve the understanding of erosion-corrosion of carbon steel in CO_2 oil and gas pipe flow conditions, shown in Figure 10.1.

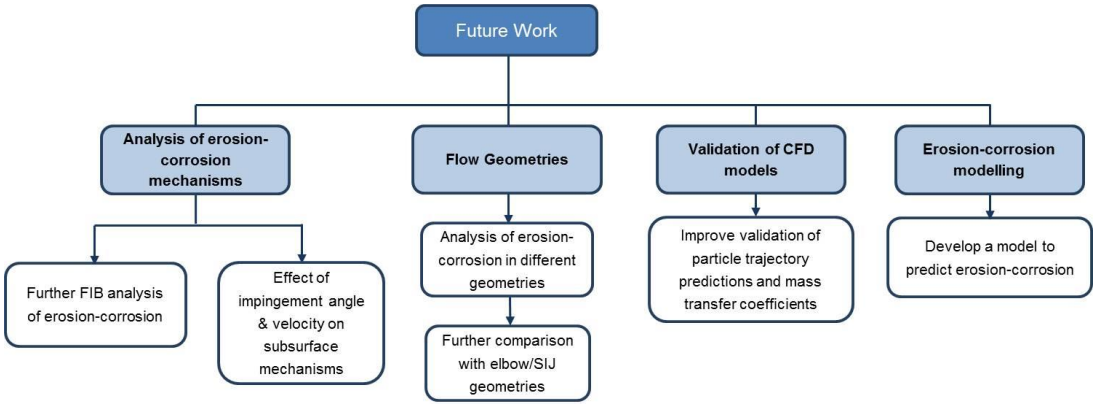

Figure 10.1 Future work suggestions in the field of erosion-corrosion of carbon steel in oil and gas conditions

One of the current major limitations in erosion-corrosion research is a lack of the influence of understanding of particle impact angles and impact velocities

on the surface of the target material in fluid flow environments. The use of CFD is an effective method to determine the flow of particles through different flow geometries, but validation of the models is challenging. Particle imaging velocimetry and laser Doppler velocimetry have been shown to be effective at measuring the position of particles. However, it is uncertain how effective they are in high sand concentrations, high velocity flows. Acoustic emission monitoring has also been shown to be useful for detecting particle impact energy [144, 145]. The combination of acoustic emission techniques, particle imaging techniques and CFD could potentially give more understanding about the nature of impacts of sand particles on carbon steel samples used in SIJ or elbow tests. Validation of mass transfer coefficients would also prove the reliability of using CFD to define erosion-corrosion flow effects.

Mathematical models of erosion-corrosion are lacking, and there is currently no reliable method of predicting erosion-corrosion rates of carbon steel in a wide range of conditions. The use of mass transfer coefficients and particle impact predictions could be beneficial for the development of an erosion-corrosion model, as knowledge of impact velocities and impact angles are essential for erosion modelling and corrosion rates, under certain conditions, can be defined by the mass transfer coefficient. Existing erosion and corrosion models are likely to be capable of predicting the pure erosion and flow-induced corrosion terms, but do not account for the interactions between erosion and corrosion. A model could be developed to predict the thickness loss for a known impact angle, impact velocity and mass transfer coefficient, determined using CFD, on the surface of an SIJ sample. Predicting the removal of work-hardened layers and rate of grain refinement could potentially enable a reliable prediction of corrosion-enhanced erosion, but more research is required to understand the mechanisms of corrosion-enhanced erosion at different impact angles and impact velocities in addition to the high impact angle analysis completed in this thesis. Further analysis of carbon steel surfaces using FIB at a range of different impact angles and impact velocities could help to understand the erosion-corrosion mechanisms in a wider range of conditions.

References

1. Salama, M.M., *Sand Production Management.* Journal of Energy Resources Technology, 2000. **122**(1): p. 29-33.
2. Chen, X., B.S. McLaury, and S.A. Shirazi, *Application and experimental validation of a computational fluid dynamics (CFD)-based erosion prediction model in elbows and plugged tees.* Computers & Fluids, 2004. **33**(10): p. 1251-1272.
3. Nešić, S., *Key issues related to modelling of internal corrosion of oil and gas pipelines – A review.* Corrosion Science, 2007. **49**(12): p. 4308-4338.
4. Humphrey, J.A.C., *Fundamentals of fluid motion in erosion by solid particle impact.* International Journal of Heat and Fluid Flow, 1990. **11**(3): p. 170-195.
5. Kermani, M. and A. Morshed, *Carbon dioxide corrosion in oil and gas production - A compendium.* Corrosion, 2003. **59**(8): p. 659-683.
6. Neville, A. and C. Wang, *Erosion–corrosion of engineering steels - Can it be managed by use of chemicals?* Wear, 2009. **267**(11): p. 2018-2026.
7. Schmitt, G., T. Simon, and R. Hausler. *CO_2 Erosion Corrosion and its Inhibition Under Extreme Shear Stress II. Performance of Inhibitors*. in *CORROSION/93*. 1993. Houston, TX: NACE International.
8. Burson-Thomas, C.B. and R.J. Wood, *Developments in Erosion–Corrosion Over the Past 10 Years.* Journal of Bio-and Tribo-Corrosion, 2017. **3**(2): p. 14.
9. Kermani, M. and D. Harr, *The impact of corrosion on oil and gas industry.* SPE Production & Facilities, 1996. **11**(3): p. 186-190.
10. Parsi, M., K. Najmi, F. Najafifard, S. Hassani, B.S. McLaury, and S.A. Shirazi, *A comprehensive review of solid particle erosion modeling for oil and gas wells and pipelines applications.* Journal of Natural Gas Science and Engineering, 2014. **21**: p. 850-873.
11. Salama, M.M., *Influence of sand production on design and operations of piping systems*, in *CORROSION 2000*. 2000, NACE International: Orlando, FL.
12. Dugstad, A., *Fundamental aspects of CO_2 metal loss corrosion-part 1: mechanism*, in *CORROSION 2006*. 2006, NACE International: San Diego, CA.
13. Versteeg, H.K. and W. Malalasekera, *An introduction to computational fluid dynamics: the finite volume method*. 2007, Harlow: Pearson Education.
14. Neville, A., M. Reyes, and H. Xu, *Examining corrosion effects and corrosion/erosion interactions on metallic materials in aqueous slurries.* Tribology International, 2002. **35**(10): p. 643-650.
15. Wood, R.J.K. and S.P. Hutton, *The synergistic effect of erosion and corrosion: trends in published results.* Wear, 1990. **140**(2): p. 387-394.
16. Hutchings, I.M. and P. Shipway, *Tribology: Friction and Wear of Engineering Materials*. 2nd ed. 2017, London: Butterworth-Heinemann.
17. Finnie, I., *Erosion of surfaces by solid particles.* Wear, 1960. **3**(2): p. 87-103.
18. Finnie, I., *Some observations on the erosion of ductile metals.* Wear, 1972. **19**(1): p. 81-90.

19. Bitter, J.G.A., *A study of erosion phenomena part I.* Wear, 1963. **6**(1): p. 5-21.
20. Bitter, J.G.A., *A study of erosion phenomena: Part II.* Wear, 1963. **6**(3): p. 169-190.
21. Sheldon, G., *Similarities and differences in the erosion behavior of materials.* Journal of Basic Engineering, 1970. **92**(3): p. 619-626.
22. Revie, R.W. and H.H. Uhlig, *Corrosion and Corrosion Control*. 4th ed. 2008, Hoboken, NJ: Wiley.
23. Papavinasam, S., *Corrosion control in the oil and gas industry*. 2013, Amsterdam: Elsevier.
24. Tait, W.S., *An introduction to electrochemical corrosion testing for practicing engineers and scientists*. 1994, Racine, WI: Pair O Docs Publications.
25. Stansbury, E.E. and R.A. Buchanan, *Fundamentals of electrochemical corrosion*. 2000, Materials Park, OH: ASM international.
26. Perez, N., *Electrochemistry and corrosion science*. 2004, London: Kluwer Academic.
27. Tu, J., G.H. Yeoh, and C. Liu, *Computational fluid dynamics: a practical approach*. 2nd ed. 2012, Boston: Butterworth-Heinemann.
28. Efird, K.D., *Jet impingement testing for flow accelerated corrosion*, in *CORROSION 2000*. 2000, NACE International: Orlando, FL.
29. Efird, K.D., *Flow accelerated corrosion testing basics*, in *CORROSION 2006*. 2006, NACE International: San Diego, CA.
30. Nešić, S., G.T. Solvi, and J. Enerhaug, *Comparison of the Rotating Cylinder and Pipe Flow Tests for Flow-Sensitive Carbon Dioxide Corrosion.* Corrosion, 1995. **51**(10): p. 773-787.
31. Nesic, S., G.T. Solvi, and S. Skjerve, *Comparison of rotating cylinder and loop methods for testing CO_2 corrosion inhibitors.* British Corrosion Journal, 1997. **32**(4): p. 269-276.
32. API, *API RP 14E Recommended Practice for Design and Installation of Offshore Production Platform Piping Systems, third ed*. 1981, American Petroleum Institute: Washington, DC. p. 22.
33. Salama, M.M., *An Alternative to API 14E Erosional Velocity Limits for Sand-Laden Fluids.* Journal of Energy Resources Technology, 2000. **122**(2): p. 71-77.
34. Hu, X. and A. Neville, *CO_2 erosion–corrosion of pipeline steel (API X65) in oil and gas conditions - A systematic approach.* Wear, 2009. **267**(11): p. 2027-2032.
35. Barker, R.J. 2017. *Erosion-corrosion of carbon steel pipework on an offshore oil and gas facility*. Ph.D. thesis, University of Leeds.
36. Efird, K., E. Wright, J. Boros, and T. Hailey, *Correlation of steel corrosion in pipe flow with jet impingement and rotating cylinder tests.* Corrosion, 1993. **49**(12): p. 992-1003.
37. Nesic, S., J. Postlethwaite, and S. Olsen, *An electrochemical model for prediction of corrosion of mild steel in aqueous carbon dioxide solutions.* Corrosion, 1996. **52**(4): p. 280-294.
38. Schmitt, G. and M. Horstemeier, *Fundamental aspects of CO_2 metal loss corrosion - Part II: Influence of different parameters on CO_2 corrosion mechanisms*, in *CORROSION 2006*. 2006, NACE Interational: San Diego, CA.

39. Tran, T., B. Brown, and S. Nesic, *Corrosion of mild steel in an aqueous CO_2 environment - basic electrochemical mechanisms revisited*, in *CORROSION 2015*. 2015, NACE International: Dallas, TX.
40. De Waard, C. and D.E. Milliams, *Carbonic Acid Corrosion of Steel.* Corrosion, 1975. **31**(5): p. 177-181.
41. Burkle, D.P. 2017. *Understanding the Formation of Protective $FeCO_3$ on to Carbon Steel Pipelines during CO_2 Corrosion*. Ph.D. thesis, University of Leeds.
42. Burkle, D., R. De Motte, W. Taleb, A. Kleppe, T. Comyn, S. Vargas, A. Neville, and R. Barker, *In situ SR-XRD study of $FeCO_3$ precipitation kinetics onto carbon steel in CO_2-containing environments: The influence of brine pH.* Electrochimica Acta, 2017. **255**: p. 127-144.
43. Bockris, J.M., D. Drazic, and A. Despic, *The electrode kinetics of the deposition and dissolution of iron.* Electrochimica Acta, 1961. **4**(2-4): p. 325-361.
44. Nesic, S., N. Thevenot, J.-L. Crolet, and D. Drazic, *Electrochemical properties of iron dissolution in the presence of CO_2 - basics revisited*, in *CORROSION 96*. 1996, NACE International: Houston, TX.
45. Hua, Y., R. Barker, T. Charpentier, M. Ward, and A. Neville, *Relating iron carbonate morphology to corrosion characteristics for water-saturated supercritical CO_2 systems.* The Journal of Supercritical Fluids, 2015. **98**: p. 183-193.
46. Sun, W. and S. Nešic, *Kinetics of corrosion layer formation: part 1 - iron carbonate layers in carbon dioxide corrosion.* CORROSION, 2008. **64**(4): p. 334-346.
47. Akbar, A., X. Hu, C. Wang, and A. Neville. *The influence of flow rate, sand and inhibitor on iron carbonate scales under erosion-corrosion conditions using a submerged impingement jet*. in *CORROSION 2012*. 2012. Salt Lake City, UT: NACE International.
48. Al-Aithan, G., F. Al-Mutahar, J. Shadley, S. Shirazi, E. Rybicki, and K. Roberts. *A Mechanistic Erosion-Corrosion Model for Predicting Iron Carbonate ($FeCO_3$) Scale Thickness in a CO_2 Environment with Sand*. in *CORROSION 2014*. 2014. San Antonio, TX: NACE International.
49. Malka, R., S. Nešić, and D.A. Gulino, *Erosion–corrosion and synergistic effects in disturbed liquid-particle flow.* Wear, 2007. **262**(7–8): p. 791-799.
50. Poulson, B., *Advances in understanding hydrodynamic effects on corrosion.* Corrosion Science, 1993. **35**(1–4): p. 655-665.
51. Gulbrandsen, E. and A. Grana, *Testing of Carbon Dioxide Corrosion Inhibitor Performance at High Flow Velocities in Jet Impingement Geometry. Effects of Mass Transfer and Flow Forces.* CORROSION, 2007. **63**(11): p. 1009-1020.
52. Silverman, D., *The rotating cylinder electrode for examining velocity-sensitive corrosion-a review.* CORROSION, 2004. **60**(11): p. 1003-1023.
53. Silverman, D.C., *Rotating Cylinder Electrode - Geometry Relationships for Prediction of Velocity-Sensitive Corrosion.* CORROSION, 1988. **44**(1): p. 42-49.
54. Silverman, D.C., *Technical Note: Conditions for Similarity of Mass-Transfer Coefficients and Fluid Shear Stresses between the Rotating Cylinder Electrode and Pipe.* CORROSION, 2005. **61**(6): p. 515-518.

55. Berger, F.P. and K.F.F.L. Hau, *Mass transfer in turbulent pipe flow measured by the electrochemical method.* International Journal of Heat and Mass Transfer, 1977. **20**(11): p. 1185-1194.
56. Eisenberg, M., C. Tobias, and C. Wilke, *Ionic mass transfer and concentration polarization at rotating electrodes.* Journal of the Electrochemical Society, 1954. **101**(6): p. 306-320.
57. Neville, A., S. Ramachandran, and V. Jovancicevic, *Erosion-Corrosion Mitigation Using Chemicals*, in *CORROSION 2003*. 2003, NACE International: San Diego, CA.
58. Aribo, S., R. Barker, X. Hu, and A. Neville, *Erosion–corrosion behaviour of lean duplex stainless steels in 3.5% NaCl solution.* Wear, 2013. **302**(1): p. 1602-1608.
59. Barik, R.C., J.A. Wharton, R.J.K. Wood, and K.R. Stokes, *Electro-mechanical interactions during erosion–corrosion.* Wear, 2009. **267**(11): p. 1900-1908.
60. Barker, R., X. Hu, A. Neville, and S. Cushnaghan, *Inhibition of flow-induced corrosion and erosion-corrosion for carbon steel pipe work from an offshore oil and gas facility.* Corrosion, 2012. **69**(2): p. 193-203.
61. Hu, X., R. Barker, A. Neville, and A. Gnanavelu, *Case study on erosion–corrosion degradation of pipework located on an offshore oil and gas facility.* Wear, 2011. **271**(9): p. 1295-1301.
62. Neville, A. and C. Wang, *Erosion–corrosion mitigation by corrosion inhibitors—An assessment of mechanisms.* Wear, 2009. **267**(1–4): p. 195-203.
63. Neville, A. and C. Wang, *Study of the Effect of Inhibitors on Erosion-Corrosion in CO_2-Saturated Condition with Sand.* SPE Projects Facilities & Construction, 2009. **4**(01): p. 1-10.
64. Giralt, F., C.-J. Chia, and O. Trass, *Characterization of the impingement region in an axisymmetric turbulent jet.* Industrial & Engineering Chemistry Fundamentals, 1977. **16**(1): p. 21-28.
65. Poreh, M., Y. Tsuei, and J.E. Cermak, *Investigation of a turbulent radial wall jet.* Journal of Applied Mechanics, 1967. **34**(2): p. 457-463.
66. Keating, A. and S. Nešić, *Numerical prediction of erosion-corrosion in bends.* CORROSION, 2001. **57**(7): p. 621-633.
67. Wang, J., S. Shirazi, J. Shadley, E. Rybicki, and E. Dayalan, *A correlation for mass transfer coefficients in elbows*, in *CORROSION 98*. 1998, NACE International: San Diego, CA.
68. El-Gammal, M., H. Mazhar, J.S. Cotton, C. Shefski, J. Pietralik, and C.Y. Ching, *The hydrodynamic effects of single-phase flow on flow accelerated corrosion in a 90-degree elbow.* Nuclear Engineering and Design, 2010. **240**(6): p. 1589-1598.
69. Keshtkar, K., M. Nematollahi, and A. Erfaninia, *CFX study of flow accelerated corrosion via mass transfer coefficient calculation in a double elbow.* International Journal of Hydrogen Energy, 2016. **41**(17): p. 7036-7046.
70. Srinivasan, V., *Evaluation of Flow Coupled CO_2 Corrosion Using CFD: Kinetics & Hydrodynamics*, in *CORROSION 2015*. 2015, NACE International: Dallas, TX.
71. Cañizares, P., J. García-Gómez, I.F. de Marcos, M. Rodrigo, and J. Lobato, *Measurement of mass-transfer coefficients by an*

electrochemical technique. Journal of Chemical Education, 2006. **83**(8): p. 1204.
72. Hutchings, I. and R. Winter, *The erosion of ductile metals by spherical particles.* Journal of Physics D: Applied Physics, 1975. **8**(1): p. 8.
73. Hutchings, I.M., *A model for the erosion of metals by spherical particles at normal incidence.* Wear, 1981. **70**(3): p. 269-281.
74. Hutchings, I.M. and R.E. Winter, *Particle erosion of ductile metals: a mechanism of material removal.* Wear, 1974. **27**(1): p. 121-128.
75. Clark, H.M., *On the impact rate and impact energy of particles in a slurry pot erosion tester.* Wear, 1991. **147**(1): p. 165-183.
76. Levy, A.V., *The solid particle erosion behavior of steel as a function of microstructure.* Wear, 1981. **68**(3): p. 269-287.
77. Clark, H.M. and L.C. Burmeister, *The influence of the squeeze film on particle impact velocities in erosion.* International Journal of Impact Engineering, 1992. **12**(3): p. 415-426.
78. Clark, H.M. and K.K. Wong, *Impact angle, particle energy and mass loss in erosion by dilute slurries.* Wear, 1995. **186–187, Part 2**(0): p. 454-464.
79. Finnie, I., *Some reflections on the past and future of erosion.* Wear, 1995. **186**: p. 1-10.
80. Finnie, I., G.R. Stevick, and J.R. Ridgely, *The influence of impingement angle on the erosion of ductile metals by angular abrasive particles.* Wear, 1992. **152**(1): p. 91-98.
81. Hutchings, I. and A. Levy, *Thermal effects in the erosion of ductile metals.* Wear, 1989. **131**(1): p. 105-121.
82. Kesana, N.R., J.M. Throneberry, B.S. McLaury, S.A. Shirazi, and E.F. Rybicki, *Effect of Particle Size and Liquid Viscosity on Erosion in Annular and Slug Flow.* Journal of Energy Resources Technology, 2013. **136**(1): p. 012901-012901.
83. Lynn, R.S., K.K. Wong, and H.M. Clark, *On the particle size effect in slurry erosion.* Wear, 1991. **149**(1-2): p. 55-71.
84. McCabe, L.P., G.A. Sargent, and H. Conrad, *Effect of microstructure on the erosion of steel by solid particles.* Wear, 1985. **105**(3): p. 257-277.
85. Oka, Y.I., M. Matsumura, and T. Kawabata, *Relationship between surface hardness and erosion damage caused by solid particle impact.* Wear, 1993. **162**: p. 688-695.
86. Oka, Y.I. and T. Yoshida, *Practical estimation of erosion damage caused by solid particle impact: Part 2: Mechanical properties of materials directly associated with erosion damage.* Wear, 2005. **259**(1): p. 102-109.
87. Shirazi, S.A., J.R. Shadley, B.S. McLaury, and E.F. Rybicki, *A Procedure to Predict Solid Particle Erosion in Elbows and Tees.* Journal of Pressure Vessel Technology, 1995. **117**(1): p. 45-52.
88. Okita, R., Y. Zhang, B.S. McLaury, and S.A. Shirazi, *Experimental and Computational Investigations to Evaluate the Effects of Fluid Viscosity and Particle Size on Erosion Damage.* Journal of Fluids Engineering, 2012. **134**(6): p. 061301-061301.
89. Wood, R.J.K., Y. Puget, K.R. Trethewey, and K. Stokes, *The performance of marine coatings and pipe materials under fluid-borne sand erosion.* Wear, 1998. **219**(1): p. 46-59.

90. Levy, A.V., *The platelet mechanism of erosion of ductile metals.* Wear, 1986. **108**(1): p. 1-21.
91. Hutchings, I., *Prediction of the resistance of metals to erosion by solid particles.* Wear, 1975. **35**(2): p. 371-374.
92. Levy, A.V. and P. Yau, *Erosion of steels in liquid slurries.* Wear, 1984. **98**: p. 163-182.
93. Adler, W.F., *Assessment of the State of Knowledge Pertaining to Solid Particle Erosion*. 1979, Santa Barbara, CA: Effects Technology Inc.
94. Dosanjh, S. and J.A.C. Humphrey, *The influence of turbulence on erosion by a particle-laden fluid jet.* Wear, 1985. **102**(4): p. 309-330.
95. Brown, G., *Erosion prediction in slurry pipeline tee-junctions.* Applied Mathematical Modelling, 2002. **26**(2): p. 155-170.
96. Hutchings, I., *Wear by particulates.* Chemical Engineering Science, 1987. **42**(4): p. 869-878.
97. Wong, K.K. and H.M. Clark, *A model of particle velocities and trajectories in a slurry pot erosion tester.* Wear, 1993. **160**(1): p. 95-104.
98. Oka, Y.I., M. Nishimura, K. Nagahashi, and M. Matsumura, *Control and evaluation of particle impact conditions in a sand erosion test facility.* Wear, 2001. **250**(1): p. 736-743.
99. Clark, H.M., *The influence of the squeeze film in slurry erosion.* Wear, 2004. **256**(9): p. 918-926.
100. Douglas, J.F., J.M. Gasiorek, J.A. Swaffield, and L.B. Jack, *Fluid Mechanics*. 5th ed. 2005, Harlow: Pearson/Prentice Hall.
101. Shirazi, S.A., B.S. McLaury, and M. Ali, *Sand monitor evaluation in multiphase flow*, in *CORROSION 2000*. 2000, NACE International: Orlando, FL.
102. Kesana, N.R., R. Vieira, B.S. McLaury, and S.A. Shirazi, *Experimental Study of Sand Particle Concentration Profiles in Straight and Pipe Elbow for Horizontal Multiphase Flows.* Journal of Energy Resources Technology, 2014. **136**(3): p. 033001-033001.
103. Tilly, G. and W. Sage, *The interaction of particle and material behaviour in erosion processes.* Wear, 1970. **16**(6): p. 447-465.
104. Hu, X. 2003. *The corrosion and erosion-corrosion behaviour of high alloy stainless steels*, in *Department of Mechanical and Chemical Engineering*. Ph.D. thesis, Heriot-Watt University.
105. Gnanavelu, A.B. 2010. *A geometry independent integrated method to predict erosion wear rates in a slurry environment*. Ph.D. thesis, University of Leeds.
106. Levy, A.V. and P. Chik, *The effects of erodent composition and shape on the erosion of steel.* Wear, 1983. **89**(2): p. 151-162.
107. Brown, R., S. Kosco, and E. Jun, *The effect of particle shape and size on erosion of aluminum alloy 1100 at 90^{o} impact angles.* Wear, 1983. **88**(2): p. 181-193.
108. Rajahram, S.S., T.J. Harvey, J.C. Walker, S.C. Wang, R.J.K. Wood, and G. Lalev, *A study on the evolution of surface and subsurface wear of UNS S31603 during erosion–corrosion.* Wear, 2011. **271**(9–10): p. 1302-1313.
109. McLaury, B.S. and S.A. Shirazi, *An Alternate Method to API RP 14E for Predicting Solids Erosion in Multiphase Flow.* Journal of Energy Resources Technology, 2000. **122**(3): p. 115-122.

110. Chen, X., B.S. McLaury, and S.A. Shirazi, *Numerical and experimental investigation of the relative erosion severity between plugged tees and elbows in dilute gas/solid two-phase flow.* Wear, 2006. **261**(7–8): p. 715-729.
111. Mulhearn, T. and L. Samuels, *The abrasion of metals: a model of the process.* Wear, 1962. **5**(6): p. 478-498.
112. Stack, M.M., S.M. Abdelrahman, and B.D. Jana, *A new methodology for modelling erosion–corrosion regimes on real surfaces: Gliding down the galvanic series for a range of metal-corrosion systems.* Wear, 2010. **268**(3–4): p. 533-542.
113. Arabnejad, H., A. Mansouri, S. Shirazi, and B. McLaury, *Development of mechanistic erosion equation for solid particles.* Wear, 2015. **332**: p. 1044-1050.
114. Ahlert, K.R. 1994. *Effects of particle impingement angle and surface wetting on solid particle erosion of AISI 1018 steel*. Ph.D. thesis, University of Tulsa.
115. McLaury, B.S., E.F. Rybicki, S.A. Shirazi, and J.R. Shadley, *How operating and environmental conditions affect erosion.* CORROSION 99, 1999.
116. Edwards, J.K., B.S. McLaury, and S.A. Shirazi, *Modeling Solid Particle Erosion in Elbows and Plugged Tees.* Journal of Energy Resources Technology, 2001. **123**(4): p. 277-284.
117. McLaury, B.S., S.A. Shirazi, and T.L. Burden, *Effect of Entrance Shape on Erosion in the Throat of Chokes.* Journal of Energy Resources Technology, 2000. **122**(4): p. 198-204.
118. Oka, Y.I., K. Okamura, and T. Yoshida, *Practical estimation of erosion damage caused by solid particle impact: Part 1: Effects of impact parameters on a predictive equation.* Wear, 2005. **259**(1): p. 95-101.
119. Mazumder, Q.H., S.A. Shirazi, and B.S. McLaury, *A Mechanistic Model to Predict Erosion in Multiphase Flow in Elbows Downstream of Vertical Pipes*, in *CORROSION 2004*. 2004, NACE International: New Orleans, LA.
120. Gnanavelu, A., N. Kapur, A. Neville, and J.F. Flores, *An integrated methodology for predicting material wear rates due to erosion.* Wear, 2009. **267**(11): p. 1935-1944.
121. Mansouri, A., H. Arabnejad, S. Karimi, S.A. Shirazi, and B.S. McLaury, *Improved CFD modeling and validation of erosion damage due to fine sand particles.* Wear, 2015. **338–339**: p. 339-350.
122. Mansouri, A., H. Arabnejad, S.A. Shirazi, and B.S. McLaury, *A combined CFD/experimental methodology for erosion prediction.* Wear, 2015. **332–333**: p. 1090-1097.
123. Vieira, R.E., A. Mansouri, B.S. McLaury, and S.A. Shirazi, *Experimental and computational study of erosion in elbows due to sand particles in air flow.* Powder Technology, 2016. **288**: p. 339-353.
124. Zhang, Y., B.S. McLaury, S.A. Shirazi, and E.F. Rybicki, *A two-dimensional mechanistic model for sand erosion prediction including particle impact characteristics*, in *CORROSION 2010*. 2010, NACE International: San Antonio, TX.
125. Clift, R., J.R. Grace, and M.E. Weber, *Bubbles, drops, and particles*. 1978, London: Academic Press.

126. Zhao, B., C. Yang, X. Yang, and S. Liu, *Particle dispersion and deposition in ventilated rooms: Testing and evaluation of different Eulerian and Lagrangian models.* Building and Environment, 2008. **43**(4): p. 388-397.
127. Zhao, B., Y. Zhang, X. Li, X. Yang, and D. Huang, *Comparison of indoor aerosol particle concentration and deposition in different ventilated rooms by numerical method.* Building and Environment, 2004. **39**(1): p. 1-8.
128. Nešič, S. and J. Postlethwaite, *Hydrodynamics of disturbed flow and erosion–corrosion. Part II - Two-phase flow study.* The Canadian Journal of Chemical Engineering, 1991. **69**(3): p. 704-710.
129. Njobuenwu, D.O. and M. Fairweather, *Modelling of pipe bend erosion by dilute particle suspensions.* Computers & Chemical Engineering, 2012. **42**(0): p. 235-247.
130. Elghobashi, S. and G. Truesdell, *Direct simulation of particle dispersion in a decaying isotropic turbulence.* Journal of Fluid Mechanics, 1992. **242**: p. 655-700.
131. Berlemont, A., P. Desjonqueres, and G. Gouesbet, *Particle Lagrangian simulation in turbulent flows.* International Journal of Multiphase Flow, 1990. **16**(1): p. 19-34.
132. Meng, H. and C. Van der Geld, *Particle trajectory computations in steady non-uniform liquid flows.* ASME, Fluids Engineering Division, 1991. **118**: p. 183-193.
133. Elghobashi, S., *On predicting particle-laden turbulent flows.* Applied scientific research, 1994. **52**(4): p. 309-329.
134. Bozzini, B., M.E. Ricotti, M. Boniardi, and C. Mele, *Evaluation of erosion–corrosion in multiphase flow via CFD and experimental analysis.* Wear, 2003. **255**(1–6): p. 237-245.
135. Zhang, Y., B.S. McLaury, and S.A. Shirazi, *Improvements of Particle Near-Wall Velocity and Erosion Predictions Using a Commercial CFD Code.* Journal of Fluids Engineering, 2009. **131**(3): p. 031303-1-031303-9.
136. Grant, G. and W. Tabakoff, *Erosion prediction in turbomachinery resulting from environmental solid particles.* Journal of Aircraft, 1975. **12**(5): p. 471-478.
137. Forder, A., M. Thew, and D. Harrison, *A numerical investigation of solid particle erosion experienced within oilfield control valves.* Wear, 1998. **216**(2): p. 184-193.
138. Rajahram, S., T. Harvey, and R. Wood, *Full factorial investigation on the erosion–corrosion resistance of UNS S31603.* Tribology International, 2010. **43**(11): p. 2072-2083.
139. Rajahram, S.S., T.J. Harvey, J.C. Walker, S.C. Wang, and R.J.K. Wood, *Investigation of erosion–corrosion mechanisms of UNS S31603 using FIB and TEM.* Tribology International, 2012. **46**(1): p. 161-173.
140. Rajahram, S.S., T.J. Harvey, and R.J.K. Wood, *Erosion–corrosion resistance of engineering materials in various test conditions.* Wear, 2009. **267**(1–4): p. 244-254.
141. Wood, R.J.K., *Erosion–corrosion interactions and their effect on marine and offshore materials.* Wear, 2006. **261**(9): p. 1012-1023.
142. Wood, R.J.K., J.C. Walker, T.J. Harvey, S. Wang, and S.S. Rajahram, *Influence of microstructure on the erosion and erosion–corrosion*

characteristics of 316 stainless steel. Wear, 2013. **306**(1–2): p. 254-262.
143. Hu, X., K. Alzawai, A. Gnanavelu, A. Neville, C. Wang, A. Crossland, and J. Martin, *Assessing the effect of corrosion inhibitor on erosion–corrosion of API-5L-X65 in multi-phase jet impingement conditions.* Wear, 2011. **271**(9–10): p. 1432-1437.
144. Ukpai, J.I., R. Barker, X. Hu, and A. Neville, *Exploring the erosive wear of X65 carbon steel by acoustic emission method.* Wear, 2013. **301**(1): p. 370-382.
145. Ukpai, J.I., R. Barker, X. Hu, and A. Neville, *Determination of particle impacts and impact energy in the erosion of X65 carbon steel using acoustic emission technique.* Tribology International, 2013. **65**(0): p. 161-170.
146. Wang, C., A. Neville, and S. Ramachandran. *Understanding Inhibitor Action on Components of Erosion Corrosion and their Interactions in CO2-Containing Slurries*. in *SPE International Symposium on Oilfield Corrosion*. 2004. Society of Petroleum Engineers.
147. Shadley, J.R., E.F. Rybicki, S.A. Shirazi, and E. Dayalan, *Velocity Guidelines for Avoiding Erosion-Corrosion Damage in Sweet Production With Sand.* Journal of Energy Resources Technology, 1998. **120**(1): p. 78-83.
148. Shadley, J.R., S.A. Shirazi, E. Dayalan, M. Ismail, and E.F. Rybicki, *Erosion-Corrosion of a Carbon Steel Elbow in a Carbon Dioxide Environment.* CORROSION, 1996. **52**(9): p. 714-723.
149. Islam, M.A. and Z. Farhat, *Erosion-corrosion mechanism and comparison of erosion-corrosion performance of API steels.* Wear, 2017. **376–377, Part A**: p. 533-541.
150. Zhou, S., M. Stack, and R. Newman, *Characterization of synergistic effects between erosion and corrosion in an aqueous environment using electrochemical techniques.* CORROSION, 1996. **52**(12): p. 934-946.
151. Stack, M.M. and S.M. Abdelrahman, *A CFD model of particle concentration effects on erosion–corrosion of Fe in aqueous conditions.* Wear, 2011. **273**(1): p. 38-42.
152. Stack, M.M. and G.H. Abdulrahman, *Mapping erosion-corrosion of carbon steel in oil exploration conditions: Some new approaches to characterizing mechanisms and synergies.* Tribology International, 2010. **43**(7): p. 1268-1277.
153. Stack, M.M. and G.H. Abdulrahman, *Mapping erosion–corrosion of carbon steel in oil–water solutions: Effects of velocity and applied potential.* Wear, 2012. **274–275**: p. 401-413.
154. Stack, M.M., N. Corlett, and S. Turgoose, *Some recent advances in the development of theoretical approaches for the construction of erosion–corrosion maps in aqueous conditions.* Wear, 1999. **233–235**: p. 535-541.
155. Stack, M.M., N. Corlett, and S. Zhou, *A methodology for the construction of the erosion-corrosion map in aqueous environments.* Wear, 1997. **203–204**: p. 474-488.
156. Stack, M.M., N. Corlett, and S. Zhou, *Impact angle effects on the transition boundaries of the aqueous erosion–corrosion map.* Wear, 1999. **225–229, Part 1**: p. 190-198.

157. Stack, M.M. and B.D. Jana, *Modelling particulate erosion–corrosion in aqueous slurries: some views on the construction of erosion–corrosion maps for a range of pure metals.* Wear, 2004. **256**(9–10): p. 986-1004.
158. Stack, M.M., S. Lekatos, and F.H. Stott, *Erosion-corrosion regimes: number, nomenclature and justification?* Tribology International, 1995. **28**(7): p. 445-451.
159. Stack, M.M. and N. Pungwiwat, *Erosion–corrosion mapping of Fe in aqueous slurries: some views on a new rationale for defining the erosion–corrosion interaction.* Wear, 2004. **256**(5): p. 565-576.
160. Stack, M.M. and F.H. Stott, *An approach to modelling erosion-corrosion of alloys using erosion-corrosion maps.* Corrosion Science, 1993. **35**(5–8): p. 1027-1034.
161. Stack, M.M., S. Zhou, and R.C. Newman, *Identification of transitions in erosion-corrosion regimes in aqueous environments.* Wear, 1995. **186–187, Part 2**: p. 523-532.
162. Li, W. and D.Y. Li, *Influence of surface morphology on corrosion and electronic behavior.* Acta Materialia, 2006. **54**(2): p. 445-452.
163. Islam, M.A. and Z.N. Farhat, *The synergistic effect between erosion and corrosion of API pipeline in CO_2 and saline medium.* Tribology International, 2013. **68**(0): p. 26-34.
164. Guo, H.X., B.T. Lu, and J.L. Luo, *Interaction of mechanical and electrochemical factors in erosion–corrosion of carbon steel.* Electrochimica Acta, 2005. **51**(2): p. 315-323.
165. Ashby, M.F. and D.R. Jones, *Engineering materials 1: an introduction to properties, applications and design*. 3rd ed. 2011, Oxford: Elsevier Butterworth-Heinmann.
166. Naim, M. and S. Bahadur, *Work hardening in erosion due to single-particle impacts.* Wear, 1984. **98**: p. 15-26.
167. El-Danaf, E., M. Baig, A. Almajid, W. Alshalfan, M. Al-Mojil, and S. Al-Shahrani, *Mechanical, microstructure and texture characterization of API X65 steel.* Materials & Design, 2013. **47**: p. 529-538.
168. Karlsson, B. and G. Lindén, *Plastic deformation of ferrite—pearlite structures in steel.* Materials Science and Engineering, 1975. **17**(2): p. 209-219.
169. Jiang, J., M. Stack, and A. Neville, *Modelling the tribo-corrosion interaction in aqueous sliding conditions.* Tribology International, 2002. **35**(10): p. 669-679.
170. Jiang, J., Y. Xie, M.A. Islam, and M. Stack, *The Effect of Dissolved Oxygen in Slurry on Erosion–Corrosion of En30B Steel.* Journal of Bio- and Tribo-Corrosion, 2017. **3**(4): p. 45.
171. Prozhega, M., N. Tatus, S. Samsonov, O.Y. Kolyuzhni, and N. Smirnov, *Experimental study of erosion-corrosion wear of materials: A review.* Journal of Friction and Wear, 2014. **35**(2): p. 155-160.
172. Rajahram, S.S., T.J. Harvey, and R.J.K. Wood, *Evaluation of a semi-empirical model in predicting erosion–corrosion.* Wear, 2009. **267**(11): p. 1883-1893.
173. Rincon, H., J.R. Shadley, E.F. Rybicki, and K.P. Roberts, *Erosion-Corrosion of Carbon Steel in CO_2 Saturated Multiphase Flows Containing Sand.* CORROSION 2006, 2006.

174. Zeng, L., G. Zhang, and X. Guo, *Erosion–corrosion at different locations of X65 carbon steel elbow.* Corrosion Science, 2014. **85**: p. 318-330.
175. Zeng, L., G.A. Zhang, X.P. Guo, and C.W. Chai, *Inhibition effect of thioureidoimidazoline inhibitor for the flow accelerated corrosion of an elbow.* Corrosion Science, 2015. **90**: p. 202-215.
176. De Waard, C., U. Lotz, and D. Milliams, *Predictive model for CO_2 corrosion engineering in wet natural gas pipelines.* Corrosion, 1991. **47**(12): p. 976-985.
177. Halvorsen, A.M. and T. Sontvedt, *CO_2 Corrosion Model for Carbon Steel Including Wall Shear Stress Model for Multiphase Flow and Limits for Production Rate to Avoid Mesa Attack*, in *CORROSION 99*. 1999, NACE International: San Antonio, TX.
178. Harvey, T., J. Wharton, and R. Wood, *Development of synergy model for erosion–corrosion of carbon steel in a slurry pot.* Tribology-Materials, Surfaces & Interfaces, 2007. **1**(1): p. 33-47.
179. Nešiĉ, S. and J. Postlethwaite, *Hydrodynamics of disturbed flow and erosion-corrosion. Part I - Single-phase flow study.* The Canadian Journal of Chemical Engineering, 1991. **69**(3): p. 698-703.
180. Ramachandran, S. and V. Jovancicevic, *Molecular modeling of the inhibition of mild steel CO_2 corrosion by imidazolines.* CORROSION, 1998. **55**(3): p. 259-267.
181. Hassani, S., K.P. Roberts, S.A. Shirazi, J.R. Shadley, E.F. Rybicki, and C. Joia, *Characterization and Prediction of Chemical Inhibition Performance for Erosion-Corrosion Conditions in Sweet Oil and Gas Production.* Corrosion, 2012. **68**(10): p. 885-896.
182. Tan, Y.J., S. Bailey, and B. Kinsella, *An investigation of the formation and destruction of corrosion inhibitor films using electrochemical impedance spectroscopy (EIS).* Corrosion Science, 1996. **38**(9): p. 1545-1561.
183. Schmitt, G.A. and M. Mueller, *Critical Wall Shear Stresses in CO_2 Corrosion of Carbon Steel*, in *CORROSION 99*. 1999, NACE International: Houston, TX.
184. Ramachandran, S., M.B. Ward, K.A. Bartrip, and V. Jovancicevic, *Inhibition of the effects of particle impingement*, in *CORROSION 2002*. 2002, NACE International: Denver, CO.
185. Ige, O., R. Barker, X. Hu, L. Umoru, and A. Neville, *Assessing the influence of shear stress and particle impingement on inhibitor efficiency through the application of in-situ electrochemistry in a CO_2-saturated environment.* Wear, 2013. **304**(1): p. 49-59.
186. Schmitt, G., M. Bakalli, and C. Werner. *Fluid Mechanical Interactions of Turbulent Flowing Liquids with the Wall - Revisited with a New Electrochemical Tool*. in *CORROSION 2005*. 2005. Houston, TX: NACE International.
187. Schmitt, G. and M. Bakalli, *Advanced models for erosion corrosion and its mitigation.* Materials and Corrosion, 2008. **59**(2): p. 181-192.
188. Li, W., B.F.M. Pots, B. Brown, K.E. Kee, and S. Nesic, *A direct measurement of wall shear stress in multiphase flow - Is it an important parameter in CO_2 corrosion of carbon steel pipelines?* Corrosion Science, 2016. **110**: p. 35-45.

189. Schmitt, G., *Drag reduction by corrosion inhibitors – A neglected option for mitigation of flow induced localized corrosion.* Materials and Corrosion, 2001. **52**(5): p. 329-343.
190. Jovancicevic, V., S. Ramachandran, Y.S. Ahn, and B. Alink, *Corrosion Inhibition and Drag Reduction in Multiphase Flow*, in *CORROSION 2001*. 2001, NACE International: Houston, TX.
191. McMahon, A.J., J.W. Martin, and L. Harris, *Effects of Sand and Interfacial Adsorption Loss on Corrosion Inhibitor Efficiency*, in *CORROSION 2005*. 2005, NACE International: Houston, TX.
192. Ramachandran, S., Y.S. Ahn, V. Jovancicevic, and J. Bassett. *Further advances in the development of erosion corrosion inhibitors*. in *CORROSION 2005*. 2005. Houston, TX: NACE International.
193. Dave, K., K. Roberts, J. Shadley, E. Rybicki, S. Ramachandran, and V. Jovancicevic, *Effect of a corrosion inhibitor for oil and gas wells when sand is produced*, in *CORROSION 2008*. 2008, NACE International: New Orleans, LA.
194. Tummala, K., K.P. Roberts, J. Shadley, E. Rybicki, and S. Shirazi, *Effect of Sand Production and Flow Velocity on Corrosion Inhibition Under Scale Forming Conditions*, in *CORROSION 2009*. 2009, NACE International: Atlanta, GA.
195. Pedersen, A., K. Bilkova, E. Gulbrandsen, and J. Kvarekvål, *CO_2 corrosion inhibitor performance in the presence of solids: test method development*, in *CORROSION 2008*. 2008, NACE International: New Orleans, LA.
196. Ayello, F., W. Robbins, S. Richter, and S. Nesic, *Crude oil chemistry effects on inhibition of corrosion and phase wetting*, in *CORROSION 2011*. 2011, NACE International: Houston, TX.
197. Shadley, J., S. Shirazi, E. Dayalan, and E. Rybicki. *Using an Inhibitor to Combat Erosion-Corrosion in Carbon Steel Piping-How Much Does it Help?* in *Offshore Technology Conference*. 1996. Houston, TX: Offshore Technology Conference.
198. Tandon, M., J.R. Shadley, E.F. Rybicki, K.P. Roberts, S. Ramachandran, and V. Jovancicevic, *Flow Loop Studies of Inhibition of Erosion-Corrosion in CO_2 Environments with Sand*, in *CORROSION 2006*. 2006, NACE International: San Diego, CA.
199. Gamry. *Polarization Resistance Tutorial - Getting Started*. 2018; Available from: https://www.gamry.com/application-notes/corrosion-coatings/corrosion-techniques-polarization-resistance/.
200. Stern, M. and A.L. Geary, *Electrochemical polarization I. A theoretical analysis of the shape of polarization curves.* Journal of the Electrochemical Society, 1957. **104**(1): p. 56-63.
201. McCafferty, E., *Validation of corrosion rates measured by the Tafel extrapolation method.* Corrosion Science, 2005. **47**(12): p. 3202-3215.
202. Epelboin, I., M. Keddam, and H. Takenouti, *Use of impedance measurements for the determination of the instant rate of metal corrosion.* Journal of Applied Electrochemistry, 1972. **2**(1): p. 71-79.
203. Farelas, F., M. Galicia, B. Brown, S. Nesic, and H. Castaneda, *Evolution of dissolution processes at the interface of carbon steel corroding in a CO_2 environment studied by EIS.* Corrosion Science, 2010. **52**(2): p. 509-517.

204. Lorenz, W.J. and F. Mansfeld, *Determination of corrosion rates by electrochemical DC and AC methods.* Corrosion Science, 1981. **21**(9–10): p. 647-672.
205. Amirudin, A. and D. Thieny, *Application of electrochemical impedance spectroscopy to study the degradation of polymer-coated metals.* Progress in Organic Coatings, 1995. **26**(1): p. 1-28.
206. Malvern, *Determination of the particle absorption for laser diffraction size calculations.* 2009.
207. COMSOL. *Navier-Stokes Equations*. 2018; Available from: https://www.comsol.com/multiphysics/navier-stokes-equations.
208. COMSOL, *COMSOL Multiphysics 5.2a CFD Module User's Guide*. 2016.
209. Nešić, S., J. Postlethwaite, and D.J. Bergstrom, *Calculation of wall-mass transfer rates in separated aqueous flow using a low Reynolds number κ-ε model.* International Journal of Heat and Mass Transfer, 1992. **35**(8): p. 1977-1985.
210. Outirite, M., M. Lagrenée, M. Lebrini, M. Traisnel, C. Jama, H. Vezin, and F. Bentiss, *ac impedance, X-ray photoelectron spectroscopy and density functional theory studies of 3,5-bis(n-pyridyl)-1,2,4-oxadiazoles as efficient corrosion inhibitors for carbon steel surface in hydrochloric acid solution.* Electrochimica Acta, 2010. **55**(5): p. 1670-1681.
211. Angioletti, M., E. Nino, and G. Ruocco, *CFD turbulent modelling of jet impingement and its validation by particle image velocimetry and mass transfer measurements.* International Journal of Thermal Sciences, 2005. **44**(4): p. 349-356.
212. Phares, D.J., G.T. Smedley, and R.C. Flagan, *The wall shear stress produced by the normal impingement of a jet on a flat surface.* Journal of Fluid Mechanics, 2000. **418**: p. 351-375.
213. Giralt, F. and O. Trass, *Mass transfer from crystalline surfaces in a turbulent impinging jet part I. Transfer by erosion.* The Canadian Journal of Chemical Engineering, 1975. **53**(5): p. 505-511.
214. Lyu, P., *How Do I Compute Lift and Drag?*, in *COMSOL BLOG*. 2015: https://www.comsol.com/blogs/how-do-i-compute-lift-and-drag/.
215. Durst, F., D. Miloievic, and B. Schönung, *Eulerian and Lagrangian predictions of particulate two-phase flows: a numerical study.* Applied Mathematical Modelling, 1984. **8**(2): p. 101-115.
216. Clift, R. and W. Gauvin, *Motion of entrained particles in gas streams.* The Canadian Journal of Chemical Engineering, 1971. **49**(4): p. 439-448.
217. Tian, L. and G. Ahmadi, *Particle deposition in turbulent duct flows - comparisons of different model predictions.* Journal of Aerosol Science, 2007. **38**(4): p. 377-397.
218. Jordan, K.G., *Erosion in multiphase production of oil & gas*, in *CORROSION 98*. 1998, NACE International: San Diego, CA.
219. Wenglarz, R. *Boundary layer effects on impingement and erosion*. in *Proceedings of the Third Joint Thermophysics, Fluids, Plasma, and Heat Transfer Conference*. 1982. St. Louis, MO: American Society of Mechanical Engineers.
220. McLaury, B., J. Wang, S. Shirazi, J. Shadley, and E. Rybicki. *Solid particle erosion in long radius elbows and straight pipes*. in *SPE Annual*

Technical Conference and Exhibition. 1997. San Antonio, TX: Society of Petroleum Engineers.
221. Noorani, R., *3D Printing: Technology, Applications, and Selection*. 2017, London: CRC Press.
222. Ashby, M.F. and D.R.H. Jones, *Engineering materials 2: an introduction to microstructures, processing and design*. 3rd ed. 2005, London: Elsevier Butterworth-Heinemann.
223. Frei, W., *Which Turbulence Model Should I choose for My CFD Application?*, in *COMSOL Blog*. 2017.
224. Yunus, A.C. and J.M. Cimbala, *Fluid mechanics fundamentals and applications*. McGraw-Hill. 2006, Boston.
225. Enayet, M.M., M.M. Gibson, A.M.K.P. Taylor, and M. Yianneskis, *Laser-Doppler measurements of laminar and turbulent flow in a pipe bend.* International Journal of Heat and Fluid Flow, 1982. **3**(4): p. 213-219.
226. Sydberger, T. and U. Lotz, *Relation between mass transfer and corrosion in a turbulent pipe flow.* Journal of the Electrochemical Society, 1982. **129**(2): p. 276-283.
227. Byron Bird, R., Warren E. Stewart, and E.N. Lightfoot, *Transport phenomena*. 2nd ed. 2007, Chichester John Wiley & Sons.
228. Cussler, E.L., *Diffusion: mass transfer in fluid systems*. 1984, Cambridge: Cambridge University Press.
229. Tominaga, Y. and T. Stathopoulos, *Turbulent Schmidt numbers for CFD analysis with various types of flowfield.* Atmospheric Environment, 2007. **41**(37): p. 8091-8099.
230. Koeltzsch, K., *The height dependence of the turbulent Schmidt number within the boundary layer.* Atmospheric Environment, 2000. **34**(7): p. 1147-1151.
231. Wang, Y., J. Postlethwaite, and D. Bergstrom, *Modelling mass transfer entrance lengths in turbulent pipe-flow with applications to small cathodes for measuring local mass transfer rates.* Journal of Applied Electrochemistry, 1996. **26**(5): p. 471-479.
232. Atkins, P., J. De Paula, and J. Keeler, *Atkins' physical chemistry*. 9th ed. 2010, Oxford: Oxford University Press.
233. Chen, Y., T. Hong, M. Gopal, and W.P. Jepson, *EIS studies of a corrosion inhibitor behavior under multiphase flow conditions.* Corrosion Science, 2000. **42**(6): p. 979-990.
234. Hutchings, I., *Strain rate effects in microparticle impact.* Journal of Physics D: Applied Physics, 1977. **10**(14): p. L179.
235. Chia, C.-J., F. Giralt, and O. Trass, *Mass transfer in axisymmetric turbulent impinging jets.* Industrial & Engineering Chemistry Fundamentals, 1977. **16**(1): p. 28-35.

Appendix A
COMSOL Multiphysics Model Worksheets for CFD Simulations in SIJ Nozzle Flow

This appendix includes worksheets for each of the SIJ models developed in this thesis, detailing the steps required to develop each model and how results were obtained using the model. All CFD models were developed using COMSOL Multiphysics 5.2a. These worksheets follow the format of COMSOL Application Manuals. These application files assume a basic knowledge of the COMSOL Multiphysics software layout and that the user has a knowledge of how to create basic models on COMSOL Multiphysics, e.g. able to add Physics or run Studies etc. It should be noted that later versions of COMSOL Multiphysics may differ from the instructions given in this Appendix.

A.1 Simulation of Particle Trajectories in an SIJ Nozzle

MODEL WIZARD

1. New Model Wizard
2. In Select Space Dimension, select **2D Axisymmetric**
3. In Select Physics select, select Fluid Flow > Single Phase Flow > Turbulent Flow > **Turbulent Flow, k-ω (spf)**
4. Click **Add**
5. Click **Study**
6. In Select Study, select Preset Studies > **Stationary**
7. Click **Done**

ADD FURTHER STUDIES

1. Select Physics tab, **Add Physics**
2. In Select Physics select, select Fluid Flow > Particle Tracing > **Particle Tracing for Fluid Flow (fpt)**
3. Click **Add to Component**
4. Select Study tab, **Add Study**
5. In Select Study, select Preset Studies > **Time Dependent**

PARAMETERS

The following parameters in Table A.1 were added to Global Definitions.

Table A.1 Parameters for particle tracking SIJ nozzle model

Name	Expression	Value	Description
u_mean	20[m/s]	20 m/s	Flow velocity
rho_in	983.2[kg/m^3]	983.2 kg/m^3	Input fluid density
mu_in	4.67e-4[Pa*s]	4.67 x 10^{-4} Pa·s	Input fluid viscosity
ra	2[mm]	0.002 m	SIJ nozzle radius
H	5[mm]	0.005 m	SIJ nozzle height to sample
visc_ramp	1	1	Viscosity ramping parameter
dp	250[um]	2.5 x 10^{-4} m	Particle diameter
rho_p	2650[kg/m^3]	2650 kg/m^3	Particle density
g	9.81[m/s^2]	9.81 m/s^2	Acceleration due to gravity

GEOMETRY

The SIJ nozzle geometry in Figure A.1 was constructed using the **Line** function in the **Geometry** tab.

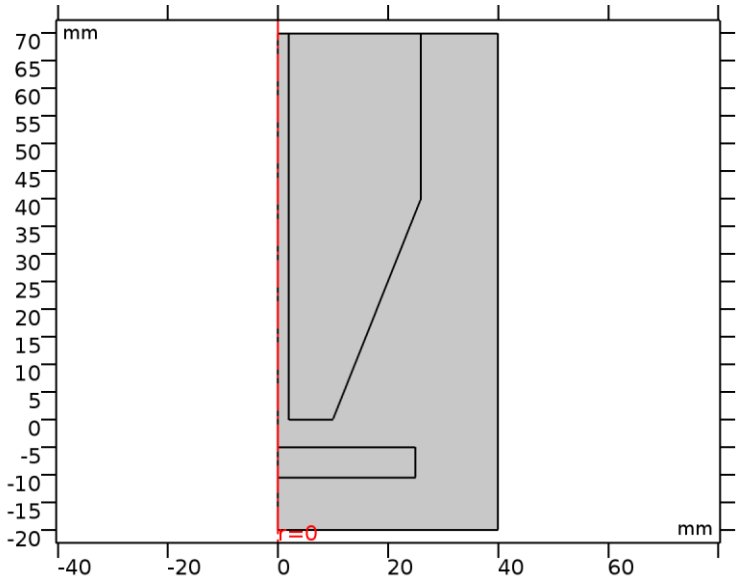

Figure A.1 SIJ nozzle model geometry used for fluid flow and particle tracking predictions

The SIJ geometry consisted of three polygons:

1. SIJ nozzle
2. Sample and sample holder
3. Fluid domain

Each individual line drawn in the three polygons had the control points as listed in Table A.2, Table A.3 and Table A.4. Each segment refers to a different Line that was constructed to form the shape.

Table A.2 Control points for SIJ nozzle polygon consisting of linear segments

Segment	r1 (mm)	r2 (mm)	z1 (mm)	z2 (mm)
1	ra	10	0	0
2	10	26	0	40
3	26	26	40	70
4	26	ra	70	70
5	ra	ra	70	0

Table A.3 Control points for SIJ sample and sample holder consisting of linear segments

Segment	r1 (mm)	r2 (mm)	z1 (mm)	z2 (mm)
1	0	25	-H	-H
2	25	25	-H	-H-5.5
3	25	0	-H-5.5	-H-5.5
4	0	0	-H-5.5	-H-5.5

Table A.4 Control points for fluid flow domain consisting of linear segments

Segment	r1 (mm)	r2 (mm)	z1 (mm)	z2 (mm)
1	0	40	70	70
2	40	40	70	-20
3	40	0	-20	-20

MATERIALS

Water flow was specified with the required density and viscosity to represent 60°C water flow in the SIJ. A **Blank Material** was added by right-clicking **Materials**. The fluid flow domain was required to be selected to define which parts of the geometry these material conditions applied to. **Domain 1** was chosen as shown in Figure A.2, where the fluid flow domain is highlighted in blue.

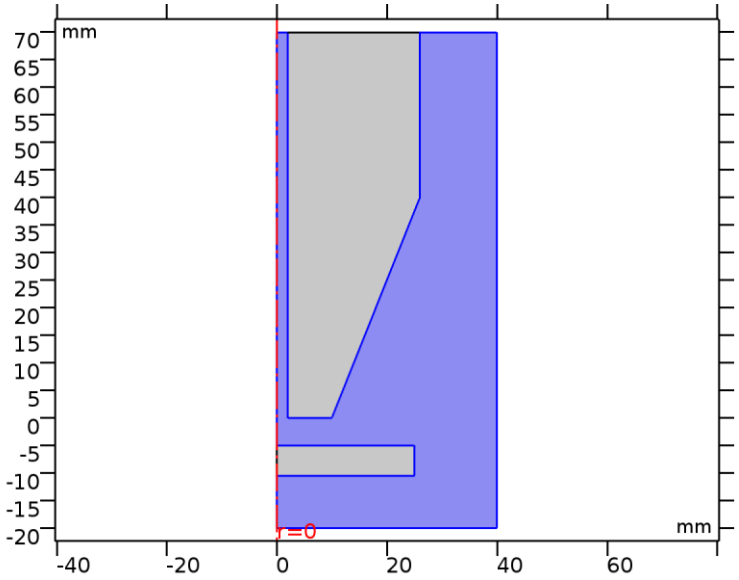

Figure A.2 Domain 1 showing the geometry of the SIJ nozzle and the regions where fluid flow was modelled, highlighted in blue

The parameters shown in Table A.5 where added to the **Expression** output properties in **Basic (def)** settings.

Table A.5 Parameters added to material properties settings

Name	Value	Unit
Density	rho_in	kg/m³
Dynamic viscosity	visc_ramp*mu_in	Pa·s

TURBULENT FLOW, k-ω (SPF)

The following parameters were used as default:

1. Default settings for the turbulent flow properties were assumed for incompressible flow. Gravity and swirl flow were not included.
2. Fluid properties were defined for both viscosity and density **From material**.
3. Initial values of velocity and pressure were assumed to be 0 with standard initial values for k and ω used.
4. Axial symmetry was defined automatically from the model geometry
5. **Wall functions** were applied at all walls

An **Inlet** boundary condition was added to the Physics, by right clicking **Turbulent Flow, k-ω (spf)**. Boundary '7' was chosen as the inlet at the top of the nozzle, as shown in Figure A.3 (highlighted in blue). A **Normal inflow velocity** of **u_mean** was specified and default **Turbulent intensity** and **Turbulence length scale** parameters were chosen.

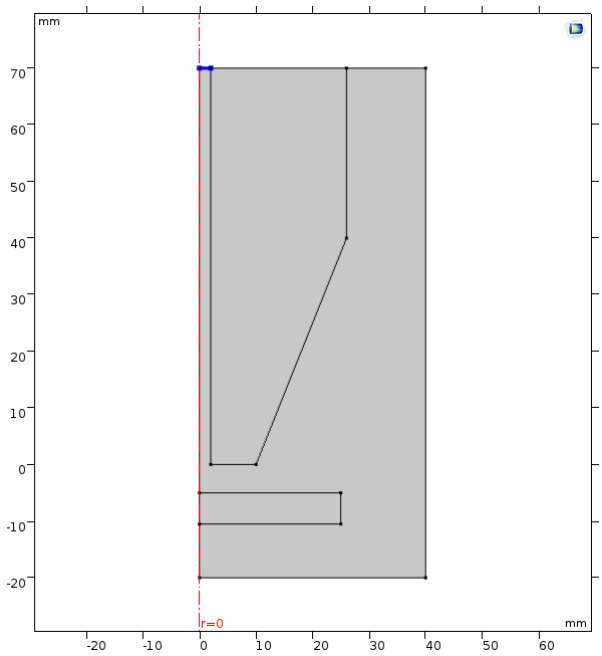

Figure A.3 Inlet boundary (highlighted in blue) at the top of the SIJ nozzle used as fluid inlet

An **Outlet** boundary condition was added to the Physics, by right clicking **Turbulent Flow, *k-ω* (spf)**. Boundaries '2' and '14' were chosen as the outlet at the top and bottom of the SIJ reservoir, as shown in Figure A.4 (highlighted in blue). A **Pressure** boundary condition was chosen at a value of 0 Pa (gauge pressure), and **Suppress backflow** was chosen.

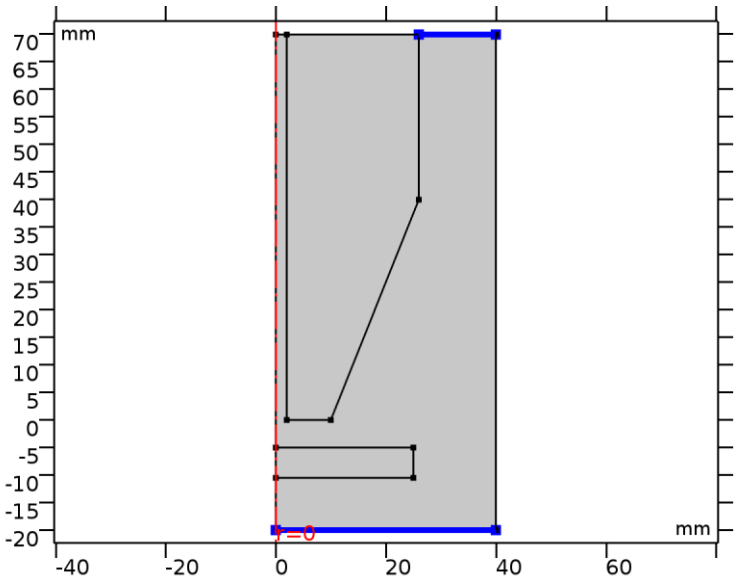

Figure A.4 Outlet boundaries (highlighted in blue) at the top and bottom of the SIJ fluid reservoir used as fluid outlets

PARTICLE TRACING FOR FLUID FLOW (fpt)

The following parameters were used as default:

1. Default settings for the particle properties assuming **Newtonian** formulation and the **Specify mass flow rate** condition for **Domain 1**
2. **Axial Symmetry** boundary chosen automatically based on geometry with the **Bounce** wall condition and **None** primary particle condition
3. **Freeze** wall condition chosen for all walls and **None** primary particle condition
4. **Particle density** specified in **Particle Properties** as *rho_p* and **Particle diameter** specified as *dp*
5. **Particle type** specified as **Solid particles**
6. **Charge number** = 0 specified in **Particle Properties**

An **Inlet** boundary condition was specified as the inlet boundary as fluid flow, Boundary '7'. **Density** was chosen for **Initial position**, **50,000** particles specified for **Number of particles per release** and **Density proportional to spf.U**. An **Initial velocity** of **Expression** was chosen and **Velocity field** of **Velocity field (spf)** was chosen to link fluid flow to particles. All other parameters were kept as default parameters.

Drag Force was added by right clicking **Particle Tracing for Fluid Flow (fpt)**. **Domain 1** was chosen for the fluid flow where the force acts on the particles. The following parameters were input:

- Drag law: **Schiller-Naumman**
- Velocity field: **Velocity field (spf)**
- Dynamic viscosity: **From material**
- Density: **From material**
- Turbulent dispersion model: **Discrete random walk**
- Turbulent kinetic energy: **Turbulent kinetic energy (spf)**
- Turbulent dissipation rate: **Turbulent dissipation rate (spf/fp1)**
- Lagrangian time scale coefficient: **0.2**
- Particles to affect: **All**

Additional forces were added by right clicking and selecting **Force** in the Particle Tracing for Fluid Flow module (fpt). **Buoyancy** force was added with Equation (6.11) entered, Equation (6.10) entered for **Pressure Gradient** and Equation (6.12) for **Added Mass**. All forces were specified for **Domain 1**.

MESH

A **Free Triangular** mesh was specified for **Domain 1** with the **Size** parameters specified in Table A.6. Note, these parameters were specified in Size for the overall mesh, not an additional Size added within the Free Triangular settings.

Table A.6 Mesh size parameters for SIJ nozzle mesh

Description	Value
Maximum element size	0.4
Minimum element size	0.0008
Curvature factor	0.25
Maximum element growth rate	1.2

A **Distribution** mesh was also added by right clicking **Free Triangular** to increase the number of elements in the mesh around the exit of the SIJ nozzle to improve accuracy, as shown in Figure A.5. Boundary '9' was chosen in **Boundary Selection** with **Predefined distribution type** in **Distribution properties**. The following properties were added:

- Number of elements: **40**
- Element ratio: **5**
- Distribution method: **Arithmetic sequence**
- **Reverse direction** selected

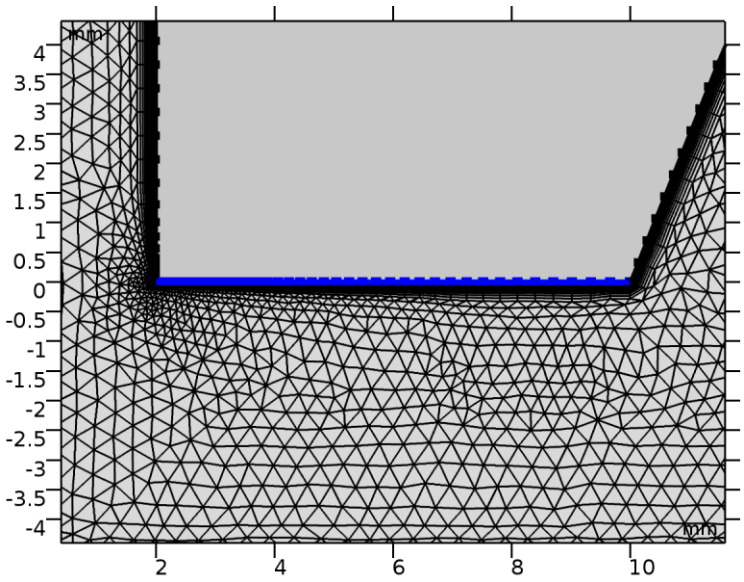

Figure A.5 Distribution mesh on boundary '9' (highlighted in blue), with a higher concentration of elements in this region

Boundary Layers were also included to improve the accuracy of predictions near to the wall, with smaller rectangular boundary elements added close to the wall. Boundary Layers were added on all walls in the geometry. The following parameters were included:

- Number of boundary layers: **40**
- Boundary layer stretching factor: **1.2**
- Thickness of first layer: **Manual**
- Thickness: **1e-4**

STUDY

Study 1 (Stationary study) is solved for the **Turbulent Flow k-ω (spf)** physics to predict fluid flow through the SIJ nozzle. All parameters not detailed below are kept as default. The following parameters are changed:

- Physics and Variables Selection: **Turbulent Flow, k-ω** ONLY. Particle Tracing should NOT be solved in this Study.
- **Study Extensions** > **Auxiliary Sweep** selected.
- Sweep type: **Specified combinations**
- Parameter name: **visc_ramp**
- Parameter value list: **10 1**
- Run continuation for: **Last parameter**

An **Auxiliary Sweep** is run to improve convergence in low viscosity conditions at higher temperatures. Viscosity is multiplied by factor of 10, with it being more favourable to solve fluid flow models with a higher viscosity fluid. The solution from this simulation is then used as an initial estimate for the actual viscosity, improving convergence of the model. A **Parametric Sweep** can also be completed in **Study 1** to complete parametric sweeps for different parameters input in the model, such as flow velocity, to automatically complete simulations for different flow velocities.

Study 2 (Time-dependent study) is solved for the **Particle Tracing for Fluid Flow (fpt)** physics. All parameters not detailed below are kept as default. The following parameters are changed:

- Physics and Variables Selection: **Particle Tracing for Fluid Flow** ONLY. Fluid flow should NOT be solved in this Study.
- Time unit: **s** in **Study Settings**
- Times: **range(0,5.0e-5,0.1)**
- Tolerance: **Physics controlled**

The following settings were changed in **Values of Dependent** Variables. **Physics** controlled was selected for **Initial values of variables solved for**. The following settings were used for **Value of variables not solved for**:

- Settings: **User controlled**
- Method: **Solution**
- Study: **Study 1, Stationary**
- Parameter value (visc_ramp): **1**

RESULTS

To calculate shear stress a **1D Plot Group** was added by right-clicking **Results**. **Study 1/Solution 1 (sol1)** was chosen for **Data** Set. **Line Graph 1**

was added by right-clicking **1D Plot Group** to plot shear stress. Equation (6.5) was added into **Expression** to calculate shear stress across boundary ‘6’ the surface of the sample exposed to the flow in the SIJ.

To export data for particle impact properties, **Data** was added by right-clicking **Export**. The following properties were specified to output particle impact angles, particle position and particle impact velocities:

- Data set: **Particle 1**
- Time selection: **Last**
- Four rows added in Expression for the following parameters: **qr**, **qz**, **fpt.V**, **fpt.phii**

A.2 Simulation of Particle Trajectories in an Elbow

The same methodology as explained in Appendix A.1 for the SIJ was used to predict fluid flow and particle trajectories in an elbow, with the exception of the geometry. A 3D model was developed within **Geometry**.

A.3 Prediction of Mass Transfer Coefficients in the SIJ

Detail is provided for predicting mass transfer coefficients in the SIJ geometry as used for the particle tracking SIJ model. The following **Physics** and **Study** options were chosen to model fluid flow and mass transfer coefficients.

- Physics 1: **Turbulent Flow, k-ω**
- Physics 2: **Turbulent Flow, SST (spf2)**
- Physics 3: **Transport of Diluted Species (tds)**
- Study 1: **Stationary**
- Study 2: **Stationary with Initialization**
- Study 3: **Stationary**

The following **Parameters** were included in the model, shown in Table A.7.

GEOMETRY

The same geometry settings were used as described in Appendix A.1 for the SIJ particle tracking model.

Table A.7 Parameters for SIJ mass transfer coefficient predictions

Name	Expression	Value	Description
u_mean	20[m/s]	20 m/s	Flow velocity
ra	2[mm]	0.002 m	Nozzle Radius
H	5.0[mm]	0.005 m	Nozzle height to sample
visc_ramp	1	1	Ramping Parameter
D0	9.31e-9[m^2/s]	9.31E−9 m²/s	Diffusion coefficient H+
Hin	10^ - 3[mol/L]	1 mol/m³	Initial Concentration of H+
mu_in	0.467e-3[Pa*s]	4.67E−4 Pa·s	Input Fluid Viscosity
rho_in	982.3[kg/m^3]	982.3 kg/m³	Input Fluid Density
Re	rho_in*u_mean*2*ra/mu_in[1]	1.6827E5	Reynolds Number
Cf	(((2*log10(Re)) - 0.65)^ - 2.3)[1]	0.0052477	Skin Friction
fric_vel	((Cf*0.5*rho_in*u_mean^2)/rho_in)^0.5	1.0245 m/s	Friction Velocity
yplus	0.5	0.5	Desired y plus
ycell	(yplus*mu_in/(rho_in*fric_vel))	2.3203E−7 m	Estimated distance to first cell
T0	298.15	298.15	Reference temperature
Tin	333.15[K]	333.15 K	Actual temperature
mu0	0.89e-3[Pa*s]	8.9E−4 Pa·s	Reference viscosity
D	D0*(mu0/mu_in)*(Tin/T0)	1.9826E−8 m²/s	Diffusion coefficient at actual temperature

MATERIALS

The same material settings were used as described in Appendix A.1 for the SIJ particle tracking model.

TURBULENT FLOW, k-ω (SPF)

The same **Turbulent Flow, k-ω (spf)** settings were used as described in Appendix A.1 for the SIJ particle tracking model. The k-ω was solved initially as it has a higher convergence success rate than the SST turbulence model, providing an initial solution for the SST turbulence model used for mass transfer coefficient predictions.

TURBULENT FLOW, SST (SPF2)

All parameters for the **Turbulent Flow, SST (spf2)** were identical to the **Turbulent Flow, k-ω (spf)** settings, with the exception of the following parameters, unique to the SST model settings:

- Boundary conditions in **Wall** settings: **No slip**
- All initial turbulence parameters kept as default settings for **spf2**

TRANSPORT OF DILUTED SPECIES (TDS)

The **Transport of Diluted Species** (tds) physics was added in **Add Physics > Chemical Species Transport > Transport of Diluted Species (tds)**. This module was used to simulate the transport of H^+ ions through the SIJ nozzle to calculate mass transfer coefficients on the SIJ sample surface.

To calculate mass transfer coefficients, a mass transfer coefficient variable was added to **Variables** by right-clicking **Definitions** in **Component 1**. The following was input as a variable:

- Name: **mtc**
- Expression: **tds.bndFlux_c/Hin**

This expression calculates the flux at a specified boundary in the **Results**, explained later, and is the expression that represents Equation (8.19).

In the **Transport of Diluted Species (tds)** settings, **Convection** is selected from **Additional transport mechanisms** and **Domain 1** is selected for the region in the geometry of species transport.

The following properties are specified for **Transport Properties**, with default parameters unchanged for all other settings:

- Velocity field: **Velocity field (spf2)**
- Material: **None**
- Diffusion coefficient: **User defined**
- Value for diffusion coefficient: **D**
- Property of diffusion coefficient: **Isotropic**

A **Turbulent Mixing** setting is also added by right-clicking **Transport Properties**. The **Turbulent kinematic viscosity (spf2/fp1)** is chosen (note: NOT spf1 so this parameter is taken from the SST model solution). A **Turbulent Schmidt number** of 0.5 is specified.

Axial Symmetry is auto-selected from the model geometry.

No Flux is specified on all walls with the exception of the sample surface wall.

Initial Values is set as a concentration of 0 mol/m^3

A **Concentration** setting is added for the sample surface, with the concentration at this surface boundary '6' set to 0 mol/m^3. Note: this does not need to be added to the model and a **No Flux** condition can be assumed. However, this model is defined as consuming all H^+ ions at this wall. This **Concentration** is used to make reference to this for the benefit of the user of the model, but is not essential.

An **Inflow** setting is added and specifies the species inlet as the same as the fluid flow inlet boundary '7'. The **Concentration** at inlet is defined as **Hin**.

An **Outflow** setting is also added to the model and specifies the species outlet as the same as the fluid flow outlet (boundary '2' and boundary '14').

MESH

The same mesh components (i.e. **Free Triangular** and **Boundary Layers**) were used in the mesh for the SIJ nozzle for mass transfer coefficient predictions. The Size parameters listed in Table A.8 were used for the mesh.

Table A.8 Parameters for SIJ nozzle mesh used for mass transfer coefficient predictions

Description	Value
Maximum element size	0.24
Minimum element size	0.001
Curvature factor	0.2

A **Distribution** mesh was also used again on the same boundary as the particle tracking model (boundary ‘9’). However, an **Element ratio** of **10** was used for the mass transfer coefficient model.

Two **Boundary Layers** were added to the mesh. One was used to refine the mesh near to the wall of the sample surface where mass transfer coefficients were calculated and one on all other walls, which did not require the same refinement for accurate predictions.

Boundary Layers 1 was used for the boundary layer mesh on the sample surface wall (boundary ‘6’) and boundary ‘12’, as shown in Figure A.6. Boundary ‘12’ was also included to improve the refinement at the edge of boundary ‘6’ which produced a poor quality mesh in this region when boundary ‘12’ was not included **Boundary Layers 1**. The **Number of boundary layers** was set at 23, **Boundary layer stretching factor** of 1.25, **Thickness of first layer** set as Manual and a **Thickness** of *ycell* added.

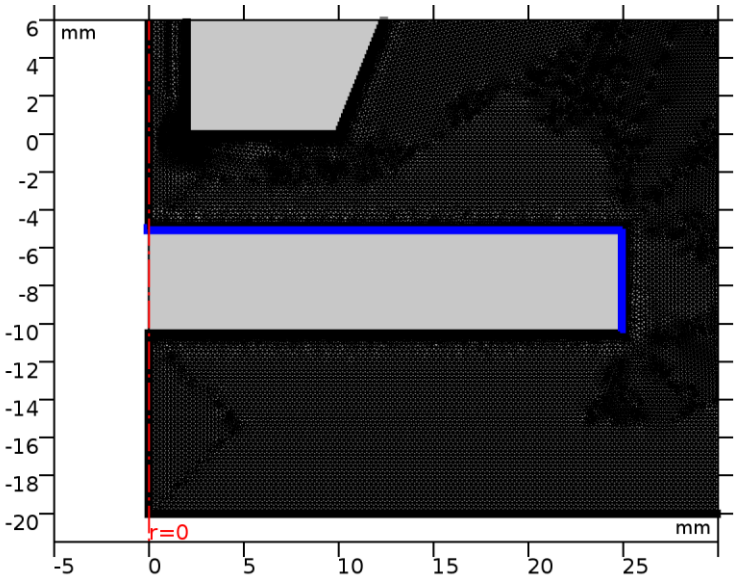

Figure A.6 Boundary layer mesh on ‘boundary 6’ and ‘boundary 12’ (highlighted in blue), for a highly refined mesh at the sample surface to complete mass transfer coefficient predictions.

For **Boundary Layers 2**, the **Number of boundary layers** was set at 12, **Boundary layer stretching factor** of 1.2, **Thickness of first layer** set as Automatic and a **Thickness adjustment factor** of 0.5 added.

STUDY

Study 1 was used to solve **Turbulent Flow, k-ω (spf)** ONLY, using the same settings detailed in Appendix A.1.

Study 2 was used to solve **Turbulent Flow, SST (spf2)** ONLY. For the **Values of Dependent Variables > Values of variables not solved for** in the **Step 1: Wall Distance Initialization** setting the following parameters were specified:

- Settings: **User controlled**
- Method: **Solution**
- Study: **Study 1, Stationary**
- Solution: **Solution 1 (sol1)**
- Parameter value (visc_ramp): **1**

All other parameters were kept as default. An **Auxiliary Sweep** was completed in **Step 2: Stationary** with the same settings as **Study 1**.

Study 3 was used to solve **Transport of Diluted Species (tds)** ONLY. For the **Values of Dependent Variables > Values of variables not solved for** in the **Step 1: Stationary** setting the following parameters were specified:

- Settings: **User controlled**
- Method: **Solution**
- Study: **Study 2, Stationary**
- Solution: **Solution 2 (sol2)**
- Parameter value (visc_ramp): **1**

RESULTS

To plot mass transfer coefficients, the variable **mtc** can be defined in the expression in a **1D Plot Group** > **Line Graph** plot. **Study 3** is chosen for the **Data Set** and **mtc** is defined in the **Expression** with the surface boundary chosen for which the mass transfer coefficient is calculated over boundary ‘6’.

A.4 Mass Transfer Coefficients in Other Geometries

The same methodology as the method defined in Appendix A.3 was used for all other geometries, with the appropriate geometry and conditions defined and the desired wall chosen for mass transfer coefficient calculations.